**TECHNISCHE
UNIVERSITÄT
DRESDEN**

# Quantum signatures of partial barriers in phase space

Dissertation
zur Erlangung des akademischen Grades
Doctor rerum naturalium


vorgelegt von

Matthias Daniel Michler
geboren am 13.07.1982 in Görlitz


Institut für Theoretische Physik
Fachrichtung Physik
Fakultät für Mathematik und Naturwissenschaften
Technische Universität Dresden
2011

Eingereicht am 19.07.2011

1. Gutachter:   Prof. Dr. Roland Ketzmerick

2. Gutachter:   Prof. Dr. Steven L. Tomsovic

Verteidigt am 30.09.2011

# Abstract

Generic Hamiltonian systems have a mixed phase space, in which regular and chaotic motion coexist. In the chaotic sea the classical transport is limited by partial barriers, which allow for a flux $\Phi$ given by the corresponding turnstile area. Quantum mechanically the transport is suppressed if Planck's constant is large compared to the classical flux, $h \gg \Phi$, while for $h \ll \Phi$ classical transport is recovered. For the transition between these limiting cases there are many open questions, in particular concerning the correct scaling parameter and the width of the transition.

To investigate this transition in a controlled way, we design a kicked system with a particularly simple phase-space structure, consisting of two chaotic regions separated by one dominant partial barrier. We find a universal scaling with the single parameter $\Phi/h$ and a transition width of almost two orders of magnitude in $\Phi/h$. In order to describe this transition, we consider several matrix models. While the numerical data is not well described by the random matrix model proposed by Bohigas, Tomsovic, and Ullmo, a deterministic $2 \times 2$-model, a channel coupling model, and a unitary model are presented, which describe the transitional behavior of the designed kicked system. This is also confirmed for the generic standard map, suggesting a universal scaling behavior for the quantum transition of a partial barrier.

# Zusammenfassung

Generische Hamilton'sche Systeme besitzen einen gemischten Phasenraum, in dem sowohl reguläre als auch chaotische Dynamik vorkommen. Der klassische Transport in der chaotischen See wird durch partielle Barrieren begrenzt, die nur einen Fluss $\Phi$ hindurch lassen. Der quantenmechanische Transport ist stark unterdrückt, wenn die Planck'sche Konstante groß gegen den klassischen Fluss ist, $h \gg \Phi$. Ist hingegen $h \ll \Phi$ folgt die Quantenmechanik der klassischen Dynamik. Für den Übergangsbereich zwischen diesen Grenzfällen gibt es noch viele offene Fragen, insbesondere bezüglich des richtigen Skalierungsparameters und der Breite des Übergangs.

Um gezielt diesen Übergang zu untersuchen, haben wir ein System mit einem besonders einfachen Phasenraum entworfen. Er besteht aus zwei chaotischen Gebieten, die durch eine dominante partielle Barriere getrennt sind. Es zeigt sich, dass das universelle Verhalten durch den Parameter $\Phi/h$ beschrieben wird und der Übergang sich über zwei Größenordnungen erstreckt. Wir betrachten verschiedene Matrixmodelle um diesen Übergang zu verstehen. Die numerischen Daten werden nicht durch das Zufallsmatrixmodell von Bohigas, Tomsovic und Ullmo beschrieben. Ein deterministisches $2 \times 2$-Modell, eine Kanalkopplung und ein unitäres Matrixmodell beschreiben hingegen den Übergang des entworfenen gekickten Systems. Die Tatsache, dass auch die generische Standardabbildung diesem Verhalten folgt, spricht für ein universelles Verhalten des Quantenübergangs einer partiellen Barriere.

per aspera ad astra

# Contents

# 1 Introduction

In the 1960s Edward N. Lorenz performed meteorological simulations at the Massachusetts Institute of Technology and observed that close-by initial weather conditions yield very different final outcomes [1,2]. This phenomenon of sensitive dependence on initial conditions is known as the butterfly effect and is characteristic for chaotic motion [3]. Although the dynamics obeys deterministic differential equations, the predictability of the motion is limited. The reason for this is the imprecise knowledge of the initial state and the exponential growth of small deviations under the time evolution. Therefore the resulting dynamics seems random and is often described using statistical measures rather than individual trajectories. The opposite extreme of a dynamical system, compared to the chaotic situation, is an integrable system. In such a system the number of conserved quantities equals the number of degrees of freedom $f$ and the dynamics is confined to $f$-dimensional tori in the $2f$-dimensional phase space. Variation of the initial condition changes the final outcomes only slightly and the motion is called regular.

Typical Hamiltonian systems are neither integrable nor chaotic, but have a mixed phase space, in which regular and chaotic motion coexist [4]. Figure 1.1(a) shows an illustration of such a generic two-dimensional mixed phase space. Regular orbits are confined to one-dimensional lines and the whole set of such lines is called regular island. The regular island is surrounded by chaotic orbits. They uniformly fill a two-dimensional region in phase space, which is called chaotic sea. Inside all the holes of the chaotic sea further regular islands exist.

For an ensemble of orbits started in some phase-space region almost all of them will eventually return to the initial region according to the Poincaré recurrence theorem [3, Sec. 7.1.3]. This statement, however, does not provide any information about the time at which a certain orbit returns. Therefore the distribution of recurrence times $R(t)$ is an interesting quantity. For fully chaotic systems it decays exponentially $R(t) \propto \exp(-\alpha \cdot t)$ [5]. This behavior changes completely if we consider systems with a mixed phase space. At large times one typically obtains a power law for the return of chaotic orbits to some initial region $R(t) \propto t^{-\gamma}$ [6].

Such an algebraic decay has also been observed in experiments [7,8], where ultra-cold atoms are placed inside an open billiard system and the number of remaining atoms is recorded as a function of time. For the stadium billiard with hard walls, which is fully chaotic, the fraction of remaining atoms decays exponentially, in accordance with the theoretical prediction. However, if the billiard walls are soft an algebraic decay $t^{-\gamma}$ is observed, which is attributed to regular islands arising in the chaotic sea.
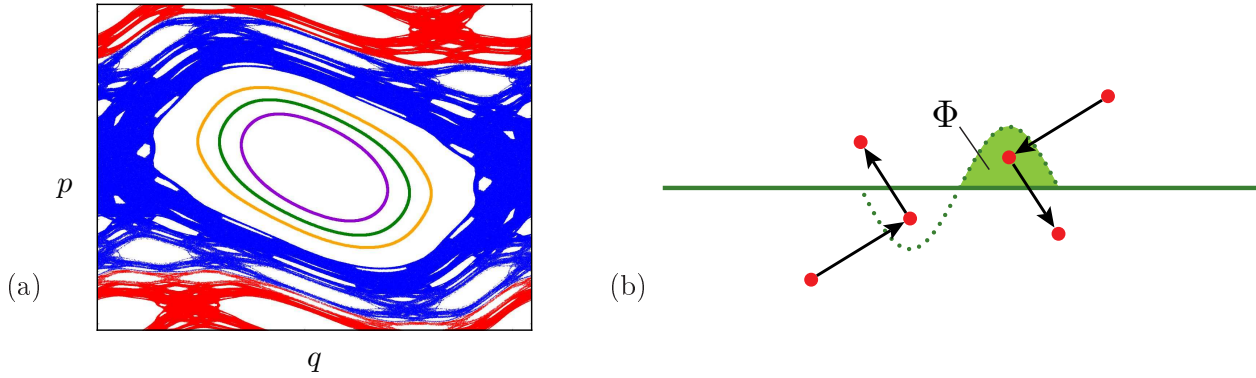
**Figure 1.1:** (a) Illustration of a system with a mixed phase space. In the center three regular tori (violet, green, and orange) in the regular island are shown. They are surrounded by the chaotic sea, which is indicated by two chaotic orbits (blue and red). (b) Illustration of the action of a partial barrier (solid green horizontal line) with flux $\Phi$ crossing it (light green shaded region). The preimage of the partial barrier is indicated by the dotted green line and together with the partial barrier it forms the turnstile. Chaotic orbits, indicated by red dots, entering the turnstile are mapped (arrow) to the opposite region.

What is the reason for the drastic change in the decay behavior? If the regular regions would not affect the chaotic dynamics one would expect an exponential decay also for the mixed phase space. However, in such systems with a mixed phase space chaotic orbits typically remain close to regular islands for long times. This phenomenon has been called stickiness [9–12]. It is the origin of the qualitative change in the return time distribution $R(t)$ and in the decay of correlations [6, 12, 13].

The reason for the stickiness around regular regions are partial barriers [14–20], which are the main topic of this thesis. Partial barriers are lines in the two-dimensional phase space with a non-vanishing flux $\Phi$ crossing them; i.e. a certain amount of phase-space volume $\Phi$ is transported across this line per unit time. Due to area preservation in Hamiltonian systems the volume transported from one side to the other and vice versa is the same. The mechanism of a partial barrier is illustrated in Fig. 1.1(b). Orbits from above the partial barrier enter the right part of the turnstile and are mapped to below, whereas orbits from below may enter the left part of the turnstile and are mapped to above the partial barrier. The two chaotic orbits in Fig. 1.1(a) are separated by such a partial barrier and at large times fill the whole chaotic region. In general there are infinitely many partial barriers in the chaotic part of phase space. However, only those partial barriers, which have the smallest flux are relevant, as they are most limiting for the transport in the chaotic sea. These partial barriers allow for a decomposition of the chaotic sea into sub-regions, that are each quickly mixing within the time scale in which orbits typically leave a region and enter another sub-region. This kind of decomposition gives rise to Markov models for the transport in the chaotic sea, which explain the algebraic decay of recurrence time distributions [17–20].

A partial barrier can originate from a cantorus, the remainder of a torus with quasiperiodic

motion which has been destroyed by a perturbation [21, 22]. Another mechanism giving rise to a partial barrier is the combination of the stable and the unstable manifold of a hyperbolic fixed point [22, 23].

The impact of partial barriers on the classical transport was described in the 1980s. Another question of fundamental importance is the implication of partial barriers to the corresponding quantum system. MacKay, Meiss, and Percival conjectured that for the corresponding quantum system the size of the turnstile $\Phi$ needs to be compared to the size of Planck's constant $h$ [15]. Depending on the ratio $\Phi/h$ the quantum evolution uses the classical transport channel ($\Phi \gg h$) or quantum transport is suppressed ($\Phi \ll h$). For $\Phi \ll h$ quantum mechanics is even more restrictive than classical mechanics. The partial barrier acts as a barrier for the quantum system, because the classical transport channel is not resolved by the quantum system, whose resolution is determined by $h$. The phenomenon of quantum suppression of transport gives rise to localization of wave packets, started in one chaotic region, for large times [23–28]. For example it was observed for the multiphoton ionization of excited atoms that the classical flux needs to exceed Planck's constant in order to find significant ionization [21]. In this case the partial barrier acts like a torus for large $h$. Also experimentally the role of partial barriers for the quantum system has been investigated [29]. Here, the quantum suppression of transport implies the localization of eigenstates in regions limited by partial barriers. In the neighborhood of a regular island a hierarchy of partial barriers gives rise to the localization of chaotic eigenstates close to the regular region, so-called 'hierarchical states' [30]. Recently the quantum signatures of partial barriers were studied for microcavities [31, 32], which can be used e.g. to build microlasers [33, 34]. Generically these microcavities have a mixed phase space and partial barriers exist in the chaotic sea. Experimental evidence for the impact of turnstile transport on the quantum system is presented in Refs. [31, 35]. In Ref. [36] it was speculated that oscillations in the quality factor of the lasing modes arise due to partial barriers in the chaotic part of phase space.

While the quantum transition of a partial barrier from quantum suppression for $\Phi \ll h$ to classical transport for $\Phi \gg h$ is qualitatively understood, a quantitative description is still missing. In particular there are several open questions: Is the ratio $\Phi/h$ the correct scaling parameter of the transition? Does the transition take place at $\Phi = h$? How broad is this transition?

The aim of this thesis is to answer these questions and to give a quantitative description of the quantum transition of a partial barrier from quantum suppression to classical transport. To investigate this transition in a controlled way, we design a system with one isolated partial barrier. This is in contrast to the generic case that usually provides infinitely many partial barriers arranged in a hierarchical manner. Using this designed system we are able to answer the open questions and give a quantitative description of the transition in terms of a suitable measure.

Furthermore we discuss matrix models in order to describe the quantum transition of a partial barrier. On the level of matrix modeling this corresponds to a transition of two uncoupled chaotic sub-systems (quantum suppression) to one large system (classical transport). The onset of the classically established transport through the turnstile for increasing ratio $\Phi/h$ corresponds to an enhanced coupling between the formerly independent chaotic regions separated by the partial barrier. This transitional behavior is similar to the flooding of the regular island by chaotic states, which arises due to the tunneling coupling between the classically distinct regions [37–39]. Moreover it is related to symmetry breaking, where two distinct sub-systems are coupled by an additional force [40]. Bohigas, Tomsovic, and Ullmo used this analogy to propose a random matrix model to describe the impact of a partial barrier on the corresponding quantum system [23]. We find that this matrix model does not reproduce the numerical data for the quantum transition of the partial barrier. Hence, we introduce a channel coupling model, unitary matrix models, and a deterministic $2 \times 2$-model, which are able to describe the quantum transition of a partial barrier. To understand the different results for the matrix models we study the spectral statistics of the system with one partial barrier.

In Chap. 2 the considered example systems and their properties are discussed. In Chap. 3 we investigate the phenomenon of quantum suppression and design a map with a particularly simple phase space, which allows to study the quantum transition of a partial barrier in detail. Several modeling approaches for the quantum transition are presented in Chap. 4. Spectral signatures of partial barriers are discussed in Chap. 5. We conclude by a summary and outlook.

# 2 Kicked systems

In this chapter we first discuss basic properties of classical Hamiltonian systems (see Sec. 2.1). As a prominent example we introduce the standard map in Sec. 2.2 to illustrate the phase-space structures found in Hamiltonian systems (see Sec. 2.3) and discuss the impact of these structures on the transport (see Sec. 2.4). In Sec. 2.5 we explain time reversal invariance. The quantization of kicked systems and time-independent systems is presented in Sec. 2.6 and 2.7, respectively. The Husimi distribution as phase-space representation of a quantum state is introduced in Sec. 2.8.

## 2.1 Hamiltonian systems

The deterministic mathematical description for the time evolution of possible states of a (physical) system is called 'dynamical system' [3, Sec. 1.3]. The state of the system is characterized by a vector $x$ inside the space of all possible states (e.g. $G \subseteq \mathbb{R}^n$) called phase space. For time continuous systems the evolution is described by $x(t)$ at times $t \in \mathbb{R}$. This function $x(t)$ is the solution of the differential equation according to the dynamical system

$$\dot{x} = f(x, t) \tag{2.1}$$

with initial condition $x(0) = x_0$. The information about the system dynamics is completely contained in the function $f : G \times \mathbb{R} \to \mathbb{R}^n$, which returns a vector as value. The resulting graph $\{x(t, x_0) : t \in \mathbb{R}\}$ is called trajectory.

Hamiltonian systems are a special class of dynamical systems. They are completely described by one scalar function, namely the Hamiltonian or Hamiltonian function $H(q, p, t)$. This function depends on the canonical coordinates $q$ (position) and $p$ (momentum), which describe states as points $x = (q, p)$ in the phase space. In order to find the Hamiltonian for a mechanical system one usually starts with the Lagrangian $L(q, \dot{q}, t)$, which depends on positions $q$ and velocities $\dot{q}$. Both functions, $H(q, p, t)$ and $L(q, \dot{q}, t)$, are related by a Legendre transformation

$$H(q, p, t) = p \cdot \dot{q} - L(q, \dot{q}, t). \tag{2.2}$$

By use of this transformation the dependence on velocities $\dot{q}$ is replaced by a dependence on the conjugate momenta $p = \frac{\partial L}{\partial \dot{q}}$. The equations of motion are derived using Hamilton's principle.

In order to do so we define the action

$$S(q, t_1, t_2) = \int\limits_{t_1}^{t_2} L(q(t), \dot{q}(t), t) \, dt \tag{2.3}$$

along a path $q(t)$ between times $t_1$ and $t_2$. The system will take the route between the fixed end points $q(t_1)$ and $q(t_2)$, which yields minimal or rather stationary action: $\delta S = 0$. Using the calculus of variations, Euler-Lagrange equations,

$$\frac{d}{dt} \frac{\partial L(q, \dot{q}, t)}{\partial \dot{q}} - \frac{\partial L(q, \dot{q}, t)}{\partial q} = 0 \tag{2.4}$$

as well as Hamilton's equations of motion,

$$\begin{aligned} \dot{q} &= \phantom{-}\frac{\partial H(q, p, t)}{\partial p}, \\ \dot{p} &= -\frac{\partial H(q, p, t)}{\partial q}, \end{aligned} \tag{2.5}$$

(according to the above Legendre transformation) can be derived. Both, Euler-Lagrange equations and Hamilton's equations of motion, completely describe the dynamics. The latter set of equations, Eq. (2.5), are of the type of Eq. (2.1). We identify $x = (q, p)$ and

$$f(q, p, t) = \Omega \cdot \begin{pmatrix} \frac{\partial H(q, p, t)}{\partial q} \\ \frac{\partial H(q, p, t)}{\partial p} \end{pmatrix} \tag{2.6}$$

with the symplectic matrix

$$\Omega = \begin{pmatrix} 0 & \mathbb{1} \\ -\mathbb{1} & 0 \end{pmatrix}, \tag{2.7}$$

where $0$ and $\mathbb{1}$ are the zero and identity matrix of dimension according to $q$; and therefore $p$.

A mapping $F$ of the kind

$$x(t_{i+1}) = F(x(t_i)) \tag{2.8}$$

defines a time discrete dynamical system. In this case time takes only discrete values $t_i = t_0 + i \cdot \Delta t$ with $i \in \mathbb{Z}$. Such a mapping may arise from a time continuous system, Eq. (2.1), by sampling of the trajectory and observation only at discrete times $\{t_i\}$. This is especially useful for periodic functions $f$: $f(x, t) = f(x, t + \Delta t)$ and the resulting map is called stroboscopic. For simplicity we will assume $\Delta t = 1$ in the following, which means that all times are measured in multiples of $\Delta t$. The rescaled time only takes integer values and Eq. (2.8) can be written as

$$x_{t+1} = F(x_t) \quad \text{with } t \in \mathbb{Z}. \tag{2.9}$$

In the following we restrict ourselves to two-dimensional mappings. They arise for instance from systems with one degree of freedom, that are periodically driven. In contrast to time-independent systems with one degree of freedom, which are always integrable, these systems may exhibit chaos and a mixed phase space (see Sec. 2.3). Furthermore the dynamics inside two-dimensional billiard systems, which have a four-dimensional phase space, can be described by use of so called Birkhoff coordinates [22]. These coordinates map the time continuous dynamics onto a two-dimensional phase space with time discrete dynamics.

The set of states (points in phase space) visited by a particle initially located at $x_0$ is called orbit. The time evolution is given by Eq. (2.9) and an orbit can therefore be written as

$$\{x_t : x_t = F^t x_0, t \in \mathbb{N}\}, \tag{2.10}$$

where we define $F^2 x := FFx = F(Fx)$. If the inverse mapping $F^{-1}$ is also defined, we consider the set

$$\{x_t : x_t = F^t x_0, t \in \mathbb{Z}\}. \tag{2.11}$$

Based on that, we define an orbit segment as finite subset of an orbit between time $t_1$ and $t_2$. If we talk about orbits in the following, we have orbit segments in mind, which reflect typical properties of an orbit.

One class of mappings, which result from stroboscopic observation of a Hamiltonian system, are kicked systems. Their Hamiltonian is given by

$$H(q, p, t) = T(p) + V(q) \sum_{i \in \mathbb{Z}} \delta(t - i). \tag{2.12}$$

Thereby $T(p)$ is the kinetic energy and the potential $V(q)$ acts instantaneously at integer times $t = i$. The resulting Hamilton's equations of motion are

$$
\begin{aligned}
\dot{q} &= \frac{\partial H}{\partial p} = T'(p), \\
\dot{p} &= -\frac{\partial H}{\partial q} = -V'(q) \sum_{i \in \mathbb{Z}} \delta(t - i).
\end{aligned} \tag{2.13}
$$

In order to get a stroboscopic mapping, we first integrate the equations over one period of the driving. For the mapping we observe the dynamics just after the kick and consider

$$
\begin{aligned}
q_t &:= \lim_{\epsilon \to 0 \ (\epsilon > 0)} q(t + \epsilon) \ \text{ and} \\
p_t &:= \lim_{\epsilon \to 0 \ (\epsilon > 0)} p(t + \epsilon),
\end{aligned} \tag{2.14}
$$

respectively. The new coordinates after one period $q_{t+1}$ and $p_{t+1}$ are given by

$$q_{t+1} = q_t + T'(p_t),$$
$$p_{t+1} = p_t - V'(q_{t+1}) \tag{2.15}$$

in terms of the old coordinates at time $t$.

Another choice for the observation time is given by splitting the kick into two parts and considering the half kick mapping

$$\tilde{p} = p_t - \frac{1}{2}V'(q_t),$$
$$q_{t+1} = q_t + T'(\tilde{p}),$$
$$p_{t+1} = \tilde{p} - \frac{1}{2}V'(q_{t+1}). \tag{2.16}$$

We will use this kind of mapping in Sec. 3.1.6 to define a composed map, which obeys time reversal invariance.

An important property of Hamiltonian systems is area conservation. If one considers the time evolution of a given phase-space region, the measure of the time evolved region is conserved according to Liouville's theorem as the corresponding mapping is symplectic. Locally this symplecticity is described by

$$DF(q,p)^\dagger \ \Omega \ DF(q,p) = \Omega, \tag{2.17}$$

where $\Omega$ is the symplectic matrix from Eq. (2.7) and $DF(q,p)$ is the Jacobian matrix. The elements of the latter are the first derivatives of the new coordinates with respect to the old ones and the role of $DF$ will be discussed in more detail later in this section. A general characterization of symplectic maps can be found in the review article [22].

## Fixed points and periodic orbits

A special class of orbits arises from fixed points. A fixed point of a mapping is a point $x^*$ in phase space with

$$x^* = F(x^*). \tag{2.18}$$

That is, it is invariant under the application of the mapping $F$ and all images fall on top of each other. Therefore the point $x^*$ and the orbit $\{x^*\}$ are identified. Fixed points are the special case of the more general question of periodic orbits. Such orbits are invariant under the $n$-fold

iterated mapping

$$x_i = F^n(x_i), \quad i = 0, \ldots, n-1 \tag{2.19}$$

and consist of $n$ distinct points $x_i$, which arise from each other by multiple application of the mapping. The image of the $n$-th point, $x_{n-1}$, under $F$ is just the first point $x_0$. The periodic orbit consists of the set

$$\{x_i \in G : x_{i+1} = F(x_i) \text{ for } i = 0, \ldots, n-1 \text{ and } x_0 = x_n\}. \tag{2.20}$$

Fixed points are categorized according to their stability, which is determined by the behavior of close-by orbits. For that purpose we consider the linearized mapping

$$F(x) \approx F(x^*) + DF(x^*) \cdot (x - x^*), \tag{2.21}$$

which is determined by the monodromy or Jacobian matrix $DF$ at the fixed point $x^*$

$$DF(x^*) = \left( \frac{\partial F_{(i)}}{\partial x_{(j)}} \right)_{i,j} (x^*) = \begin{pmatrix} \frac{\partial F_{(1)}}{\partial x_{(1)}} & \frac{\partial F_{(1)}}{\partial x_{(2)}} \\ \frac{\partial F_{(2)}}{\partial x_{(1)}} & \frac{\partial F_{(2)}}{\partial x_{(2)}} \end{pmatrix} (x^*). \tag{2.22}$$

The indexes $(i)$ and $(j)$ in Eq. (2.22) label the components of the considered vectors $x$ and $F(x)$. The stability properties can be determined from the eigenvalue equation

$$DF(x^*) \cdot \xi = \lambda \cdot \xi \tag{2.23}$$

with the displacement $\xi = x - x^*$.

In the following we will discuss the general case of a periodic orbit. To analyze its stability, we consider the linear approximation of the $n$-fold mapping $DF^n := D(F^n)$ at the point $x = x_0$:

$$\Delta x_n = DF^n(x_0) \ \Delta x_0, \tag{2.24}$$

where $\Delta x_i$ is the displacement from the periodic orbit after $i$ steps in linear approximation and $\Delta x_0$ the initial distance from $x_0$. We use $x_0$ for simplicity, however, all statements hold for each point of the periodic orbit. The linearization $DF^n(x_0)$ follows according to the chain rule

$$DF^n(x_0) = DF(x_{n-1}) \cdot DF(x_{n-2}) \cdot \ldots \cdot DF(x_0). \tag{2.25}$$

We consider the eigenvalue equation

$$DF^n(x_0) \cdot \xi = \lambda \cdot \xi. \tag{2.26}$$

For two-dimensional maps the corresponding eigenvalues are

$$\lambda_{1,2} = \frac{1}{2}\left(\mathrm{Tr}\{DF^n\} \pm \sqrt{(\mathrm{Tr}\{DF^n\})^2 - 4}\right), \tag{2.27}$$

where we introduced the trace of the matrix $DF^n$ as $\mathrm{Tr}\{DF^n\}$ and used the symplecticity of $F^n$ (see Ref. [22]) to replace its determinant by 1. The eigenvalues of $DF^n(x_0)$ only depend on the trace $\mathrm{Tr}\{DF^n(x_0)\}$, which is independent of the particular choice of $x_0$ within the orbit points.

Depending on the trace $\mathrm{Tr}\{DF^n\}$ there are four types of periodic orbits for two-dimensional maps [22], namely

- hyperbolic: Both eigenvalues are real, positive, and form the pair $\lambda, 1/\lambda$ for $\mathrm{Tr}\{DF^n\} > 2$. The resulting properties are discussed later.

- elliptic: The eigenvalues have unit modulus and form a complex conjugate pair for $\mathrm{Tr}\{DF^n\} \in (-2, 2)$. This is the only stable fixed point [22]. Close-by orbits circulate on ellipses around the fixed point.

- reflection hyperbolic: Both eigenvalues are real and form the pair $\lambda, 1/\lambda$. In contrast to the hyperbolic case both eigenvalues are negative and the trace is $\mathrm{Tr}\{DF^n\} < -2$.

- parabolic: Both eigenvalues are $+1$ or $-1$ for $\mathrm{Tr}\{DF^n\} = \pm 2$.

## Hyperbolic fixed points

In the neighborhood of a hyperbolic fixed point there are orbits approaching the fixed point at large time and orbits diverging from it. They are associated with the two eigendirections of the $DF^n(x_0)$ with one eigenvalue $\lambda$ smaller than 1 and one eigenvalue $1/\lambda$ larger than 1. The collection of all orbits, which approach the fixed point $x_0$ of $F^n$ at large times is called stable manifold

$$W_s(x_0) = \{x \in G : x_0 = \lim_{j \to \infty} F^{j \cdot n} x\}. \tag{2.28}$$

All orbits that approach the fixed point for iteration with the inverse map $F^{-n}$ are collected into the unstable manifold. It is given by

$$W_u(x_0) = \{x \in G : x_0 = \lim_{j \to -\infty} F^{j \cdot n} x\}. \tag{2.29}$$

The stable and unstable manifold are invariant under the mappings $F^n$ and $F^{-n}$. That is, orbits started on such a manifold, will remain on it forever. Because of the uniqueness of the mapping and the continuous dependence on initial conditions, other orbits cannot cross the

stable or unstable manifold. Therefore these manifolds are total transport barriers in phase space.

By use of the stable manifold theorem, approximations of the above defined sets $W_s(x_0)$ and $W_u(x_0)$ can be numerically determined [22]. This theorem implies that the eigenvectors of the Jacobian matrix $DF$ are tangential to the corresponding manifold at the fixed point. By placing initial conditions close to the fixed point along the unstable direction and iterating these points forward in time, an approximation of the unstable manifold is obtained. The stable manifold can be approximated by orbits starting on the stable direction and being iterated backward in time or forward in time with the inverse mapping. In Figure 2.1 these approximations of stable and unstable manifold of the hyperbolic fixed point $(0, 0)$ for the standard map are shown.

The stable and unstable manifold cannot intersect with itself because of the uniqueness of the mapping, but the stable and unstable manifold may intersect one another as shown in Fig. 2.1. Such intersections are called homoclinic or heteroclinic points. Homoclinic points are intersections between the stable and unstable manifold of one fixed point. All of their images lie on both stable and unstable manifold, and they approach the fixed point for forward and backward iteration following the stable and unstable manifold, respectively. Heteroclinic points are intersections of the stable and the unstable manifold of different fixed points. The structure of the stable and the unstable manifold – indicated in Fig. 2.1 – is called homoclinic tangle.
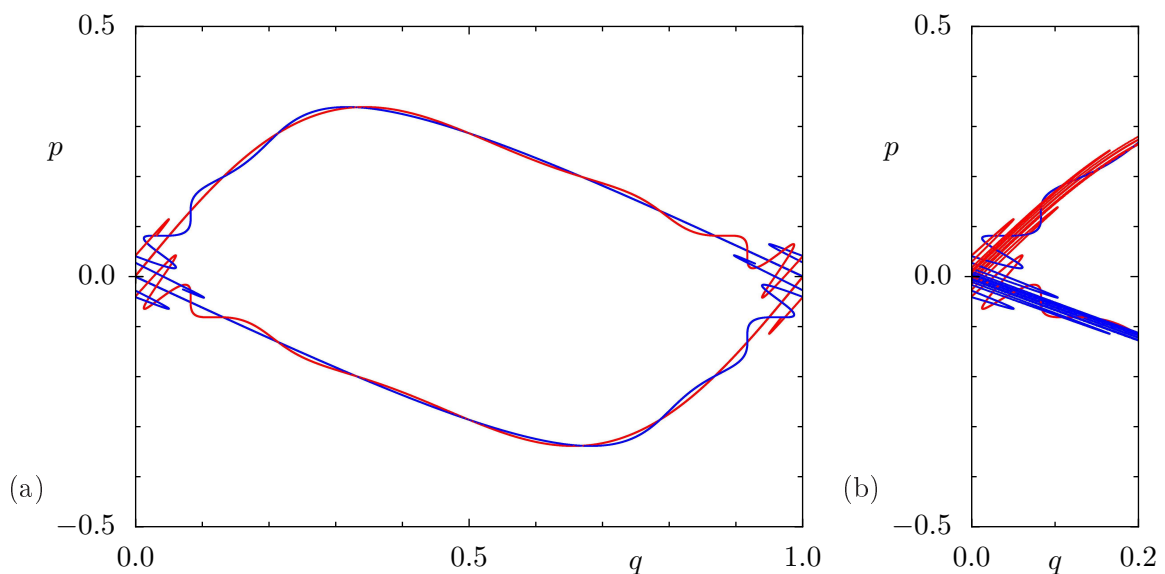


**Figure 2.1:** (a) Part of the stable manifolds (blue) and the unstable manifolds (red) of the hyperbolic fixed point $(q, p) = (0, 0)$ ($\widehat{=}(1, 0)$) for the standard map with kicking strength $K = 1$ and (b) fraction of (a) with longer branches of the manifolds.

## 2.2  Standard map

One famous example of a Hamiltonian system is the standard map, which was introduced by Chirikov in 1979 [41], sometimes called Chirikov-(Taylor-)map. It describes essential properties of several systems. The standard map is a one-parametric family of maps and provides all generic features of Hamiltonian systems [41].

It is an example of a kicked system and its Hamiltonian function in terms of dimensionless position $q$ and momentum $p$ is

$$H(q,p) = \frac{p^2}{2} + \frac{K}{(2\pi)^2} \cos(2\pi q) \sum_{i \in \mathbb{Z}} \delta(t - i), \tag{2.30}$$

where the potential term acts instantaneously at integer times and vanishes otherwise. The only parameter is the kicking strength $K$. The Hamilton's equations of motion, Eq. (2.13), are

$$\dot{q} = \phantom{-}\frac{\partial H}{\partial p} = p,$$
$$\dot{p} = -\frac{\partial H}{\partial q} = -\frac{\partial V}{\partial q} = \frac{K}{2\pi} \sin(2\pi q) \sum_{i \in \mathbb{Z}} \delta(t - i). \tag{2.31}$$

If we observe the dynamics once per period of the driving, we get a stroboscopic mapping similar to Eq. (2.15). Here we choose for the observation time the moment just after the $i$-th kick and obtain the standard map as

$$q_{i+1} = q_i + p_i,$$
$$p_{i+1} = p_i + \frac{K}{2\pi} \sin(2\pi q_{i+1}) \tag{2.32}$$

or as a mapping $F : (q, p) \mapsto (q', p')$

$$q' = q + p,$$
$$p' = p + \frac{K}{2\pi} \sin(2\pi q'). \tag{2.33}$$

The change in momentum $p$ in Eq. (2.33) is periodic with period 1 and therefore the position variable $q$ can be restricted to $[0, 1)$ with periodic boundary conditions like it was an angle. Considering this periodic boundary condition in $q$ for the change of $q$ in Eq. (2.33) one may choose the same period for the momentum $p$ and finally get the dynamics on a torus. The Jacobian matrix, Eq. (2.22), of the standard map is

$$DF(q,p) = \begin{pmatrix} \frac{\partial q'}{\partial q} & \frac{\partial q'}{\partial p} \\ \frac{\partial p'}{\partial q} & \frac{\partial p'}{\partial p} \end{pmatrix} = \begin{pmatrix} 1 & 1 \\ K \cdot \cos(2\pi q') & 1 + K \cdot \cos(2\pi q') \end{pmatrix}. \tag{2.34}$$

## 2.3  Phase-space structure

In this section important aspects of the phase-space structure and their origin are discussed. In the following, the standard map will be used as a typical example, because it provides all generic features of symplectic maps.

### Integrable motion

A given Hamiltonian system is called integrable, if there exists a canonical transformation to new variables $(J, \Theta)$ with the following property: The dynamics of $J$ and $\Theta$ is described by the
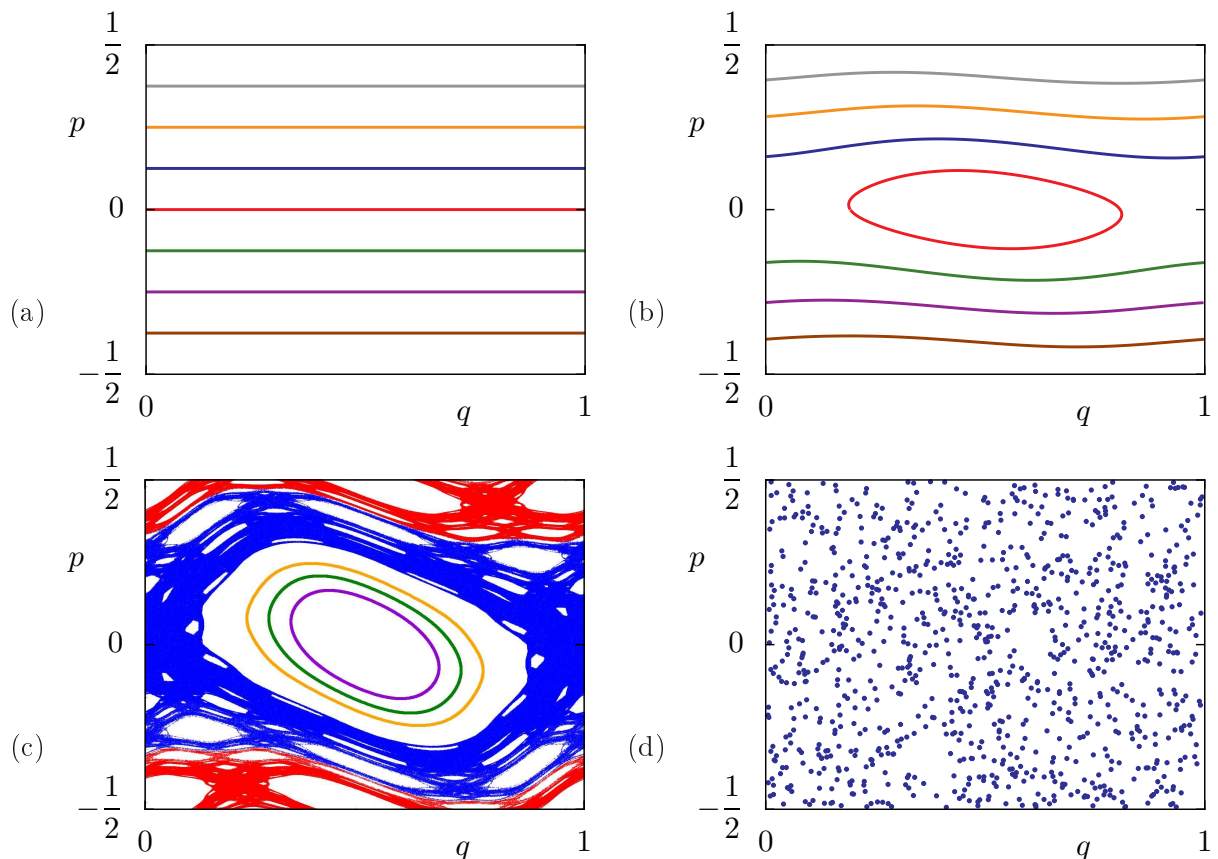


**Figure 2.2:** Phase space of the standard map: (a) integrable motion on horizontal tori with preserved momenta $p$ for $K = 0$, (b) dynamics of slightly deformed horizontal tori and orbits circulating around the elliptical fixed point at $(q, p) = (1/2, 0)$ for $K = 0.2$, (c) mixed phase space composed of regular regions, which are enclosed by chaotic orbits for $K = 1$, and (d) there are no regular regions visible and the plotted chaotic orbit fills the whole phase space uniformly for $K = 10$.

Hamilton function $\tilde{H}(J)$, which is independent of $\Theta$. The Hamilton's equations of motion read

$$\dot{\Theta} = \frac{\partial \tilde{H}(J)}{\partial J} =: \nu(J),$$
$$\dot{J} = 0. \tag{2.35}$$

The solution of these differential equations has the form

$$\Theta(t) = \Theta(0) + \nu(J) \cdot t,$$
$$J = \text{const.} \tag{2.36}$$

That is, the action $J$ is preserved and the angle $\Theta$ increases constantly. It corresponds to the motion on the circle with fixed velocity $\nu(J)$, which is called winding frequency. The action conservation restricts the motion to a one-dimensional line in phase space, which is called torus. In the following we will consider $\Theta$ as an angle between 0 and 1.

Figure 2.2(a) shows the phase space of such an integrable motion, where the action-angle variables are denoted by $p$ and $q$. For vanishing kicking strength $K$ the standard map, Eq. (2.32), reduces to Eq. (2.36) with the winding frequency $\nu(p) = p$.

Depending on the winding frequency orbits can be classified as periodic or quasiperiodic. For rational winding frequency $\nu = \frac{m}{n}$ with $m \in \mathbb{Z}, n \in \mathbb{N}$ the orbit is periodic on the torus with period $n$. Such an orbit is called $(m,n)$-orbit. For integrable systems the set of $(m,n)$-orbits form the torus of winding frequency $\nu = \frac{m}{n}$. For irrational winding frequency the orbit is not periodic, but densely fills a one-dimensional line with recurring close visits of the initial point.

## Chaotic motion

In addition to the integrable motion the chaotic motion is another limiting case of a dynamical system and will be discussed in the following before the mixed phase space is considered, where both motions coexist. As discussed in the introduction, chaotic dynamics is characterized by the sensitive dependence on the initial conditions. Although the dynamics is deterministic it is impossible to predict the exact evolution of an initial condition neither numerically nor experimentally. This becomes clear by considering the time evolution of two close-by initial conditions. For two such initial conditions in the phase space of the standard map with $K = 10$ (see Fig. 2.2(d)), we consider their distance at time $t$,

$$d\left(x_t^{(1)}, x_t^{(2)}\right) = \left\| \left(q_t^{(1)}, p_t^{(1)}\right) - \left(q_t^{(2)}, p_t^{(2)}\right) \right\| = \sqrt{\left(q_t^{(2)} - q_t^{(1)}\right)^2 + \left(p_t^{(2)} - p_t^{(1)}\right)^2}. \tag{2.37}$$

The result is plotted in Fig. 2.3 and shows an exponential growth as a function of time,

$$d\left(x_t^{(1)}, x_t^{(2)}\right) \propto \exp\{L \cdot t\} \cdot d\left(x_0^{(1)}, x_0^{(2)}\right), \tag{2.38}$$
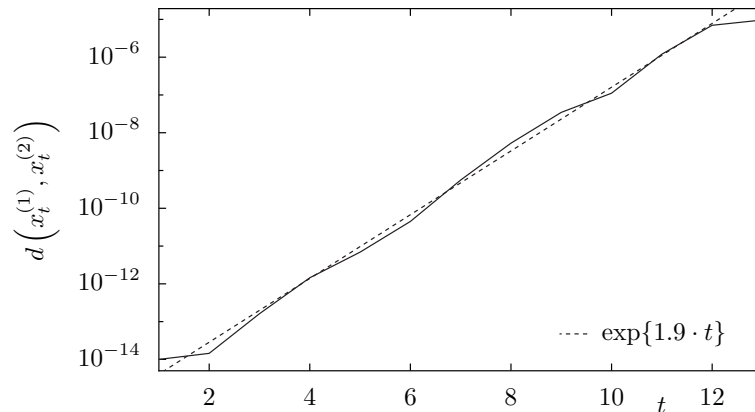
**Figure 2.3:** Distance of two orbits of the standard map for $K = 10$ with initial conditions $q_0^{(1,2)} = 1/2$, $p_0^{(1)} = 1/4$ and $p_0^{(2)} = p^{(1)} + 10^{-14}$ in comparison to an exponential growth.

which is characteristic for chaotic systems. This growth is described by the Lyapunov exponent $L$ [3, Sec. 4.4]. In general it depends on the direction of the initial displacement and it is obtained in the limit of vanishing displacement and arbitrary large observation time. For practical estimations finite time Lyapunov exponents are useful. They are based on the larger eigenvalue $\lambda_1$ of the Jacobian matrix along a chaotic orbit started in $x$ and given by [3, Sec. 9.4]

$$L(x,t) = \frac{\ln \lambda_1(x,t)}{t} \approx \frac{\text{Tr}\{DF^t(x)\}}{t}, \tag{2.39}$$

where $\lambda_1$ of Eq. (2.27) is approximated by the trace of the Jacobian matrix, which is valid at large times. Due to the area preservation of Hamiltonian systems, additionally to the exponential divergence of nearby orbits, there is a direction in which separated orbits approach each other. The latter is the tangent to the local stable manifold (see Sec. 2.1).

## Mixed phase space

Besides the limiting cases of the regular and the chaotic system, in general both dynamics coexist – the mixed phase space. Such a mixed phase space is illustrated in Fig. 2.2(c). Depending on the initial conditions the resulting orbit is either regular, confined to a one-dimensional line, or chaotic and fills a two-dimensional region in phase space. The sets of regular tori form regular islands within the chaotic sea.

According to Ref. [4] the mixed phase space is the generic case of a Hamiltonian system. It may arise from an integrable system $H_0(J)$ by adding a small perturbation $\varepsilon H_1(J,\Theta)$. The description of the effects governed by the perturbation is given by Kolmogorov, Arnol'd, and Moser and nowadays known as KAM theory (see Refs. [3, Chap. 7] and [22]).

Pursuant to the KAM theorem, almost all tori (except for sets of measure zero) of the unperturbed problem exist in the limit of vanishing perturbation $\varepsilon \to 0$. For non-vanishing

perturbation the preserved tori are more or less deformed and are called KAM tori to distinguish them from the tori of the unperturbed system. Both kinds of tori form invariant sets in phase space.

The impact of an increasing perturbation on KAM tori with rational or irrational winding frequency is quite different. A torus with rational winding frequency $\nu = \frac{m}{n}$ is broken by an arbitrary small perturbation [14, 15]. According to the Poincaré-Birkhoff theorem (see Ref. [3, Sec. 7.2.2]) this rational torus is replaced by an island chain, which consists of $n$ elliptical islands. In between the elliptical islands there are hyperbolic fixed points. For the case of the standard map the perturbation is given by the kicking potential determined by the kicking strength $K$. In the phase space shown in Fig. 2.2 the horizontal torus with $(m, n) = (0, 1)$ for vanishing kicking strength (Fig. 2.2(a)) has been replaced by one elliptical island in the center around $(q, p) = (\frac{1}{2}, 0)$ and one hyperbolic fixed point at the boundary, $(q, p) = (0, 0) \widehat{=} (1, 0)$, in Fig. 2.2(b) and (c).

Even within the tori with irrational winding frequency the effect of the perturbation is not uniform. Depending on how well the irrational frequency can be approximated by rational numbers, the torus will persist even strong perturbations or not [11, 42, 43]. A well settled tool to approximate irrational numbers is the continued fraction expansion (see Ref. [22, p. 814]). The golden ratio is the irrational number, whose continued fraction expansion converges most slowly. Therefore tori with a golden winding frequency or more general a noble winding frequency should break up only for very strong perturbations.

The breakup of a tori with irrational winding frequency yields a Cantor set. Due to the quasiperiodic motion there exist infinitely many holes along the formerly closed torus. Such a set is called cantorus and allows for a non-vanishing flux crossing it. Their impact on the transport in phase space is discussed in Sec. 2.4.

Starting with an integrable system, we obtain a mixed phase space by introducing a perturbation. Depending on the strength of the perturbation tori are deformed or even break up into island chains. Locally the dynamics in the islands is again regular and if we increase the perturbation strength further the above procedure repeats for these islands ( [3, Sec. 7.2.2], [22, p. 810]). This repetition on smaller and smaller scales give rise to the hierarchical phase-space structure observed in systems with a mixed phase space. Around each island, there are again smaller islands and this repeats ad infinitum yielding as self-similar phase space.

## 2.4  Transport in Hamiltonian systems

In this section we consider the impact of the structures discussed in the previous section on the transport. For integrable systems the dynamics is equivalent to a rotation with the winding frequency $\nu(J)$, which depends on the action $J$ (see Fig. 2.2(a) with $J = p$). For quasiperiodic motion (irrational winding frequency) the orbit visits all points of the torus uniformly. In fully

chaotic systems an orbit again explores the available region uniformly, but in contrast to the integrable case it explores the whole two-dimensional phase space. Therefore it is appropriate to describe the main features of the transport in terms of stochastic models although the dynamics is deterministic. For instance the time a chaotic orbit spends in some phase-space region is statistically proportional to the area of the region [44].

In the mixed phase space both kinds of dynamics coexist. Depending on the initial condition orbits can be classified into regular or chaotic. Orbits started in the chaotic sea never enter the regular islands and vice versa. If the regular islands were only holes in the chaotic sea the description of the transport in the chaotic sea would be the same as for the fully chaotic case. However, as already mentioned in the introduction this is not the case.

Let us consider the time evolution of two orbits started in the chaotic sea with slightly different initial conditions. Their distance as a function of time is shown in Fig. 2.4 (a) and exhibits an exponential growth at times up to $t = 18$. This is the same as for the fully chaotic case shown in Fig. 2.3. However, at $t \in [19, 26]$ the distance $d(x_t^{(1)}, x_t^{(2)})$ stays almost constant before it again increases up to the system size. The plateau at times in between is related to the regular islands around $(\frac{1}{4}, 0)$, because for these iterations the orbit pair sticks to these islands. That is, the exponential growth slows down and the Lyapunov exponent drops to zero close to the island. This impact of the regular islands on the dynamics of chaotic orbits is discussed in the following.
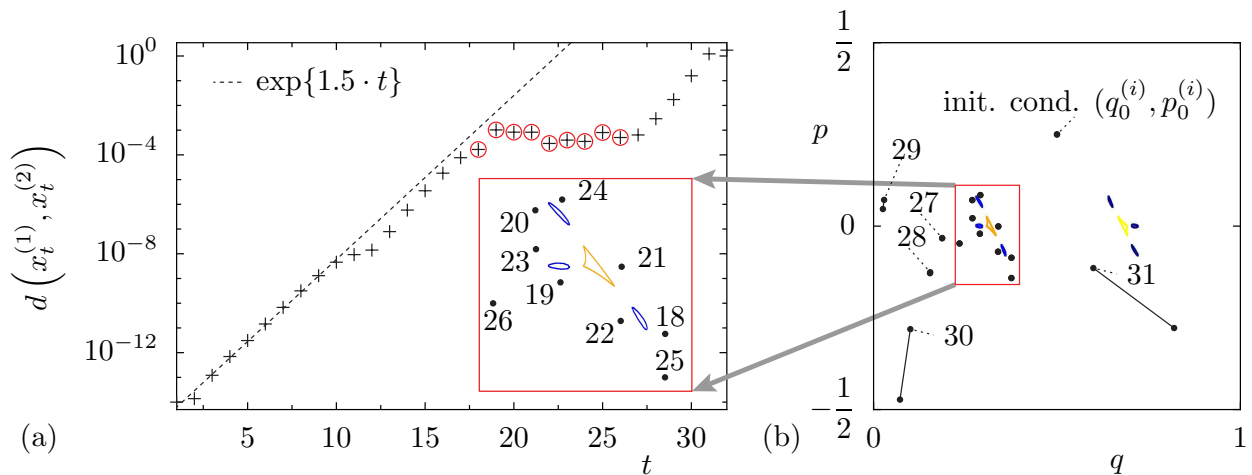


**Figure 2.4:** (a) Distance $d(x_t^{(1)}, x_t^{(2)})$ of two orbits in the mixed phase space (standard map with $K = 6.908745$). The initial conditions are $q_0^{(1,2)} = 1/2$, $p_0^{(1)} = 1/4$ and $p_0^{(2)} = p_0^{(1)} + 10^{-14}$. The distance is compared to an exponential growth. At certain iteration times indicated by the numbers the orbit pair is shown within the phase space (see inset of (a) and (b)). The regular islands in phase space are indicated by the colored tori. At times larger than $t = 29$ the orbits are significantly apart from each other, indicated by the line connecting the two orbits. The orbit points in the inset correspond to the encircled values of the distance $d(x_t^{(1)}, x_t^{(2)})$ in (a).
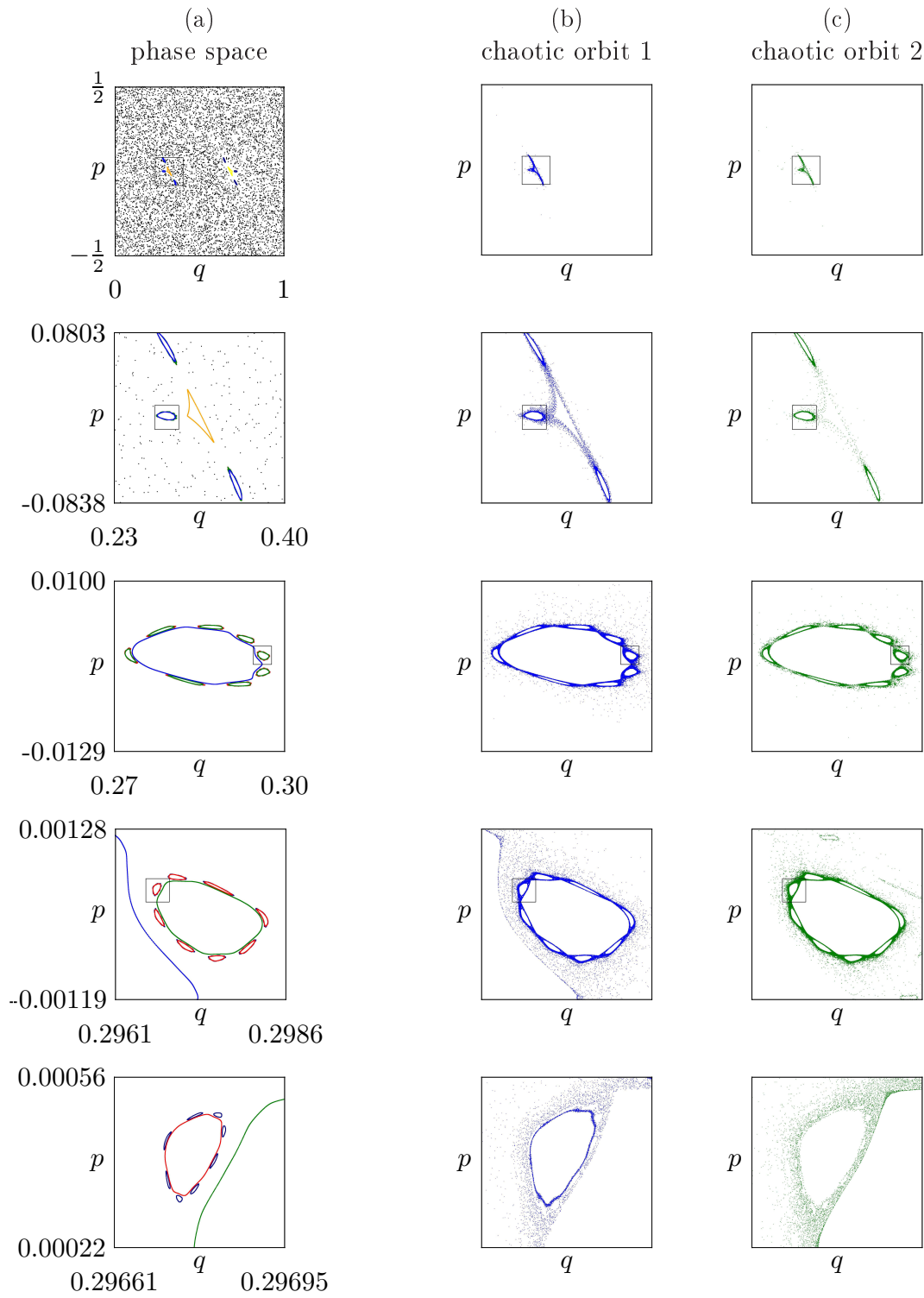
**Figure 2.5:** Trapping of chaotic orbits close to the regular islands: (a) shows the phase space of the standard map with $K = 6.908745$ whereas the two chaotic orbits, which stay close to the regular islands for at least $t = 10^6$ iterations are shown in (b) and (c). The rows show magnifications of the region indicated by a box in the previous row.

Figure 2.5(a) shows the phase space of the standard map with $K = 6.908745$, where the value of $K$ is chosen because of the nice self-similar island around island structure [45, 46]. Figure 2.5(b) and (c) display two chaotic orbits, which stay for more than $10^6$ iterations close to the regular region. Chaotic orbits are somehow trapped in the neighborhood of the regular islands. This phenomenon is called stickiness and is mentioned by several authors [6, 11–13, 41]. Comparing the two chaotic orbits in Fig. 2.5, we see that they follow the self-similar island around island structure for many magnifications and only in the last magnification they stick to different islands. This indicates that there is a huge number of phase-space regions a chaotic orbit may stick to [47, 48].

The above idea that regular regions are simple holes within the chaotic sea is wrong. Close to the islands there are structures giving rise to limitation of the chaotic transport. In contrast to total barriers in phase space, orbits can pass these structures. However, it may last several iterations before the orbit does so.

## Flux in phase space and partial barriers

The reason for the stickiness of regular islands are partial barriers, which we discuss here. First of all we introduce the term flux in phase space. The flux across a smooth curve $\mathcal{C}$ is the measure $\Phi$ of the phase-space volume transported across the curve $\mathcal{C}$ per unit time. It is given by the area between the curve $\mathcal{C}$ and its preimage $F^{-1}(\mathcal{C})$ shown in Fig. 2.6. For curves, which are invariant under the map $F$ like regular tori, the flux crossing them vanishes. Such curves are called total transport barriers. Partial barriers are defined as curves in phase space, that allow for a non-vanishing flux crossing them. They can be constructed for instance from the stable and the unstable manifold of a hyperbolic periodic orbit or from cantori [14, 15, 22]. For the designed map we discuss the construction of the partial barrier in Sec. 3.1.3.
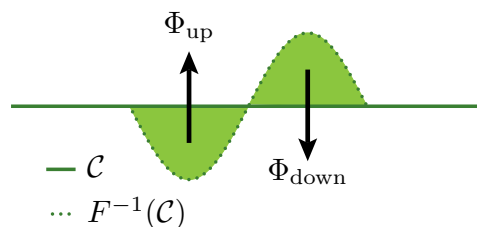


**Figure 2.6:** Illustration of the flux $\Phi$ across a curve $\mathcal{C}$ (solid line). The flux is given by the size of the shaded regions between $\mathcal{C}$ and its preimage $F^{-1}(\mathcal{C})$ (dotted). For simplicity we assume that the two curves deviate only in the central part forming the turnstile and are on top of each other outside.

The netto flux across the curve is given by the difference of upward and downward flux

$$\Phi_{\text{netto}} = \Phi_{\text{up}} - \Phi_{\text{down}} \tag{2.40}$$

and for area preserving maps it is zero. That is, volumes of equal size are exchanged between the upper and lower region,

$$\Phi = \Phi_{\text{up}} = \Phi_{\text{down}}. \tag{2.41}$$

Therefore the central part of Fig. 2.6, where the curve and its preimage differ, is called turnstile. In this way orbits pass the partial barrier by entering the turnstile and being mapped to the other side of the partial barrier.

Although there are infinitely many partial barriers in a mixed phase space, those with minimal flux are most restrictive for the transport and therefore of special interest. They allow for a decomposition of the phase space into regions of strong mixing that are connected by the slow transport across the partial barrier.

## 2.5  Time reversal invariance

In this section the property of time reversal invariance is introduced and the implications for the composition of maps are discussed. This is important for Sec. 3.1.6, where we define a mapping as composition of two maps.

Time reversal invariance $\tau$ is one example of an anticanonical symmetry of the classical system described by the map $F$ [49],

$$\tau \circ F \circ \tau = F^{-1} \tag{2.42}$$

with $\tau^2 = \tau \circ \tau = \mathbb{1}$. This symmetry induces an antiunitary symmetry $K$ to the corresponding quantum system described by the time evolution operator $U$,

$$KUK^{-1} = U^{-1}. \tag{2.43}$$

Consider the two time reversal invariant maps $F_i$,

$$\tau \circ F_i \circ \tau = F_i^{-1} \quad \text{for} \quad i = 1, 2 \tag{2.44}$$

and use them to construct two new maps $F'$ and $\tilde{F}$ by

$$F' = F_2 \circ F_1 \tag{2.45}$$

$$\tilde{F} = \sqrt{F_2} \circ F_1 \circ \sqrt{F_2}, \tag{2.46}$$

where we assume that there exists a map denoted by $\sqrt{F_2}$ with $\sqrt{F_2} \circ \sqrt{F_2} = F_2$ and that $\sqrt{F_2}$ fulfills time reversal invariance, too. The corresponding inverse mappings are $(F')^{-1} = F_1^{-1} \circ F_2^{-1}$ and $\tilde{F}^{-1} = \sqrt{F_2}^{-1} \circ F_1^{-1} \circ \sqrt{F_2}^{-1}$. Now let us check the time reversal invariance of $\tilde{F}$

$$\begin{aligned}
\tau \circ \tilde{F} \circ \tau &= \tau \circ \sqrt{F_2} \circ F_1 \circ \sqrt{F_2} \circ \tau \\
&= \tau \circ \sqrt{F_2} \circ \tau^2 \circ F_1 \circ \tau^2 \circ \sqrt{F_2} \circ \tau \\
&= \sqrt{F_2}^{-1} \circ F_1^{-1} \circ \sqrt{F_2}^{-1} = \tilde{F}^{-1},
\end{aligned} \tag{2.47}$$

where we inserted $\tau^2 = \mathbb{1}$ and used the time reversal invariance of $F_1$ and $\sqrt{F_2}$.

For the map $F'$ the above symmetry $\tau$ is not satisfied

$$\begin{aligned}
\tau \circ F' \circ \tau &= \tau \circ F_2 \circ F_1 \circ \tau = \tau \circ F_2 \circ \tau^2 \circ F_1 \circ \tau \\
&= F_2^{-1} \circ F_1^{-1} = (F_1 \circ F_2)^{-1} \neq F'^{-1}.
\end{aligned} \tag{2.48}$$

Therefore we consider a symmetry $\tau' := \sqrt{F_2} \circ \tau \circ \sqrt{F_2}^{-1}$ with $(\tau')^2 = \mathbb{1}$, which is canonically conjugated to $\tau$ and therefore also anticanonical

$$\begin{aligned}
\tau' \circ F' \circ \tau' &= \sqrt{F_2} \circ \tau \circ \sqrt{F_2}^{-1} \circ F_2 \circ F_1 \circ \sqrt{F_2} \circ \tau \circ \sqrt{F_2}^{-1} \\
&= \sqrt{F_2} \circ \tau \circ \sqrt{F_2} \circ F_1 \circ \sqrt{F_2} \circ \tau \circ \sqrt{F_2}^{-1} \\
&= \sqrt{F_2} \circ \sqrt{F_2}^{-1} \circ F_1^{-1} \circ \sqrt{F_2}^{-1} \circ \sqrt{F_2}^{-1} \\
&= F_1^{-1} \circ F_2^{-1} = F'^{-1},
\end{aligned} \tag{2.49}$$

where Eq. (2.47) is used. This generalized time reversal invariance $\tau'$ gives rise to an antiunitary symmetry of the quantum system. Therefore the spectral statistics of $F'$ is the same as for $\tilde{F}$ with time reversal invariance $\tau$ [49].

In preparation for Sec. 3.1.6 we here mention that half kick maps, defined by Eq. (2.16), obey the generalized time reversal invariance

$$\tilde{\tau} : \begin{pmatrix} q \\ p \end{pmatrix} \mapsto \begin{pmatrix} -q \\ p \end{pmatrix} \tag{2.50}$$

if the derivative of the potential is an odd function: $V'(-q) = -V'(q)$, which can be shown by evaluating Eq. (2.42) for this situation.

## 2.6  Quantization of kicked systems

Here we derive a quantization rule for kicked systems based on the famous paper of Chang and Shi from 1986 [50] and the lecture notes [51]. The starting point for the quantization scheme is the Hamilton operator of a kicked system

$$H(\hat{q}, \hat{p}, t) = T(\hat{p}) + V(\hat{q}) \sum_{n \in \mathbb{Z}} \delta(t - n). \tag{2.51}$$

The discrete time evolution of a state $|\psi(t)\rangle$ can be written as

$$|\psi(t+1)\rangle = U|\psi(t)\rangle \tag{2.52}$$

with some unitary time evolution operator $U$. In order to find an expression for $U$ we use the time continuous evolution and restrict our observation by means of after kicked maps. The time evolution operator is expressed in terms of the Hamilton operator as

$$U = \lim_{\varepsilon \to 0} \hat{\mathcal{T}} \exp \left\{ -\frac{i}{\hbar_{\text{eff}}} \int_{t+\varepsilon}^{t+1+\varepsilon} dt \, H(\hat{q}, \hat{p}, t) \right\}, \tag{2.53}$$

where $\hat{\mathcal{T}}$ indicates the time ordering needed for time-dependent Hamiltonians and $\hbar_{\text{eff}}$ is Planck's constant measured in multiples of a typical action $S_0$ found in the system: $\hbar_{\text{eff}} = \hbar/S_0$. Because of the instantaneous action of the kick at integer times the time evolution is split into free evolution and the kick

$$U = \lim_{\varepsilon \to 0} \hat{\mathcal{T}} \exp \left\{ -\frac{i}{\hbar_{\text{eff}}} \int_{t+1-\varepsilon}^{t+1+\varepsilon} dt \, H(\hat{q}, \hat{p}, t) \right\} \hat{\mathcal{T}} \exp \left\{ -\frac{i}{\hbar_{\text{eff}}} \int_{t+\varepsilon}^{t+1-\varepsilon} dt \, H(\hat{q}, \hat{p}, t) \right\} \tag{2.54}$$

$$= \lim_{\varepsilon \to 0} \hat{\mathcal{T}} \exp \left\{ -\frac{i}{\hbar_{\text{eff}}} \int_{t+1-\varepsilon}^{t+1+\varepsilon} dt \, \left[ T(\hat{p}) + V(\hat{q}) \sum_{n \in \mathbb{Z}} \delta(t - n) \right] \right\} \hat{\mathcal{T}} \exp \left\{ -\frac{i}{\hbar_{\text{eff}}} \int_{t+\varepsilon}^{t+1-\varepsilon} dt \, T(\hat{p}) \right\} \tag{2.55}$$

$$= \lim_{\varepsilon \to 0} \exp \left\{ -\frac{i}{\hbar_{\text{eff}}} \left[ 2\varepsilon T(\hat{p}) + V(\hat{q}) \right] \right\} \exp \left\{ -\frac{i}{\hbar_{\text{eff}}} [1 - 2\varepsilon] T(\hat{p}) \right\} \tag{2.56}$$

$$= \exp \left\{ -i V(\hat{q})/\hbar_{\text{eff}} \right\} \exp \left\{ -i T(\hat{p})/\hbar_{\text{eff}} \right\}. \tag{2.57}$$

Note that in the special case of kicked systems the splitting into free evolution $(e^{-iT(\hat{p})/\hbar_{\text{eff}}})$ and kick $(e^{-iV(\hat{q})/\hbar_{\text{eff}}})$ is exact in contrast to other systems, where the split-operator technique is an approximation (see Ref. [52, Sec. 2.3.2]). The reason for this is the instantaneous action of the potential as $\delta$-kick, which is zero at almost all times ('free evolution') and arbitrary large at integer times.

In position representation the time evolution is given as

$$\psi(q, t+1) = \langle q | \psi(t+1) \rangle = \langle q | e^{-\frac{i}{\hbar_{\text{eff}}} V(\hat{q})} \, e^{-\frac{i}{\hbar_{\text{eff}}} T(\hat{p})} \psi(t) \rangle = e^{-\frac{i}{\hbar_{\text{eff}}} V(q)} \, \langle q | e^{-\frac{i}{\hbar_{\text{eff}}} T(\hat{p})} \psi(t) \rangle. \quad (2.58)$$

Inserting unity operators in position and momentum space, $\mathbb{1} = \int \mathrm{d}q' |q'\rangle\langle q'|$ and $\mathbb{1} = \int \mathrm{d}p |p\rangle\langle p|$, and using the position-space representation of a momentum eigenstate

$$\langle q | p \rangle = \frac{1}{\sqrt{h_{\text{eff}}}} \, e^{\frac{i}{\hbar_{\text{eff}}} q \cdot p} \quad (2.59)$$

we have

$$\psi(q, t+1) = \frac{1}{h_{\text{eff}}} \, e^{-\frac{i}{\hbar_{\text{eff}}} V(q)} \int \mathrm{d}q' \int \mathrm{d}p \, e^{-\frac{i}{\hbar_{\text{eff}}} T(p)} e^{\frac{i}{\hbar_{\text{eff}}} (q-q') \cdot p} \, \psi(q', t). \quad (2.60)$$

In order to obtain quantum mechanics on the classical torus, we have to assume periodicity of $e^{-\frac{i}{\hbar_{\text{eff}}} T(p)}$ as a function of $p$ with period $M_p \in \mathbb{R}$. This implies, that we can replace the integration over $\mathbb{R}$ by an integration over one period and an infinite sum

$$\int \mathrm{d}p \mapsto \int\limits_{p_{\min}}^{p_{\min}+M_p} \mathrm{d}p \sum_{m_p \in \mathbb{Z}} \quad (2.61)$$

$$p \mapsto p + m_p \cdot M_p, \quad (2.62)$$

which yields

$$\psi(q, t+1) = \frac{1}{h_{\text{eff}}} \, e^{-\frac{i}{\hbar_{\text{eff}}} V(q)} \int \mathrm{d}q' \int\limits_{p_{\min}}^{p_{\min}+M_p} \mathrm{d}p \sum_{m_p \in \mathbb{Z}} e^{-\frac{i}{\hbar_{\text{eff}}} T(p+m_p \cdot M_p)} e^{\frac{i}{\hbar_{\text{eff}}} (q-q') \cdot (p+m_p \cdot M_p)} \, \psi(q', t). \quad (2.63)$$

The summation over $m_p$ can be performed using Poisson summation formula

$$\sum_{m_p \in \mathbb{Z}} e^{\frac{i}{\hbar_{\text{eff}}} (q-q') \cdot m_p \cdot M_p} = \sum_{m_p \in \mathbb{Z}} e^{2\pi i \cdot m_p \frac{(q-q') \cdot M_p}{h_{\text{eff}}}}$$

$$= \sum_{j \in \mathbb{Z}} \delta\left( \frac{(q-q') \cdot M_p}{h_{\text{eff}}} - j \right) = \sum_{j \in \mathbb{Z}} \frac{h_{\text{eff}}}{M_p} \delta\left( q - q' - j \frac{h_{\text{eff}}}{M_p} \right) \quad (2.64)$$

and gives

$$\psi(q, t+1) = \frac{1}{M_p} e^{-\frac{i}{\hbar_{\text{eff}}} V(q)} \int \mathrm{d}q' \int\limits_{p_{\min}}^{p_{\min}+M_p} \mathrm{d}p \, e^{-\frac{i}{\hbar_{\text{eff}}} T(p)} e^{\frac{i}{\hbar_{\text{eff}}} (q-q') \cdot p} \sum_{j \in \mathbb{Z}} \delta\left( q - q' - j \frac{h_{\text{eff}}}{M_p} \right) \psi(q', t).$$

$$(2.65)$$

Now we consider the implications for the position variable $q$. The distance between two positions is discretized and we therefore can restrict ourselves to $q$-values of the following grid

$$q_k = q_0 + \frac{h_{\text{eff}}}{M_p}k \quad \text{or} \quad q_k = \frac{h_{\text{eff}}}{M_p}(k + \theta_p) \quad \text{with } k \in \mathbb{Z}. \tag{2.66}$$

This result and the role of $\theta_p$ can be understood in the following way. The time evolution operator describes all properties of the quantum system and commutes with the translation operator in momentum space ($p \mapsto p + M_p$). Therefore these operators have a common set of eigenstates. One set of eigenstates of the translation operator in momentum space are periodic functions of the momentum $p$ with period $M_p \in \mathbb{R}$. They can be expressed as a Fourier series

$$f(p) = \sum_{n \in \mathbb{Z}} c_n e^{2\pi i n p / M_p} = \sum_{n \in \mathbb{Z}} c_n e^{i q_n p / \hbar_{\text{eff}}} \quad \text{with} \quad q_n = \frac{2\pi \hbar_{\text{eff}}}{M_p}n. \tag{2.67}$$

In quantum mechanics the last expression is the sum of position eigenstates with eigenvalues $q_n$ in momentum representation. That is, in the description of a periodic function we only need a discrete set of position eigenvalues $q_n$.

Let us now extend our consideration to a function, which is built by the product of a periodic function and a phase factor with $\theta_p \in [0, 1)$, which is the most general case for an eigenstate of the above translation operator

$$g(p) = e^{2\pi i \theta_p p / M_p} f(p) = \sum_{n \in \mathbb{Z}} c_n e^{i q_n p / \hbar_{\text{eff}}} \quad \text{with} \quad q_n = \frac{2\pi \hbar_{\text{eff}}}{M_q}(\theta_p + n). \tag{2.68}$$

It is again given by a sum of position eigenstates with eigenvalues $q_n$ in momentum representation. However, in contrast to the above expression, Eq. (2.67), the discrete positions $q_n$ are shifted with $\theta_p$ in Eq. (2.68), which originates from the eigenvalue of the translation operator.

With this definition, Eq. (2.66), we can replace $q$ and $q'$ in Eq. (2.65) with grid points $q_n$ and $q_k$, respectively. In the next step the sum over $j$ is replaced by a sum over $k$ by performing the integration over the $\delta$-function and considering $q_n = q_{k+j}$. More precisely in the first step the integration over $q_k$ is performed and therefore $q_k$ is replaced by $q_n - j \cdot \frac{h_{\text{eff}}}{M_p}$, where we sum over integer $j$ from $-\infty$ to $+\infty$. This summation can be replaced by a summation over k from $-\infty$ to $+\infty$ using the redefinition of $q_n - j \cdot \frac{h_{\text{eff}}}{M_p}$ being $q_k$ again.

The final expression can be written as

$$\psi(q_n, t+1) = \sum_{k \in \mathbb{Z}} \langle q_n | U | q_k \rangle\, \psi(q_k, t)$$

$$\text{with} \quad \langle q_n | U | q_k \rangle = \frac{1}{M_p} e^{-\frac{i}{\hbar_{\text{eff}}} V(q_n)} \int\limits_{p_{\min}}^{p_{\min}+M_p} dp\; e^{-\frac{i}{\hbar_{\text{eff}}} T(p)} e^{\frac{i}{\hbar_{\text{eff}}}(q_n - q_k) \cdot p}. \tag{2.69}$$

If we now additionally involve the periodicity of the function $\mathrm{e}^{-\frac{\mathrm{i}}{\hbar_{\mathrm{eff}}}V(q)}$ with some period $M_q \in \mathbb{R}$, we can replace the infinite sum over the position grid points by a sum over one period and an infinite sum

$$\sum_{k\in\mathbb{Z}} \mapsto \sum_{\substack{k\in\mathbb{Z}:\\ q_k\in[q_{\min},q_{\min}+M_q)}} \sum_{m_q\in\mathbb{Z}} \tag{2.70}$$

$$q_k \mapsto q_k + m_q \cdot M_q. \tag{2.71}$$

Furthermore this periodicity implies, that the possible $q$-values in Eq. (2.66) have to fulfill $q_k + M_q = q_{k+N}$ for some natural number $N$, which means that the $q$-grid is commensurable to the period $M_q$. It follows

$$M_q = N \cdot \frac{h_{\mathrm{eff}}}{M_p} \qquad \text{or} \qquad h_{\mathrm{eff}} = \frac{M_q M_p}{N}. \tag{2.72}$$

With that we can restrict ourselves to $q_n, q_k \in [q_{\min}, q_{\min}+M_q)$ in the consideration of eigenstates of $U$, because $\langle q_n|U|q_k\rangle$ is periodic in position space and the whole eigenfunction can therefore be reconstructed by an additional Bloch phase $\theta_q$

$$\psi(q_k + m_q \cdot M_q, t) = \psi(q_k, t)\, \mathrm{e}^{\mathrm{i}2\pi\theta_q\cdot m_q}. \tag{2.73}$$

Performing the same steps as above resulting from the periodicity of position variable yields a discrete lattice for the momentum variable

$$p_j = \frac{h_{\mathrm{eff}}}{M_q}(\theta_q + j) \quad \text{with } j \in \mathbb{Z} \tag{2.74}$$

and finally gives

$$\psi(q_n, t+1) = \sum_{\substack{k\in\mathbb{Z}:\\ q_k\in[q_{\min},q_{\min}+M_q)}} \langle q_n|U|q_k\rangle\, \psi(q_k, t)$$

$$\text{with} \quad \langle q_n|U|q_k\rangle = \frac{1}{N}\mathrm{e}^{-\frac{\mathrm{i}}{\hbar_{\mathrm{eff}}}V(q_n)} \sum_{\substack{j\in\mathbb{Z}:\\ p_j\in[p_{\min},p_{\min}+M_p)}} \mathrm{e}^{-\frac{\mathrm{i}}{\hbar_{\mathrm{eff}}}T(p_j)}\mathrm{e}^{\frac{\mathrm{i}}{\hbar_{\mathrm{eff}}}(q_n-q_k)\cdot p_j}. \tag{2.75}$$

The possible $p$-values in the interval $[p_{\min}, p_{\min} + M_p)$ are obtained by rewriting Eq. (2.74),

$$p_j = \frac{M_p}{N}(\theta_q + j + n_p^{(0)}) \quad \text{for} \quad j = 0, \ldots, N-1, \tag{2.76}$$

where we introduce an offset $n_p^{(0)}$, which can be derived as follows.

$$p_0 \in [p_{\min}, p_{\min} + M_p/N) \tag{2.77}$$

$$p_0 = \frac{M_p}{N}(\theta_q + n_p^{(0)}) \stackrel{!}{\geq} p_{\min} \tag{2.78}$$

$$n_p^{(0)} := \left\lceil \frac{N}{M_p} p_{\min} - \theta_q \right\rceil . \tag{2.79}$$

In the last expression $\lceil x \rceil$ denotes the smallest integer number greater than or equal to $x$. A similar derivation for $q$ gives

$$q_k = \frac{M_q}{N}(\theta_p + k + n_q^{(0)}) \quad \text{for} \quad k = 0, \ldots, N-1 \quad \text{and} \quad n_q^{(0)} := \left\lceil \frac{N}{M_q} q_{\min} - \theta_p \right\rceil . \tag{2.80}$$

For the case of a unit cell $[0, M_q) \times [0, M_p)$ the integral offsets $n_q^{(0)}$ and $n_p^{(0)}$ vanish.

With an explicit incorporation of the grids the above time evolution reads

$$\psi(q_{\mathbf{n}}, t+1) = \underbrace{\mathrm{e}^{-\frac{\mathrm{i}}{\hbar_{\mathrm{eff}}}V(q_{\mathbf{n}})}}_{\text{mult. in } q}\mathrm{e}^{\frac{2\pi\mathrm{i}}{N}\mathbf{n}\cdot(\theta_q+n_p^{(0)})} \underbrace{\frac{1}{\sqrt{N}}\sum_{\mathbf{j}=0}^{N-1}\mathrm{e}^{\frac{2\pi\mathrm{i}}{N}\mathbf{n}\cdot\mathbf{j}}\underbrace{\mathrm{e}^{-\frac{\mathrm{i}}{\hbar_{\mathrm{eff}}}T(\theta_q+n_p^{(0)}+\mathbf{j})}}_{\text{mult. in } p}}_{\mathrm{IFT}\,p\,\mapsto\,q}$$

$$\times \underbrace{\frac{1}{\sqrt{N}}\sum_{\mathbf{k}=0}^{N-1}\mathrm{e}^{-\frac{2\pi\mathrm{i}}{N}\mathbf{k}\cdot\mathbf{j}}}_{\mathrm{FT}\,q\,\mapsto\,p}\mathrm{e}^{-\frac{2\pi\mathrm{i}}{N}\mathbf{k}\cdot(\theta_q+n_p^{(0)})}\psi(q_{\mathbf{k}}, t). \tag{2.81}$$

This equation provides an efficient way of performing the time evolution using the forward and backward discrete Fourier transformation as well as multiplications in position and momentum space, because these transformations have very fast numerical implementations in several libraries.

Note that in the derivation of Eq. (2.75) for the time evolution operator in the finite discrete basis of position and momentum, we used the periodicities

$$\mathrm{e}^{-\mathrm{i}T(p)/\hbar_{\mathrm{eff}}} = \mathrm{e}^{-\mathrm{i}T(p+M_p)/\hbar_{\mathrm{eff}}} \quad \text{with some period} \quad M_p \in \mathbb{R} \quad \text{and} \tag{2.82}$$

$$\mathrm{e}^{-\mathrm{i}V(q)/\hbar_{\mathrm{eff}}} = \mathrm{e}^{-\mathrm{i}V(q+M_q)/\hbar_{\mathrm{eff}}} \quad \text{with some period} \quad M_q \in \mathbb{R}. \tag{2.83}$$

If the quantum system under consideration incorporates these periodicities the above quantization procedure holds. If this is not the case, we have the possibility to choose a lattice of $q$ or $p$-values (by choosing $\theta_q$ or $\theta_p$), which leads to

$$\mathrm{e}^{-\mathrm{i}T(p_n)/\hbar_{\mathrm{eff}}} = \mathrm{e}^{-\mathrm{i}T(p_n+M_p)/\hbar_{\mathrm{eff}}} \quad \text{for} \quad n = 0, \ldots, N-1 \quad \text{and} \tag{2.84}$$

$$\mathrm{e}^{-\mathrm{i}V(q_k)/\hbar_{\mathrm{eff}}} = \mathrm{e}^{-\mathrm{i}V(q_k+M_q)/\hbar_{\mathrm{eff}}} \quad \text{for} \quad k = 0, \ldots, N-1. \tag{2.85}$$

That is, for the finite matrix $U$ the periodicities are inherent and therefore numerics cannot distinguish between such an apparent periodicity and a real periodicity of the system.

## 2.7  Direct quantization of time-independent systems

In this section we review a quantization procedure for time-independent systems [53], which will be used in Sec. 3.1.6. The starting point is the time-independent Schrödinger equation

$$H(\hat{q}, \hat{p})|\psi\rangle = E|\psi\rangle \tag{2.86}$$

in position representation

$$\int \mathrm{d}q' \langle q|H(\hat{q}, \hat{p})|q'\rangle \langle q'|\psi\rangle = \langle q|E|\psi\rangle, \tag{2.87}$$

where the unity operator in position representation $\mathbb{1} = \int \mathrm{d}q'|q'\rangle\langle q'|$ was inserted. In order to evaluate this expression further, we insert also the unity operator in momentum representation $\mathbb{1} = \int \mathrm{d}p|p\rangle\langle p|$. For the matrix elements we obtain

$$\langle q|H(\hat{q}, \hat{p})|q'\rangle = \frac{1}{2}\int \mathrm{d}p \left\{ \langle q|H(\hat{q}, \hat{p})|p\rangle\langle p|q'\rangle + \langle q|p\rangle\langle p|H(\hat{q}, \hat{p})|q'\rangle \right\} \tag{2.88}$$

which for a Hamiltonian $H(\hat{q}, \hat{p}) = T(\hat{p}) + V(\hat{q})$ can be evaluated using

$$\langle q|H(\hat{q}, \hat{p})|p\rangle = \langle q|T(\hat{p}) + V(\hat{q})|p\rangle = T(p)\langle q|p\rangle + V(q)\langle q|p\rangle = H(q, p)\langle q|p\rangle. \tag{2.89}$$

Therefore we obtain for the matrix elements

$$\langle q|H(\hat{q}, \hat{p})|q'\rangle = \frac{1}{2}\int \mathrm{d}p \left[ H(q, p) + H(q', p) \right] \langle q|p\rangle\langle p|q'\rangle \tag{2.90}$$

$$= \frac{1}{2}\int \mathrm{d}p \left[ H(q, p) + H(q', p) \right] \frac{1}{h_{\mathrm{eff}}} \exp\left\{ \frac{\mathrm{i}}{\hbar_{\mathrm{eff}}}(q - q') \cdot p \right\}, \tag{2.91}$$

in which only the classical Hamilton function $H(q, p)$ enters. If the Hamiltonian is not of the above type the ordering of $q$ and $p$ needs to be adapted in order to evaluate the expressions. In those cases Eq. (2.91) neglects terms of the order $\hbar_{\mathrm{eff}}^2$.

In order to obtain the eigenstates of $H$ on the torus we first assume periodicity in momentum space. That is, the Hamiltonian fulfills $H(q, p) = H(q, p + M_p)$ such that the infinite integration in momentum space can be replaced by an integration over one unit cell and an infinite sum

$$\langle q|H(\hat{q}, \hat{p})|q'\rangle = \frac{1}{2h_{\mathrm{eff}}} \sum_{m_p \in \mathbb{Z}} \int_{p_{\min}}^{p_{\min}+M_p} \mathrm{d}p \left[ H(q, p) + H(q', p) \right] \exp\left\{ \frac{\mathrm{i}}{\hbar_{\mathrm{eff}}}(q - q')(p + m_p \cdot M_p) \right\}. \tag{2.92}$$

The summation over $m_p$ can be performed using the Poisson summation formula (see Eq. (2.64) of Sec. 2.6). Inserting this result into Eq. (2.87) and performing the integration over $q'$ gives

$$\sum_{j \in \mathbb{Z}} \frac{1}{2M_p} \int_{p_{\min}}^{p_{\min}+M_p} \mathrm{d}p \left[ H(q,p) + H(q',p) \right] \exp \left\{ \frac{\mathrm{i}}{\hbar_{\mathrm{eff}}} \left( q - q' \right) p \right\} \psi(q') = E\psi(q), \qquad (2.93)$$

where $q' = q - j\frac{h_{\mathrm{eff}}}{M_p}$. In analogy to Sec. 2.6 the periodicity in momentum establishes a discrete lattice for the position space with spacing $h_{\mathrm{eff}}/M_p$

$$q_n = q_0 + n\frac{h_{\mathrm{eff}}}{M_p} \qquad (2.94)$$

and therefore the above equation needs to be evaluated for positions $q = q_n$ and $q' = q - jh/M_p = q_{n-j} =: q_k$ only,

$$\sum_{k \in \mathbb{Z}} \frac{1}{2M_p} \int_{p_{\min}}^{p_{\min}+M_p} \mathrm{d}p \left[ H(q_n,p) + H(q_k,p) \right] \exp \left\{ \frac{\mathrm{i}}{\hbar_{\mathrm{eff}}} \left( q_n - q_k \right) p \right\} \psi(q_k) = E\psi(q_n). \qquad (2.95)$$

Finally, the position space is restricted to $N$ values between $q_{\min}$ and $q_{\max} = q_{\min} + M_q$, where $N = M_q M_p/h$. This yields a matrix equation

$$\sum_{k=0}^{N-1} H_{nk}\psi(q_k) = E\psi(q_n) \qquad (2.96)$$

with the Hermitian matrix

$$H_{nk} = \frac{1}{2M_p} \int_{p_{\min}}^{p_{\min}+M_p} \mathrm{d}p \left[ H(q_n,p) + H(q_k,p) \right] \exp \left\{ \frac{\mathrm{i}}{\hbar_{\mathrm{eff}}} \left( q_n - q_k \right) p \right\}. \qquad (2.97)$$

The assumption of periodicity in momentum space is crucial to derive Eq. (2.97) on a discrete lattice and the restriction in position space gives rise to a finite dimensional matrix. Both facts limit the applicability of this approach to obtain eigenstates of the time-independent system. However, for the lower excited states located far from the boundary of the unit cell these assumptions are well fulfilled and we find excellent agreement with analytical expressions for the eigenstates evaluated on the lattice.

## 2.8 Husimi representation

Quantum eigenstates are given in position representation or by use of Fourier transform also in momentum representation. In order to compare properties of the quantum states with clas-

sical phase-space structures we need a phase-space representation of a quantum state. This is achieved by the Husimi representation. Starting point for the Husimi representation are coherent states. They are the quantum analogue of classical points respecting Heisenberg's uncertainty relation. They are a Gaussian function in position as well as momentum representation such that the product of the standard deviation fulfills $\sigma_q \sigma_p = \hbar_{\text{eff}}/2$. A coherent state at a phase-space point $(\tilde{q}_0, \tilde{p}_0)$ in position representation is given as

$$\alpha(q_n, \tilde{q}_0, \tilde{p}_0) = \left(\frac{2h}{M_p^2}\right)^{1/4} \exp\left\{-\frac{(q_n - \tilde{q}_0)^2}{2\hbar_{\text{eff}}}\right\} \exp\left\{\frac{\mathrm{i}}{\hbar_{\text{eff}}}\tilde{p}_0 q_n\right\}, \qquad (2.98)$$

where we choose $\sigma_q = \sigma_p = \sqrt{\hbar_{\text{eff}}/2}$ and normalized with respect to the vector norm, because all eigenstates of a quantum map are described on discrete lattice points according to Sec. 2.6.

With that we can write down the Husimi representation as projection of an arbitrary state to a coherent state at point $(\tilde{q}_0, \tilde{p}_0)$,

$$H_\phi(\tilde{q}_0, \tilde{p}_0) := \frac{1}{h_{\text{eff}}}\left|\langle\alpha(\tilde{q}_0, \tilde{p}_0)|\phi\rangle\right|^2 = \frac{1}{h_{\text{eff}}}\left|\sum_n \alpha^*(q_n, \tilde{q}_0, \tilde{p}_0) \cdot \phi(q_n)\right|^2. \qquad (2.99)$$

That is, the Husimi function at phase-space point $(\tilde{q}_0, \tilde{p}_0)$ is the overlap of a quantum state $\phi$ with a coherent state located at $(\tilde{q}_0, \tilde{p}_0)$. One can show that the integral of the Husimi function over the entire phase space gives one for normalized states. Moreover the integration over all momenta gives back the squared modulus of the state in position representation. Therefore, and because $H_\phi$ is non-negative, it is useful to interpret the Husimi function as probability density in phase space.

# 3 Quantum signatures of partial barriers in phase space

In this chapter we design a map with one isolated partial barrier (Sec. 3.1) for a quantitative study of the quantum transition of a partial barrier from quantum suppression to the classical transport behavior. This effect and quantitative measures to describe the transition curve are discussed in Sec. 3.2. In Sec. 3.3 we present results for these quantitative measure using the designed maps. Results for the standard map are discussed in Sec. 3.4.

## 3.1 Designed map with one partial barrier

In Sec. 2.4 it was pointed out that a generic mixed phase space exhibits infinitely many partial barriers. These partial barriers have different fluxes and form a hierarchical decomposition of the phase space. A detailed analysis of the infinitely many partial barriers is impossible. In order to investigate the impact of partial barriers on quantum systems, we therefore restrict ourselves to the case of one partial barrier. We design a system with a particularly simple phase-space structure, namely two chaotic regions separated by one dominant partial barrier, which significantly limits the transport in the chaotic region. There still might exist other partial barriers, but their flux is large compared to the dominant partial barrier.

### 3.1.1 Map with a regular stripe

At this point we review a mapping introduced by Ishikawa, Tanaka, and Shudo in Ref. [54], because it inspired the design of our map with one partial barrier, see Sec. 3.1.2. Rescaled to a phase space of size 1, this kicked system is described by the first derivative of kinetic and potential energy

$$T'(p) = \frac{1}{2\pi} \left( 8\pi a p + \frac{1}{2}(d_1 - d_2) + \frac{1}{2} \left[ 8\pi a p - \omega + d_1 \right] \tanh \left[ b(8\pi p - p_d) \right] \right. \tag{3.1}$$

$$\left. + \frac{1}{2} \left[ -8\pi a p + \omega + d_2 \right] \tanh \left[ b(8\pi p + p_d) \right] \right)$$

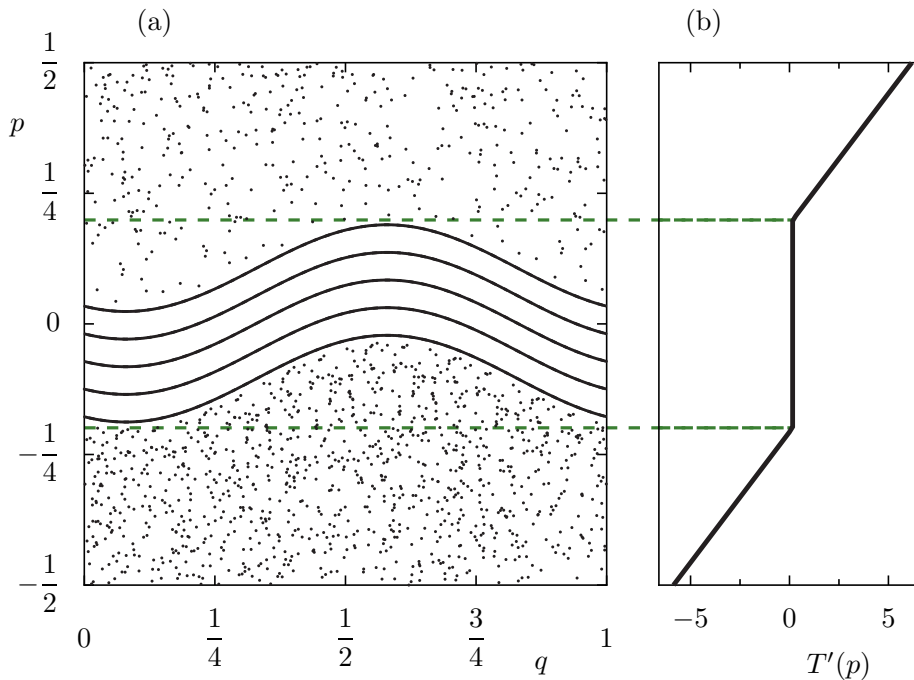$$V'(q) = -\frac{K}{8\pi} \sin(2\pi q) \tag{3.2}$$

**Figure 3.1:** (a) Phase-space portrait of the map with a regular stripe defined by Eqs. (3.1) and (3.2) with the parameters $a = 5, b = 100, d_1 = -24, d_2 = -26, \omega = 1, p_d = 5$, and $K = 2$ as in Ref. [54]. The horizontal regular tori (lines) and the chaotic sea (dots) are sharply separated. The function $T'(p)$ of Eq. (3.1) determines the phase space structure and is shown in (b). The dashed green lines are at $p = \pm p_d/(8\pi)$ and indicate the border of almost constant $T'(p)$ and therewith the border of the regular region in the phase space (a).

with parameters $a, b, d_1, d_2, \omega, p_d$ for the kinetic part. The potential is identical to the standard map, Eq. (2.30), except for the prefactor $\frac{1}{4}$ of the kicking strength $K$.

Figure 3.1 shows the phase space and the first derivative of the kinetic energy of the map defined by Eqs. (3.1) and (3.2). The phase space is well separated into regular tori and a chaotic sea surrounding them. This is achieved by the different slopes of $T'(p)$ as shown in Fig. 3.1. For almost vanishing slope around $p = 0$ we find regular motion and for large slopes the dynamics is chaotic. This will be discussed in Sec. 3.1.2 in more detail.

## 3.1.2  Design of the map $F_{\mathrm{pb}}$ with one partial barrier

We now design a map with one dominant partial barrier. For this we compose $T'(p)$ of linear segments similar to the map with a regular stripe discussed in Sec. 3.1.1. For the potential energy we use the one of the standard map (except for the sign), which is defined as

$$V(q) = -\frac{K'}{(2\pi)^2}\cos(2\pi q),$$

$$V'(q) = +\frac{K'}{2\pi}\sin(2\pi q), \tag{3.3}$$

with kicking strength $K'$. For the derivative of the kinetic energy $T'(p)$ we use piecewise linear functions (see Fig. 3.2)

$$T'(p) = \begin{cases} \omega_{\mathrm{reg}} & \text{for} \quad p \leq p_{\mathrm{d,reg}} \\ \omega_{\mathrm{reg}} + b_{\mathrm{left}} \cdot (p - p_{\mathrm{d,reg}}) & \text{for} \quad p_{\mathrm{d,reg}} \leq p \leq p_{\mathrm{fix}} - p_{\mathrm{d,lo}} \\ \omega_{\mathrm{fix}} + b \cdot (p - p_{\mathrm{fix}}) & \text{for} \quad p_{\mathrm{fix}} - p_{\mathrm{d,lo}} \leq p \leq p_{\mathrm{fix}} + p_{\mathrm{d,up}} \\ \omega_{\mathrm{reg}} + b_{\mathrm{right}} \cdot (p - p_{\mathrm{fix}} - p_{\mathrm{d,up}}) & \text{for} \quad p_{\mathrm{fix}} + p_{\mathrm{d,up}} \leq p \leq 1 - p_{\mathrm{d,reg}} \\ \omega_{\mathrm{reg}} & \text{for} \quad 1 - p_{\mathrm{d,reg}} \leq p \leq 1 \end{cases} \qquad (3.4)$$

with parameters $b, p_{\mathrm{fix}}, p_{\mathrm{d,reg}}, p_{\mathrm{d,up}}, p_{\mathrm{d,lo}} \in \mathbb{R}$, $\omega_{\mathrm{reg}} \in \mathbb{R} \setminus \mathbb{Z}$, $\omega_{\mathrm{fix}} \in \mathbb{Z}$ and the derived slopes

$$b_{\mathrm{left}} = \frac{\omega_{\mathrm{fix}} - b \cdot p_{\mathrm{d,lo}} - \omega_{\mathrm{reg}}}{p_{\mathrm{fix}} - p_{\mathrm{d,lo}} - p_{\mathrm{d,reg}}} \quad \text{and}$$

$$b_{\mathrm{right}} = \frac{\omega_{\mathrm{reg}} - \omega_{\mathrm{fix}} - b \cdot p_{\mathrm{d,up}}}{1 - p_{\mathrm{d,reg}} - p_{\mathrm{fix}} - p_{\mathrm{d,up}}}, \qquad (3.5)$$

respectively. The resulting function $T'(p)$ is shown in Fig. 3.2(b). This defines a kicked system and we call the corresponding mapping $F_{\mathrm{pb}}$. For $p \leq p_{\mathrm{d,reg}}$ and $p \geq 1 - p_{\mathrm{d,reg}}$ the winding
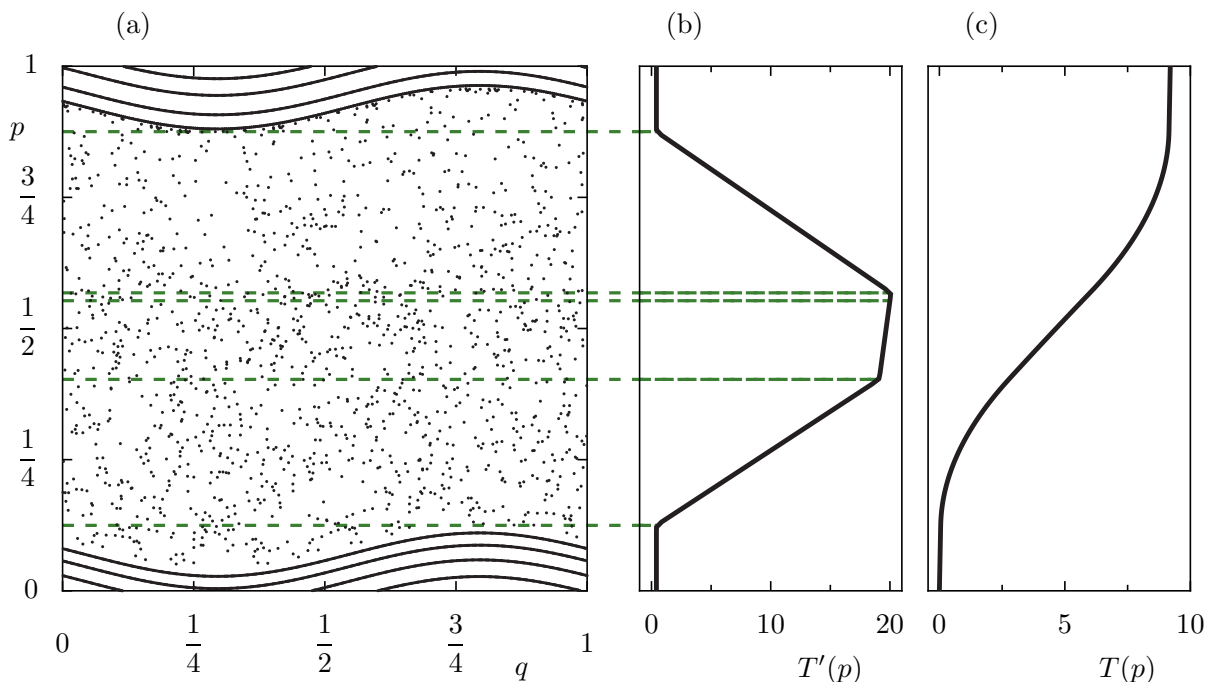


**Figure 3.2:** (a) The phase space of the map with one partial barrier $F_{\mathrm{pb}}$ consists of a large chaotic sea (dots) between the upper and lower regular tori (lines). (b), (c) Illustration of $T'(p)$, Eq. (3.4), and $T(p)$. At momenta $p$, where $T'(p)$ is constant, regular motion occurs, while at $p$, where $T'(p)$ behaves linearly, the dynamics is chaotic. The dashed green lines indicate the borders in the piecewise defined $T'(p)$ and are at $p = p_{\mathrm{d,reg}}$, $p_{\mathrm{fix}} - p_{\mathrm{d,lo}}$, $p_{\mathrm{fix}}$, $p_{\mathrm{fix}} + p_{\mathrm{d,up}}$, and $1 - p_{\mathrm{d,reg}}$.

frequency is constant and regular tori can exist. Around $p = \frac{1}{2}$ we find three different slopes, which lead to a chaotic region.

In order to gain a deeper understanding of the map $F_{\mathrm{pb}}$ we discuss the implications of a region, where $T'(p)$ has non-vanishing slope $\tilde{b}$ and winding frequency $\tilde{\omega}$

$$T'(p) = \tilde{\omega} + \tilde{b} \cdot p, \tag{3.6}$$

which yields the following mapping

$$q' = q + \tilde{\omega} + \tilde{b} \cdot p \qquad\qquad \mathrm{mod} \quad 1, \tag{3.7}$$

$$p' = p - \frac{K'}{2\pi} \sin(2\pi q') \qquad\qquad \mathrm{mod} \quad 1. \tag{3.8}$$

We now compare this mapping to the famous Chirikov's standard map (see Sec. 2.2)

$$Q' = Q + T'_{\mathrm{stdmap}}(P) = Q + P \qquad\qquad \mathrm{mod} \quad 1, \tag{3.9}$$

$$P' = P - V'_{\mathrm{stdmap}}(Q') = P + \frac{K}{2\pi} \sin(2\pi Q) \qquad\qquad \mathrm{mod} \quad 1, \tag{3.10}$$

where we introduced capital letters for position and momentum.

In order to translate the coordinates $q, p$ into the coordinates $Q, P$ of the standard map, we identify

$$Q = q, \tag{3.11}$$

$$P = \tilde{b} \cdot p, \tag{3.12}$$

$$K = -\tilde{b} \cdot K'. \tag{3.13}$$

Except for the additional winding due to $\tilde{\omega}$, locally the map $F_{\mathrm{pb}}$ behaves like the standard map if the momentum and the absolute value of the kicking strength are rescaled by the slope of $T'(p)$. This needs to be considered whenever features of the standard map like chaoticity are used to describe features of the map $F_{\mathrm{pb}}$. Furthermore, $p$ is periodic with period $1/\tilde{b}$, because $q$ is only defined up to modulo 1.

After this comparison with the standard map the resulting phase-space structure of the designed map $F_{\mathrm{pb}}$ can be understood: The large slopes in the upper and lower region (see Fig. 3.2) yield a high value for the standard map kicking strength and therefore chaotic motion. The central part has only a small slope and its properties need to be compared with the standard map with smaller kicking strength $K$. This feature is the decisive property of our map $F_{\mathrm{pb}}$, as it allows for different effective kicking strengths in one system. For non-integer $\tilde{\omega}$ an additional winding is induced, which is needed for the regular region defined by $(\omega_{\mathrm{reg}}, p_{\mathrm{d,reg}})$ in order to provide the horizontal tori.

Up to now only an inhomogeneous chaotic region has been introduced and we need to discuss the existence of a partial barrier in the central part of the phase space. By construction we find a fixed point of the mapping at $(\frac{1}{2}, p_{\mathrm{fix}})$

$$F_{\mathrm{pb}}(\tfrac{1}{2}, p_{\mathrm{fix}}) = \left( \tfrac{1}{2} + \omega_{\mathrm{fix}} + b \cdot 0, p_{\mathrm{fix}} - \frac{K'}{2\pi} \sin(2\pi[\tfrac{1}{2} + \omega_{\mathrm{fix}}]) \right) \mathrm{mod} \quad 1 = \left( \tfrac{1}{2}, p_{\mathrm{fix}} \right), \qquad (3.14)$$

and at $(0, p_{\mathrm{fix}})$

$$F_{\mathrm{pb}}(0, p_{\mathrm{fix}}) = \left( 0 + \omega_{\mathrm{fix}} + b \cdot 0, p_{\mathrm{fix}} - \frac{K'}{2\pi} \sin(2\pi[0 + \omega_{\mathrm{fix}}]) \right) \mathrm{mod} \quad 1 = (0, p_{\mathrm{fix}}), \qquad (3.15)$$

as long as $\omega_{\mathrm{fix}}$ is chosen as an integer value.

The stability of the fixed point is characterized by the Jacobian matrix of the mapping (see Sec. 2.1), which for map $F_{\mathrm{pb}}$ is

$$DF_{\mathrm{pb}}(q, p) = \begin{pmatrix} \frac{\partial q'}{\partial q} & \frac{\partial q'}{\partial p} \\ \frac{\partial p'}{\partial q} & \frac{\partial p'}{\partial p} \end{pmatrix}(q, p) = \begin{pmatrix} 1 & b \\ -K' \cos(2\pi q') & 1 - K' \cos(2\pi q')b \end{pmatrix}(q, p) \qquad (3.16)$$

and at the fixed point $(q_{\mathrm{fix}}, p_{\mathrm{fix}})$ reads

$$DF_{\mathrm{pb}}(q_{\mathrm{fix}}, p_{\mathrm{fix}}) = \begin{pmatrix} 1 & b \\ -K' \cos(2\pi q_{\mathrm{fix}}) & 1 - K' \cos(2\pi q_{\mathrm{fix}})b \end{pmatrix}. \qquad (3.17)$$

The trace of the Jacobian matrix is

$$\mathrm{Tr} DF_{\mathrm{pb}}(q_{\mathrm{fix}}, p_{\mathrm{fix}}) = 2 - K' \cos(2\pi q_{\mathrm{fix}})b = \begin{cases} 2 - bK' & \text{for} \quad q_{\mathrm{fix}} = 0 \\ 2 + bK' & \text{for} \quad q_{\mathrm{fix}} = \tfrac{1}{2}. \end{cases} \qquad (3.18)$$

For $bK' \in (-4, 4)$ we have one stable (elliptic) fixed point at $(0, p_{\mathrm{fix}})$ and one unstable (hyperbolic) fixed point at $(\frac{1}{2}, p_{\mathrm{fix}})$. A similar discussion of possible fixed points applies for the region above $p_{\mathrm{fix}} + p_{\mathrm{d,up}}$ and below $p_{\mathrm{fix}} - p_{\mathrm{d,lo}}$, too. In contrast to the central region the periodicity in $p$ determined by $1/b_{\mathrm{left}}$ and $1/b_{\mathrm{right}}$ is much smaller and their instabilities determined by Eq. (3.18) are much larger for the parameters used in this thesis.

Quantum mechanically, we consider the map $F_{\mathrm{pb}}$ on the torus as discussed in Sec. 2.6. This requires the periodicity of the potential energy, which is indeed fulfilled by $V(q)$ in Eq. (3.3), and of

$$\exp\{-\mathrm{i}T(p)/\hbar_{\mathrm{eff}}\} = \exp\{-2\pi\mathrm{i} \cdot N \cdot T(p)/(M_p M_q)\} \overset{M_q=M_p=1}{=} \exp\{-2\pi\mathrm{i} \cdot N \cdot T(p)\} \qquad (3.19)$$

as a function of $p$, which in general is not fulfilled. We introduce $\Delta T := [T(1) - T(0)]$ as an abbreviation for the difference of the kinetic energy between the lower and upper boundary of

the phase space. In order to achieve periodicity of the quantity in Eq. (3.19) the product $N \cdot \Delta T$ needs to be an integer. To permit this constraint at least for some $N = 1/h_{\text{eff}}$, we slightly vary the value of $p_{\text{d,reg}}$: We redefine $p_{\text{d,reg}} \rightarrow p_{\text{d,reg}} + \delta p_{\text{d,reg}}$ such that $N_0 \cdot \Delta T \in \mathbb{Z}$ for some $N_0 \in \mathbb{N}$ and achieve the periodicity of Eq. (3.19) for all $N$, which are multiples of $N_0$. The change of $p_{\text{d,reg}}$ can be calculated explicitly as

$$\delta p_{\text{d,reg}} := \frac{\lfloor N_0 \cdot \Delta T_{\text{old}} \rfloor / N_0 - \Delta T_{\text{old}}}{\omega_{\text{reg}} - \omega_{\text{fix}} + b/2(p_{\text{d,lo}} - p_{\text{d,up}})}, \tag{3.20}$$

where $\lfloor x \rfloor$ is the largest integer value smaller or equal to $x$ and $\Delta T_{\text{old}}$ denotes the difference of the kinetic energy without introducing $\delta p_{\text{d,reg}}$. An upper bound for $\delta p_{\text{d,reg}}$ is given by

$$|\delta p_{\text{d,reg}}| \leq \frac{0.5/N_0}{\omega_{\text{reg}} - \omega_{\text{fix}} + b/2(p_{\text{d,lo}} - p_{\text{d,up}})}, \tag{3.21}$$

which has to be compared to $p_{\text{d,reg}}$ in order to evaluate the change caused by $\delta p_{\text{d,reg}}$ on the mapping.

### 3.1.3  Construction of a partial barrier

The starting point for the construction of a partial barrier in the designed map $F_{\text{pb}}$ is the stable and the unstable manifold of the hyperbolic fixed point at $(\frac{1}{2}, p_{\text{fix}})$. We will choose the upper extension of the central region given by $p_{\text{d,up}}$ to be almost zero such that the upper branches of the stable and the unstable manifold have almost no support on the plateau with slope $b$ (see Fig. 3.2). Their dynamics is mainly governed by the upper region, which is much more chaotic, because the effective kicking strength $b_{\text{right}} K'$ is much larger than in the central region as $b_{\text{right}} \gg b$ in all examples considered in the following. Therefore the transport limitation due to these branches is negligible and we can restrict ourselves to the lower branch of the stable and the unstable manifold, which are located on the central part of $T'(p)$ (see Fig. 3.2).

These branches are shown in Fig. 3.3 and can be used to quantify the flux transported through this region. In order to construct almost invariant subsets of the phase space, the invariant stable and unstable manifold need to be combined. Starting with the hyperbolic fixed point we choose the stable manifold and at some arbitrary intersection point switch to the unstable manifold following it until we reach the fixed point again. The intersection point of switching is arbitrary and all partial barriers constructed in that way will have the same flux $\Phi$. Each image and preimage of one of the partial barriers again gives rise to a partial barrier with the same flux and the same size of area below and above the partial barrier due to area preservation (see Fig. 3.3(c) for comparison of a partial barrier and its preimage). For the classical dynamics there is no distinguished partial barrier and we therefore choose a simple looking one for our investigation. This is supported by the Husimi representation of eigenstates, which respects
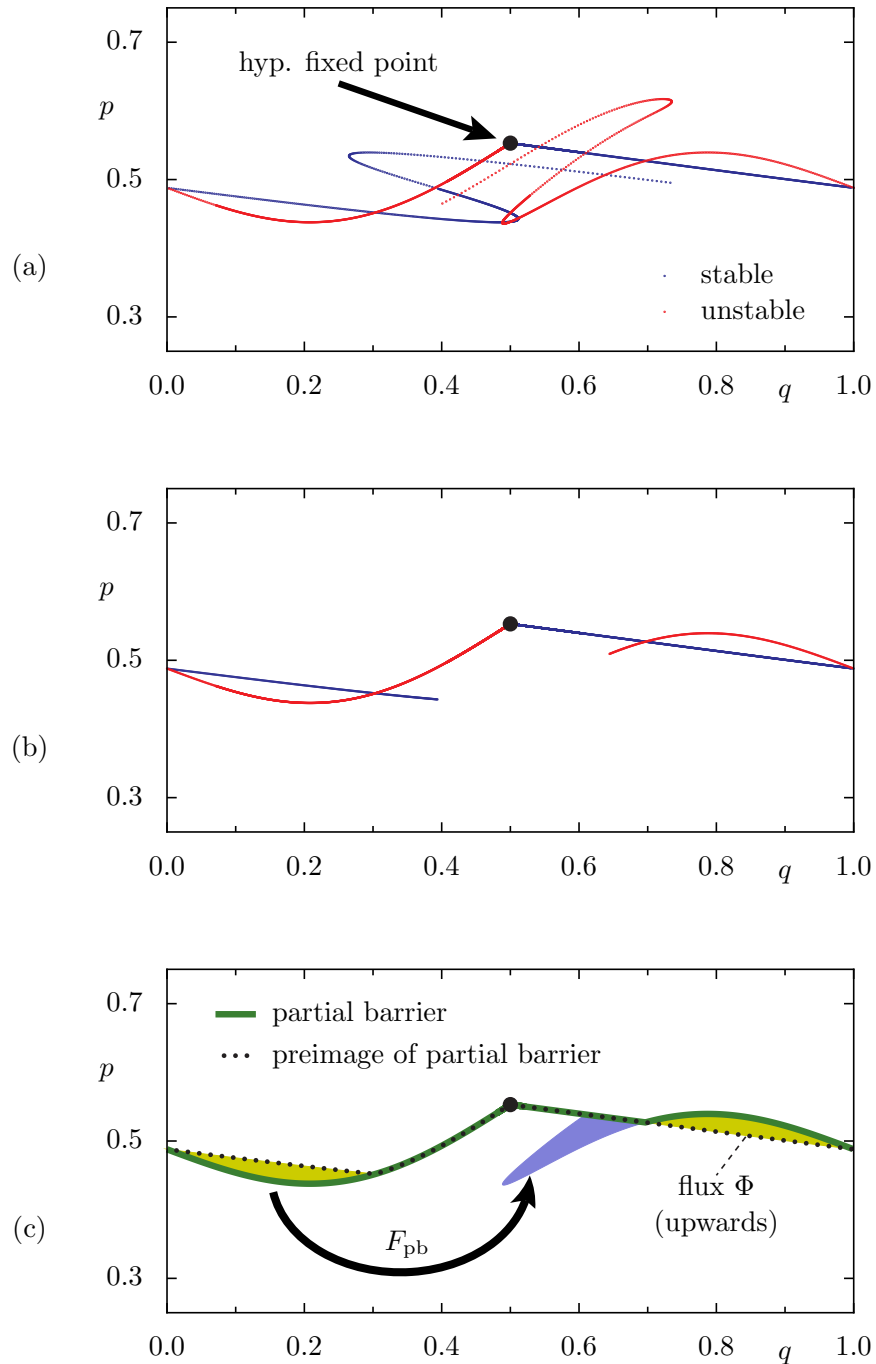
**Figure 3.3:** Illustration of a partial barrier built from stable and unstable manifolds of a hyperbolic fixed point for the map $F_{\mathrm{pb}}$. In (a) the lower branch of the stable manifold (blue) and the unstable manifold (red) are shown. (b) Shorter versions of them are used to define the partial barrier and construct their preimage in (c). The flux $\Phi$ towards the upper region as well as the flux towards the lower region are colored. The image of the flux towards the lower region under $F_{\mathrm{pb}}$ is illustrated by the arrow.

this partial barrier. Nonetheless the partial barrier is not uniquely defined in the quantum system. We observe that the Husimi representation of some eigenstates respects the partial barrier whereas other eigenstates ignore the partial barrier.

### 3.1.4 Definition of examples for the map $F_{\mathrm{pb}}$

In the following, we will consider several parameter sets for the map $F_{\mathrm{pb}}$ introduced in Sec. 3.1.2. In this section we provide the parameter values and introduce four different examples.

For all considered examples we choose

$$\omega_{\mathrm{fix}} = 20, \tag{3.22}$$

$$\omega_{\mathrm{reg}} = 0.411, \tag{3.23}$$

$$p_{\mathrm{d,reg}} = 0.125, \tag{3.24}$$

$$K' = 0.5, \tag{3.25}$$

$$N_0 = 10. \tag{3.26}$$

In order to vary the flux of the partial barrier discussed in Sec. 3.1.3, we choose different slopes $b$ for the examples (see Tab. 3.1). Larger slope $b$ yields a larger effective kicking strength $bK'$ and therefore stronger chaos such that the flux $\Phi$ increases with $b$. The lower limit of the central region determined by $p_{\mathrm{d,lo}}$ is adjusted such that the lower branches of the stable and the unstable manifold are not affected up the first intersections. If $p_{\mathrm{d,lo}}$ is chosen too small the partial barrier constructed from the lower branches will have a much larger flux (see discussion of upper branches of Sec. 3.1.3), because none of the loops is located in the central region and

| Example | 1 | 2 | 3 | 4 |
|---|---|---|---|---|
| $p_{\mathrm{fix}}$ | 0.553 | 0.578 | 0.599 | 0.613 |
| $p_{\mathrm{d,lo}}$ | 0.15 | 0.15 | 0.1725 | 0.195 |
| $p_{\mathrm{d,up}}$ | 0.015 | 0.015 | 0.025 | 0.025 |
| $b$ | 6.0 | 3.0 | 2.0 | 1.5 |
| $b_{\mathrm{left}}$ | 67.16 | 62.93 | 64.44 | 66.22 |
| $b_{\mathrm{right}}$ | -64.05 | -69.34 | -77.89 | -83.88 |
| $\Delta T_{\mathrm{old}}$ | 9.19486 | 9.27773 | 9.61681 | 9.8451 |
| $\delta p_{\mathrm{d,reg}}$ | -0.00027 | -0.00115 | 0.000865 | 0.00232 |
| $\Delta T$ | 9.2 | 9.3 | 9.6 | 9.8 |
| $A_{\mathrm{ch,up}}$ | 0.422 | 0.422 | 0.419 | 0.424 |
| $A_{\mathrm{ch,lo}}$ | 0.421 | 0.423 | 0.419 | 0.424 |
| $A_{\mathrm{reg}}$ | 0.157 | 0.1511 | 0.162 | 0.152 |
| $\Phi$ | 0.0053 | 0.0012 | 0.0003 | 0.0001 |
| $1/\Phi$ | 187.9 | 823.8 | 3065.7 | 9675.4 |
| $1/\Phi'$ | 327 | 1814 | 7357 | 38722 |

**Table 3.1:** Parameter values of the examples of map $F_{\mathrm{pb}}$. The first 4 rows provide additional parameters for the individual example to the common given parameters of Eq. (3.22). The 5 central rows are quantities, which are calculated from these parameters (see Eq. (3.5) and Eq. (3.20)). The last rows are determined from the corresponding phase space except for $\Phi'$, which will be defined in Sec. 3.1.5.

they are stretched into the lower chaotic region. The upper limit $p_{\mathrm{d,up}}$ is chosen such that the upper branches of the stable and the unstable manifold have almost no support on the central region and therefore yield no additional transport limitation as discussed in Sec. 3.1.3. From these parameters the slopes $b_{\mathrm{left}}$ and $b_{\mathrm{right}}$ for the straight lines in $T'(p)$ given in Eq. (3.4) can be calculated using Eq. (3.5). Furthermore the variation $\delta p_{\mathrm{d,reg}}$ of $p_{\mathrm{d,reg}}$ follows according to Eq. (3.20), which is indeed a small change in the definition of the map. Therewith, also the old and new difference of the kinetic energy at upper and lower phase-space limit $\Delta T_{\mathrm{old}}$ and $\Delta T$ are fixed. All these values are given in Tab. 3.1 for four different examples.

Figure 3.4 shows the central part of the phase space for the introduced examples. The hyperbolic fixed point with its lower branch of the stable and of the unstable manifold as well as the limits $p_{\mathrm{fix}} - p_{\mathrm{d,lo}}$ and $p_{\mathrm{fix}} + p_{\mathrm{d,up}}$ are plotted. The surrounding phase space exhibits only small islands.

For each of the examples defined in Tab. 3.1 we construct the partial barrier as discussed in
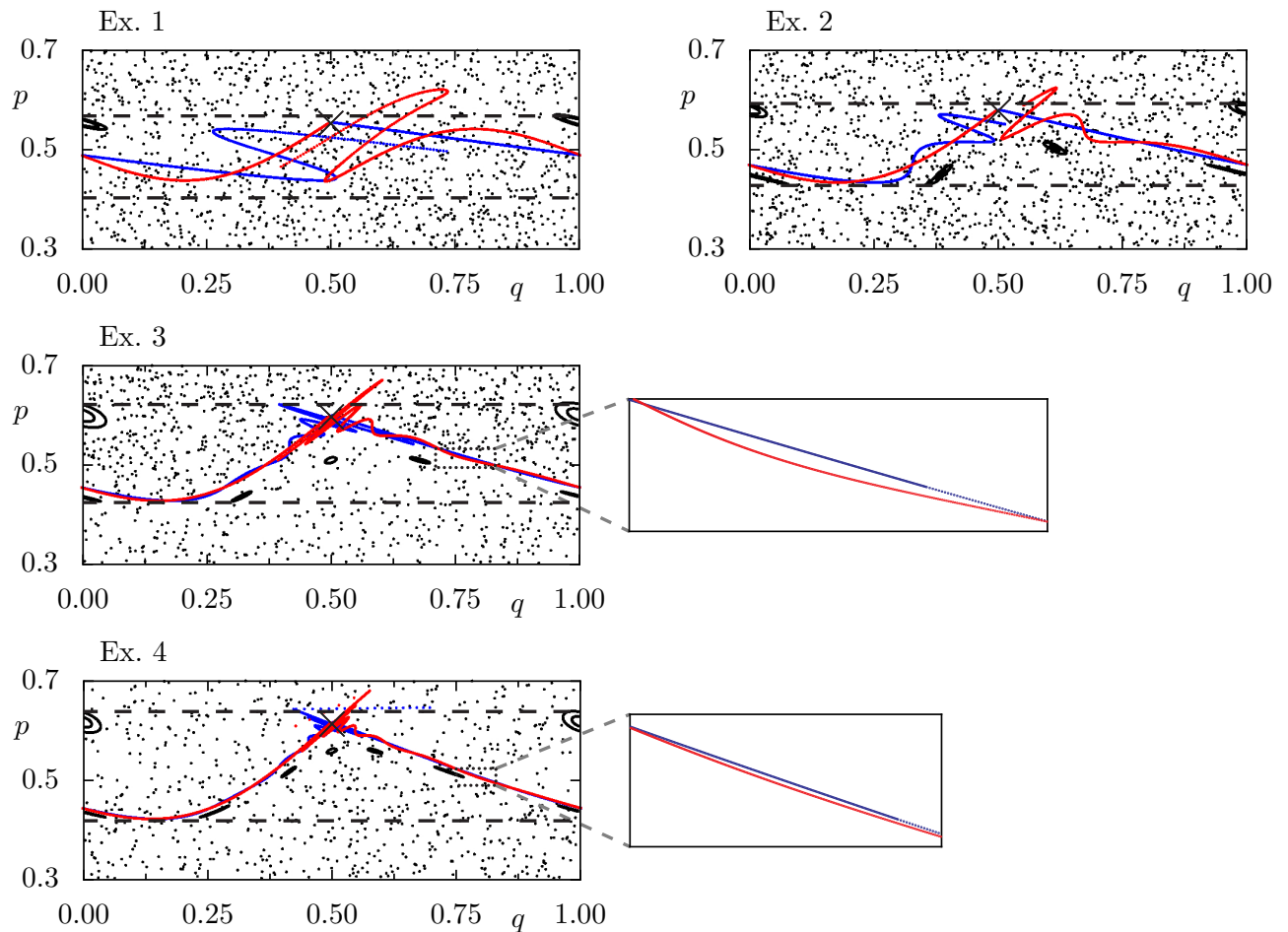


**Figure 3.4:** Stable manifold (blue solid line) and unstable manifold (red solid line) of the hyperbolic fixed point at $(0.5, p_{\mathrm{fix}})$ for the examples 1 ($\Phi \approx 1/200$), 2 ($\Phi \approx 1/800$), 3 ($\Phi \approx 1/3000$), and 4 ($\Phi \approx 1/10^4$) of the map $F_{\mathrm{pb}}$. The black dashed lines indicate the positions of $p_{\mathrm{fix}} - p_{\mathrm{d,lo}}$ and $p_{\mathrm{fix}} + p_{\mathrm{d,up}}$. The area of one loop between the stable and the unstable manifold is the flux $\Phi$ across the partial barrier constructed from these manifolds.

Sec. 3.1.3. As second border of the chaotic regions we use the regular torus closest to the chaotic sea, where the latter is only an approximation, because it is hard to find the last surviving KAM torus [9, 55]. Therewith the size of the upper chaotic region $A_{ch,up}$ and the lower chaotic region $A_{ch,lo}$ is fixed (see Tab. 3.1). Although the size of the regular region is fixed by the choice of $p_{d,reg}$ the measured values vary slightly, which indicates the accuracy of the measurement of the region sizes.

Numerically the flux $\Phi$ is determined from the loop area between the stable and the unstable manifold by use of a polygon approximation. Therefore the accuracy of the flux depends on the quality of the manifolds, which we constructed by forward and backward iterations of points close to the fixed point.

### 3.1.5  Characterization of the classical system $F_{pb}$

We now characterize the mapping with one partial barrier $F_{pb}$ introduced in the last section to check the predicted classical property, that the discussed partial barrier is the one with smallest flux. The impact of a partial barrier on the classical system is the limitation of the escape of orbits from the enclosed region for intermediate times. Orbits are trapped for several iterations until they enter the turnstile and are mapped into the other region. The number of iterations needed to leave the initial region is called escape time and a quantitative measure of the trapping is given by the distribution of these escape times. In the case of a chaotic region this distribution decays exponentially [5]

$$p(t) \propto \exp\{-\alpha t\}. \tag{3.27}$$

It is determined by the escape rate $\alpha$, i.e. the probability to leave a chaotic region through the turnstile. Its inverse is the average escape time, called dwell time $t_{dwell}$.

The classical escape rate $\alpha$ is given by the ratio of the flux across the partial barrier $\Phi$ and the size of the accessible region $A_{access,i}$

$$\alpha_i = \frac{1}{t_{dwell,i}} = \frac{\Phi}{A_{access,i}}. \tag{3.28}$$

There are several ways of defining escape time distributions $p(t)$. We first apply a definition which uses one long orbit. The segments of the orbit are labeled by 'upper' and 'lower' according to the upper and lower chaotic region. The escape time is defined as the number of consecutive iterations before the orbit enters the opposite region. The densities $p'_{up}(t)$ and $p'_{lo}(t)$ contain all escape times for the upper and the lower chaotic region, respectively. Figure 3.5 shows the resulting distributions for example 2 of the map $F_{pb}$. The average escape time of upper $\langle t_{up} \rangle \approx 345$ and lower region $\langle t_{lo} \rangle \approx 348$ are in good agreement with the expected value $t_{dwell,i} = A_{access,i}/\Phi \approx 346$. Also the density of escape times of the upper region $p'_{up}(t)$ is
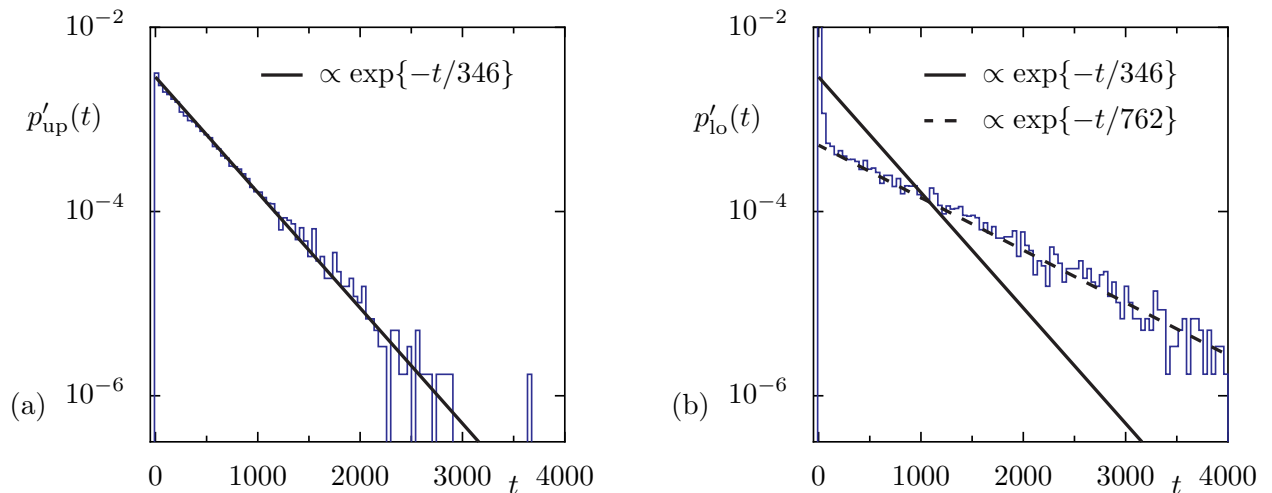
**Figure 3.5:** Escape time distribution for the example 2 of the map $F_{\mathrm{pb}}$ (expected flux $\Phi \approx 1/825$) of an orbit started at $(q, p) = (0.25, 0.75)$ and iterated $10^7$ times. The numerically determined densities of escapes times from the upper and the lower region, $p'_{\mathrm{up}}$ and $p'_{\mathrm{lo}}$, are shown as blue histograms in (a) and (b), respectively. They are compared with the expected exponential decay proportional to $\exp\{-t/t_{\mathrm{dwell},i}\}$ (solid black line) with the dwell time $t_{\mathrm{dwell},i} = A_{\mathrm{access},i}/\Phi \approx 346$. The distribution $p'_{\mathrm{up}}$ is well described by this exponential decay. However, the distribution $p'_{\mathrm{lo}}$ shows a different exponential decay proportional to $\exp\{-t/762\}$ (dashed black line).

well described by the exponential decay using $t_{\mathrm{dwell},i}$. However, for the lower chaotic region the distribution $p'_{\mathrm{lo}}(t)$ clearly deviates from the expected behavior. Here the decay is rather described by $\exp\{-t/762\}$, which is consistent with a smaller flux $\Phi' \approx 1/1800$ (assuming that the area $A_{\mathrm{access},i}$ is unchanged). This finding indicates the existence of at least one further partial barrier in the central region $p \in [p_{\mathrm{fix}} - p_{\mathrm{d,lo}}, p_{\mathrm{fix}} + p_{\mathrm{d,up}}]$. For the other examples such kind of mismatch of $p'_{\mathrm{lo}}(t)$ is also observed. Note that the average value of the escape times is independent of this finding, because it depends only on the flux across the considered partial barrier. In terms of the distributions shown in Fig. 3.5, the correct average escape time is achieved due to many quickly escaping events of the orbit. At these events the orbit enters the lower region, but returns to the upper chaotic region before it passes the additional partial barrier.

In order to examine this finding in more detail, we introduce the survival probability as another measure of the trapping. For this, many orbits are started inside one region and are iterated until they leave this region. The survival probability $P(t)$ is the fraction of orbits, which stay in the initial region at least up to time $t$. The definition of the upper and the lower region depends on the definition of the border of the regular region. Therefore eventually regular or nearly regular orbits might be included. Hence, orbits which are trapped up to the maximal time are assumed to be regular and removed from the statistics. Figure 3.6 shows the survival probability of the upper and the lower region of the same example as in Fig. 3.5.
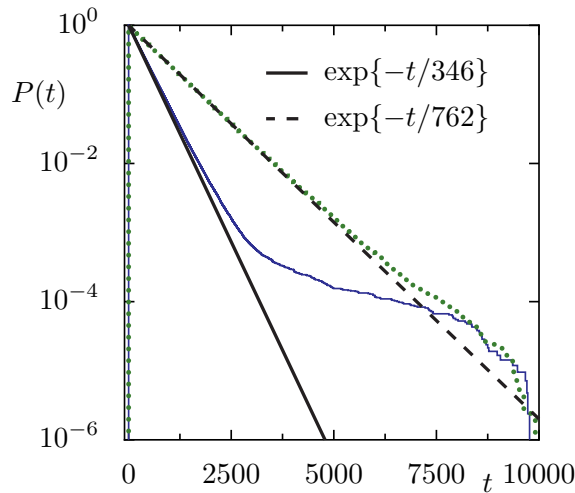
**Figure 3.6:** Survival probability $P_{\mathrm{up}}(t)$ and $P_{\mathrm{lo}}(t)$ for the example 2 of the map $F_{\mathrm{pb}}$ of orbits started equidistantly in the upper chaotic region (blue solid histogram) and in the lower chaotic region (green dotted histogram). At small times $P_{\mathrm{up}}(t)$ is described by an exponential decay with $t_{\mathrm{dwell},i} \approx 346$. In contrast, $P_{\mathrm{lo}}(t)$ follows a slower exponential decay with $t_{\mathrm{dwell},i} \approx 762$ indicating the existence of a partial barrier with a smaller flux in the lower chaotic region.

Again the distribution associated with the lower chaotic region exhibits a slower exponential decay given by the enhanced dwell time $t_{\mathrm{dwell,\ lo}} \approx 762$.

Finally, we conclude that there is an additional partial barrier below the partial barrier constructed in Sec. 3.1.3 and this additional partial barrier has smaller flux. The value of this flux is derived from exponential fits to the survival probability assuming that the change of the areas is negligible. This fitted flux for the examples considered up to now is given as $\Phi'$ in Tab. 3.1. This additional partial barrier might be attributed to a cantorus or the stable and the unstable manifolds of a periodic orbit of any period. As within this thesis, this additional partial barrier could not be constructed, we remove this one by an approach presented in the following section and restrict ourselves to the investigation of the partial barrier constructed in Sec. 3.1.3.

## 3.1.6 Extension of the map $F_{\mathrm{pb}}$ – phase-space drilling

We want to investigate the impact of the partial barrier constructed in Sec. 3.1.3 and get rid of the unknown additional partial barriers discussed in Sec. 3.1.5. Therefore the previously discussed map $F_{\mathrm{pb}}$ is composed with a local rotation defined in some circular phase-space region. We call this approach phase-space drilling. The rotation is given by

$$F_{\mathrm{rot}} : \begin{pmatrix} q \\ p \end{pmatrix} \mapsto \begin{pmatrix} q_{\mathrm{c}} \\ p_{\mathrm{c}} \end{pmatrix} + \begin{pmatrix} \cos(\omega_{\mathrm{c}}) & -\sin(\omega_{\mathrm{c}}) \\ \sin(\omega_{\mathrm{c}}) & \cos(\omega_{\mathrm{c}}) \end{pmatrix} \begin{pmatrix} q - q_{\mathrm{c}} \\ p - p_{\mathrm{c}} \end{pmatrix} \qquad (3.29)$$

for points inside a circle of radius $r_{\mathrm{c}}$ around $(q_{\mathrm{c}}, p_{\mathrm{c}})$. The points are rotated by an angle of $\omega_{\mathrm{c}}$ in counterclockwise direction and all points outside the circle are unchanged. The resulting mapping is discontinuous on the circle line. While the rotation itself is an integrable motion and the distance to the point $(q_{\mathrm{c}}, p_{\mathrm{c}})$ is unchanged by the mapping, the composition $F_{\mathrm{pb,rot}}$ of $F_{\mathrm{pb}}$ and $F_{\mathrm{rot}}$ yields stronger chaos in the sense of less transport limitations inside the chaotic region.

Figure 3.7 illustrates the idea of the destruction of partial barriers using the additional rotation. If we, for example, assume that the green horizontal line in Fig. 3.7 is a partial barrier with a very small flux, then the flux of the composed mapping $F_{\mathrm{pb,rot}} = F_{\mathrm{rot}} \circ F_{\mathrm{pb}}$ is determined by the fraction of the blue crosses located below the partial barrier. Therefore the composed mapping has an enhanced flux across the green horizontal line.

The quantum version of the map introduced above is the composition of the unitary time evolution operators of the original map $U_{\mathrm{pb}}$ and the rotation $U_{\mathrm{rot}}$. For $U_{\mathrm{rot}}$ the quantization procedure is not straightforward, but can be performed using the eigenstates of the harmonic oscillator. We use the set of harmonic oscillator eigenstates $\{\eta_m\}$ as a basis set inside the circle around $(q_{\mathrm{c}}, p_{\mathrm{c}})$. We define the projector onto the corresponding sub-space and the associated
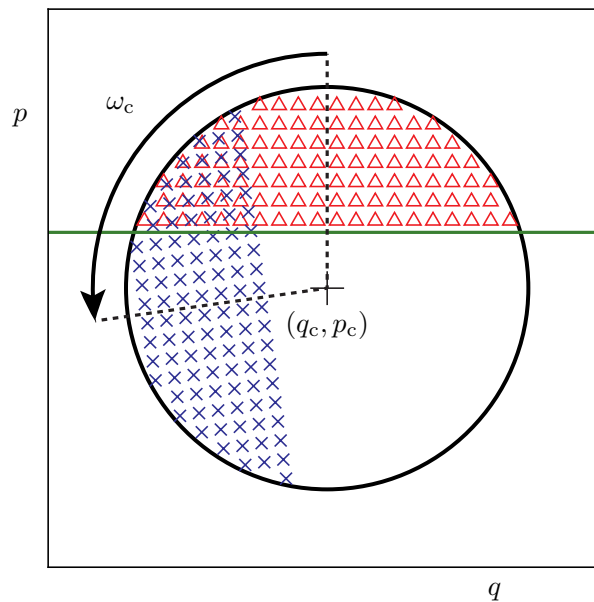


**Figure 3.7:** Illustration of the action of the map $F_{\mathrm{rot}}$. During one application of $F_{\mathrm{rot}}$ the red triangles located above the green horizontal line are mapped to the blue crosses and some of them are below the green horizontal line. This transport of points below the green horizontal line gives rise to an enhanced flux across this line. The flux is maximal for $\omega_{\mathrm{c}} = \pi$.

time evolution operator as

$$P_{\mathrm{HO}} := \sum_{m=0}^{N_{\mathrm{HO}}-1} |\eta_m\rangle\langle\eta_m|, \tag{3.30}$$

$$U_{\mathrm{HO}} := \sum_{m=0}^{N_{\mathrm{HO}}-1} \lambda_m |\eta_m\rangle\langle\eta_m|, \tag{3.31}$$

where $\lambda_m = \exp\{+\mathrm{i}(m + \frac{1}{2})\omega_{\mathrm{c}}\}$ is the eigenvalue for the eigenstate $\eta_m$ and the number of considered states $N_{\mathrm{HO}} < N$ is chosen according to $N_{\mathrm{HO}} = \lfloor \frac{1}{2} + \pi r_{\mathrm{c}}^2/h_{\mathrm{eff}}\rfloor$. Note that the eigenvalue has the opposite sign as expected for the harmonic oscillator, because $\omega_{\mathrm{c}}$ is the counterclockwise increase of the angle whereas orbits in the harmonic oscillator evolve clockwise in time. An important property of the states $\{\eta_m\}$ is that they are well localized inside the circle and have almost no tails into the region outside of the circle. Therefore they give a sharp projection onto the circle, smoothened on the size of Planck's constant.

The quantum time evolution corresponding to the classical rotation is given by

$$U_{\mathrm{rot}} = (\mathbb{1} - P_{\mathrm{HO}}) + U_{\mathrm{HO}}P_{\mathrm{HO}} = (\mathbb{1} - P_{\mathrm{HO}}) + U_{\mathrm{HO}}. \tag{3.32}$$

That is, the projection of a state onto the circle with $\{\eta_m : m = 0, ..., N_{\mathrm{HO}} - 1\}$ is time evolved using $U_{\mathrm{HO}}$ whereas the other components, orthogonal to the set $\{\eta_m\}$, are unchanged. One checks the unitarity of $U_{\mathrm{rot}}$ using the unitarity of $U_{\mathrm{HO}}$ and the orthogonality of the states $\{\eta_m\}$. Therefore the total time evolution operator

$$U_{\mathrm{pb,rot}} := U_{\mathrm{rot}}U_{\mathrm{pb}} \tag{3.33}$$

is unitary, too.

An approach to obtain eigenstates corresponding to the classical rotation numerically is the direct quantization of the time-independent harmonic oscillator. This is discussed in Sec. 2.7 and extends the applicability of this approach to eigenstates of the harmonic oscillator, for which the analytical expressions, in particular the Hermite polynomials, cannot be evaluated numerically with sufficient precision.

This kind of modification of a given map by superimposing an additional mapping is not restricted to rotations on harmonic oscillator like islands. More generally, one may consider an arbitrary island and follow the dynamics inside the island, while outside the mapping is the identity. The quantum version of such a map can be derived as above by replacing the eigenstates of the harmonic oscillator $\{\eta_m\}$ by eigenstates of the island and the $\lambda_m$ by eigenvalues of the corresponding quantum map. In order to have properly localized states one has to restrict the used states to those located well inside the island with almost no overlap with the chaotic region.

In order to preserve time reversal invariance of the composed map, we have to recall the discussion of Sec. 2.5 and investigate the assumptions needed for the composed map to possess time reversal invariance. Although the kicked map $F_{\mathrm{pb}}$ and the local rotation $F_{\mathrm{rot}}$ fulfill time reversal invariance it is not obvious that the composed map $F_{\mathrm{pb,rot}} = F_{\mathrm{rot}} \circ F_{\mathrm{pb}}$ does. The map $F_{\mathrm{pb,rot}}$ is of the type of Eq. (2.45), where we identify $F_1$ with $F_{\mathrm{pb}}$ and $F_2$ with $F_{\mathrm{rot}}$. The definition of $\sqrt{F_2}$ is a rotation with a change of the angle of $\omega_{\mathrm{c}}/2$.

As the first step, we show that the map $F_{\mathrm{pb}}$ possesses an anticanonical symmetry. In order to do so, we have to consider the map in the half kick representation $F_{\mathrm{pb,hk}}$, which is canonical conjugated to the map itself. The anticanonical symmetry fulfilled by $F_{\mathrm{pb,hk}}$ is (see Sec. 2.5)

$$\tilde{\tau} : (q, p) \mapsto (1 - q, p) \tag{3.34}$$

with $\tilde{\tau}^2 = \mathbb{1}$ and we can show that

$$\tilde{\tau} \circ F_{\mathrm{pb,hk}} \circ \tilde{\tau} = F_{\mathrm{pb,hk}}^{-1} \iff V'(1 - q) = V'(q), \tag{3.35}$$

which is fulfilled for the potential chosen in Eq. (3.3).

In order to prove the time reversal invariance of Eq. (2.45), it was used that both maps possess the same anticanonical symmetry. Therefore also the rotation $F_{\mathrm{rot}}$ needs to fulfill

$$\tilde{\tau} \circ F_{\mathrm{rot}} \circ \tilde{\tau} = F_{\mathrm{rot}}^{-1}, \tag{3.36}$$

which is equivalent to $1 - q_{\mathrm{c}} = q_{\mathrm{c}}$ and therefore the center of the circle needs to lie on the line $q = \frac{1}{2}$. If one considers a rotation with a center not located on this line, one has to choose two non-overlapping circles with $p_{\mathrm{c},1} = p_{\mathrm{c},2}$, $q_{\mathrm{c},1} = 1 - q_{\mathrm{c},2}$ and $\omega_{\mathrm{c},1} = \omega_{\mathrm{c},2}$. It is important that these two circles do not overlap in order to think of the two local rotations as one mapping.

## 3.1.7  Definition of examples for the map $F_{\mathrm{pb,rot}}$

The mapping $F_{\mathrm{pb,rot}}$ defined in the last section is composed of the half kick version of map $F_{\mathrm{pb}}$ introduced in Sec. 3.1.2 and a rotation. For map $F_{\mathrm{pb}}$ we use the parameters of Tab. 3.1 and choose $p_{\mathrm{d,up}} = 0.005$ for all considered examples. For the rotation $F_{\mathrm{rot}}$ the values determining the rotation are given in Tab. 3.2. The rotation frequency $\omega_{\mathrm{c}}$ is chosen close to $\pi$ in order to maximize the impact of the additional rotation as illustrated in Fig. 3.7. The position and radius of the rotating region are chosen such that the additional partial barrier are removed, which is checked in the next section.

| Example | 1 | 2 | 3 |
|---|---|---|---|
| $q_{c,1}$ | 0.5 | 0.5 | 0.5 |
| $p_{c,1}$ | 0.33 | 0.46 | 0.48 |
| $r_{c,1}$ | 0.2 | 0.1 | 0.1 |
| $\omega_{c,1}$ | 3.0 | 3.0 | 3.0 |
| $\pi r_{c,1}^2$ | 0.13 | 0.03 | 0.03 |
| $q_{c,2}$ | 0.2 | | |
| $p_{c,2}$ | 0.66 | | |
| $r_{c,2}$ | 0.15 | | |
| $\omega_{c,2}$ | 3.0 | | |
| $\pi r_{c,2}^2$ | 0.07 | | |

**Table 3.2:** Parameter values of the basic examples of map $F_{\mathrm{pb,rot}}$ in addition to values given in Tab. 3.1. The third drilled region is determined by $q_{c,3} = 1 - q_{c,2}$, $p_{c,3} = p_{c,2}$, $r_{c,3} = r_{c,2}$, and $\omega_{c,3} = \omega_{c,2}$. The impact of the drilling can be estimated by the size of the drilling region $\pi r_{c,i}^2$ compared to the size of the phase space.

## 3.1.8 Characterization of the classical system $F_{\mathrm{pb,rot}}$

After introducing the map with local rotation $F_{\mathrm{pb,rot}}$, we have to verify that now only the expected partial barrier significantly limits the transport between the upper and the lower chaotic region. In analogy to Sec. 3.1.5 we consider the survival probability of orbits started in the upper and the lower chaotic region, respectively. Figure 3.8 compares the resulting distributions $P_{\mathrm{up}}(t)$ and $P_{\mathrm{lo}}(t)$ of example 2 of the map $F_{\mathrm{pb}}$ to example 2 of the new map $F_{\mathrm{pb,rot}}$. By use of the phase-space drilling the additional partial barrier with much smaller



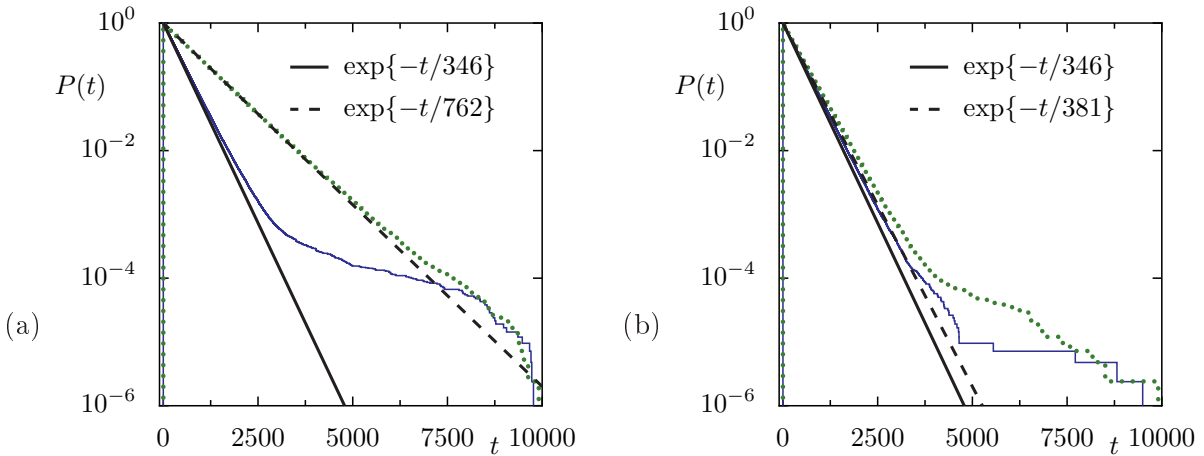**Figure 3.8:** Survival probability for (a) example 2 of the map $F_{\mathrm{pb}}$ ($\Phi' \approx 1/1800$) and (b) example 2 of the map $F_{\mathrm{pb,rot}}$ ($\Phi \approx 1/800$, right picture): $P_{\mathrm{up}}(t)$ and $P_{\mathrm{lo}}(t)$ of orbits started in the upper (blue solid histogram) and lower (green dotted histogram) chaotic region. In (a) the dwell time according to the flux $\Phi'$ is shown as dashed line and in (b) an exponential decay with a dwell time enhanced by a factor of 1.1 is shown as dashed line.

flux is removed and the survival probability in the lower region is in good agreement with the exponential decay determined by the dwell time $t_{\mathrm{dwell},i} = A_{\mathrm{access},i}/\Phi$. In Fig. 3.8(a) a slower decay is plotted as a dashed line and gives an estimate of the previously found exponential decay caused by the additional partial barrier. The dashed line in Fig. 3.8(b) corresponds to a dwell time enhanced by a factor of 1.1 and gives an estimation of the agreement with the expected exponential decay.

The distributions for the example 2 and also for the other examples of map $F_{\mathrm{pb,rot}}$ are in good agreement with the expected decay. Therefore we conclude that using the phase-space drilling the additional partial barrier has been destroyed. The partial barrier constructed in Sec. 3.1.3 is the only limitation for classical transport.

## 3.2   Quantum suppression of transport

As described in Sec. 2.4 a classical particle started in the upper chaotic region (see Fig. 3.9(a)) will eventually enter the turnstile and in the next step is mapped to the lower chaotic region. Therefore any orbit initially located in the upper chaotic region will at large times fill the whole chaotic sea quite uniformly. Hence, partial barriers influence the classical dynamics only on intermediate time scales, where a typical orbit is restricted to one part of phase space. At large times such a chaotic orbit will explore the whole chaotic sea.

In contrast to the classical dynamics, the corresponding quantum system can be more restrictive as illustrated in Fig. 3.9(b). In analogy to a classical initial condition $(q, p)$, quantum mechanically we use a coherent state with minimal uncertainty (see Sec. 2.8) centered at $(q, p)$ as initial state. Although under time evolution this initial state spreads, almost no weight is transmitted into the lower chaotic region. This observation holds even at arbitrary large times, which will become clear if properties of eigenstates are considered. This is surprising as typically a quantum system has, due to tunneling, more transport channels than the corresponding classical system. Here, however, quantum mechanics is more restrictive than classical mechanics.

For small Planck's constant the classical behavior of a partial barrier is recovered as illustrated in Fig. 3.9(c). At large times, the wave packet spreads over the whole chaotic region quite uniformly. As a function of Planck's constant we find that a partial barrier behaves in different ways: like a barrier for large Planck's constant and like a partial barrier for small Planck's constant.

The impact of partial barriers on the corresponding quantum system was first mentioned in Ref. [15]. Here, MacKay, Meiss, and Percival conjectured: 'The quantization is limited by the size of the turnstiles in units of Planck's constant. Since the turnstiles vary in a very complicated way as a function of frequency, this criterion is difficult to apply in practice.' The impact of a partial barrier on the quantum system is governed by the ratio of the classical
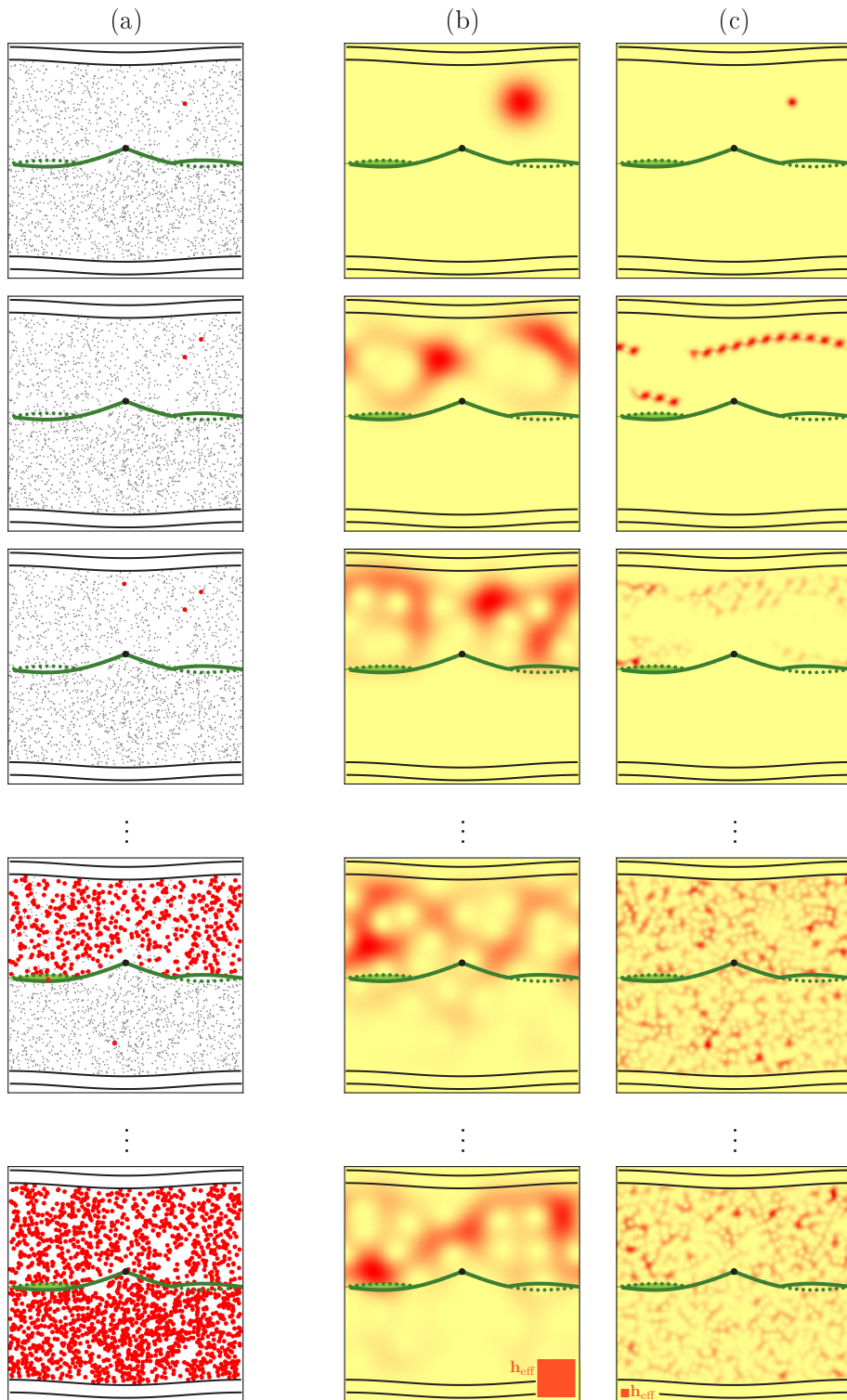
**Figure 3.9:** Classical (a) and quantum (b, c) time evolution across the partial barrier (solid green line) of the map $F_{\mathrm{pb,rot}}$. The classical flux $\Phi$ equals $1/190$ (light green shaded region) and Planck's constant is $1/40$ in (b) and $1/1000$ in (c). The size of Planck's constant $h_{\mathrm{eff}}$ is illustrated by an orange square in the last row. The rows correspond to times $t = 0, 1, 2,$ 500, and 2000 (top to bottom).
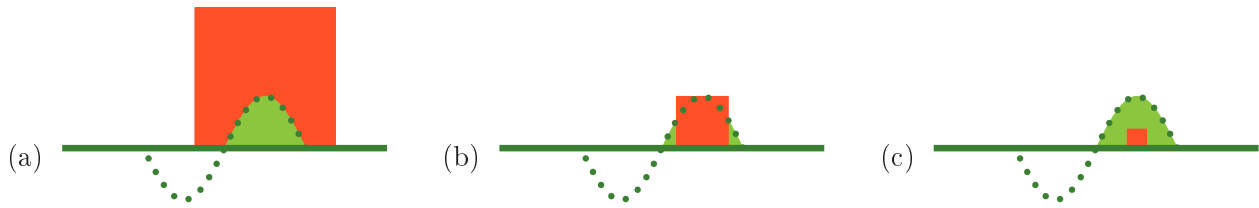
**Figure 3.10:** Comparison of the size of Planck's constant (orange square) to the classical flux $\Phi$, which is the size of one part of the turnstile (light green shaded region within the solid line indicating the partial barrier and the dotted line indicating the preimage of the partial barrier). (a) Planck's constant exceeds the classical flux and the quantum system cannot resolve the classical transport channel (quantum suppression of transport). (c) Planck's constant is small compared to the classical flux and quantum wave packets behave classically with respect to the partial barrier. (b) Planck's constant and the classical flux are of the same order and we find a transition from quantum suppression of transport to classical behavior of the partial barrier.

flux divided by Planck's constant, where both correspond to areas in phase space. This idea is illustrated in Fig. 3.10. For Planck's constant being large compared to the classical flux we find quantum suppression of transport. Whereas in the opposite case of small Planck's constant classical transport behavior is recovered. In the Sec. 3.2.3 we define suitable measures in order to investigate the quantum transition of a partial barrier between these two limiting cases.

In order to get rid of the ambiguity of the final time when the time evolution has settled, we now consider properties of eigenstates of the quantum map. Figures 3.11 and 3.12 show Husimi and momentum-space representations of eigenstates, which represent the typical behavior of eigenstates. The states in Fig. 3.11 are localized and the one in Fig. 3.12 is delocalized with respect to the partial barrier. These two opposite behaviors correspond to Planck's constant being large and small compared to the classical flux. In the latter case chaotic eigenstates extend over the whole chaotic region quite uniformly. As discussed in Sec. 3.2.3, properties of eigenstates can be used to give an equivalent description of the quantum transition of a partial barrier.
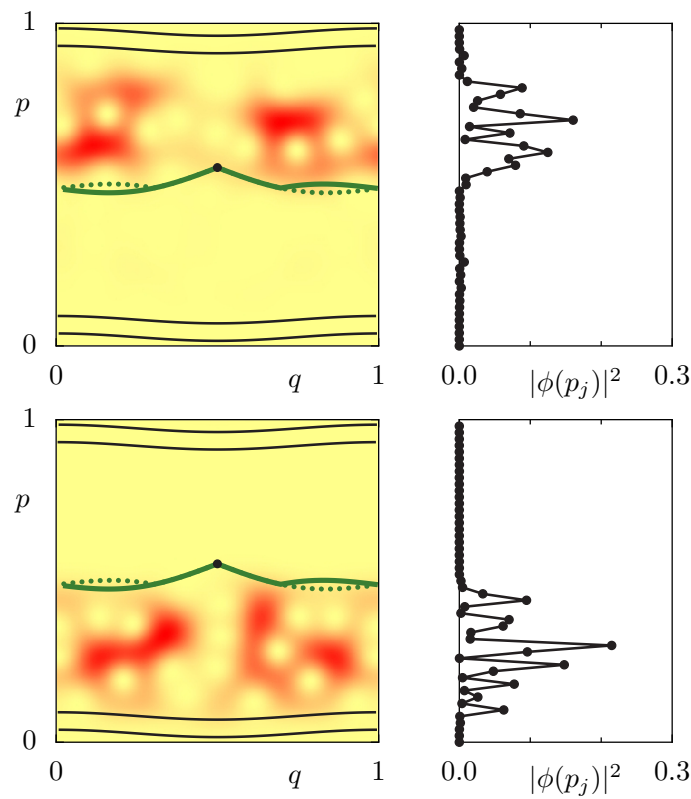
**Figure 3.11:** Husimi and momentum representation of states localized in one chaotic region for the map $F_{\mathrm{pb,rot}}$. The classical flux $\Phi$ equals $1/190$ and Planck's constant is $1/50$. Typical chaotic eigenstates either localize above or below the partial barrier.
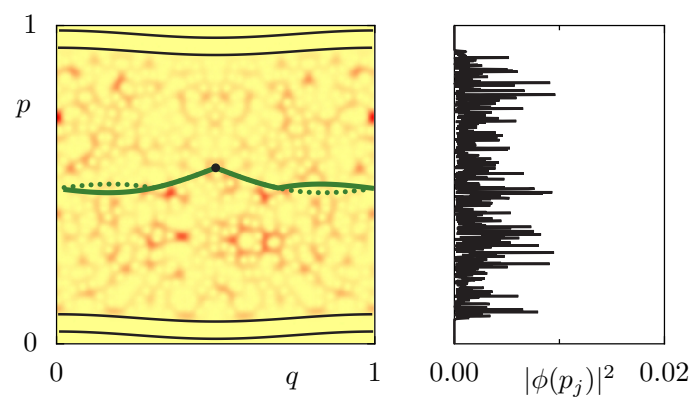


**Figure 3.12:** Husimi and momentum representation of a delocalized state for the map $F_{\mathrm{pb,rot}}$. The classical flux $\Phi$ equals $1/190$ and Planck's constant is $1/800$. Typical chaotic eigenstates extend over the whole chaotic region.

## 3.2.1  Time scales for quantum transport

Up to now we discussed the quantum transition of a partial barrier as a function of the ratio of the classical flux $\Phi$ and the effective Planck's constant $h_{\text{eff}}$. An alternative interpretation of the quantum suppression of transport is provided by the consideration of the involved time scales. The classical impact of a partial barrier can be described either by its flux $\Phi$ or by the time a typical orbit remains on one side of the partial barrier, which we refer to as dwell time $t_{\text{dwell}}$. The dwell time in region $i$ is given by (see e.g. Ref. [44])

$$t_{\text{dwell},i} = \frac{A_{\text{access},i}}{\Phi} \quad i = 1, 2, \tag{3.37}$$

where $A_{\text{access},i}$ is the area an orbit in region $i$ can access.

As a matter of fact the discreteness of quantum levels remains hidden up to a certain time, the so-called Heisenberg time $t_{\text{H}}$, which therefore defines a further system specific time scale. Equivalently, one may obtain this quantity as the time at which the mean level spacing $\langle \Delta \varphi \rangle$ contributes $2\pi$ in the exponent of the time evolution, which for maps reads $\exp\{i\langle \Delta \varphi \rangle t_{\text{H}}\}$ and with $\langle \Delta \varphi \rangle = 2\pi/N$ yields

$$t_{\text{H}} = N = \frac{1}{h_{\text{eff}}}. \tag{3.38}$$

Associated with region $i$ there are $N_{\text{ch},i}$ chaotic states and therefore the Heisenberg time for this sub-system is

$$t_{\text{H},i} = N_{\text{ch},i} = A_{\text{access},i} N = A_{\text{access},i} t_{\text{H}}. \tag{3.39}$$

By use of these time scales the ratio of the flux and Planck's constant can be written as

$$\frac{\Phi}{h_{\text{eff}}} = N\Phi = t_{\text{H}}\Phi = t_{\text{H}} \frac{A_{\text{access},i}}{t_{\text{dwell},i}} = \frac{t_{\text{H},1}}{t_{\text{dwell},1}} = \frac{t_{\text{H},2}}{t_{\text{dwell},2}}; \tag{3.40}$$

namely as the ratio of the Heisenberg time and the dwell time associated with regions 1 and 2, respectively. This gives rise to the following alternative interpretation of the quantum suppression of transport across the partial barrier. For Heisenberg time being small compared to the dwell time we find this quantum suppression. In this situation a typical orbit of length $t_{\text{H}}$ will not have visited the region behind the partial barrier. Semiclassically, the spectral properties of a chaotic quantum system are determined by periodic orbits up to length $t_{\text{H}}/2$, which is shown by Berry and Keating by resummation of periodic orbit sums [56–58] and reviewed in Ref. [59, Sec. 10.5]. As long as the properties of the quantum system are described by short (compared to the dwell time) periodic orbits, wave packets will localize in the initial region. This is similar to the phenomenon called 'scarring', introduced by Heller in 1984 [60], where quantum states localize on short unstable periodic orbits and give rise to nonuniformly

distributed wave functions. In the opposite situation, where the Heisenberg time is large compared to the dwell time, a typical orbit of length $t_{\text{H}}$ will extend over the region behind the partial barrier and according to semiclassics, also a wave packet of the quantum system will spread over this region.

Note that for open systems the ratio of the Heisenberg time and the dwell time can be related to the number of open channels (see Ref. [61–63] and references therein). For chaotic open systems the classical dwell time can be related to the (quantum) Wigner delay time and therefore also to the ratio of the Heisenberg time and the size of the scattering matrix (number of open channels). A system with a partial barrier may be considered as being composed of two open systems, which are connected at the opening. The connection via the openings corresponds to the turnstile, which allows for an exchange of phase-space volume between the two sub-systems. Applying the results of open systems to this situation gives rise to the identification of Eq. (3.40) with the number of channels $n$ connecting the two sub-systems. This is consistent with associating $n$ states with the phase-space region $\Phi$. This identification will be used in Sec. 4.3, where we introduce a matrix model to describe the quantum transition of a partial barrier.

**Ehrenfest time**

The Ehrenfest time $t_{\text{E},i}$ is the time scale on which a phase-space area of the size of Planck's constant $h_{\text{eff}}$ is stretched onto the accessible phase-space area $A_{\text{access},i}$ in terms of the classical dynamics

$$\sqrt{A_{\text{access},i}} \approx \sqrt{h_{\text{eff}}} \; \exp\{L \cdot t_{\text{E},i}\}, \tag{3.41}$$

$$t_{\text{E},i} = \frac{\ln(A_{\text{access},i}/h_{\text{eff}})}{2L} = \frac{\ln(A_{\text{access},i}) - \ln(h_{\text{eff}})}{2L}, \tag{3.42}$$

where $L$ is the largest Lyapunov exponent in the accessible region $A_{\text{access},i}$ (see Sec. 2.3). It is the time scale of mixing in the classical system and it has to be small compared to the other involved time scales

$$t_{\text{E},i} = \frac{\ln(t_{\text{H},i})}{2L} \ll t_{\text{H},i} \,, \tag{3.43}$$

$$t_{\text{E},i} = \frac{\ln(t_{\text{H},i})}{2L} = \frac{\ln(t_{\text{dwell},i} \cdot \Phi/h_{\text{eff}})}{2L} \ll t_{\text{dwell},i} \tag{3.44}$$

in order to allow for random matrix predictions, because random matrices correspond to instantaneous mixing. We will confirm the validity of Eqs. (3.43) and (3.44) in Sec. 4.2.4, where we compare the results for our designed map to a random matrix model.

## 3.2.2  Transition parameter-flux relation

In order to describe universal features of the quantum transition for a partial barrier from quantum suppression to classical transport, we introduce a scaling parameter $\Lambda$ in terms of system properties like the classical flux $\Phi$ and Planck's constant $h_{\text{eff}}$. This $\Lambda$-flux relation is needed to compare the results for random matrix models with the results for the quantum map.

The following derivation is similar to Sec. 5.2 of Ref. [23], but here we consider maps based on kicked systems instead of continuous flows. In order to relate the classical flux to a coupling in the quantum system we have to make the assumption that the quantum rate of transport across the partial barrier equals the corresponding classical rate. The classical rate (for systems with period 1) is given by

$$\frac{\Phi}{A_{\text{ch},1}} = \frac{\Phi}{f_1 A_{\text{ch}}}, \tag{3.45}$$

where $A_{\text{ch},1}$ is the chaotic region, in which we start, and $f_1$ denotes its fraction of the total chaotic region. For the quantum system Fermi's golden rule gives a rate [64, p. 1299 ff.]

$$\frac{2\pi}{\hbar_{\text{eff}}} v^2 f_2 \rho_{\text{ch}} \tag{3.46}$$

where $v^2$ is the average squared matrix element between the upper and lower chaotic states and $f_2 \rho_{\text{ch}}$ is the density of chaotic states in the transmission region. The equality of the classical and the quantum rate reads

$$\frac{2\pi}{\hbar_{\text{eff}}} v^2 f_2 \rho_{\text{ch}} = \frac{\Phi}{f_1 A_{\text{ch}}}. \tag{3.47}$$

By replacing $A_{\text{ch}}$ using the density of states

$$\rho_{\text{ch}} = \frac{N_{\text{ch}}}{\hbar_{\text{eff}}\omega} \stackrel{\omega=2\pi}{=} \frac{N_{\text{ch}}}{h_{\text{eff}}} = \frac{A_{\text{ch}}}{h_{\text{eff}}^2} \tag{3.48}$$

we have

$$\frac{2\pi}{\hbar_{\text{eff}}} v^2 f_2 \rho_{\text{ch}} = \frac{\Phi}{f_1 h_{\text{eff}}^2 \rho_{\text{ch}}} \tag{3.49}$$

and define the scaling or transition parameter as the ratio of the mean coupling and the mean level spacing of the uncoupled system [23]

$$\Lambda = \frac{v^2}{D_{\text{ch}}^2} = v^2 \rho_{\text{ch}}^2 = \frac{1}{4\pi^2 f_1 f_2} \frac{\Phi}{h_{\text{eff}}}. \tag{3.50}$$

The universal scaling behavior depends not only on the ratio of flux $\Phi$ and Planck's constant

$h_{\text{eff}}$ as pointed out in the sections before, but also on the relative size of the chaotic region involved $f_1$ and $f_2$ as given in the $\Lambda$-flux relation Eq. (3.50). The main assumption in the above derivation is the equality of classical and quantum rate, which is expected to be true in the semiclassical limit. The latter is achieved for large numbers of states in each region ($N_{\text{ch},i} = A_{\text{ch},i}/h_{\text{eff}} \gg 1$) and for not too small ratio $\Phi/h_{\text{eff}}$.

### 3.2.3  Quantitative measures for quantum suppression

In this section we define quantitative measures to describe the quantum transition of a partial barrier from quantum suppression to classical transport. Figure 3.9 (see beginning of Sec. 3.2) shows the time evolution of a coherent state for different values of Planck's constant $h_{\text{eff}}$. The quantum suppression occurs for large $h_{\text{eff}}$ and is reflected in the fact that almost no weight is transmitted into the lower chaotic region even for very long times. Therefore we introduce the notion of 'asymptotic transmitted weight' (ATW) as a quantitative measure. It is the weight of the wave packet transmitted across the partial barrier as time goes to infinity. Alternatively one can use the projection onto the transmission region averaged over time (see Eq. (6.4) on page 114 of Ref. [23]).

For a wave packet $\psi(t)$ started above the partial barrier we record the transmitted weight in some measuring box in the lower chaotic region (either the whole region or some part of it). The resulting value for $t \to \infty$ is compared to the case without a barrier. If there was no partial barrier a wave packet would uniformly extend over the whole chaotic sea and therefore its weight inside a measuring box is given by

$$\mu[\Psi_{\text{uniform}}] = \frac{A_\mu}{A_{\text{ch}}}, \tag{3.51}$$

where we introduce $\Psi_{\text{uniform}}$ for a fictitious state uniformly distributed in the chaotic sea of area $A_{\text{ch}}$ and $A_\mu$ corresponding to the phase-space region of the measuring box. If the measure $\mu$ includes the whole lower chaotic region, Eq. (3.51) reduces to the relative fraction of the region $f_{\text{lo}} = A_{\text{ch,lo}}/A_{\text{ch}}$ as used in Ref. [23]. In this thesis, however, we also consider measuring regions, that do not extend over the whole lower chaotic region, so that they exclude the region close to the partial barrier. With this remarks the asymptotic transmitted weight is given by

$$\text{ATW} \equiv \tilde{\mu}_\infty[\psi(t=0)] := \lim_{T \to \infty} \frac{1}{T} \sum_{t=0}^{T-1} \frac{\mu[\psi(t)]}{\mu[\Psi_{\text{uniform}}]} \tag{3.52}$$

$$=: \frac{\mu_\infty[\psi(t=0)]}{\mu[\Psi_{\text{uniform}}]}. \tag{3.53}$$

Before we discuss definitions of suitable measures $\mu$, we introduce another way of quantifying the level of suppression; namely by use of properties of eigenstates. As Figs. 3.11 and 3.12 suggest there is also a transition from localized to delocalized behavior in the eigenstates. As starting point we choose a momentum resolved version of the above quantity Eq. (3.52) following Refs. [26, 27]. For simplicity, we take a momentum eigenstate as initial state

$$\psi(t = 0) = |p_0\rangle \tag{3.54}$$

and consider the asymptotic distribution in momentum representation,

$$P(p, p_0) = \lim_{T \to \infty} \frac{1}{T} \sum_{t=0}^{T-1} |\langle p|U^t|p_0\rangle|^2. \tag{3.55}$$

Using the eigenvalue equation

$$U|\phi_j\rangle = \exp\{\mathrm{i}\varphi_j\}|\phi_j\rangle \quad j = 0, \ldots, N-1, \tag{3.56}$$

we can express the time evolution operator in terms of its eigenstates $\{\phi_j\}$

$$P(p, p_0) = \lim_{T \to \infty} \frac{1}{T} \sum_{t=0}^{T-1} \left| \sum_j \langle p|\phi_j\rangle \exp\{\mathrm{i}\varphi_j t\} \langle \phi_j|p_0\rangle \right|^2 \tag{3.57}$$

$$= \lim_{T \to \infty} \frac{1}{T} \sum_{t=0}^{T-1} \sum_{j,j'} \langle p|\phi_j\rangle \langle \phi_j|p_0\rangle \langle \phi_{j'}|p\rangle \langle p_0|\phi_{j'}\rangle \exp\{\mathrm{i}[\varphi_j - \varphi_{j'}] \cdot t\} \tag{3.58}$$

$$= \lim_{T \to \infty} \frac{1}{T} \sum_{t=0}^{T-1} \left[ \sum_j |\langle p|\phi_j\rangle|^2 \cdot |\langle \phi_j|p_0\rangle|^2 \quad + \right. \tag{3.59}$$

$$\left. \sum_{j \neq j'} \langle p|\phi_j\rangle \langle \phi_j|p_0\rangle \langle \phi_{j'}|p\rangle \langle p_0|\phi_{j'}\rangle \exp\{\mathrm{i}[\varphi_j - \varphi_{j'}] \cdot t\} \right]. \tag{3.60}$$

That is, $P(p, p_0)$ can be written as a sum of a time-independent term and a term, which is finite and rapidly oscillates with time. This term is proportional to

$$\lim_{T \to \infty} \frac{1}{T} \sum_{t=0}^{T-1} \exp\{\mathrm{i}[\varphi_j - \varphi_{j'}] \cdot t\} \tag{3.61}$$

and therefore vanishes for $j \neq j'$, because the eigenphases are uncorrelated. The remaining part is

$$P(p, p_0) = \sum_{j=0}^{N-1} |\langle p_0|\phi_j\rangle|^2 \cdot |\langle p|\phi_j\rangle|^2. \tag{3.62}$$

The summands in Eq. (3.62) measure the overlap of an eigenstate of the quantum system $\phi_j$ with the final state $p$ and initial state $p_0$ of the time evolution. In this way we related the time evolution result to properties of the eigenstates of the quantum system.

In the following we are interested in the total transmitted weight rather than in the momentum resolved quantity of Eq. (3.62). Hence, we evaluate Eq. (3.62) in measuring boxes in momentum space. They are defined as follows (see Fig. 3.13)

$$\mu_{\mathrm{up}} := \sum_{\tilde{p}_{\mathrm{up},1} < p_n < \tilde{p}_{\mathrm{up},2}} |\psi(p_n)|^2, \tag{3.63}$$

$$\mu_{\mathrm{lo}} := \sum_{\tilde{p}_{\mathrm{lo},1} < p_n < \tilde{p}_{\mathrm{lo},2}} |\psi(p_n)|^2, \tag{3.64}$$

using the parameters $\tilde{p}_i$ and the points of the momentum lattice $p_n$ of the quantum system. We will denote the area of the measuring boxes by $A_{\mu_i}$, which is given by the difference of the corresponding $\tilde{p}_i$.

Collecting all contributions in the lower measuring box yields

$$\mu_{\mathrm{lo},\infty}[|p_0\rangle] = \sum_{\tilde{p}_{\mathrm{lo},1} < p < \tilde{p}_{\mathrm{lo},2}} P(p,p_0) = \sum_{\tilde{p}_{\mathrm{lo},1} < p < \tilde{p}_{\mathrm{lo},2}} \sum_{j=0}^{N-1} |\langle p_0|\phi_j\rangle|^2 \cdot |\langle p|\phi_j\rangle|^2 = \sum_{j=0}^{N-1} |\langle p_0|\phi_j\rangle|^2 \cdot \mu_{\mathrm{lo}}[\phi_j] \tag{3.65}$$
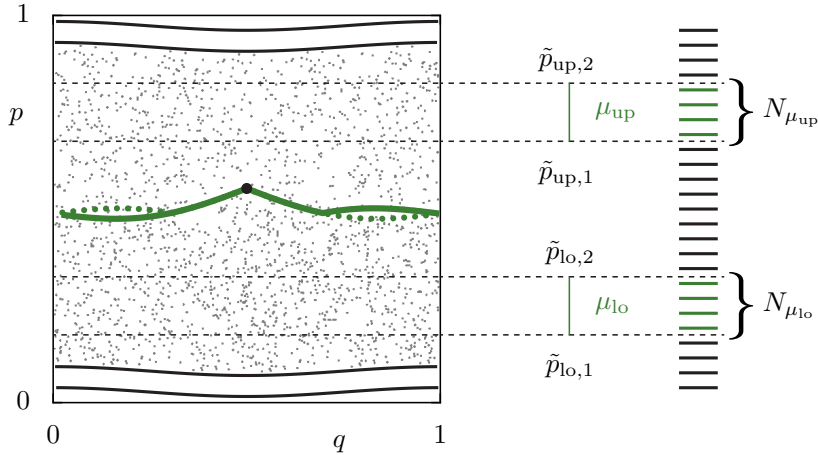


**Figure 3.13:** Illustration of the momentum measures $\mu_{\mathrm{up}}$ and $\mu_{\mathrm{lo}}$ defined by Eqs. (3.63) and (3.64), respectively. Each of the measures is determined by its two bounds, $\tilde{p}_{\mathrm{up},i}$ for the upper weight and $\tilde{p}_{\mathrm{lo},i}$ for the lower weight. On the left hand side the phase space with the partial barrier (solid green line) and its preimage (green dotted line) is shown. The set of vertical lines on the right hand side indicates the momentum lattice $p_n$ of the quantum system, which consists of $N = 1/h_{\mathrm{eff}}$ sites. Those sites within the two bounds of the upper and lower weight (colored sites) are considered in the calculation of the corresponding measures. The number of sites for the upper and lower weight are denoted by $N_{\mu_{\mathrm{up}}}$ and $N_{\mu_{\mathrm{lo}}}$, respectively.

and therefore the relative asymptotic transmitted weight reads

$$\tilde{\mu}_{\text{lo},\infty}[|p_0\rangle] = \frac{\mu_{\text{lo},\infty}[|p_0\rangle]}{\mu_{\text{lo}}[\Psi_{\text{uniform}}]} = \frac{1}{\mu_{\text{lo}}[\Psi_{\text{uniform}}]} \sum_{j=0}^{N-1} |\langle p_0|\phi_j\rangle|^2 \cdot \mu_{\text{lo}}[\phi_j]. \tag{3.66}$$

Now we perform an average over all $p_0$ in the upper measuring box. In order to have a quantity, which is symmetric with respect to upper and lower measuring box, we use the same spacing $\propto \frac{1}{N}$ for the initial conditions as for the $p$-values in the lower measuring box

$$\langle \tilde{\mu}_{\text{lo},\infty}[|p_0\rangle]\rangle_{p_0} = \frac{1}{N_{\mu_{\text{up}}}} \sum_{\tilde{p}_{\text{up},1} < p_0 < \tilde{p}_{\text{up},2}} \tilde{\mu}_{\text{lo},\infty}[|p_0\rangle] \tag{3.67}$$

$$= \frac{1}{N_{\mu_{\text{up}}}} \frac{1}{\mu_{\text{lo}}[\Psi_{\text{uniform}}]} \sum_{j=0}^{N-1} \mu_{\text{up}}[\phi_j]\mu_{\text{lo}}[\phi_j]. \tag{3.68}$$

On average, $N \cdot A_{\mu_{\text{up}}}$ points $p_0$ are inside the upper measuring region and we therefore write

$$\langle \tilde{\mu}_{\text{lo},\infty}[|p_0\rangle]\rangle_{p_0} = \frac{1}{N \cdot A_{\mu_{\text{up}}}} \frac{1}{\mu_{\text{lo}}[\Psi_{\text{uniform}}]} \sum_{j=0}^{N-1} \mu_{\text{up}}[\phi_j]\, \mu_{\text{lo}}[\phi_j] \tag{3.69}$$

$$= \frac{1}{N \cdot A_{\text{ch}} \cdot \mu_{\text{up}}[\Psi_{\text{uniform}}]} \frac{1}{\mu_{\text{lo}}[\Psi_{\text{uniform}}]} \sum_{j=0}^{N-1} \mu_{\text{up}}[\phi_j]\, \mu_{\text{lo}}[\phi_j] \tag{3.70}$$

$$= \frac{1}{N_{\text{ch}}} \sum_{j=0}^{N_{\text{ch}}-1} \frac{\mu_{\text{up}}[\phi_j]}{\mu_{\text{up}}[\Psi_{\text{uniform}}]} \frac{\mu_{\text{lo}}[\phi_j]}{\mu_{\text{lo}}[\Psi_{\text{uniform}}]}. \tag{3.71}$$

In the last step we inserted $N_{\text{ch}} = NA_{\text{ch}}$ and dropped the regular states from the sum. This is possible, because the measures are defined inside the chaotic region and regular states have only exponential tails into this region. Therefore the product $\mu_{\text{up}}[\phi_j]\mu_{\text{lo}}[\phi_j]$ for a regular state is small compared to a state uniformly distributed in the chaotic sea. Equation (3.71) is an average over all chaotic eigenstates of the quantity

$$M[\phi] := \frac{\mu_{\text{up}}[\phi]}{\mu_{\text{up}}[\Psi_{\text{uniform}}]} \frac{\mu_{\text{lo}}[\phi]}{\mu_{\text{lo}}[\Psi_{\text{uniform}}]} = \tilde{\mu}_{\text{up}}[\phi]\tilde{\mu}_{\text{lo}}[\phi] \tag{3.72}$$

with the relative measures

$$\tilde{\mu}_{\text{up}}[\phi] := \frac{\mu_{\text{up}}[\phi]}{\mu_{\text{up}}[\Psi_{\text{uniform}}]}, \tag{3.73}$$

$$\tilde{\mu}_{\text{lo}}[\phi] := \frac{\mu_{\text{lo}}[\phi]}{\mu_{\text{lo}}[\Psi_{\text{uniform}}]} \tag{3.74}$$

which we call 'product measure' for obvious reason. Before we discuss properties of this product measure and compare it to the asymptotic transmitted weight, we have to add one remark here. The choice of the momentum states as a basis for the initial and final states is not essential and we can replace the $\{|p_0\rangle\}$ and $\{|p\rangle\}$ by an arbitrary basis set. In particular for the asymptotic transmitted weight one can choose an arbitrary initial state and some final measure.

The product measure defined by Eq. (3.72) gives the contribution of an eigenstate to the ATW. For an eigenstate $\phi_j$ which is localized in only one or even none of the measuring boxes the contribution $M[\phi_j]$ vanishes. For a state uniformly distributed in the chaotic sea the contribution is one by definition. However, this is not the only state with contribution equal to one. A state $\phi$ with

$$\mu_{\text{up}}[\phi] = \mu_{\text{lo}}[\Psi_{\text{uniform}}], \tag{3.75}$$

$$\mu_{\text{lo}}[\phi] = \mu_{\text{up}}[\Psi_{\text{uniform}}] \tag{3.76}$$

gives $M = 1$, too, although it is not uniformly distributed. Furthermore, the individual contribution $M[\phi_j]$ is not bounded in general. Therefore one might define a normalized version of the product measure as

$$\tilde{M}[\phi] := 4 \cdot \frac{\tilde{\mu}_{\text{up}}[\phi]\tilde{\mu}_{\text{lo}}[\phi]}{(\tilde{\mu}_{\text{up}}[\phi] + \tilde{\mu}_{\text{lo}}[\phi])^2} \in [0, 1], \tag{3.77}$$

whose values are limited by zero and one and the $\tilde{M} = 1$ corresponds to the uniformly distributed state. For the case of measuring boxes of equal size, we have $\mu_{\text{up}}[\Psi_{\text{uniform}}] = \mu_{\text{lo}}[\Psi_{\text{uniform}}]$ and Eq. (3.77) reduces to

$$\tilde{M}[\phi] := 4 \frac{\mu_{\text{up}}[\phi]\mu_{\text{lo}}[\phi]}{(\mu_{\text{up}}[\phi] + \mu_{\text{lo}}[\phi])^2}. \tag{3.78}$$

Equation (3.78) is related to an inverse participation ratio IPR defined as

$$\text{IPR}[\phi] := \frac{\mu_{\text{up}}[\phi]^2 + \mu_{\text{lo}}[\phi]^2}{(\mu_{\text{up}}[\phi] + \mu_{\text{lo}}[\phi])^2} \tag{3.79}$$

by the following equation

$$1 = \frac{(\mu_{\text{up}}[\phi] + \mu_{\text{lo}}[\phi])^2}{(\mu_{\text{up}}[\phi] + \mu_{\text{lo}}[\phi])^2} = \text{IPR}[\phi] + \frac{1}{2}\tilde{M}[\phi]. \tag{3.80}$$

Equation (3.79) is the inverse participation ratio of a state, if we consider the two measuring boxes as the only two sites of a system. The normalized weight in the upper and in the lower

region is

$$\frac{\mu_{\mathrm{up}}[\phi]}{\mu_{\mathrm{up}}[\phi] + \mu_{\mathrm{lo}}[\phi]} \quad \text{and} \quad \frac{\mu_{\mathrm{lo}}[\phi]}{\mu_{\mathrm{up}}[\phi] + \mu_{\mathrm{lo}}[\phi]}. \tag{3.81}$$

Their squared sum is the IPR as defined by Eq. (3.79) and it lies between 1, i.e. the state is localized on one site and the other measure vanishes, and $\frac{1}{2}$ for a state $\phi$ with $\mu_{\mathrm{up}}[\phi] = \mu_{\mathrm{lo}}[\phi]$, i.e. a state uniformly distributed with respect to the two measuring boxes.

For measures which extend over the entire accessible region, i.e. $\mu_{\mathrm{up}}[\phi] + \mu_{\mathrm{lo}}[\phi] = 1$, the denominator in Eq. (3.78) drops and we have

$$\tilde{M}[\phi] := 4\mu_{\mathrm{up}}[\phi]\mu_{\mathrm{lo}}[\phi], \tag{3.82}$$

which is the same as Eq. (3.72) for $\mu_{\mathrm{up}}[\Psi_{\mathrm{uniform}}] = \mu_{\mathrm{lo}}[\Psi_{\mathrm{uniform}}] = \frac{1}{2}$. Therefore $M$ and $\tilde{M}$ are the same on the level of a $2 \times 2$ model and their values are limited by one.

Figure 3.14 shows contour lines of the product measure $M$ defined by Eq. (3.72) and $\tilde{M}$ defined by Eq. (3.77) for the case of $\mu_{\mathrm{up}}[\phi] + \mu_{\mathrm{lo}}[\phi] = 1$ and relative chaotic regions $f_{\mathrm{up}}$ and $f_{\mathrm{lo}}$, which are the measures of the uniformly distributed state in this situation: $f_{\mathrm{up}} = \mu_{\mathrm{up}}[\Psi_{\mathrm{uniform}}]$



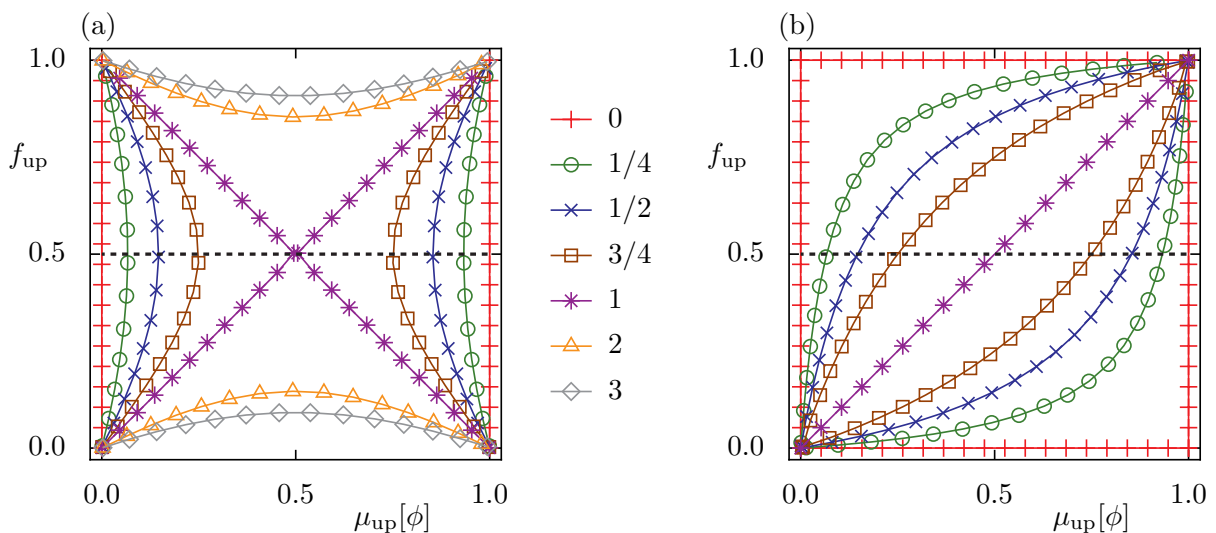**Figure 3.14:** Contour lines of (a) $M[\phi]$, Eq. (3.83), and (b) $\tilde{M}[\phi]$, Eq. (3.77), for the case $\mu_{\mathrm{up}}[\phi] + \mu_{\mathrm{lo}}[\phi] = 1$. That is, the two measuring regions together capture the total space available for eigenstates $\phi$. A horizontal slice with fixed $f_{\mathrm{up}}$ corresponds to one system and shows all possible values as function of $\mu_{\mathrm{up}}[\phi] = 1 - \mu_{\mathrm{lo}}[\phi]$. At the $f_{\mathrm{up}} = f_{\mathrm{lo}} = \frac{1}{2}$ (black dashed line) the contour lines of (a) and (b) fall on top of each other and are given by Eq. (3.82). Note that $\tilde{M}[\phi]$ is limited by 1 for all $f_{\mathrm{up}}$ whereas $M[\phi]$ is limited by 1 only for the case $f_{\mathrm{up}} = f_{\mathrm{lo}} = \frac{1}{2}$.

and $f_{\text{lo}} = \mu_{\text{lo}}[\Psi_{\text{uniform}}]$. Equation (3.72) reduces to

$$M[\phi] = \frac{\mu_{\text{up}}[\phi]}{f_{\text{up}}} \frac{\mu_{\text{lo}}[\phi]}{f_{\text{lo}}} = \frac{\mu_{\text{up}}[\phi]}{f_{\text{up}}} \frac{1 - \mu_{\text{up}}[\phi]}{1 - f_{\text{up}}} \equiv \tilde{\mu}_{\text{up}}[\phi]\tilde{\mu}_{\text{lo}}[\phi] \tag{3.83}$$

and its upper bound depends on the relative phase-space area $f_{\text{up}} = 1 - f_{\text{lo}}$ and tends to infinity for vanishing $f_{\text{up}}$ or $f_{\text{lo}}$

$$M[\phi] \leq \frac{1/4}{f_{\text{up}}[1 - f_{\text{up}}]} \xrightarrow{f_{\text{up}} \to 0} \infty. \tag{3.84}$$

On the line $f_{\text{up}} = f_{\text{lo}} = \frac{1}{2}$ (dashed black horizontal line in Fig. 3.14) Eqs. (3.72) and (3.77) are the same (see Eq. (3.82)). In both pictures the diagonal line $f_{\text{up}} = \mu_{\text{up}}$ corresponds to the uniformly distributed state. The additional diagonal line $f_{\text{up}} = 1 - \mu_{\text{up}} = \mu_{\text{lo}}$ in Fig. 3.14(a) corresponds to the state of Eq. (3.75), which is not uniformly distributed. For $\tilde{M}$ all states, that are not uniformly distributed with respect to the measure, have $\tilde{M}[\phi]$ smaller than one and states with the same value of $\tilde{M}$ are arranged symmetrically around the diagonal $\tilde{M}[\phi] = 1$ (see Fig. 3.14(b)).

The interpretation of the individual value $\tilde{M}[\phi]$ is much simpler than the interpretation of $M[\phi]$, because $\tilde{M}[\phi]$ lies between zero and one, which are the limiting cases of a state localized in one region and of a state delocalized (uniformly distributed) with respect to the two measuring regions. However, we will use $M[\phi]$, defined by Eq. (3.72), in the following, because it is the contribution of an eigenstate to the ATW and therewith its average $\langle M \rangle$ has a well settled meaning as ATW.

## 3.3  Results for the designed maps with one partial barrier

In this section results for the designed maps $F_{\text{pb}}$ and $F_{\text{pb,rot}}$ are presented. Based on the transmitted weight as function of time (Sec. 3.3.1) we determine the ATW introduced in Sec. 3.2.3 using momentum measures in Sec. 3.3.2. The properties of eigenfunctions are described by the product measure $M$ in Sec. 3.3.3. The results using Husimi measures for ATW and product measure are discussed in Sec. 3.3.4. With these definitions of the measures we quantify the quantum transition of a partial barrier from quantum suppression to classical transport behavior. We check the influence of the width of the regular region in Sec. 3.3.5 and consider examples with $A_{\text{ch,up}} \neq A_{\text{ch,lo}}$ in Sec. 3.3.6. The results are summarized in Sec. 3.3.7.

### 3.3.1  Transmitted weight as a function of time

Before discussing the asymptotics of the transmitted weight, we investigate the initial increase of the transmitted weight. The transmitted weight of a wave packet $\psi(t)$ initially located in

the upper region is

$$\tilde{\mu}_{\mathrm{trans}}[\psi(t)] = \tilde{\mu}_{\mathrm{lo}}[\psi(t)] = \frac{\mu_{\mathrm{lo}}[\psi(t)]}{\mu_{\mathrm{lo}}[\Psi_{\mathrm{uniform}}]}. \tag{3.85}$$

In order to interpret the resulting curves $\tilde{\mu}_{\mathrm{trans}}[\psi(t)]$ for quantum wave packets, we need to compare them to their classical expectation. The classical counterpart of the time evolution of wave packets is the time evolution of an orbit density in phase space $\varrho(q, p, t)$, which is normalized to one if integrated over the entire phase space. Based on this density we introduce the weight of orbits in the upper and lower chaotic region as

$$\mu_{\mathrm{up,\ class}}(t) = \int\limits_{A_{\mathrm{ch,up}}} \mathrm{d}q\,\mathrm{d}p\,\varrho(q, p, t), \tag{3.86}$$

$$\mu_{\mathrm{lo,\ class}}(t) = \int\limits_{A_{\mathrm{ch,lo}}} \mathrm{d}q\,\mathrm{d}p\,\varrho(q, p, t). \tag{3.87}$$

These weights give the probability to find an orbit in the upper and lower region at time $t$. Assuming instantaneous mixing in the individual regions and a Markovian description of the dynamics, we set up a Master equation describing the change in the orbit weights [65]

$$\frac{\partial}{\partial t}\begin{pmatrix}\mu_{\mathrm{up,\ class}}(t)\\\mu_{\mathrm{lo,\ class}}(t)\end{pmatrix} = \begin{pmatrix}-\frac{\Phi}{A_{\mathrm{ch,up}}} & \frac{\Phi}{A_{\mathrm{ch,lo}}}\\\frac{\Phi}{A_{\mathrm{ch,up}}} & -\frac{\Phi}{A_{\mathrm{ch,lo}}}\end{pmatrix}\begin{pmatrix}\mu_{\mathrm{up,\ class}}(t)\\\mu_{\mathrm{lo,\ class}}(t)\end{pmatrix} =: B\begin{pmatrix}\mu_{\mathrm{up,\ class}}(t)\\\mu_{\mathrm{lo,\ class}}(t)\end{pmatrix}. \tag{3.88}$$

The Markov matrix $B$ includes the rates of transitions between the two regions. These rates are the inverse of the corresponding dwell times $1/t_{\mathrm{dwell},i} = \Phi/A_{\mathrm{access},i}$. The elements in each column of the matrix $B$ add up to zero, which accounts for the conservation of the total weight and yields one vanishing eigenvalue of $B$. The eigenvalue equation for $B$ reads

$$B\zeta_i = b_i\zeta_i \tag{3.89}$$

and has the solutions

$$b_1 = 0 \qquad\qquad \text{with}\quad \zeta_1 = \begin{pmatrix}1\\1\end{pmatrix}, \tag{3.90}$$

$$b_2 = -\left(\frac{\Phi}{A_{\mathrm{ch,up}}} + \frac{\Phi}{A_{\mathrm{ch,lo}}}\right) =: -\Gamma \qquad\qquad \text{with}\quad \zeta_2 = \begin{pmatrix}1\\-1\end{pmatrix}. \tag{3.91}$$

The first solution corresponds to the conservation of the total weight and the second describes the relaxation to an equilibrium distribution, for which we introduce a rate $\Gamma = -b_2$ following Ref. [65]. Now we consider the time evolution of a density $\varrho(q, p, t)$ initially located in the upper

region. The resulting weights are

$$\begin{pmatrix} \mu_{\text{up, class}}(t) \\ \mu_{\text{lo, class}}(t) \end{pmatrix} = \frac{1}{2} \begin{pmatrix} 1 + \exp\{-\Gamma t\} \\ 1 - \exp\{-\Gamma t\} \end{pmatrix}. \tag{3.92}$$

In this situation the transmitted weight is given by

$$\mu_{\text{trans, class}}(t) = \mu_{\text{lo, class}}(t) = \frac{1}{2}\left[1 - \exp\{-\Gamma t\}\right] = \begin{cases} \frac{\Gamma}{2}t & \text{for} \quad \Gamma t \ll 1 \\ \frac{1}{2} & \text{for} \quad \Gamma t \gg 1. \end{cases} \tag{3.93}$$

The decay of the density initially located in the upper region is determined by the rate

$$\frac{\Gamma}{2} = \frac{1}{2}\left(\frac{\Phi}{A_{\text{ch,up}}} + \frac{\Phi}{A_{\text{ch,lo}}}\right) = \frac{1}{2}\left(\frac{1}{t_{\text{dwell, up}}} + \frac{1}{t_{\text{dwell, lo}}}\right), \tag{3.94}$$

which gives the inverse dwell time $1/t_{\text{dwell, up}}$ if both regions are of equal size. In the following we restrict ourselves to the case that both regions have the same size. In analogy to Eq. (3.85), we consider the ratio $\tilde{\mu}_{\text{trans, class}}(t)$ of the transmitted weight $\mu_{\text{trans, class}}(t)$, Eq. (3.93), to the weight of a uniformly distributed state, which is given by $\frac{1}{2}$ in each region,

$$\tilde{\mu}_{\text{trans, class}}(t) = \frac{\mu_{\text{trans, class}}(t)}{1/2} = 1 - \exp\{-\Gamma t\} = \begin{cases} \Gamma t & \text{for} \quad \Gamma t \ll 1 \\ 1 & \text{for} \quad \Gamma t \gg 1. \end{cases} \tag{3.95}$$

At small times the relative transmitted weight $\tilde{\mu}_{\text{trans, class}}(t)$ increases linearly with slope $\Gamma$ and for large times it approaches one, which is the limit of no barrier.

Now let us turn to the time evolution of a wave packet. As transmitted weight we consider the momentum measures in the upper and lower region defined by Eqs. (3.63) and (3.64), respectively. The momentum limits are chosen as

$$\tilde{p}_{\text{lo},1} = 0.175, \tag{3.96}$$

$$\tilde{p}_{\text{lo},2} = 0.325, \tag{3.97}$$

$$\tilde{p}_{\text{up},1} = 0.675, \tag{3.98}$$

$$\tilde{p}_{\text{up},2} = 0.825. \tag{3.99}$$

In Fig. 3.15 the increase of the transmitted weight in time, Eq. (3.85), is illustrated. For one fixed initial condition and fixed Bloch phase $\theta_q$ (see Fig. 3.15(a)) the transmitted weight strongly fluctuates and shows Rabi-like oscillations, which is due to the oscillatory term in Eq. (3.61). Averaging over different values of the Bloch phase $\theta_q$ (system average) and different initial wave packets $\psi(0)$ yields a smooth curve as a function of time (see Fig. 3.15(b)). For decreasing $h_{\text{eff}} = 1/N$ the curves approach the classical result of Eq. (3.95) apart from a small shift in the time (see below).
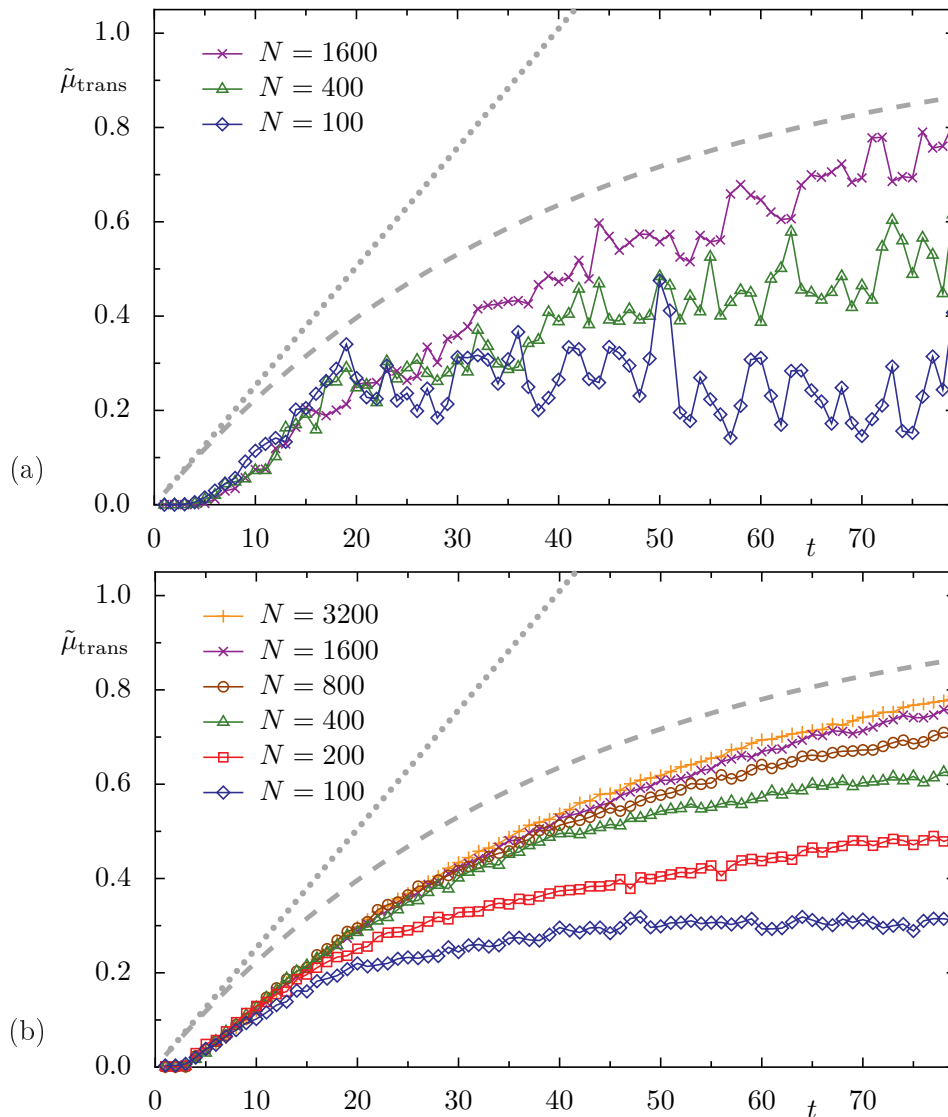
**Figure 3.15:** Transmitted momentum weight $\tilde{\mu}_{\text{trans}}[\psi(t)]$ for the example 1 of the map $F_{\text{pb,rot}}$ ($\Phi \approx 1/200$) with time up to the dwell time of the upper (and lower) region in comparison to the classical expectation Eq. (3.95) (dashed) and its linear approximation (dotted). (a) The transmitted weight of a state $\psi(t)$ with $\psi(0) = |p_0\rangle = |0.3\rangle$ exhibits strong fluctuations. (b) Averaging $\tilde{\mu}_{\text{trans}}$ over 20 values of $\theta_q$ and four initial conditions (two momentum eigenstates with $p_0 = 0.3, 0.7$ and two coherent states initially located at $(q, p) = (0.5, 0.3)$ and $(0.5, 0.7)$) yields smooth curves, which approach the classical expectation with increasing size of $N$, i.e. decreasing $h_{\text{eff}} = 1/N$.

Larger values for Planck's constant $h_{\text{eff}} = 1/N$ yield smaller values for the transmitted weight. For instance the curve with $1/h_{\text{eff}} = N = 100$ in Fig. 3.15(b) is below the curve with $1/h_{\text{eff}} = N = 3200$, which is most prominent at large times. That is, at large times the transmitted weight is reduced if Planck's constant increases. This finding indicates the previously discussed suppression of quantum transport in the limit of Planck's constant being large compared to the classical flux.

Note that the shift in time occurs due to the non-vanishing mixing time, which is not included in the above Master-equation approach. This mixing time has two origins: The mixing in the quantum system is semiclassically determined by the Lyapunov exponent, which yields the Ehrenfest time (see Sec. 3.2.1). Moreover the wave packet needs some time to reach the box defining the momentum measure after it has crossed the partial barrier.

Figure 3.16(a) extends the data of Fig. 3.15 to larger times and thus illustrates the idea of the asymptotic transmitted weight (ATW). After the initial increase of the transmitted weight with some kind of overshooting its value saturates at the ATW. Similar overshootings are observed in the temporal flooding of regular states [39, Sec. 3.4]. The colored dashed and dotted lines indicate the average over times up to $T = 10^4$ and for times within $[T, T'] = [2^{20}, 2^{20} + 100]$, respectively. We find agreement between averaging over different ranges of time. For practical investigations it is possible to average over times up to time $T$, see Eq. (3.52), or over some range $[T, T']$, which we do in the following. In any case the time $T$ needs to be large compared
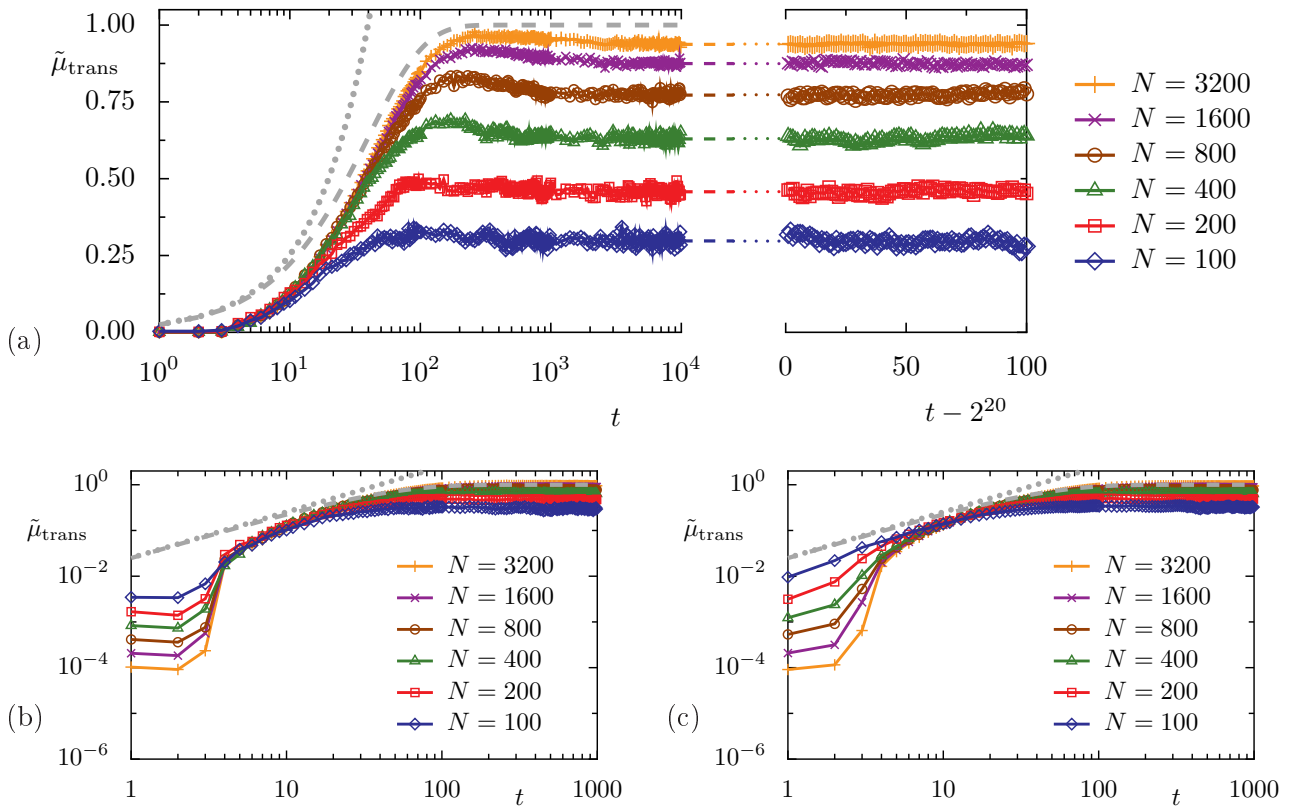


**Figure 3.16:** Transmitted weight $\tilde{\mu}_{\mathrm{trans}}[\psi(t)]$ for the example 1 of the map $F_{\mathrm{pb,rot}}$ ($\Phi \approx 1/200$) in comparison to the classical expectation, Eq. (3.95), (dashed) and its linear approximation (dotted). (a) Same quantity as in Fig. 3.15 (b), but as a function of time $t \in [1, 10^4]$ and $t \in [2^{20}, 2^{20} + 100]$. The colored dashed and dotted lines between the two graphs indicate the height of the average performed over the first and second time range, respectively. In (b) we show the first part of (a) with a logarithmically scaled ordinate, which reveals the initial behavior of $\tilde{\mu}_{\mathrm{trans}}[\psi(t)]$. Using the Husimi weight, the whole transmission region contributes. The resulting data is shown in (c), which has enhanced values at small $t$ compared to (b), but approaches the result of the momentum weight at large times.

to the involved time scales given by the dwell time and the Heisenberg time.

For $h_{\mathrm{eff}}$ going to zero, the ATW reaches larger values and the range, where the transmitted weight $\tilde{\mu}_{\mathrm{trans}}$ follows the linear increase given by the classical rate $\Gamma$, extends to larger $t$. In this limit $h_{\mathrm{eff}} \to 0$, or more precisely $\Phi/h_{\mathrm{eff}} \to \infty$, the classical behavior of a partial barrier is recovered and at large times the normalized transmitted weight $\tilde{\mu}_{\mathrm{trans}}(t)$ reaches the value one. In this limit the assumption of the quantum rate being equal to the classical rate, used in the derivation of the $\Lambda$-flux relation of Sec. 3.2.2, is well founded.

Figure 3.16(c) shows the result of the same time evolution as Figure 3.16(a) and (b), but in contrast to the other pictures the Husimi measure, which we will introduce in Sec. 3.3.4, in the whole transmission region is used as transmitted weight. At large times the resulting values are close to those of the momentum measure and therefore it is meaningful to consider a universal curve for the ATW.

Note that we find some deviations at small $t$. The reason for the additional delay in the momentum measure (Figure 3.16(b)) compared to the Husimi measure (Figure 3.16(c)) is the fact that the time evolved state has to reach the box used for the momentum measure as mentioned above. For the Husimi weight we find larger values of $\tilde{\mu}_{\mathrm{trans}}(t)$ and for the examples 2 ($\Phi \approx 1/800$) and 3 ($\Phi \approx 1/3000$), where the ratio of $\Phi/h_{\mathrm{eff}}$ is smaller than for example 1 the Husimi weight gives values larger than the classical expectation. This finding might be attributed to the transition region around the partial barrier, which is included in the Husimi measure (see discussion in Sec. 3.3.4). However, in the definition of the ATW large times $t$ are needed, where the momentum and Husimi weight agree.

## 3.3.2 ATW using momentum measures

In the following our focus is on the ATW rather than the full time dependence of the transmitted weight. In this section the transmitted weight is determined by the momentum measure defined in the transmission region. The initial state can be any state sufficiently well localized in one of the two chaotic regions. Here we choose momentum eigenstates as initial states, while coherent states would give the same ATW. The decisive property of the initial states is their localization away from the partial barrier, such that at $t = 0$ no weight is already transmitted and universal features of the quantum transport across the partial barrier are observed.

In the case of the map $F_{\mathrm{pb,rot}}$ the time evolution is performed by consecutive applications of the unitary time evolution operator $U_{\mathrm{pb,rot}}$, Eq. (3.33). Numerically the time evolution up to the lower limit of the time range is performed by an auxiliary matrix $\tilde{U}^{(n)}$ defined by the following recursion relation

$$\tilde{U}^{(0)} = U_{\mathrm{pb,rot}}, \tag{3.100}$$

$$\tilde{U}^{(k+1)} = \tilde{U}^{(k)}\tilde{U}^{(k)}. \tag{3.101}$$

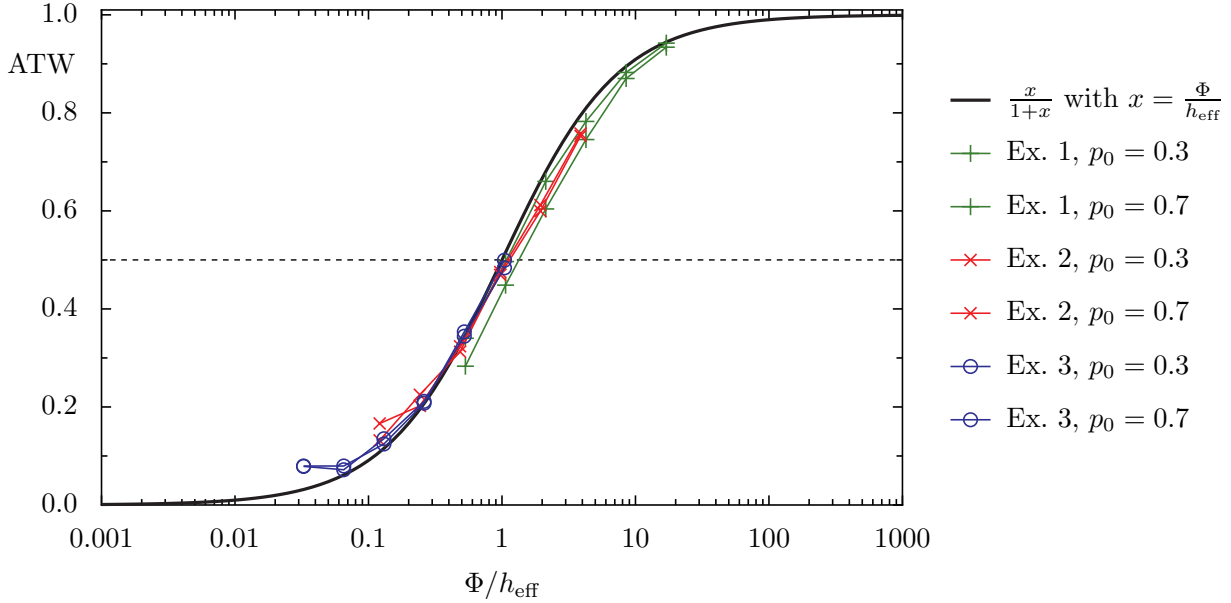Therewith only $n$ matrix-matrix multiplications are needed to reach time $T = 2^n$.

**Figure 3.17:** ATW using the momentum measures for the examples 1, 2, and 3 of the map $F_{\mathrm{pb,rot}}$. The initial state is $\psi(t=0) = |p_0\rangle$ with $p_0 = 0.3$ below and $p_0 = 0.7$ above the partial barrier. The data is averaged over 20 values of $\theta_q$ and 100 steps after time $T = 2^{20} \approx 10^6$.

Figure 3.17 shows the resulting ATW for examples 1, 2, and 3 of the map $F_{\mathrm{pb,rot}}$ for two different momentum eigenvalues as initial conditions. The ATW is shown as a function of the ratio $\Phi/h_{\mathrm{eff}}$. In order to observe universal features, the classical phase-space structures need to be reasonably resolved. That is, each of the two chaotic regions itself should be semiclassically treatable. We restrict ourselves to $1/h_{\mathrm{eff}} = N \geq 100$. This yields about 40 states in the upper and lower region if we associate $N_{\mathrm{up}} = N A_{\mathrm{ch,up}}$ and $N_{\mathrm{lo}} = N A_{\mathrm{ch,lo}}$ states with the upper and lower region (see Tab. 3.1 for values of $A_{\mathrm{ch,up}}$ and $A_{\mathrm{ch,lo}}$). All data sets in Fig. 3.17 fall on top of each other under the scaling with $\Phi/h_{\mathrm{eff}}$. We therefore conclude that $\Phi/h_{\mathrm{eff}}$ is the right scaling parameter.

The quantum transition of a partial barrier between the two limiting cases of full quantum suppression and classical behavior takes place on a logarithmic scale. That is, the ratio $\Phi/h_{\mathrm{eff}}$ needs to be varied over a large range in order to determine the whole transition curve. The overall behavior of the data is reasonably well described by

$$\mathrm{ATW} = \frac{\frac{\Phi}{h_{\mathrm{eff}}}}{1 + \frac{\Phi}{h_{\mathrm{eff}}}}. \tag{3.102}$$

Note that we varied the bounds of the momentum measures defined by Eqs. (3.63) and (3.64) and find almost no dependence on the choice of the bounds as long as the central part supporting the partial barrier and the regular regions are excluded.

For the map $F_{\mathrm{pb,rot}}$ the parameter $N = 1/h_{\mathrm{eff}}$ is limited numerically, because the full time
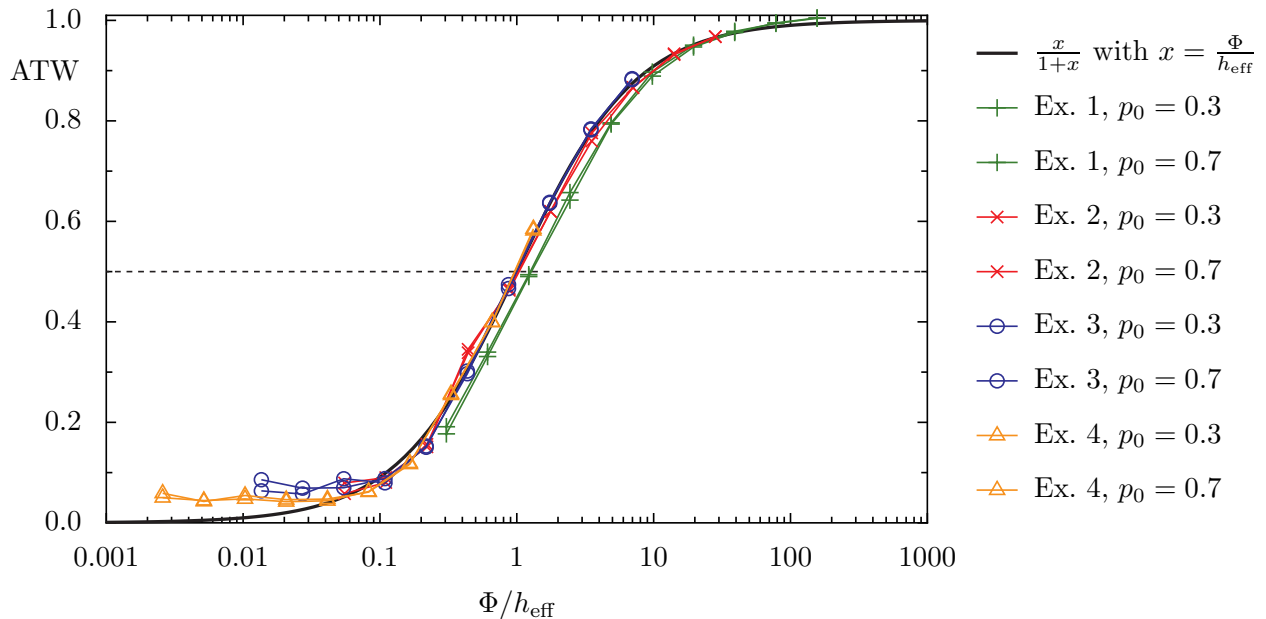
**Figure 3.18:** ATW using the momentum measures for the examples 1, 2, 3, and 4 of the map $F_{\mathrm{pb}}$. The flux $\Phi$ used for the abscissa is the flux $\Phi'$ discussed in Sec. 3.1.5. The initial state is $\psi(t=0) = |p_0\rangle$ with $p_0 = 0.3$ below and $p_0 = 0.7$ above the partial barrier. The shown data is averaged over 20 values of $\theta_q$ and 100 steps after time $T = 10^6$. The total number of states are $N = 1/h_{\mathrm{eff}} = 100, 200, ..., 51200$.

evolution operator $U_{\mathrm{pb,rot}}$ has to be used for the time evolution. In the case of the map $F_{\mathrm{pb}}$, where no projector is used, the fast Fourier transform can be used for the time evolution. Therefore $N$ can be chosen much larger. It is limited by the size of a vector representing the quantum wave packet rather than a $N \times N$ matrix needed for the time evolution of the map $F_{\mathrm{pb,rot}}$. Therefore the covered range of $\Phi/h_{\mathrm{eff}}$ for each of the examples of the map $F_{\mathrm{pb}}$ is almost doubled. Furthermore, the example 4 is included, which extends the data to smaller values of the ratio $\Phi/h_{\mathrm{eff}}$, respectively (see Fig. 3.18 in contrast to Fig. 3.17). The ATW for the map $F_{\mathrm{pb}}$ is shown in Fig. 3.18. Again we find scaling with the ratio $\Phi/h_{\mathrm{eff}}$, if we consider the flux $\Phi'$ discussed in Sec. 3.1.5. We therefore conjecture that the additional partial barriers with larger flux, present in the phase space of map $F_{\mathrm{pb}}$, have only minor impact. As long as the region between neighboring partial barriers is small (only some or even less than one $h_{\mathrm{eff}}$), it is not resolved by quantum mechanics and the quantum suppression is governed by the partial barrier with smallest flux.

### 3.3.3 Product measure using momentum measures

In Sec. 3.2.3 we derived a representation of the ATW in terms of the eigenstates. Finally, it can be computed by an average over all chaotic eigenstates of the product measure, Eq. (3.72),

$$M[\phi] = \tilde{\mu}_{\mathrm{up}}[\phi]\tilde{\mu}_{\mathrm{lo}}[\phi] \tag{3.103}$$

with the relative measures

$$\tilde{\mu}_{\mathrm{up}}[\phi] := \frac{\mu_{\mathrm{up}}[\phi]}{\mu_{\mathrm{up}}[\Psi_{\mathrm{uniform}}]}, \tag{3.104}$$

$$\tilde{\mu}_{\mathrm{lo}}[\phi] := \frac{\mu_{\mathrm{lo}}[\phi]}{\mu_{\mathrm{lo}}[\Psi_{\mathrm{uniform}}]}. \tag{3.105}$$

In the derivation we dropped the regular states, because their contribution is negligible. Moreover the product measure of a regular state will be influenced by its position with respect to the measuring boxes inside the chaotic regions, because they are much more localized. Therefore the resulting product measure does not cover the quantum suppression of transport for regular states properly. Furthermore, we assumed that all other eigenstates are chaotic. That is, the Husimi representation of these eigenstates looks uniformly distributed with respect to the upper and with respect to the lower chaotic region. This assumption is violated by states localizing close to the partial barrier – e.g. a scarred state on the hyperbolic fixed point at $(\frac{1}{2}, p_{\mathrm{fix}})$. The asymmetry of the upper and the lower weight of those states does not represent the impact of the partial barrier, but clearly depends on the relative location of the localized state and the measuring regions. Therefore we drop regular states and states localized close to the partial barrier in order to observe the impact of the partial barrier on the chaotic states only. This is achieved by introducing a minimal measure for the sum of the upper and the lower weight. Again we compare to the resulting $\mu_{\mathrm{up}}[\phi] + \mu_{\mathrm{lo}}[\phi]$ to that of a state uniformly distributed in the chaotic region and consider only states $\phi$ with

$$\mu_{\mathrm{up}}[\phi] + \mu_{\mathrm{lo}}[\phi] \geq \chi \cdot \left( \mu_{\mathrm{up}}[\Psi_{\mathrm{uniform}}] + \mu_{\mathrm{lo}}[\Psi_{\mathrm{uniform}}] \right) = \chi \cdot \left( \frac{A_{\mu_{\mathrm{up}}}}{A_{\mathrm{ch}}} + \frac{A_{\mu_{\mathrm{lo}}}}{A_{\mathrm{ch}}} \right) \tag{3.106}$$

for the average product measure. For nonzero $\chi$ all of the above mentioned states are excluded in the semiclassical limit ($h_{\mathrm{eff}} \to 0$). As long as $h_{\mathrm{eff}}$ is not yet small, some of these states will have small contributions in the measuring regions and we used $\chi = 20\%$ in the following.

Figure 3.19 shows the average product measure for the examples 1, 2, and 3 of the map $F_{\mathrm{pb,rot}}$. The average product measure is in good agreement with the ATW of Fig. 3.17. Note that excluding the regular states and those localized close to the partial barrier is equivalent to placing initial wave packets inside one of the chaotic regions, because the initial state has a small overlap with the localized states. Averaging over many initial conditions finally gives the same averaging mechanism as averaging over all chaotic states. For the product measure the upper limit of $N = 1/h_{\mathrm{eff}}$ is determined by the size of a full matrix, which can still be diagonalized on a computer.

According to Eq. (3.72) the product measure is the contribution of an eigenstate to the ATW. Therefore we can also study the distribution of the state dependent $M$-values as an extension of the above consideration of the mean value $\langle M \rangle$. Although the ATW and therefore the average
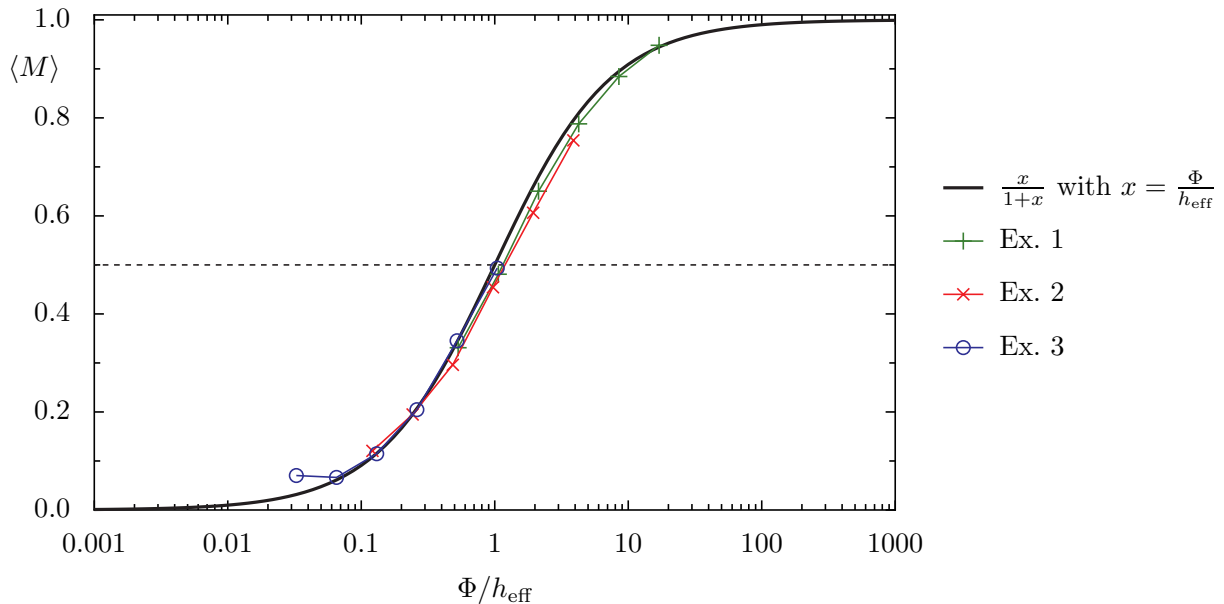
**Figure 3.19:** Average product measure $M$ using the momentum measures for the examples 1, 2, and 3 of the map $F_{\text{pb,rot}}$. The data is averaged over all states $\phi$ fulfilling Eq. (3.106) with $\chi = 20\%$ and 100 values of the Bloch phase $\theta_q$.

product measure takes values between zero and one, the contribution of an eigenstates is not limited by one. The individual product measure, Eq. (3.103), is limited by

$$M[\phi] = \frac{\mu_{\text{up}}[\phi]}{\mu_{\text{up}}[\Psi_{\text{uniform}}]} \frac{\mu_{\text{lo}}[\phi]}{\mu_{\text{lo}}[\Psi_{\text{uniform}}]} = \frac{\mu_{\text{up}}[\phi]\mu_{\text{lo}}[\phi]}{(\tilde{p}_{\text{up},2} - \tilde{p}_{\text{up},1}) \cdot (\tilde{p}_{\text{lo},2} - \tilde{p}_{\text{lo},1})/A_{\text{ch}}^2} \tag{3.107}$$

$$\leq \frac{\mu_{\text{up}}[\phi](1 - \mu_{\text{up}}[\phi])}{(\tilde{p}_{\text{up},2} - \tilde{p}_{\text{up},1}) \cdot (\tilde{p}_{\text{lo},2} - \tilde{p}_{\text{lo},1})/A_{\text{ch}}^2}, \tag{3.108}$$

where the inequality $\mu_{\text{up}}[\phi] + \mu_{\text{lo}}[\phi] \leq 1$ was used. In fact the inequality Eq. (3.108) is only a very rough estimate, because the total measure in the two momentum measure boxes is typically much smaller than one. Inserting the limits $\tilde{p}_i$ for the used momentum measures of Eqs. (3.96)–(3.99) and the size of the chaotic sea $A_{\text{ch}}$ of Tab. 3.1 gives

$$M[\phi] \leq 32\mu_{\text{up}}[\phi](1 - \mu_{\text{up}}[\phi]) \leq 8, \tag{3.109}$$

where in the last step the product of the measures is estimated from above by $\frac{1}{4}$.

Figure 3.20 shows the distribution of the product measure $d(M)$ for the examples 1–3 of the map $F_{\text{pb,rot}}$. The pictures suggest that the distributions for a fixed ratio $\Phi/h_{\text{eff}}$ coincide. Note that $\Phi/h_{\text{eff}}$ is only approximately the same for the shown data, because $\Phi$ and $N$ vary independently. As seen in Fig. 3.20(a) almost all eigenstates have a vanishing product measure for a small ratio $\Phi/h_{\text{eff}}$. In the limit of vanishing ratio $\Phi/h_{\text{eff}}$ all eigenstates either localize in the upper or in the lower region. In practice this limiting case is not reached, due to the non-
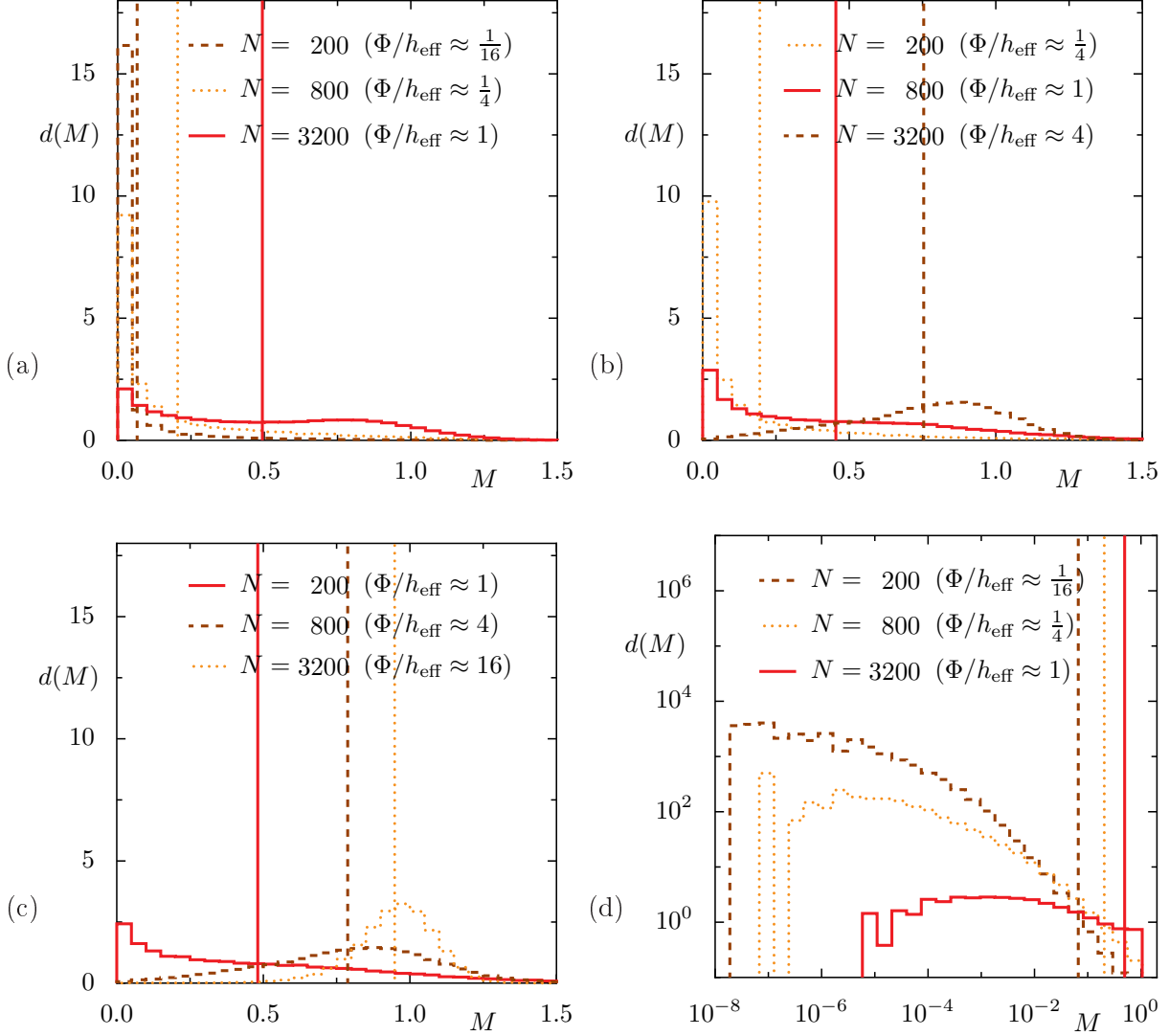
**Figure 3.20:** Distribution $d(M)$ of the product measure $M$ using the momentum measures for example 3 ($\Phi \approx 1/3000$) in (a), 2 ($\Phi \approx 1/800$) in (b), and 1 ($\Phi \approx 1/200$) in (c) for the map $F_{\mathrm{pb,rot}}$ and $N = 200, 800, 3200$. (d) Same distribution as (a), but with a logarithmic abscissa and ordinate. The selection of states is the same as in Fig. 3.19. The average of each distribution is shown as vertical line. The solid red line corresponds to the result with $\Phi/h_{\mathrm{eff}} \approx 1$. In total the data covers a range of $\Phi/h_{\mathrm{eff}} \approx 1/16$ for the smallest $N$ in (a) to $\Phi/h_{\mathrm{eff}} \approx 16$ for the largest $N$ in (c).

vanishing tunneling coupling between the two chaotic regions. The data of Fig. 3.20(a) is shown again in (d), where the distribution $d(M)$ is shown on a logarithmic scale in $M$. For decreasing $\Phi/h_{\mathrm{eff}}$ the distribution seems to approach a power law behavior. This behavior indicates the strong spreading of $M$ for small ratios $\Phi/h_{\mathrm{eff}}$ and might be attributed to tunneling. If the ratio $\Phi/h_{\mathrm{eff}}$ reaches one, shown by the solid red line in all pictures, the distribution extends over a large range in $M$. Although the average value is around $\frac{1}{2}$, some of the states are much more localized in one of the regions, whereas other states are already uniformly distributed in both regions. The above estimation of the upper bound for $M$ is clearly much too large

for the considered distribution and less than two percent of the states exceeds the value $\frac{3}{2}$. For large ratios $\Phi/h_{\text{eff}}$ the peak of the distribution starts to approach one and its width is decreasing. That is, in the semiclassical limit, $\Phi/h_{\text{eff}} \to \infty$, all states are uniformly distributed and therewith the classical behavior of a partial barrier is recovered.

### 3.3.4  ATW and product measure using Husimi measures

In generic systems the introduction of a momentum measure or similar basis sets is not obvious and therefore the Husimi function, introduced in Sec. 2.8, integrated over the upper or lower region is a good choice. Thus Eqs. (3.52) and (3.72) are evaluated by use of these upper and lower Husimi weights.

Figure 3.21 shows the resulting ATW for several examples of the map $F_{\text{pb}}$. Again we find scaling with the ratio $\Phi/h_{\text{eff}}$. This data need to be compared to the data of Fig. 3.18, where the momentum measures rather than Husimi measures are used. We see that the overall behavior is almost unchanged and therefore universal behavior is found.

For $\Phi/h_{\text{eff}} \leq 0.1$ a saturation occurs as for Fig. 3.18, which can be attributed to the non-vanishing tunneling coupling between the two regions. However, the plateau is enhanced compared to Fig. 3.18. That is, the transmitted Husimi weight is larger than the momentum measure. This is understandable, because on the one hand the Husimi function smears out
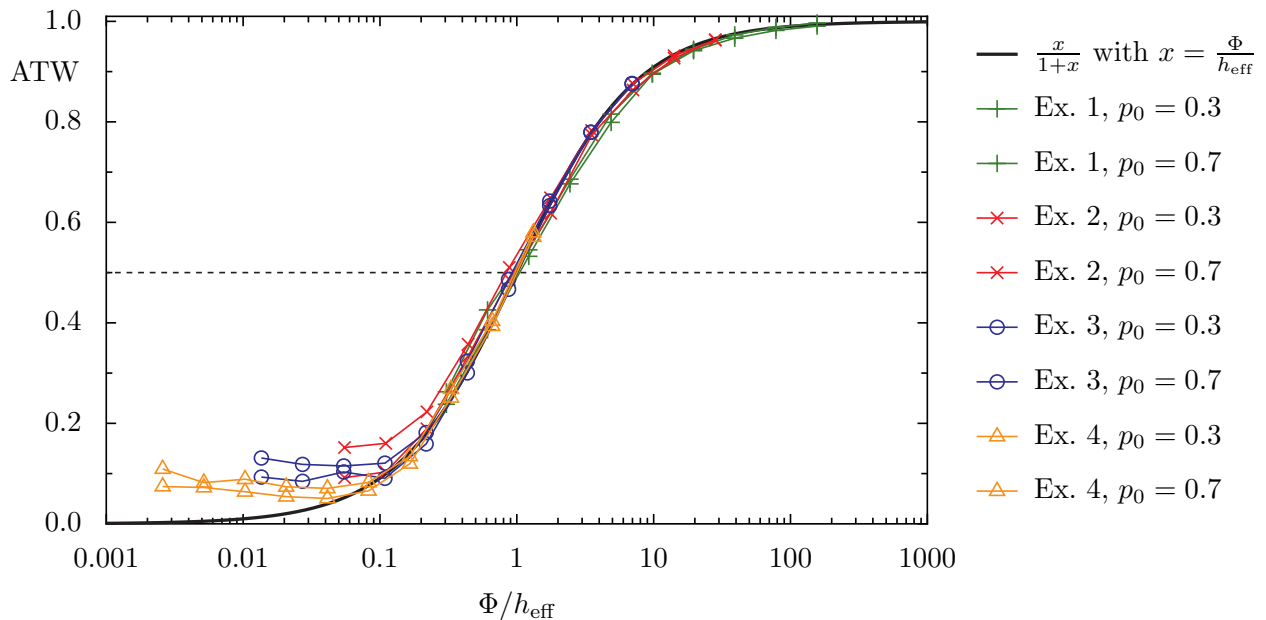


**Figure 3.21:** ATW using the Husimi weight in transmission region for the examples 1, 2, 3 and 4 of the map $F_{\text{pb}}$. The initial state is $\psi(t=0) = |p_0\rangle$ with $p_0 = 0.3$ below and $p_0 = 0.7$ above the partial barrier. The data is averaged over 20 values of $\theta_q$ and 100 steps after time $10^6$. The total number of states are $N = 1/h_{\text{eff}} = 100, 200, ..., 51200$. The universal behavior of the data is described by $x/(1+x)$ with $x = \Phi/h_{\text{eff}}$.

information on the size of Planck's constant and on the other hand the support of the Husimi weight extends up to the partial barrier. Therefore a transmitted weight is recognized by the Husimi weight while much less weight reaches the support of the momentum measure.

Note that the Husimi measure strongly depends on the definition of the partial barrier. As pointed out in Sec. 3.1.3 for the classical system at least all images and preimages of the partial barrier form again partial barriers with the same flux and the same area above and below them. Quantum mechanically there is a transition region between the upper and the lower region. We fixed the considered partial barrier and therewith made a decision what we call upper and lower. Therefore the Husimi weight of the upper or the lower region includes parts of this transition region and yields larger values than the momentum measure.

The results for map $F_{\mathrm{pb,rot}}$ are shown in Fig. 3.22(a) and need to be compared with the momentum measure results in Fig. 3.17. Again the overall behavior is unchanged and we find universal behavior by scaling the data with $\Phi/h_{\mathrm{eff}}$.

As an alternative to the time evolution, we consider the product measure averaged over the eigenstates of the quantum map. Similar to Sec. 3.3.3 we select the chaotic states by use of a minimal measure. That is, we consider all states $\phi$ with

$$\mu_{\mathrm{up}}[\phi] + \mu_{\mathrm{lo}}[\phi] \geq \chi \qquad\qquad (3.110)$$

for some $\chi > 0$. The comparison with a state uniformly distributed in the chaotic sea is not needed here, because its Husimi function integrated over the chaotic sea yields one. Therefore $\chi$ is the minimal value for the Husimi weight in the full chaotic region. This constraint with non-vanishing $\chi$ excludes again the regular states from the average. In contrast to Sec. 3.3.3 states localized close to the partial barrier and nearby the regular region are still included. Figure 3.22(b) shows the resulting average product measure. The minimal measure is chosen as $\chi = 10\%$ and we do not find a significant dependence on its value as long as it is non-vanishing. The average product measure is in good agreement with the ATW obtained by time evolution. For small ratios $\Phi/h_{\mathrm{eff}}$ the average product measure $\langle M \rangle$ is larger and for large ratios $\Phi/h_{\mathrm{eff}}$ smaller than the result using the momentum measures shown in Fig. 3.19. This difference is even more pronounced than for the ATW. Therefore also the agreement between ATW and the average product measure is not as good as for the momentum measures. The reason for this difference might be attributed to the considered eigenstates. Namely states localized on the partial barrier or close to the regular region have a product measure, which is not dominated by the partial barrier, but rather accidentally gives larger or smaller values. For small ratios $\Phi/h_{\mathrm{eff}}$ the states localized on the partial barrier have already a large product measure. Whereas for $\Phi/h_{\mathrm{eff}}$ being large localized states have small $M$, because the associated transport is suppressed due to the localization.

Figure 3.23 shows a selection of distributions of the product measure $d(M)$ considered for Fig. 3.22(b). The distributions for different examples for similar $\Phi/h_{\mathrm{eff}}$ are in reasonable agree-
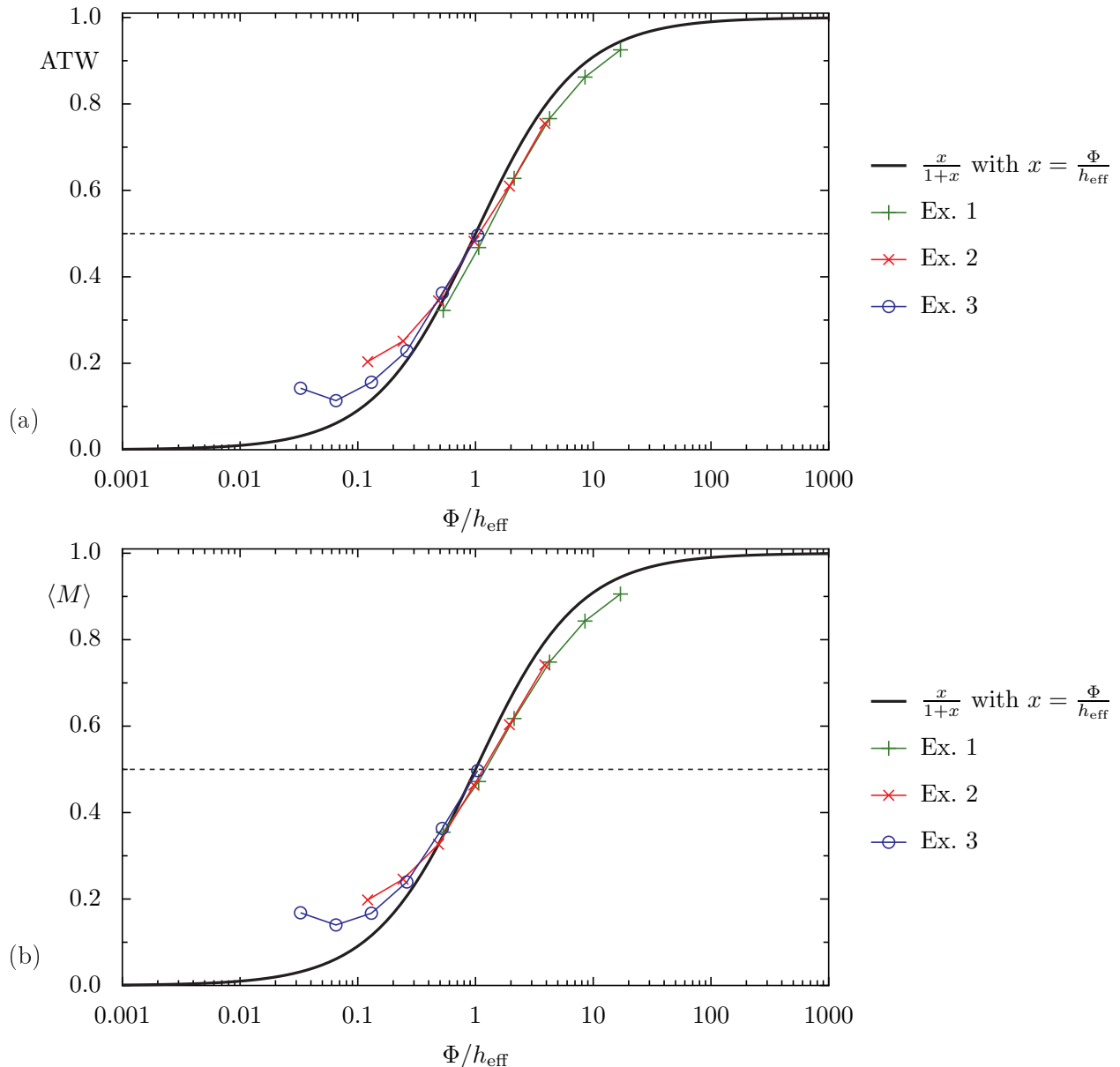
**Figure 3.22:** (a) ATW and (b) average product measure using Husimi weights for the examples 1, 2, and 3 of the map $F_{\text{pb,rot}}$. The ATW of (a) is averaged over 20 values of the Bloch phase $\theta_q$ and over 4 initial states: $\psi(t = 0) = |p_0\rangle$ with $p_0 = 0.3$ and 0.7 and coherent states at $(q_0, p_0) = (0.5, 0.3)$ and $(0.5, 0.7)$. The minimal measure $\chi$ according to Eq. (3.110) used in (b) is 10% and the data is averaged over 100 values of the Bloch phase $\theta_q$.

ment. Therefore again universal scaling with $\Phi/h_{\text{eff}}$ is found. As discussed in Sec. 3.2.3 (around Eq. (3.82)) the product measure using Husimi weights is bounded from above by one. This is in contrast to the discussion of the momentum measures. Similar to Fig. 3.20(a), for small $\Phi/h_{\text{eff}}$ the individual $M$ are small (see Fig. 3.23(a)) and therefore the corresponding eigenstates localize either in the upper or in the lower region. As illustrated in Fig. 3.23(d) the behavior for small $M$ follows a power law similar to Fig. 3.20(d).

The distributions $d(M)$ for the ratio $\Phi/h_{\text{eff}} \approx 1$ are shown as solid red lines in Fig. 3.23.
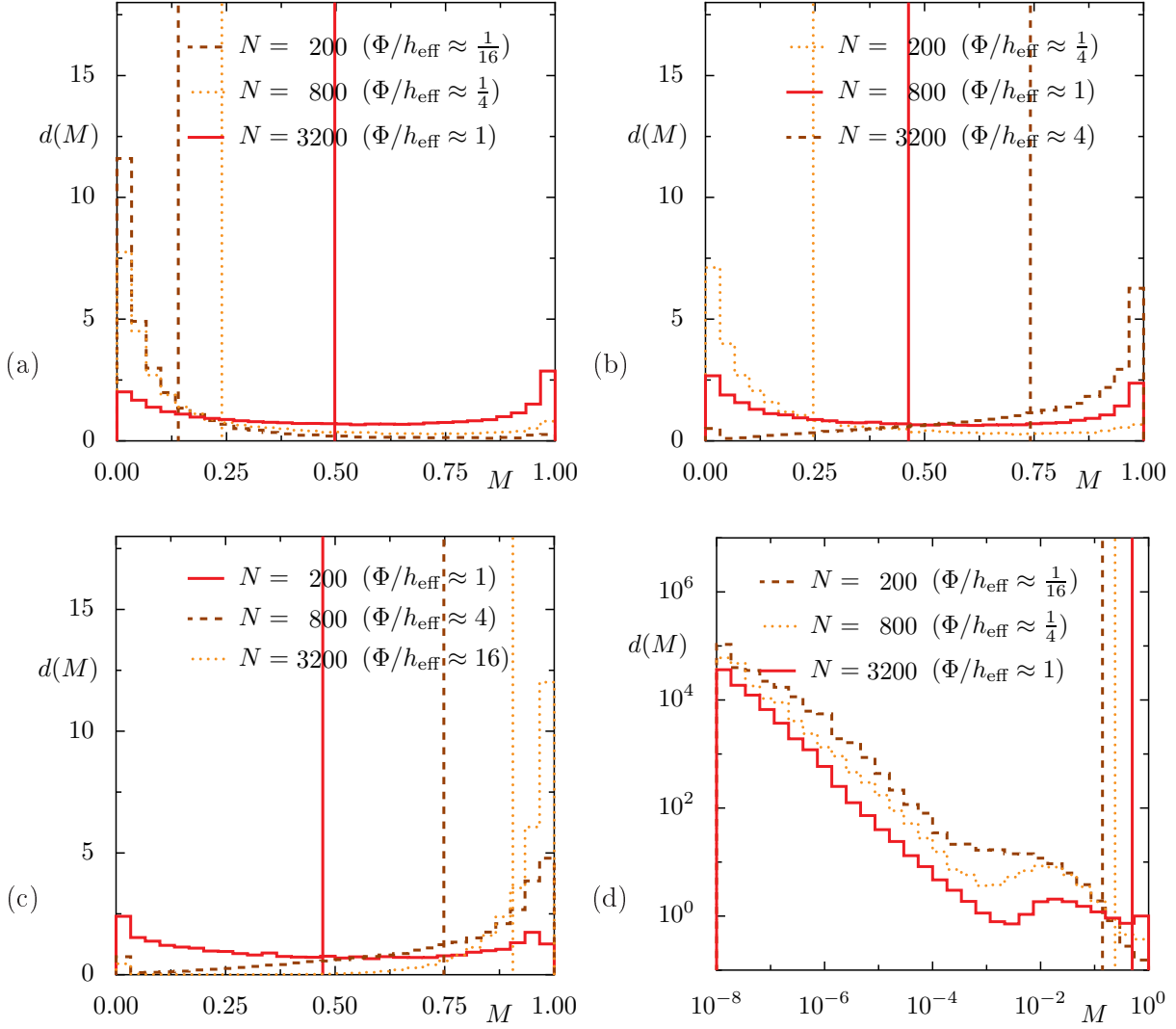
**Figure 3.23:** Distribution $d(M)$ of product measure $M$ using Husimi weights for example 3 ($\Phi \approx 1/3000$) in (a), 2 ($\Phi \approx 1/800$) in (b), and 1 ($\Phi \approx 1/200$) in (c) for the map $F_{\mathrm{pb,rot}}$ and $N = 200, 800, 3200$. (d) Same distribution as (a), but on logarithmic scale and with logarithmic ordinate. The selection of states is the same as in Fig. 3.22(b) and we consider 100 values of the Bloch phase $\theta_q$ to obtain the data. The average of the distribution is shown as vertical line. The solid red line corresponds to the result with $\Phi/h_{\mathrm{eff}} \approx 1$. In total the data cover a range of $\Phi/h_{\mathrm{eff}} \approx 1/15$ (smallest $N$ of example 3) to $\Phi/h_{\mathrm{eff}} \approx 16$ (largest $N$ of example 1).

They are quite symmetric with respect to the average value around $M = \frac{1}{2}$ and extend over the whole range $[0, 1]$ of $M$. That is, there are as many states with large $M$, being already delocalized, as with $M$ smaller than $\frac{1}{2}$, being still localized in one region. For large values of $\Phi/h_{\mathrm{eff}}$ the peak of the distributions approaches one, which is the classical expectation.

Although we find differences in the details of the transition curve considering Husimi weight rather than momentum measures, the overall behavior is the same and we believe that the universal behavior is described by the ratio $\Phi/h_{\mathrm{eff}}$.

## 3.3.5 Variation of the width of the regular region

For the designed maps $F_{\mathrm{pb}}$ and $F_{\mathrm{pb,rot}}$, quantum mechanically, the coupling between the upper and the lower chaotic region might depend on the width of the regular region rather than on the turnstile transport only. More precisely we expect an additional contribution to the quantum transport due to tunneling across the regular region if Planck's constant is large and the regular region is thin. Therefore we vary the width of the regular region and look for signatures of this additional transport channel. We consider the ATW using the Husimi weight in order to remove any ambiguity in the definition of the measuring boxes for thin and thick regular regions, which give rise to large and small chaotic regions above and below the partial barrier.

For the map $F_{\mathrm{pb}}$ and $F_{\mathrm{pb,rot}}$ the width of the regular region can be adjusted using the parameter $p_{\mathrm{d,reg}}$. Here we used $p_{\mathrm{d,reg}} = 0.045$, 0.125, and 0.25 yielding a regular region of size $A_{\mathrm{reg}} \approx 0$, $A_{\mathrm{reg}} \approx 0.16$, and $A_{\mathrm{reg}} \approx 0.4$. Note that the given numbers are also the width in $p$-direction because the width in $q$ is one. These three versions of examples 1 and 3 are considered and the resulting ATW is shown in Fig. 3.24. Except for small fluctuations the data does not depend on the width of the regular region down to the smallest ratio $\Phi/h_{\mathrm{eff}}$ considered here. For smaller ratios $\Phi/h_{\mathrm{eff}}$, we expect an influence of the width of the regular region, because at this point the coupling due to the classical turnstile transport is significantly suppressed and tunneling across the partial barrier and over the regular region might be of the same magnitude for vanishing width of the regular region.
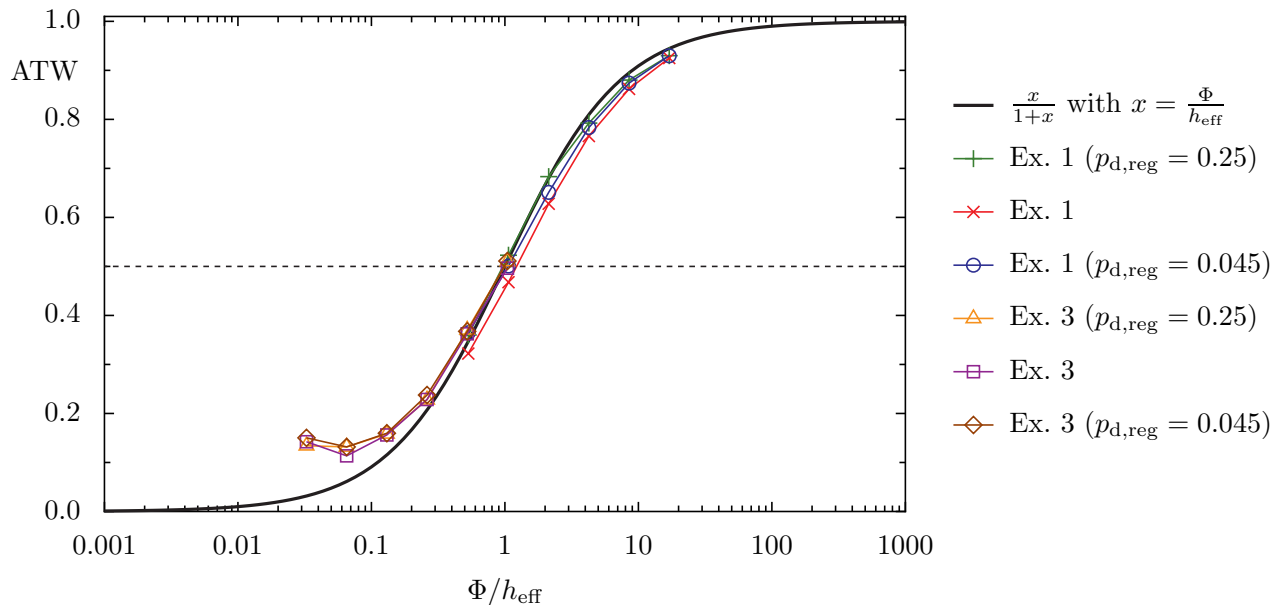


**Figure 3.24:** ATW using the Husimi weight for the examples 1 and 3 of the map $F_{\mathrm{pb,rot}}$ (same as Fig. 3.22(a)) and modified versions of them $p_{\mathrm{d,reg}} = 0.125 \rightarrow 0.045$ and $p_{\mathrm{d,reg}} = 0.125 \rightarrow 0.25$. The overall behavior is the same independently of $p_{\mathrm{d,reg}}$ and only tiny changes are observed.

### 3.3.6  Asymmetric chaotic regions

In this section we extend the discussion of the previous sections to situations, where the upper and the lower region have different size, $A_{\mathrm{ch,up}} \neq A_{\mathrm{ch,lo}}$. According to the $\Lambda$-flux relation [23], given in Eq. (3.50),

$$\Lambda = \frac{1}{4\pi^2 f_{\mathrm{up}} f_{\mathrm{lo}}} \frac{\Phi}{h_{\mathrm{eff}}}, \tag{3.111}$$

derived in Sec. 3.2.2, we expect that the scaling depends on the relative size of the two chaotic regions, $f_{\mathrm{up}}$ and $f_{\mathrm{lo}}$, in addition to the ratio of classical flux and Planck's constant. However, a reliable verification of this dependence on $f_{\mathrm{up}}$ and $f_{\mathrm{lo}}$ is not found in this section and further investigations are needed.

For the maps $F_{\mathrm{pb}}$ and $F_{\mathrm{pb,rot}}$ the relative size of the chaotic regions $f_{\mathrm{up}}$ and $f_{\mathrm{lo}}$ can be adjusted by variation of the position of the fixed point $(\frac{1}{2}, p_{\mathrm{fix}})$. Changing the parameter $p_{\mathrm{fix}}$ from the value given in Tab. 3.1 moves the partial barrier in momentum direction. In the following we restrict ourselves to example 3. Note that the parameter $p_{\mathrm{fix}}$ cannot be varied arbitrarily. Its value is limited by the constraint that each of the chaotic regions should be strongly mixing. In order to ensure this property, there has to be some space between $p_{\mathrm{d,reg}}$ and $p_{\mathrm{fix}} - p_{\mathrm{d,lo}}$ as well as between $p_{\mathrm{fix}} + p_{\mathrm{d,up}}$ and $1 - p_{\mathrm{d,reg}}$, which determine the regions of large slope $b_{\mathrm{left}}$ and $b_{\mathrm{right}}$ in $T'$ (see Eq. (3.4)). These slopes yield a large value for the effective kicking strength $b_{\mathrm{left}} K'$ and $b_{\mathrm{right}} K'$, which induces this strong mixing behavior of the map. If these regions account only for a small fraction of the upper (lower) region, the behavior of chaotic states in the respective region is dominated by the slower mixing parts close to the regular region and the partial barrier. Furthermore we choose the value of $p_{\mathrm{fix}}$ such that the additional rotations introduced in Sec. 3.1.6 are shifted according to the change of $p_{\mathrm{d,reg}}$, but preserve their size in phase space without destroying the regular regions and the considered partial barrier. In this way we ensure that the results do not depend on the modification of the rotation, but rather on the asymmetric size of the upper and lower region.

As first quantitative measure we consider the average product measure using the momentum measures as discussed in Sec. 3.3.3. The resulting data for various asymmetric versions of example 3 are shown in Fig. 3.25. The results are plotted as a function of the ratio $\Phi/h_{\mathrm{eff}}$ as well as of the parameter $\Lambda$ in order to find the universal scaling parameter. As a function of the ratio $\Phi/h_{\mathrm{eff}}$ the resulting product measure slightly increases with increasing asymmetry $A_{\mathrm{ch,up}}/A_{\mathrm{ch,lo}}$. However, this change is almost negligible. If we scale the data with the parameter $\Lambda$, the data for different pairs $(A_{\mathrm{ch,up}}, A_{\mathrm{ch,lo}})$ show deviations. Therefore we conclude that for the considered example the data scales with the ratio $\Phi/h_{\mathrm{eff}}$ rather than with the parameter $\Lambda$. Note that the relevant difference between the scaling with $\Phi/h_{\mathrm{eff}}$ and with $\Lambda$ is the factor $4f_{\mathrm{up}} f_{\mathrm{lo}}$, which is one for the symmetric examples and reaches $4f_{\mathrm{up}} f_{\mathrm{lo}} = 4 \cdot 6/49 \approx \frac{1}{2}$ for the most asymmetric case $A_{\mathrm{ch,up}}/A_{\mathrm{ch,lo}} = 6/1$ considered here. Therefore the different scaling behavior

reaches at most a factor of two, which is quite small. In order to test this scaling in more detail, systems with stronger asymmetries $A_{\mathrm{ch,up}}/A_{\mathrm{ch,lo}}$ need to be considered.

The observed scaling with $\Phi/h_{\mathrm{eff}}$ is quite unexpected, because $\Lambda$ should be the appropriate scaling parameter as discussed in Sec. 3.2.2. To verify our result we additionally considered the Husimi measures introduced in Sec. 3.3.4 to determine the average product measure as well as the ATW. The results are shown in Fig. 3.26 and Fig. 3.27, respectively. For
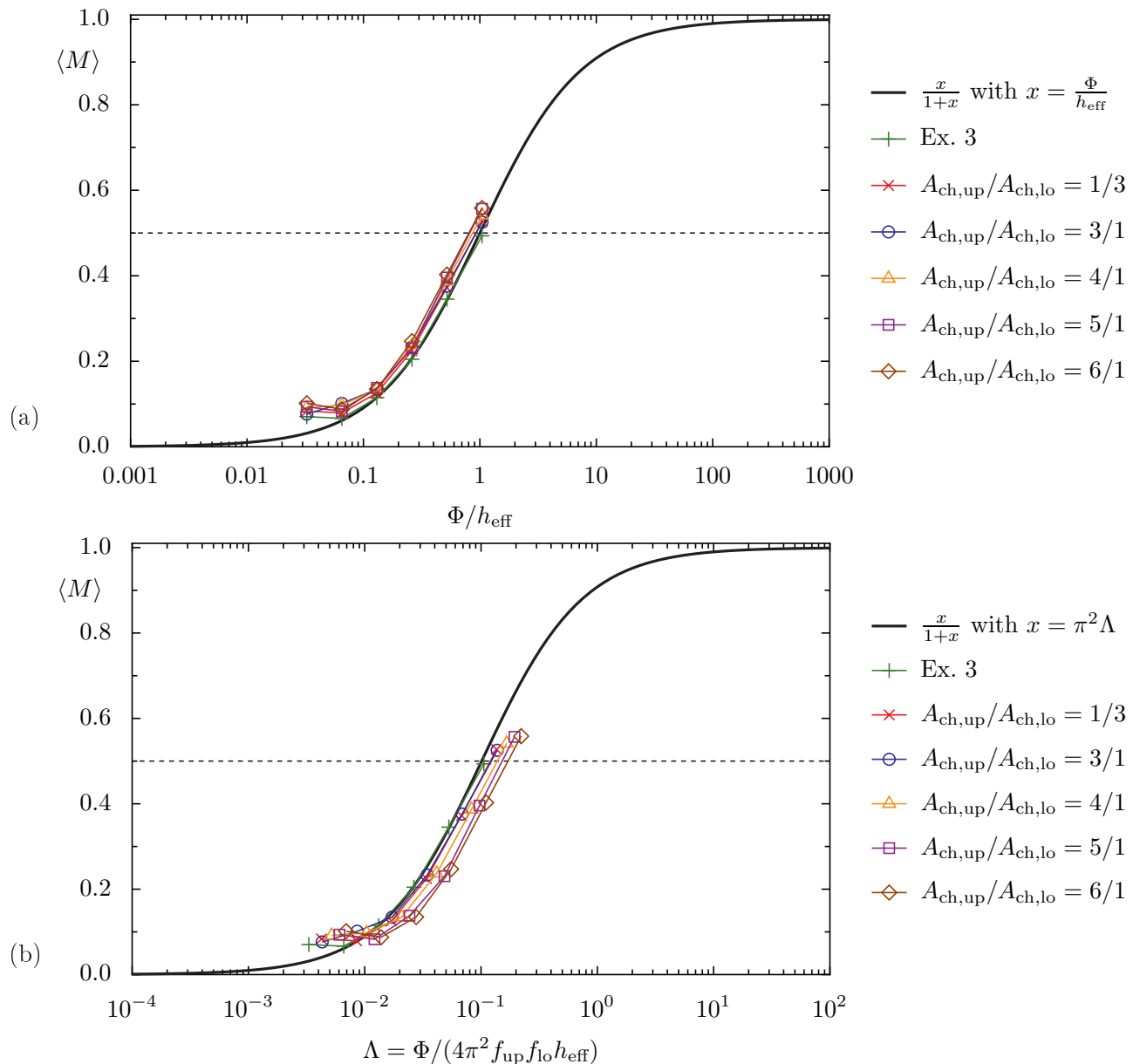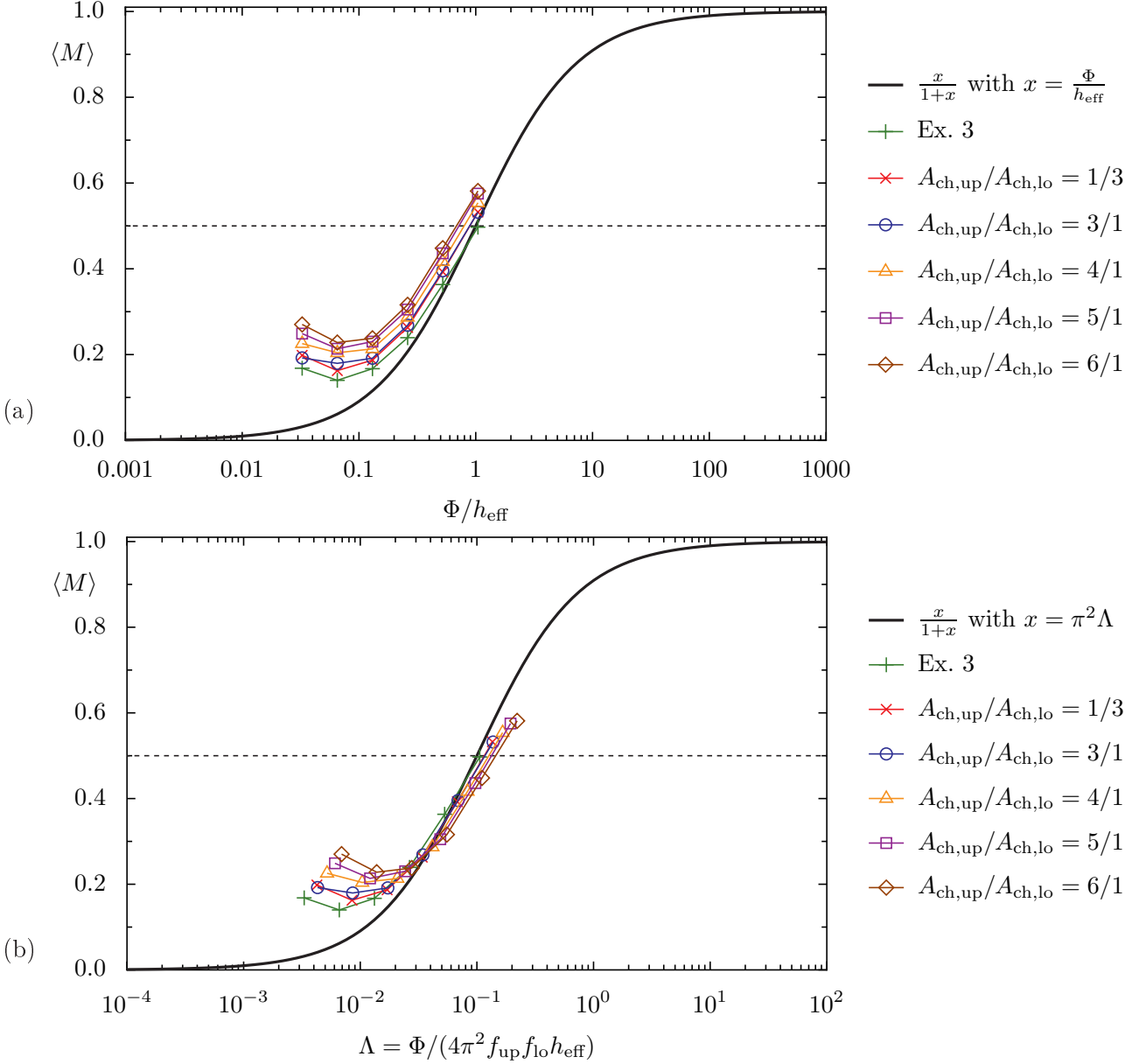


**Figure 3.25:** Average product measure $M$ using the momentum measure for the example 3 of the map $F_{\mathrm{pb,rot}}$ for various ratios $A_{\mathrm{ch,up}}/A_{\mathrm{ch,lo}}$ as a function of the ratio $\Phi/h_{\mathrm{eff}}$ in (a) and the parameter $\Lambda$ in (b). The data is averaged over 100 values of the Bloch phase $\theta_q$. It scales with the ratio $\Phi/h_{\mathrm{eff}}$ rather than the parameter $\Lambda$. The total number of states in phase space is $N = 1/h_{\mathrm{eff}} = 100, 200, \ldots, 3200$ from the left to the right for the shown data.

the average product measure using Husimi weights, we find deviations from the scaling with $\Phi/h_{\text{eff}}$ (Fig. 3.26(a)). As a function of $\Phi/h_{\text{eff}}$ the data increases with increasing asymmetry $A_{\text{ch,up}}/A_{\text{ch,lo}}$. In Fig. 3.26(b) the same data is shown as a function of $\Lambda$ and for the first data points ($N = 1/h_{\text{eff}} = 100, 200, 400$) the same enhancement with increasing asymmetry $A_{\text{ch,up}}/A_{\text{ch,lo}}$ is found whereas for larger values of $N = 1/h_{\text{eff}}$ the data for different asymmetries are close to each other. The enhancement for small $N$ might be due to the fact that the num-



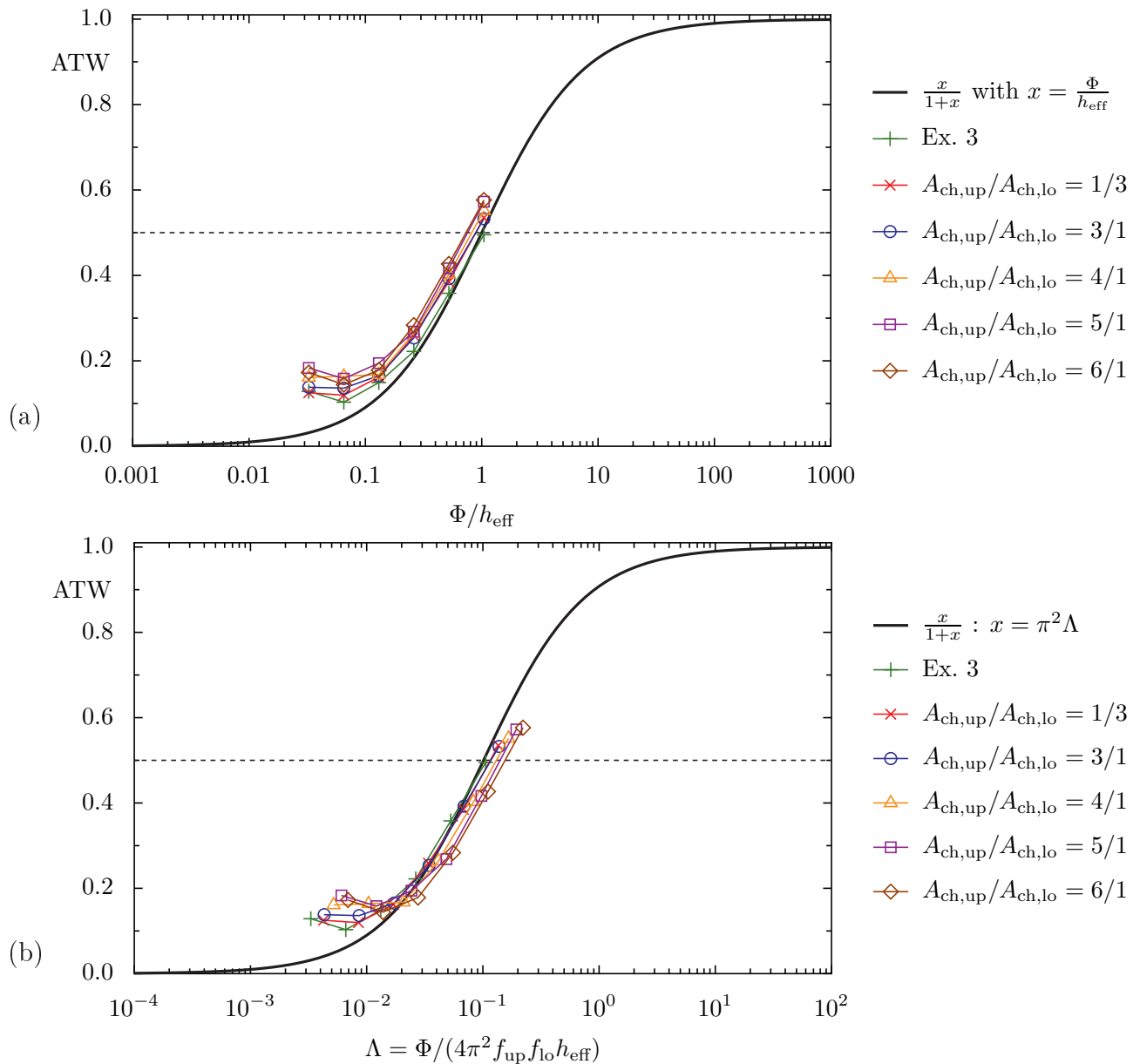**Figure 3.26:** Average product measure $M$ using the Husimi measure for the example 3 of the map $F_{\text{pb,rot}}$ for various ratios $A_{\text{ch,up}}/A_{\text{ch,lo}}$ as a function of the ratio $\Phi/h_{\text{eff}}$ in (a) and the parameter $\Lambda$ in (b). The total number of states in phase space is $N = 1/h_{\text{eff}} = 100, 200, \ldots, 3200$ from the left to the right for the shown data. The data is averaged over 100 values of the Bloch phase $\theta_q$.

ber of states associated with the smaller region is too small to observe universal features of the partial barrier. Here one may conjecture that the parameter $\Lambda$ is the more appropriate choice for the scaling of the average product measure using Husimi weights than the ratio $\Phi/h_{\text{eff}}$.

Considering the ATW using the Husimi weight gives the results shown in Fig. 3.27. The enhancement in $\langle M \rangle$ found for small $N = 1/h_{\text{eff}}$ in Fig. 3.26 is much smaller in the ATW



**Figure 3.27:** ATW using the Husimi weight for the example 3 of the map $F_{\text{pb,rot}}$ for various ratios $A_{\text{ch,up}}/A_{\text{ch,lo}}$ as a function of the ratio $\Phi/h_{\text{eff}}$ in (a) and the parameter $\Lambda$ in (b). The data is averaged over 10 initial states placed in the chaotic regions away from the partial barrier and the regular region. We use 20 values of the Bloch phase $\theta_q$. The total number of states in phase space is $N = 1/h_{\text{eff}} = 100, 200, \ldots, 3200$ from the left to the right for the shown data.

determined by time evolution. The reason for this difference are states localized close to the partial barrier or close to the regular region, which are not excited by wave packets, that are initially placed inside the upper and the lower chaotic region away from theses structures. For the ATW shown in Fig. 3.27 neither scaling with the ratio $\Phi/h_{\text{eff}}$ nor scaling with the parameter $\Lambda$ yields curves on top of each other. Both scalings agree fairly well.

As a result of this section we find different scaling behaviors for different measures considered for the description of the quantum transition of a partial barrier. Up to now we do not know the reason for these different behaviors. Therefore further investigations are needed in order to find out whether the scaling is described by the ratio $\Phi/h_{\text{eff}}$ or the parameter $\Lambda$.

### 3.3.7 Summary of the results for the designed map

In the last sections we have quantified the quantum transition of a partial barrier between quantum suppression and classical transport for the designed maps $F_{\text{pb}}$ and $F_{\text{pb,rot}}$. We describe this transition in terms of time evolution and eigenstate properties. Moreover we consider momentum and Husimi measures. As long as the two chaotic regions are equal in size, i.e. $A_{\text{ch,up}} = A_{\text{ch,lo}}$, we always find scaling of the transition with the ratio $\Phi/h_{\text{eff}}$ of the classical flux and Planck's constant. The overall behavior is well described by, Eq. (3.102),

$$\text{ATW}\left(\frac{\Phi}{h_{\text{eff}}}\right) = \frac{\frac{\Phi}{h_{\text{eff}}}}{1 + \frac{\Phi}{h_{\text{eff}}}}, \tag{3.112}$$

which we motivate by a $2 \times 2$ model in Sec. 4.1. The transition curve given by Eq. (3.112) is shown in Fig. 3.28. The transition point of the curve is at the point, where flux $\Phi$ and Planck's constant $h_{\text{eff}}$ are equal in size, because at this point $\text{ATW}(\Phi/h_{\text{eff}}) = \frac{1}{2}$. That is, it is half way between quantum suppression $\text{ATW} = 0$ and classical behavior $\text{ATW} = 1$. As we use $\Phi/h_{\text{eff}}$ on a logarithmic scale, it is meaningful to call this point the symmetry point of the transition, because the ATW has the following point symmetry,

$$\text{ATW}\left(\frac{\Phi}{h_{\text{eff}}}\right) - \text{ATW}\left(\frac{\Phi}{h_{\text{eff}}} = 1\right) = \text{ATW}\left(\frac{\Phi}{h_{\text{eff}}} = 1\right) - \text{ATW}\left(\left[\frac{\Phi}{h_{\text{eff}}}\right]^{-1}\right), \tag{3.113}$$

$$\frac{\frac{\Phi}{h_{\text{eff}}}}{1 + \frac{\Phi}{h_{\text{eff}}}} - \frac{1}{2} = \frac{1}{2} - \frac{1}{1 + \frac{\Phi}{h_{\text{eff}}}}. \tag{3.114}$$

Having this symmetry in mind the transition width should be described by a factor in the ratio $\Phi/h_{\text{eff}}$. We consider $\text{ATW} \in [0.1, 0.9]$ as the transition region between quantum suppression and classical transport, which corresponds to 10% up to 90% of the classical value. This transition region is illustrated in Fig. 3.28 using the average product measure $\langle M \rangle$. It has a width of a factor of 81. That is, the transition is broad and almost two orders of magnitude in the ratio $\Phi/h_{\text{eff}}$ are needed to investigate the quantum transition of a partial barrier.
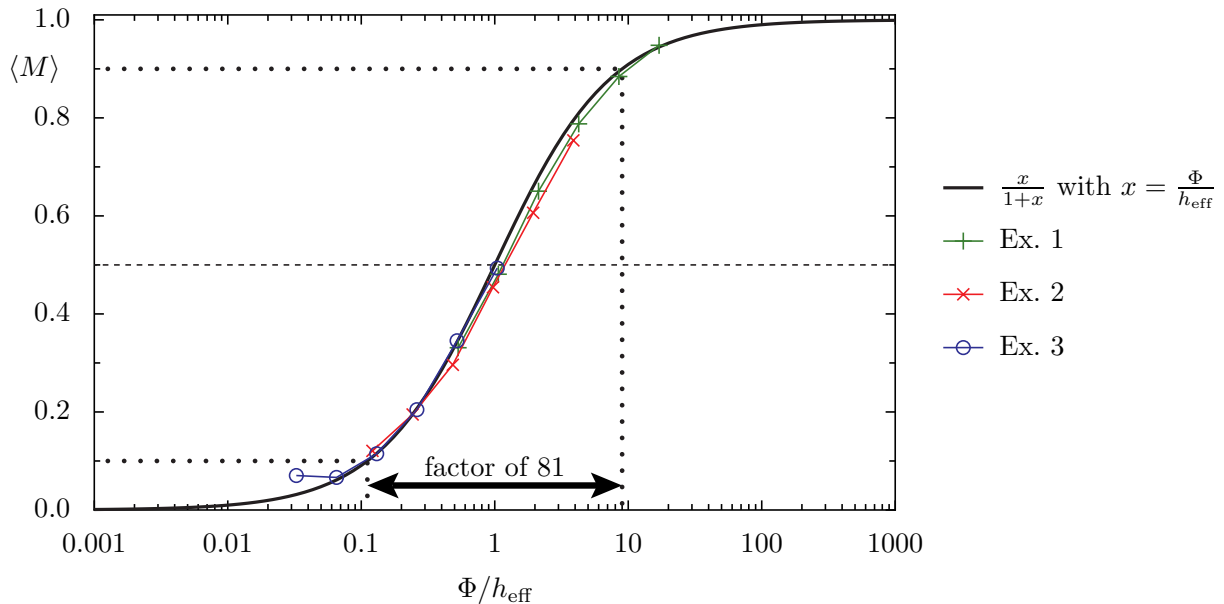
**Figure 3.28:** Average product measure $\langle M \rangle$ using the momentum measures for the examples 1, 2, and 3 of the map $F_{\mathrm{pb,rot}}$ (same as Fig. 3.19). The width of the transition between quantum suppression and classical transport is shown by the arrow. The dotted lines indicate the limits of the transition region given by $\langle M \rangle \in [0.1, 0.9]$.

## 3.4   Results for the standard map

In this section we investigate the impact of a partial barrier on the corresponding quantum system for the case of the generic standard map. We show that the results obtained for the designed maps $F_{\mathrm{pb}}$ and $F_{\mathrm{pb,rot}}$ in Sec. 3.3 also hold for this more general example system.

### 3.4.1   Considered examples and characterization of the classical system

For the generic standard map it is not possible to find such a simple phase-space structure as obtained for the map $F_{\mathrm{pb,rot}}$ in Sec. 3.1. Nevertheless we consider two examples of the standard map with kicking strength $K = 2.7$ and $K = 2.9$, such that there is a dominant partial barrier and the regular regions on each side of the partial barrier are small.

The phase space of the chosen examples is illustrated in Fig. 3.29(a) and (b) and the sizes of relevant phase-space areas are given in Tab. 3.3. In both cases the phase space consists of a large central island, which is surrounded by a chain of four islands. In between these islands there exists a hyperbolic periodic orbit and its stable and unstable manifolds are also displayed. As mentioned in Sec. 2.4 these stable and unstable manifolds give rise to a partial barrier. At each point of the hyperbolic orbit there are two branches of the stable and of the unstable manifold. Only the outer pair of the manifolds gives rise to a partial barrier, because the inner pair of the manifolds is very close to the central island and almost no chaotic region
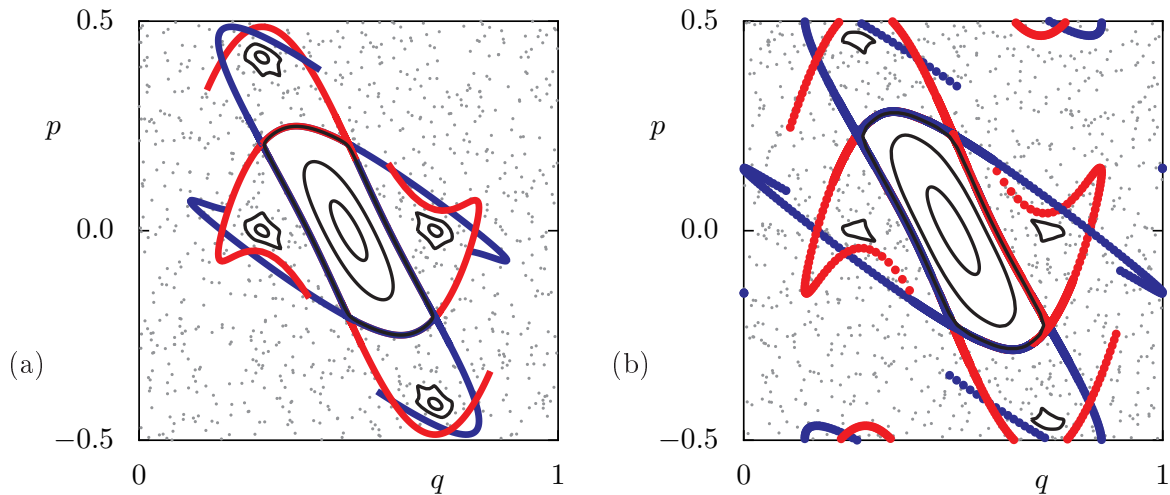
**Figure 3.29:** Phase-space portrait of the standard map with (a) $K = 2.7$ and (b) $K = 2.9$. For both examples there is a large island in the center, which is surrounded by a chain of four islands. Moreover the stable manifolds (blue) and the unstable manifolds (red) of the hyperbolic periodic orbit in between this island chain are shown.

| $K$ | 2.7 | 2.9 |
|---|---|---|
| $\Phi$ | 0.0054 | 0.0126 |
| $1/\Phi$ | 185.2 | 79.3 |
| $A_{\text{ch}}$ | 0.8902 | 0.8818 |
| $A_{\text{large island}}$ | 0.093 | 0.11 |
| $A_{\text{small island}}$ | 0.0042 | 0.002 |

**Table 3.3:** The flux $\Phi$, the total size of the chaotic region $A_{\text{ch}}$ and the size of the regular islands for the standard map with $K = 2.7$ and $K = 2.9$, whose phase space is illustrated in Fig. 3.29.

is in between the manifolds and the regular island. As pointed out in Sec. 3.1.3 the definition of the partial barrier according to the stable and unstable manifolds of a hyperbolic periodic orbit is not unique. That is, all images and preimages of a constructed partial barrier form again a partial barrier with the same flux and the same area of phase space on each side of the partial barrier. Therefore we choose some partial barrier, which seems to be relevant for the quantum system. We restrict ourselves to partial barriers, which satisfy the parity symmetry of the standard map, $(q, p) \mapsto (1 - q, -p)$. Four different versions of such partial barriers for the standard map at $K = 2.7$ are shown in Fig. 3.30. All these partial barriers have the same flux $\Phi$ (see Tab. 3.3), which is twice the area of one loop between the stable and the unstable manifolds. They enclose different phase-space regions $A_{\text{ch,in}}$ and $A_{\text{ch,out}}$, which are given in Tab. 3.4 for $K = 2.7$ and in Tab. 3.5 for $K = 2.9$.

As the next step we investigate the impact of the constructed partial barriers on the classical dynamics. As in Secs. 3.1.5 and 3.1.8 we consider orbits uniformly distributed in the chaotic sea
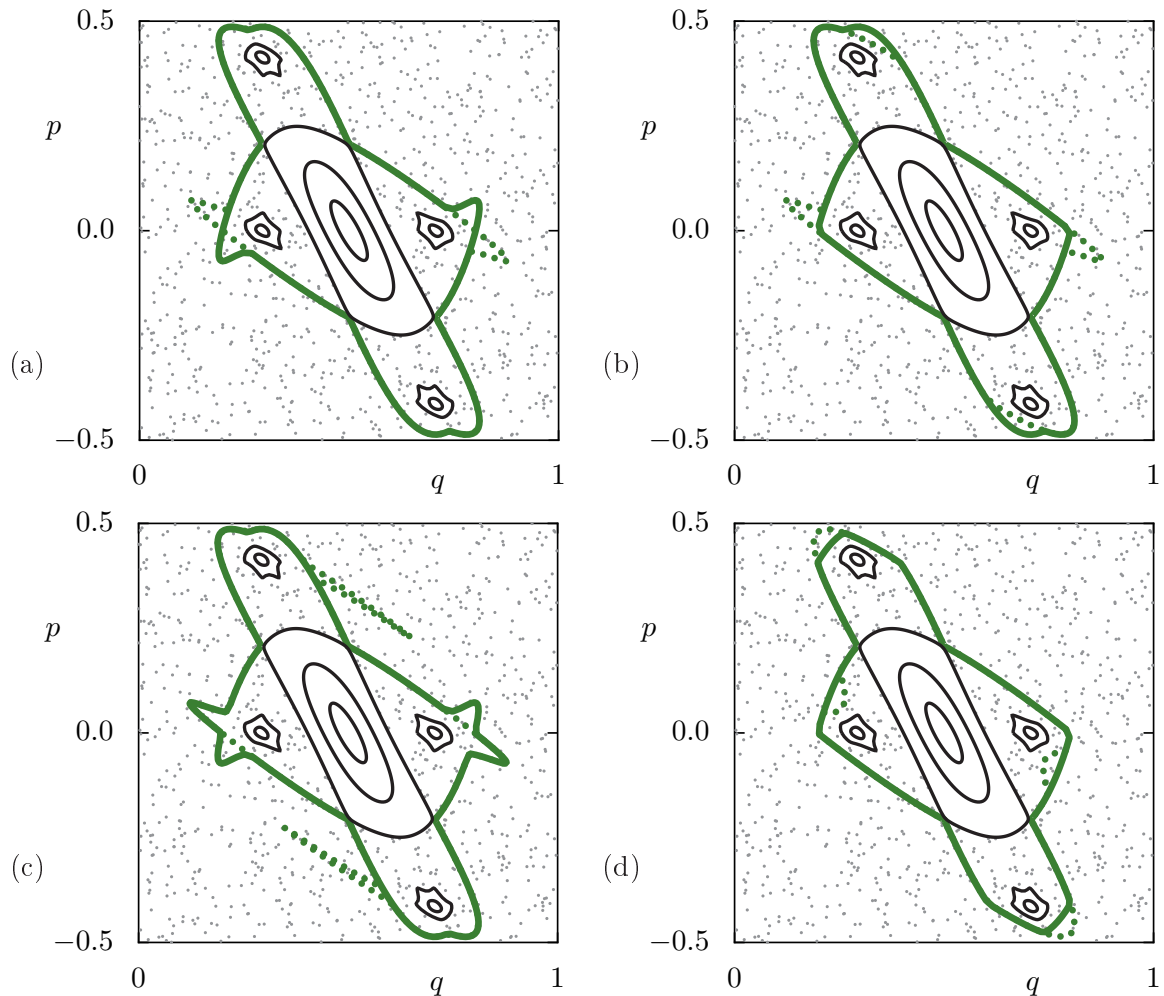
**Figure 3.30:** (a)–(d) Four different versions of partial barriers respecting the parity symmetry of the standard map with $K = 2.7$ (solid lines) as well as their preimages (dotted lines) constructed from the stable and unstable manifolds shown in Fig. 3.29(a).

|               | (a)    | (b)    | (c)    | (d)    | av.    |
|---------------|--------|--------|--------|--------|--------|
| $A_{ch,in}$   | 0.1805 | 0.1751 | 0.1859 | 0.1643 | 0.1764 |
| $A_{ch,out}$  | 0.7097 | 0.7151 | 0.7043 | 0.7259 | 0.7138 |
| $f_{ch,in}$   | 0.2027 | 0.1967 | 0.2088 | 0.1845 | 0.2    |
| $f_{ch,out}$  | 0.7973 | 0.8033 | 0.7912 | 0.8155 | 0.8    |

**Table 3.4:** Areas and relative areas of chaotic regions inside and outside the partial barrier for the standard map at $K = 2.7$. The columns correspond to the four versions of symmetric partial barriers as shown in Fig. 3.30(a)-(d) and the last column displays the average values. The ratio of the region inside the partial barrier to the region outside is approximately 1/4.

and measure the fraction of orbits, which remain on one side of the partial barrier up to time $t$. This survival probability $P(t)$ resulting from orbits started in the inner chaotic region and in the outer chaotic are shown in Fig. 3.31(a) and (b) for the example with $K = 2.7$ and $K = 2.9$,

| | (a) | (b) | (c) | (d) | av. |
|---|---|---|---|---|---|
| $A_{\mathrm{ch,in}}$ | 0.2402 | 0.2276 | 0.2528 | 0.2027 | 0.2308 |
| $A_{\mathrm{ch,out}}$ | 0.6416 | 0.6542 | 0.6289 | 0.6791 | 0.6509 |
| $f_{\mathrm{ch,in}}$ | 0.2724 | 0.2581 | 0.2867 | 0.2299 | 0.26 |
| $f_{\mathrm{ch,out}}$ | 0.7276 | 0.7419 | 0.7133 | 0.7701 | 0.74 |

**Table 3.5:** Areas and relative areas of chaotic regions inside and outside the partial barrier for the standard map at $K = 2.9$. The columns correspond to the four versions of symmetric partial barriers similar to those in Fig. 3.30 for $K = 2.7$ and the last column displays the average values. The ratio of the region inside the partial barrier to the region outside is approximately 1/3.

respectively. For both examples we consider the partial barrier illustrated in Fig. 3.30(a). As discussed in Sec. 3.1.5 we expect an exponential decay for the survival probability $P(t) \propto \exp\{-\alpha_i t\}$ with the classical escape rate $\alpha_i = 1/t_{\mathrm{dwell},i} = \Phi/A_{\mathrm{access},i}$. For both examples the survival probability of orbits started outside the partial barrier $P_{\mathrm{out}}(t)$ is in good agreement with this exponential decay as shown in Fig. 3.31. The survival probability of orbits started inside the partial barrier $P_{\mathrm{in}}(t)$ follows the exponential decay, too, but only for some time. At large times $P_{\mathrm{in}}(t)$ decays much slower. This indicates that at large times further partial barriers with smaller flux are important, which additionally limit the transport. The considered partial barrier is dominant for $P_{\mathrm{out}}(t)$ and for the short time behavior of $P_{\mathrm{in}}(t)$. However, close to the
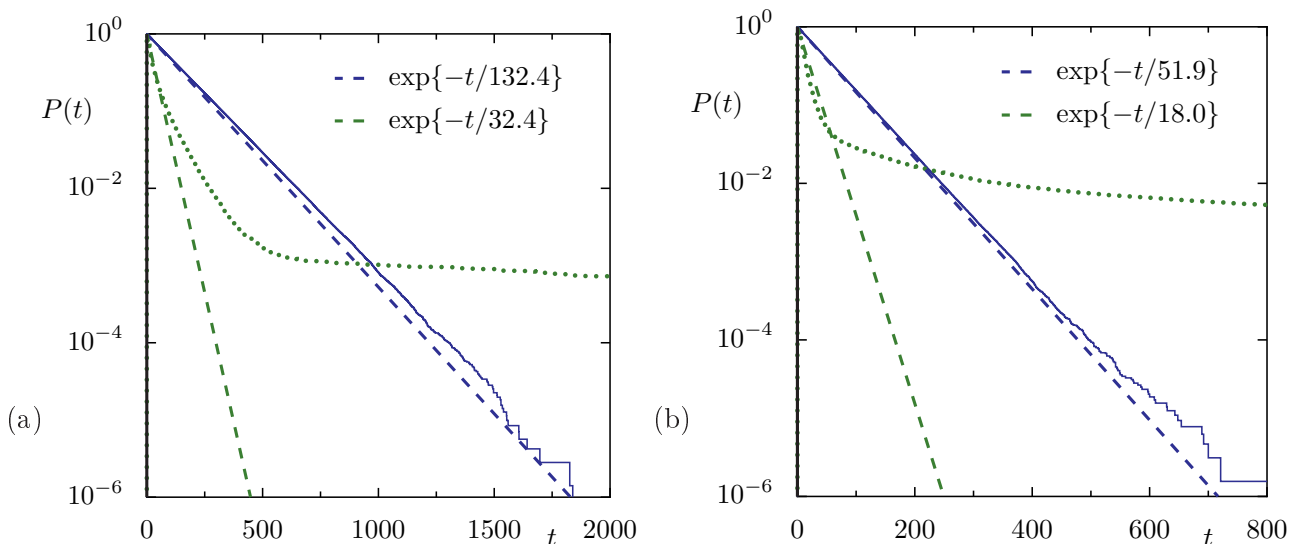


**Figure 3.31:** Survival probability $P(t)$ for the standard map at (a) $K = 2.7$ and (b) $K = 2.9$ of orbits uniformly started outside (histogram, blue solid line) and inside (histogram, green dotted line) of the partial barrier. For comparison the expected exponential decay $\exp\{-t/t_{\mathrm{dwell},i}\}$ with $t_{\mathrm{dwell},i} = A_{\mathrm{access},i}/\Phi$ is plotted (dashed lines). For $K = 2.7$ the dwell time is 132.4 for the region outside the partial barrier and 32.4 for inside whereas for $K = 2.9$ it is 51.9 and 18.0 for outside and inside.

period four island chain further partial barriers limit the transport. The question is whether these structures are resolved in the corresponding quantum system and thereby contribute to the localization of wave packets. In the following we will restrict ourselves to quantify the impact of the constructed partial barrier.

## 3.4.2 ATW and product measure using Husimi measures

In order to investigate the quantum transition of the constructed partial barrier, we consider the quantitative measures introduced in Sec. 3.2.3 for the two examples of the standard map defined in the last section. In analogy to Sec. 3.3.4 we evaluate Eqs. (3.52) and (3.72) using the Husimi function integrated over the chaotic regions inside and outside of the partial barrier.

First we consider the ATW of a wave packet initially located outside of the partial barrier. To overcome the ambiguity of the definition of the partial barrier, we consider the four different partial barriers of Fig. 3.30(a)–(d) for the transmitted weight. In Fig. 3.32 the obtained ATW is shown as a function of $\Phi/h_{\mathrm{eff}}$ and of the parameter discussed in Sec. 3.2.2, Eq. (3.50),

$$\Lambda = \frac{1}{4\pi^2 f_{\mathrm{ch,in}} f_{\mathrm{ch,out}}} \frac{\Phi}{h_{\mathrm{eff}}}. \tag{3.115}$$

The ATW depends only slightly on the choice of the partial barriers shown in Fig. 3.30. Therefore we find a universal transitional behavior. Similar to Sec. 3.3.6 it is hard to decide which scaling yields the best agreement within the considered examples with different flux. The relevant difference of the scaling with $\Lambda$ to the scaling with $\Phi/h_{\mathrm{eff}}$ is the factor $4f_{\mathrm{ch,in}} f_{\mathrm{ch,out}}$, which is one for $f_{\mathrm{ch,in}} = f_{\mathrm{ch,out}} = \frac{1}{2}$, $4f_{\mathrm{ch,in}} f_{\mathrm{ch,out}} \approx 0.64$ for the $K = 2.7$, and $4f_{\mathrm{ch,in}} f_{\mathrm{ch,out}} \approx 0.77$ for $K = 2.9$. That is, the scaling difference is at most a factor of 1.5, which is too small to observe significant differences. Therefore we conclude that both data sets are quite close to each other in both scalings. The numerical data is well described by

$$\mathrm{ATW}\left(\frac{\Phi}{h_{\mathrm{eff}}}\right) = \frac{\frac{\Phi}{h_{\mathrm{eff}}}}{1 + \frac{\Phi}{h_{\mathrm{eff}}}}, \tag{3.116}$$

which is used as description for the map $F_{\mathrm{pb,rot}}$ in Sec. 3.3.7.

Complementary to the ATW we now discuss the average product measure $\langle M \rangle$. In analogy to Sec. 3.3.4 we consider only those states $\phi$ with

$$\mu_{\mathrm{up}}[\phi] + \mu_{\mathrm{lo}}[\phi] \geq \chi \tag{3.117}$$

for some $\chi > 0$. That is, we include all eigenstates whose Husimi weight in the chaotic region is larger than $\chi$ and nonzero $\chi$ selects states with at least some component in the chaotic sea. The resulting $\langle M \rangle$ for several $\chi$ is shown in Fig. 3.33 in comparison to the ATW of Fig. 3.32. For non-vanishing $\chi$ the average product measure is close to the ATW. However, $\langle M \rangle$ is enhanced
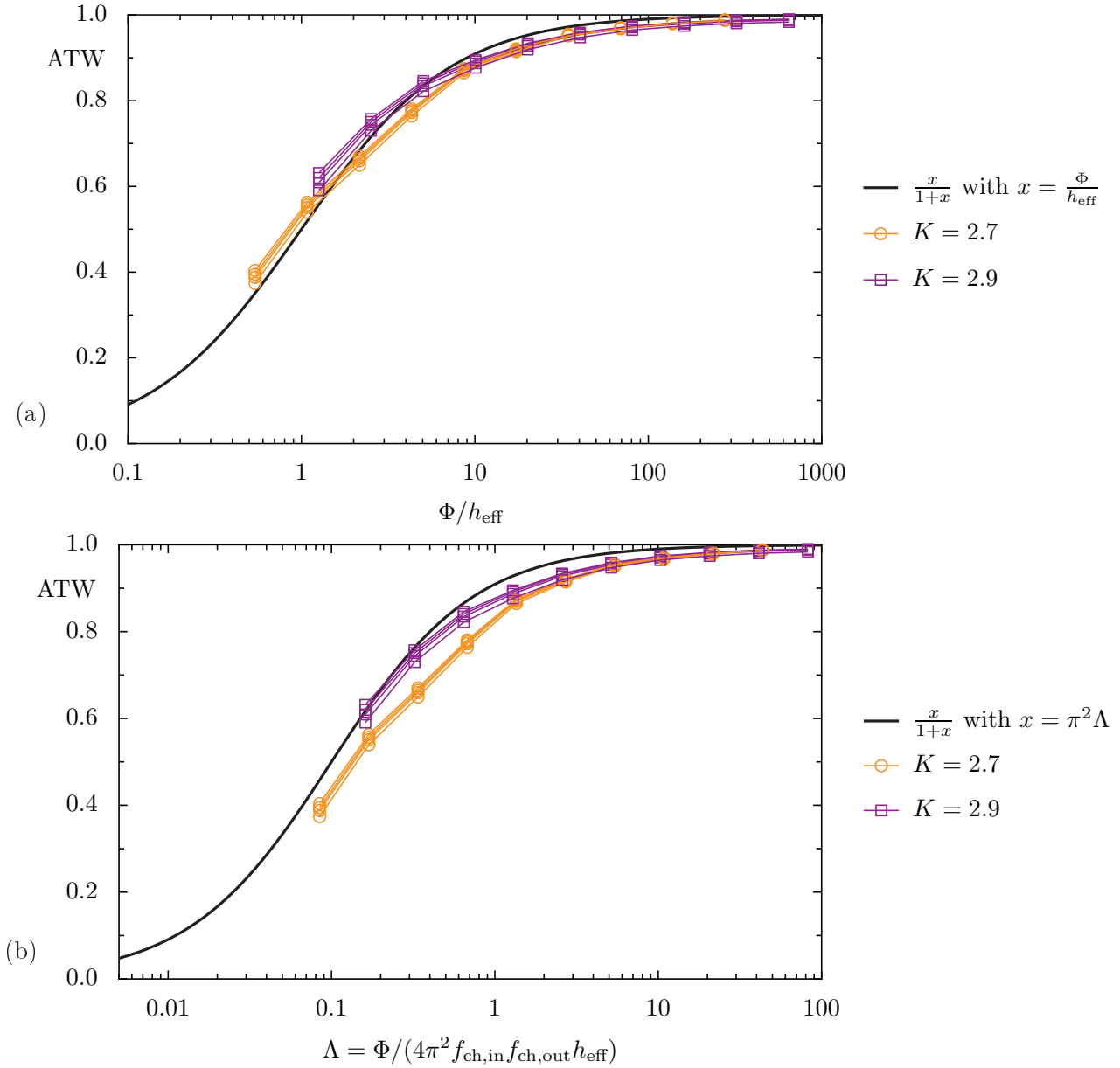
**Figure 3.32:** ATW using the Husimi weight in the transmission region for the standard map with $K = 2.7$ and $K = 2.9$ as a function of the ratio $\Phi/h_{\text{eff}}$ in (a) and the parameter $\Lambda$ in (b). The data is averaged over 15 initial conditions placed outside the partial barrier, 10 values of the Bloch phase $\theta_p$, and 100 steps after time $10^6$. The total number of states are $N = 1/h_{\text{eff}} = 100, 200, ..., 51200$.

for small $N = 1/h_{\text{eff}}$ compared to the ATW. Similar results have been obtained for the map $F_{\text{pb,rot}}$, see Fig. 3.22 in Sec. 3.3.4. We attribute this difference to states localized close to or even on the stable and unstable manifold forming the partial barrier or to scars localized on the hyperbolic orbit [60]. Their contribution to the average product measure is determined by the choice of the measuring region and does not originate from the coupling induced by the partial barrier. Figure 3.34 shows the distribution of the product measure $d(M)$ for the standard map
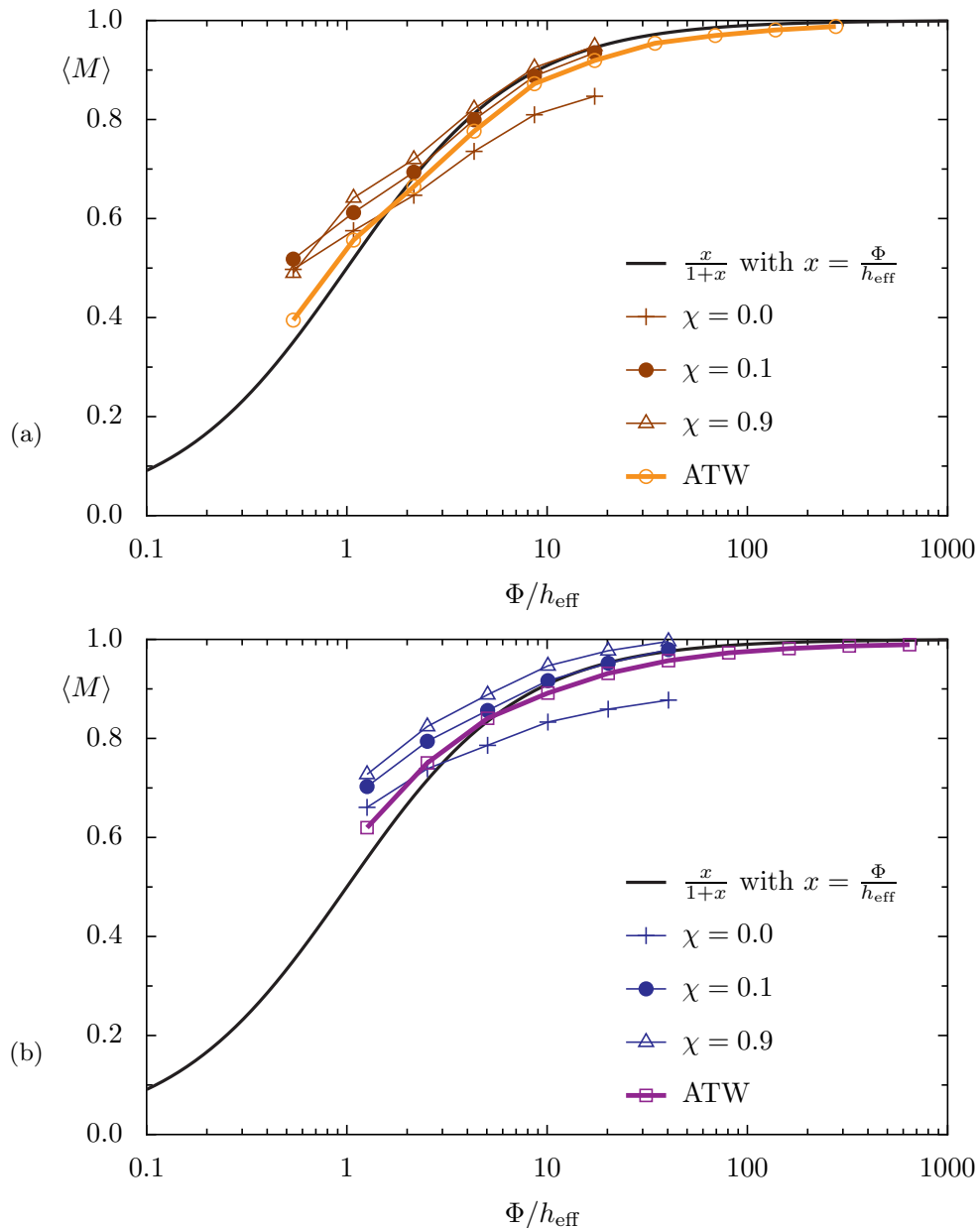
**Figure 3.33:** Average product measure for the standard map at (a) $K = 2.7$ and (b) $K = 2.9$. We consider partial barrier (a) of Fig. 3.30 for the determination of the Husimi weights. The minimal measure $\chi$ according to Eq. (3.117) is varied and thereby different selections of eigenstates contributing to $\langle M \rangle$ are obtained. The data is averaged over 100 values of the Bloch phase $\theta_p$. The ATW of Fig. 3.32 is shown for comparison.

with $K = 2.7$ and $K = 2.9$. For large ratios $\Phi/h_{\text{eff}}$ the peak of the distribution approaches $M = 1$, which corresponds to states uniformly distributed in the whole chaotic region.

Note that for the standard map, similar to Sec. 3.1.7 for the map $F_{\text{pb}}$, we introduced phase-space drilling in order to destroy the chain of regular islands inside the partial barrier. We place one circle of the rotation on top of each island of the period four island chain such that orbits started inside these islands are mapped into the chaotic region. The parameters of the rotation
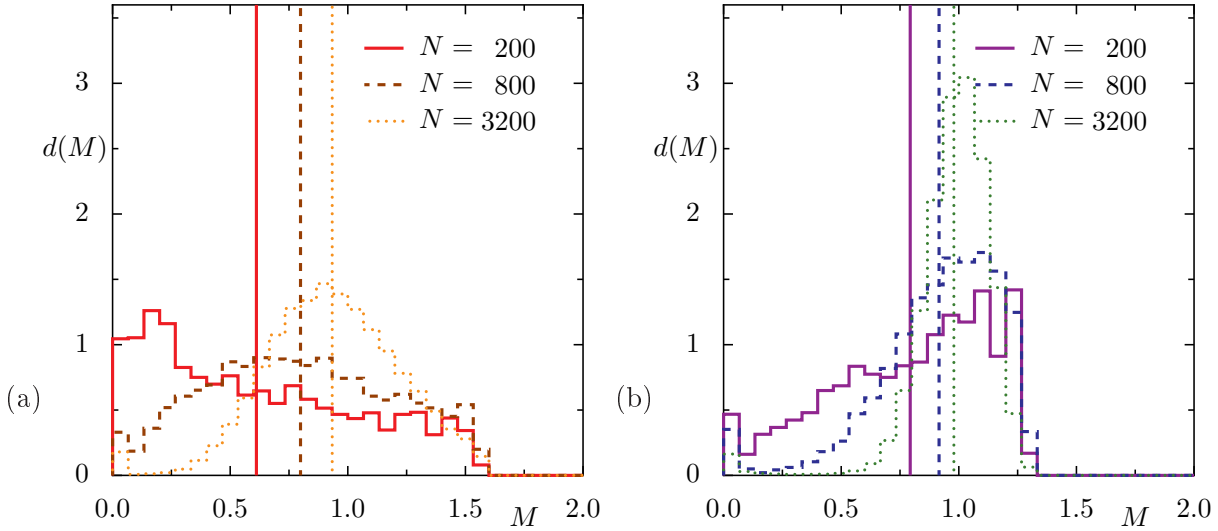
**Figure 3.34:** Distribution $d(M)$ of the product measure $M$ for the standard map with (a) $K = 2.7$ and (b) $K = 2.9$. The data is the same as for Fig. 3.33 for $\chi = 0.1$. The corresponding ratios $\Phi/h_{\mathrm{eff}}$ are approximately 1, 4, 16 for (a) and 2, 8, 32 for (b).

can be chosen such that there remain no regular tori. Quantum mechanically, however, the resulting transitional behavior of the partial barrier is almost unchanged.

Finally, we compare the results for the standard map to the results for the designed map $F_{\mathrm{pb,rot}}$ of Sec. 3.3.4 using the Husimi weight for the symmetric case ($f_{\mathrm{up}} = f_{\mathrm{lo}} = \frac{1}{2}$) in Fig. 3.35.
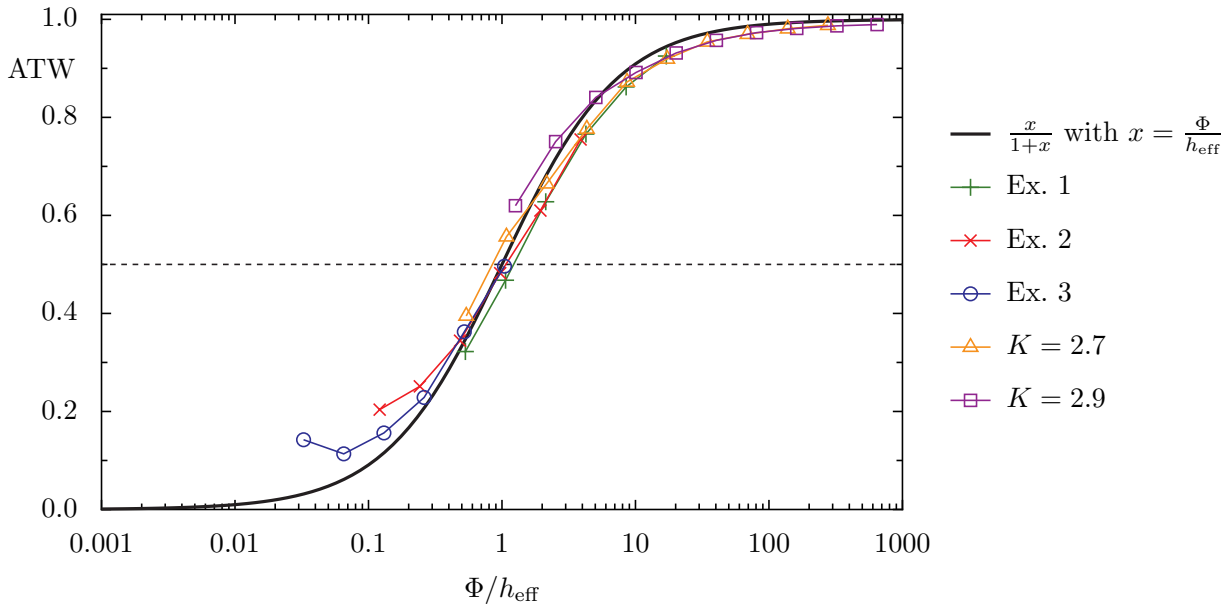


**Figure 3.35:** ATW using the Husimi weight for the examples 1, 2, and 3 of the map $F_{\mathrm{pb,rot}}$ with $f_{\mathrm{up}} = f_{\mathrm{lo}} = \frac{1}{2}$ (same as Fig. 3.22) in comparison to the result of the two examples of the standard map. The standard map data is the same as in Fig. 3.32 using the partial barrier (a) of Fig. 3.30.

Although for the standard map the inner chaotic region exhibits a hierarchical structure the constructed partial barrier is dominant and we a find transitional behavior similar to the map $F_{\mathrm{pb,rot}}$ with one partial barrier. This implies a universal behavior of the quantum transition of a partial barrier independent of the considered example system.

# 4 Modeling approaches

After we quantified the quantum transition of a partial barrier between quantum suppression and classical transport behavior, we now describe this transition in terms of matrix models in order to get a deeper insight into the impact of the partial barrier on the quantum system. The first model is a two-site model (Sec. 4.1), where the upper and the lower chaotic region are described by one site. In Sec. 4.2 we review the random matrix model, which is proposed by Bohigas, Tomsovic, and Ullmo [23], and discuss our quantitative measures. As this model does not describe the data of the designed maps $F_{\mathrm{pb}}$ and $F_{\mathrm{pb,rot}}$, we introduce a more sophisticated coupling in Sec. 4.3. We mention unitary modeling approaches in Sec. 4.4 and summarize our findings in Sec. 4.5.

## 4.1 Deterministic $2 \times 2$ model

In order to describe the transition from two uncoupled chaotic systems, where the partial barrier acts as a barrier, to one large system, where the partial barrier is transparent, we propose a simple $2 \times 2$ matrix model. Namely, we consider an avoided crossing, which is described by the Hamiltonian

$$H = \begin{pmatrix} E_0 + \Delta/2 & v \\ v & E_0 - \Delta/2 \end{pmatrix} \tag{4.1}$$

with the energy offset $E_0$, the level spacing $\Delta$, and the coupling $v$. The eigenenergies follow as

$$E_\pm = E_0 \pm \sqrt{\left(\frac{\Delta}{2}\right)^2 + v^2} \tag{4.2}$$

and are plotted in Fig. 4.1 as a function of $\Delta$. For vanishing coupling, $v = 0$, the eigenenergies $E_\pm$ cross at $\Delta = 0$ (dashed lines in Fig. 4.1), whereas nonzero coupling yields an enhanced splitting, which gives rise to an avoided crossing between the two eigenenergies. The impact of the coupling $v$ is most prominent at $\Delta = 0$ and determines the minimal splitting $2 \cdot |v|$. Far away from the crossing, $E_\pm$ approach the values of the uncoupled eigenenergies and therefore the coupling of the two sites is negligible. This limit corresponds to the quantum suppression of a partial barrier, because the two levels behave independently. At the energy crossing, however, the two levels are strongly coupled, which corresponds to the limit of the classical transport, because the two levels cannot be treated independently.
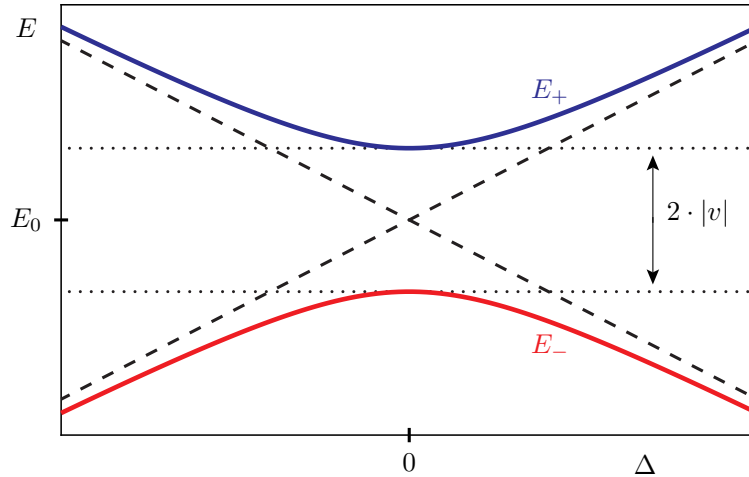
**Figure 4.1:** Eigenenergies $E_\pm$ of the deterministic $2 \times 2$ model, defined by Eq. (4.1), as a function of the uncoupled mean level spacing $\Delta$. The eigenenergies $E_\pm$ are given by Eq. (4.2) and perform an avoided crossing. The eigenenergies for vanishing coupling, $v = 0$, are shown as dashed lines and cross at $\Delta = 0$. The minimal splitting of the avoided crossing $[E_+ - E_-](\Delta = 0)$ is determined by the coupling $v$, which is indicated by the dotted lines and the arrow.

By measuring energy in multiples of the level spacing of the uncoupled system $\Delta$, we obtain

$$\varepsilon_\pm = \frac{E_\pm}{\Delta} = \varepsilon_0 \pm \sqrt{\frac{1}{4} + \lambda^2}, \tag{4.3}$$

where $\lambda := v/\Delta$ is the scaling parameter, which measures the coupling strength relative to the level spacing. The ensemble average over $\lambda^2$ would give the scaling parameter $\Lambda$ introduced in Sec. 3.2.2. We set the energy offset $E_0$ and therefore $\varepsilon_0$ to zero, because properties of eigenstates are independent of this offset. Using the scaling parameter $\lambda$ the problem is equivalent to

$$H^{\text{reduced}} = \begin{pmatrix} \frac{1}{2} & \lambda \\ \lambda & -\frac{1}{2} \end{pmatrix}, \tag{4.4}$$

which captures all universal features of the above model.

For vanishing coupling strength $v = 0$, or equivalently $\lambda = 0$ for finite $\Delta$, the eigenenergies are $\varepsilon_\pm = \pm\frac{1}{2}$ and the eigenvectors are

$$\eta_+(\lambda = 0) = \begin{pmatrix} 1 \\ 0 \end{pmatrix} \qquad \text{and} \qquad \eta_-(\lambda = 0) = \begin{pmatrix} 0 \\ 1 \end{pmatrix}. \tag{4.5}$$

As we increase the coupling the eigenvectors $\eta_\pm$ get admixtures in the other component. They

are given by

$$\eta_+ = \frac{1}{\sqrt{2\left(1+4\lambda^2+\sqrt{1+4\lambda^2}\right)}}\begin{pmatrix} 1+\sqrt{1+4\lambda^2} \\ 2\lambda \end{pmatrix},$$

$$\eta_- = \frac{1}{\sqrt{2\left(1+4\lambda^2+\sqrt{1+4\lambda^2}\right)}}\begin{pmatrix} -2\lambda \\ 1+\sqrt{1+4\lambda^2} \end{pmatrix}. \tag{4.6}$$

According to Eq. (3.72) the product measure of these eigenstates is determined by

$$M[\eta_\pm] = \frac{\mu_{\mathrm{up}}[\eta_\pm]}{\mu_{\mathrm{up}}[\Psi_{\mathrm{uniform}}]}\frac{\mu_{\mathrm{lo}}[\eta_\pm]}{\mu_{\mathrm{lo}}[\Psi_{\mathrm{uniform}}]} = 4\eta_{\pm,1}^2\eta_{\pm,2}^2, \tag{4.7}$$

where the measures of the uniformly distributed state $\Psi_{\mathrm{uniform}}$ are substituted by $\frac{1}{2}$. Inserting Eq. (4.6) for the eigenstates yields

$$M[\eta_\pm] = 4\frac{(1+2\sqrt{1+4\lambda^2}+1+4\lambda^2)\cdot 4\lambda^2}{[2(1+4\lambda^2+\sqrt{1+4\lambda^2})]^2} = \frac{4\lambda^2}{1+4\lambda^2} \tag{4.8}$$

$$\approx \begin{cases} 4\lambda^2 & \text{for} \quad \lambda \to 0 \\ 1-(2\lambda)^{-2} & \text{for} \quad \lambda \to \infty. \end{cases} \tag{4.9}$$

In addition to the product measure, we consider the time evolution of the state $\psi(t=0) = (1,0)$, which is given by

$$\psi(t) = \sum_{\sigma\in\{+,-\}} \eta_\sigma \exp\{-\mathrm{i}E_\sigma t/\hbar\} \underbrace{\eta_\sigma^T \cdot \psi(t=0)}_{\eta_{\sigma,1}}. \tag{4.10}$$

The asymptotic weight in this setup is the squared lower element of the time evolved vector,

$$(\psi(t))_2 = \sum_{\sigma\in\{+,-\}} \eta_{\sigma,2}\exp\{-\mathrm{i}E_\sigma t/\hbar\}\eta_{\sigma,1} \tag{4.11}$$

$$= \eta_{+,2}\exp\{-\mathrm{i}E_+ t/\hbar\}\eta_{+,1} + \eta_{-,2}\exp\{-\mathrm{i}E_- t/\hbar\}\eta_{-,1}, \tag{4.12}$$

which can be expressed using the eigenenergies and eigenvectors (see Eqs. (4.2), (4.3), and (4.6)) by

$$(\psi(t))_2 = \frac{2\lambda\left[1+\sqrt{1+4\lambda^2}\right]}{2\left(1+4\lambda^2+\sqrt{1+4\lambda^2}\right)}\left[\exp\left\{-\mathrm{i}\frac{\Delta\sqrt{1+4\lambda^2}t}{2\hbar}\right\} - \exp\left\{+\mathrm{i}\frac{\Delta\sqrt{1+4\lambda^2}t}{2\hbar}\right\}\right] \tag{4.13}$$

$$= \frac{\lambda}{\sqrt{1+4\lambda^2}}2\mathrm{i}\sin\left[-\Delta\sqrt{1+4\lambda^2}t/(2\hbar)\right]. \tag{4.14}$$

For the transmitted weight we obtain

$$|(\psi(t))_2|^2 = \frac{4\lambda^2}{1 + 4\lambda^2} \sin^2\left[\Delta\sqrt{1 + 4\lambda^2}t/(2\hbar)\right] = M(\lambda)\sin^2\left[\Delta\sqrt{1 + 4\lambda^2}t/(2\hbar)\right], \qquad (4.15)$$

which is the result of the product measure with some additional oscillating time dependence. Averaged over one period in time the transmitted weight compared to the case without a barrier (strong coupling) is determined by the product measure

$$\text{ATW} = \frac{|(\psi(t))_2|^2}{1/2} = M(\lambda) = \frac{4\lambda^2}{1 + 4\lambda^2}. \qquad (4.16)$$

The oscillations as a function of time depend on the energy difference between the two eigenstates and are known as Rabi oscillations [52, Sec. 3.2.2]. These oscillations also arise in the time evolution of wave packets in systems with more than two eigenstates. In those cases the oscillatory behavior depends on the energy differences of all pairs of eigenfunctions. As discussed in Sec. 3.3.1 the superposition of those oscillations gives rise to a smooth averaged behavior at large times. Therefore it is meaningful to compare our findings of this simple model, Eq. (4.16), to the results for the quantum map.

In Sec. 3.3.7 we discussed that the overall behavior of the map data is well described by, Eq. (3.112),

$$\text{ATW} = \frac{\frac{\Phi}{h_{\text{eff}}}}{1 + \frac{\Phi}{h_{\text{eff}}}}. \qquad (4.17)$$

If we identify $4\lambda^2$ with the ratio $\Phi/h_{\text{eff}}$ Eqs. (4.16) and (4.17) are the same. It is plausible to assume that $\lambda^2$ is proportional to the ratio $\Phi/h_{\text{eff}}$, because both are proportional to the scaling parameter $\Lambda$. However, the prefactor 4 is a fitting parameter.

The product measure of Eq. (4.8) as a function of the parameter $\lambda$ is shown in Fig. 4.2. In analogy to Sec. 3.3.7 the product measure $M$ has a point symmetry relative to the point $(\lambda, M) = \left(\frac{1}{2}, \frac{1}{2}\right)$. That is,

$$M(\lambda) - M\left(\lambda = \frac{1}{2}\right) = M\left(\lambda = \frac{1}{2}\right) - M\left(\frac{1/2}{\lambda}\right) \qquad (4.18)$$

$$\frac{4\lambda^2}{1 + 4\lambda^2} - \frac{1}{2} = \frac{1}{2} - \frac{(2\lambda)^{-2}}{1 + (2\lambda)^{-2}} \qquad (4.19)$$

$$1 = \frac{4\lambda^2 + 1}{1 + 4\lambda^2}. \qquad (4.20)$$

In terms of the parameter $\lambda$ the total width of the transition region defined in Sec. 3.3.7, $M \in [0.1, 0.9]$, is a factor of 9 (see Fig. 4.2).
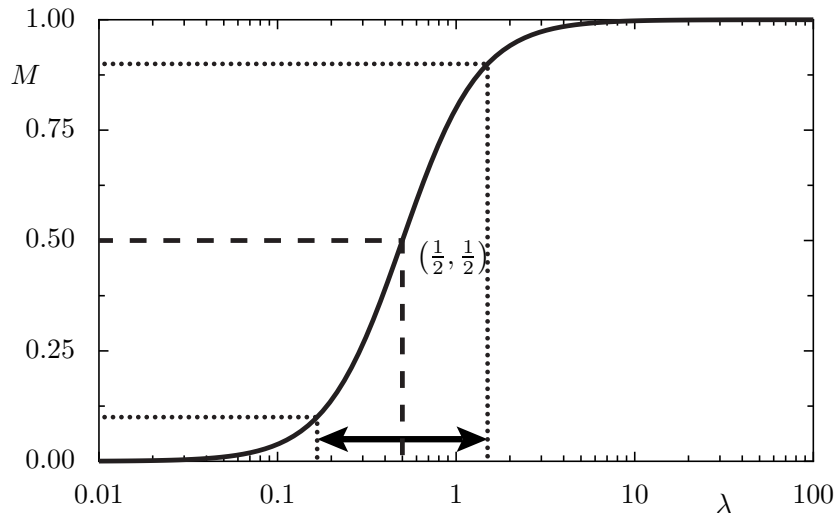
**Figure 4.2:** Product measure $M$ for the deterministic $2 \times 2$ model, Eq. (4.4), as a function of the scaling parameter $\lambda = v/\Delta$. $M$ fulfills an inversion symmetry with respect to $\left(\frac{1}{2}, \frac{1}{2}\right)$. The dotted lines and the arrow indicate the transition width if we consider anything between 10% and 90% as the transition region.

Although the approximation of the quantum map by a two site system is quite crude, this deterministic $2 \times 2$ model, Eq. (4.4), yields an excellent description of the numerical data describing the transition from quantum suppression to classical transport (see Fig. 3.28 in Sec. 3.3.7).

## 4.2 BTU matrix model

In 1993 Bohigas, Tomsovic, and Ullmo proposed a matrix model to describe the impact of partial barriers on the quantum system (BTU model) [23, 66]. The main idea of the model is to describe the transition from quantum suppression to classical transport by modeling two chaotic sub-systems, that are coupled.

In order to set up this matrix model, we need to model a chaotic region in terms of random matrix theory: In the 1960's it was found that spectral statistics of nuclei energies have universal properties, which can be modeled by suitable random matrix ensembles [67]. These matrix ensembles describe the universal properties of fully chaotic systems, which was conjectured by Bohigas, Giannoni, and Schmit in 1984 [68]. For the case of time reversal invariant systems the universal behavior is given by the Gaussian orthogonal ensemble (GOE). As all systems considered in this thesis obey time reversal invariance, we restrict ourselves to discuss this ensemble. More details can be found in Ref. [67].

For the matrix elements $H_{ij}$ in the case of the GOE ensemble one uses Gaussian random

variables with vanishing mean value and variances given by

$$\langle H_{ii}^2 \rangle = \frac{1}{2A}, \tag{4.21}$$

$$\langle H_{ij}^2 \rangle = \frac{1}{4A} \qquad \text{for } i \neq j \tag{4.22}$$

with some free parameter $A$ fixing the energy scale. This yields a density of states $\rho(E)$, whose smooth part is described by Wigner's semicircle law (see Ref. [67, Sec. 4.2] and Fig. 4.3)

$$\rho_{\text{Wig}}(E) = \begin{cases} \frac{2}{\pi} \sqrt{N \cdot A} \sqrt{1 - \left( \dfrac{E}{\sqrt{N/A}} \right)^2} & \text{for } |E| \leq \sqrt{\frac{N}{A}} \\ 0 & \text{otherwise.} \end{cases} \tag{4.23}$$

In the BTU matrix model two of these GOE matrices are used for the description of the two chaotic regions above and below the partial barrier. These matrix blocks are coupled via some coupling matrix, which depends on the ratio of classical flux $\Phi$ and Planck's constant $h_{\text{eff}}$,

$$H = \begin{pmatrix} \boxed{\begin{matrix} \textbf{GOE} & \frac{\Phi}{h_{\text{eff}}} \\ \frac{\Phi}{h_{\text{eff}}} & \textbf{GOE} \end{matrix}} \end{pmatrix}. \tag{4.24}$$
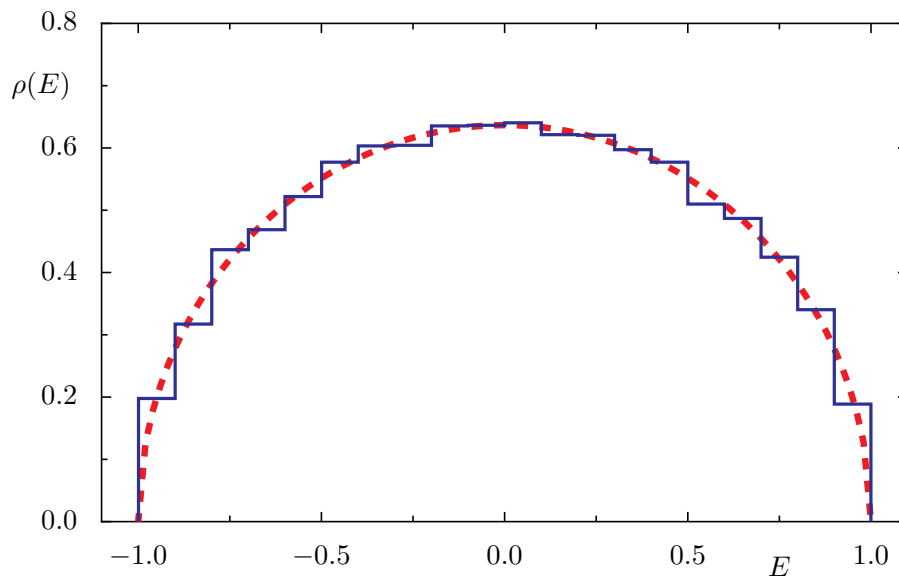


**Figure 4.3:** Density of states $\rho(E)$ for an ensemble of 100 GOE matrices of size $N \times N$ (blue histogram), where we choose $N = 100$ and the parameter $A = N$ for Eqs. (4.21) and (4.22). The histogram is in agreement with the Wigner semicircle law of Eq. (4.23), which is shown as a red dashed line.

The limiting cases of this BTU model are two uncoupled GOE sub-matrices and one large GOE matrix

$$
H = \begin{pmatrix} \boxed{\textbf{GOE}} & 0 \\ 0 & \boxed{\textbf{GOE}} \end{pmatrix} \quad \text{and} \quad H = \begin{pmatrix} \boxed{\textbf{GOE}} \end{pmatrix}, \tag{4.25}
$$

which correspond to vanishing and large classical flux $\Phi$, respectively. For small classical flux the partial barrier acts as a quantum barrier giving rise to quantum suppression and thereby uncoupled sub-systems. In the case of a large classical flux, $\Phi \gg h_{\text{eff}}$, the partial barrier has no effect on the quantum system and is negligible. Hence the whole system can be treated as one chaotic region.

A matrix model similar to Eq. (4.24) was originally introduced by Rosenzweig and Porter in 1960 in order to describe symmetry breaking in atomic level spectra [40]. Additional forces, which do not commute with the symmetry of the system yield a breakdown of the block structure and induce couplings between formerly independent levels. Since this time the model has been applied for qualitative and quantitative descriptions of symmetry breaking in various systems [69–76]. The symmetry operator for the situation with a partial barrier is

$$
\mathcal{S} = \mathcal{P}_{\text{up}} - \mathcal{P}_{\text{lo}} \tag{4.26}
$$

with the projection operators $\mathcal{P}_{\text{up}}$ and $\mathcal{P}_{\text{lo}}$ on the fictitious upper and lower sub-spaces. States localized in the upper chaotic region are eigenstates of $\mathcal{S}$ with eigenvalue $+1$ because such states are eigenstates of $\mathcal{P}_{\text{up}}$ with eigenvalue 1 and $\mathcal{P}_{\text{lo}}$ with eigenvalue 0. In analogy states localized in the lower chaotic region are eigenstates of $\mathcal{S}$ with eigenvalue $-1$. This classification of states fails in the case of non-vanishing transport between the two regions, because the eigenstates of the quantum map will have admixtures in the respective other region.

The relevant parameter in the random matrix transition is the scaling parameter, Ref. [23, Eq. (5.25)],

$$
\Lambda_{jk} = \frac{v_{jk}^2}{D^2} \,, \tag{4.27}
$$

where the local mean level spacing

$$
D = \frac{1}{\bar{\rho}(E)} \tag{4.28}
$$

is the inverse of the local mean density of states and the average matrix element $v_{jk}$ of the

coupling matrix $H_1$ is

$$v_{jk}^2 = \overline{|\langle j\alpha|H_1|k\beta\rangle|^2}. \tag{4.29}$$

Here the right hand side is averaged over all states $\alpha$ in region $j$ and all states $\beta$ in region $k$ (see Ref. [23, p. 99 ff.]). The matrix elements of $H_1$ for the BTU model are Gaussian distributed random variables with zero mean and variance $v_{jk}^2$.

In case of only two regions we drop the subscript of the scaling parameter and use $\Lambda_{jk} = \Lambda$ to describe the transition in the matrix model. The square root of the scaling parameter corresponds to the root-mean-square coupling in multiples of the mean level spacing

$$\sqrt{\Lambda} = \frac{\sqrt{v^2}}{D}. \tag{4.30}$$

It measures the strength of the coupling on the scale of the mean level spacing.

According to Ref. [23] this scaling parameter needs to be compared with the classical flux (see Eq. (5.26) in Ref. [23] for $d = 2$)

$$\Lambda = \frac{1}{4\pi^2 f_1 f_2} \frac{\Phi}{2\pi\hbar_{\text{eff}}} = \frac{\Phi}{\pi^2 h_{\text{eff}}}, \tag{4.31}$$

where in the last step it was assumed that the upper and the lower region are equal in size $f_1 = f_2 = \frac{1}{2}$. Equation (4.31) is the same as the $\Lambda$-flux relation for maps derived in Sec. 3.2.2.

In Sec. 4.2.1 the BTU matrix model with GOE blocks of equal size is discussed. That is, the model describes a phase space, where the upper and the lower region have equal size. The case of different block sizes is discussed in Sec. 4.2.2 and very good agreement with the result of the matrix model with equal block size is found. The equivalence of the ATW and the average product measure is explained in Sec. 4.2.3 and finally the results are compared to the map data in Sec. 4.2.4.

## 4.2.1  GOE blocks of equal size

The simplest case for a random matrix transition in the ensemble described above is the case of two GOE blocks of equal size $N_{\text{up}} = N_{\text{lo}}$. The upper left and lower right blocks of Eq. (4.24) are GOE matrices, whose elements are Gaussian random variables with zero mean and variances given by Eqs. (4.21) and (4.22). For the coupling blocks we choose

$$v^2 = \sigma_{\text{coupl}}^2 \langle H_{ij}^2 \rangle = \frac{\sigma_{\text{coupl}}^2}{4A}, \tag{4.32}$$

which provides the limit of two uncoupled GOEs for $\sigma_{\text{coupl}} = 0$ and the limit of one large GOE for $\sigma_{\text{coupl}} = 1$. The prefactor $\sigma_{\text{coupl}}$ in the coupling blocks is the only difference in comparison

to setting up a large GOE matrix.

In the evaluation of the matrix model we restrict ourselves to states with energies around zero in order to ensure a fixed mean level spacing for all of them. This is needed in order to detect universal features independent of variations of the mean level spacing as a function of the energy (see Fig. 4.3). According to Eq. (4.23) we obtain for the uncorrelated superposition of two GOE matrices of size $N_{\mathrm{up}}$

$$\rho(E = 0) = 2 \cdot \frac{2}{\pi} \sqrt{N_{\mathrm{up}} \cdot A}. \tag{4.33}$$

The scaling parameter follows as

$$\Lambda = \frac{v^2}{D^2} = v^2 \rho^2(E = 0) \tag{4.34}$$

$$= \frac{\sigma_{\mathrm{coupl}}^2}{4A} \frac{16 N_{\mathrm{up}} A}{\pi^2} = \frac{4 N_{\mathrm{up}} \sigma_{\mathrm{coupl}}^2}{\pi^2}. \tag{4.35}$$

Note that the scaling parameter $\Lambda$ does not depend on the choice of the energy scale $A$, but only on the choice of the coupling strength $\sigma_{\mathrm{coupl}}$ and the matrix size $N_{\mathrm{up}}$.

For each coupling strength we determine the eigenvectors of the random matrix and compute their product measure with Eq. (3.72),

$$M[\phi] = \frac{\mu_{\mathrm{up}}[\phi]}{\mu_{\mathrm{up}}[\Psi_{\mathrm{uniform}}]} \frac{\mu_{\mathrm{lo}}[\phi]}{\mu_{\mathrm{lo}}[\Psi_{\mathrm{uniform}}]}, \tag{4.36}$$

which simplifies to

$$M[\phi] = 4\mu_{\mathrm{up}}[\phi]\mu_{\mathrm{lo}}[\phi] = 4\mu_{\mathrm{up}}[\phi](1 - \mu_{\mathrm{up}}[\phi]) \tag{4.37}$$

for the case of two sub-systems of equal size $N_{\mathrm{up}} = N_{\mathrm{lo}}$, because the uniformly distributed state $\Psi_{\mathrm{uniform}}$ has measure $\frac{1}{2}$ in each region.

In Fig. 4.4 we show the resulting product measure averaged over all eigenstates with energy close to zero (we use 10% of the states) as a function of the scaling parameter. The results for different matrix sizes $N_{\mathrm{up}}$ nicely fall on top of each other. That is, universal behavior is found. The results for the matrix model are compared to the perturbative expression for the ATW derived in Ref. [23, p. 113–115],

$$\mathrm{ATW} \equiv \frac{\Delta_k^j}{f_k} \simeq \sqrt{2\pi\Lambda}. \tag{4.38}$$

We find very good agreement between the random matrix results and the perturbative expression up to $\Lambda = 10^{-2}$ (see Fig. 4.4(b)).

Furthermore, the overall behavior of the average product measure for the BTU matrix model
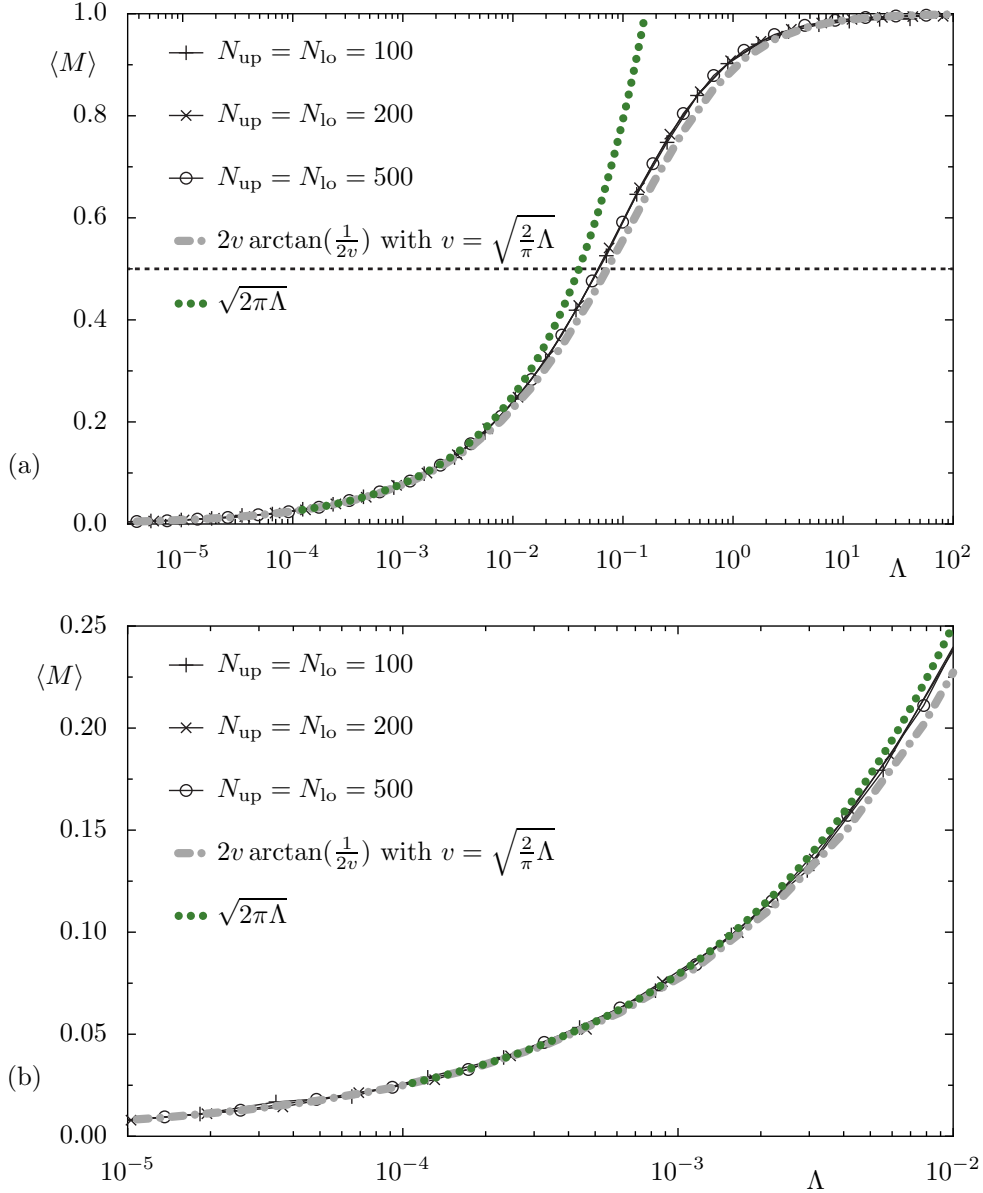
**Figure 4.4:** Average product measure $\langle M \rangle$ for the BTU model of equal size as a function of the scaling parameter $\Lambda$. The data is determined from 1000 matrices with $N_{\text{up}} = N_{\text{lo}} = 100$, 200, and 500. For the average 10% of the states around $E = 0$ are used. The overall behavior of the data is well described by a $2 \times 2$-model description derived in the context of flooding [39]: $2v \arctan \frac{1}{2v}$ (gray dash-dotted line, see also Eq. (4.41)). The effective coupling strength is $v = \sqrt{2\Lambda/\pi}$. Moreover we compare to the perturbative result $\sqrt{2\pi\Lambda}$ [23] (green dotted line). Picture (b) magnifies (a) in the perturbative regime.

is reasonably well described by the $2 \times 2$-model, introduced by Bittrich in his PhD thesis [39, Sec. 3.3.3] in the context of flooding of the regular island by chaotic states. It describes the tunneling coupling between regular and chaotic states. While classically regular and chaotic regions are separated, this coupling yields eigenstates with strong admixtures in both of the classical regions. This is similar to the case of our interest, where due to the coupling chaotic

eigenstates get admixtures in the uncoupled region if quantum transport across the partial barrier is allowed. The $2 \times 2$ random matrix model is given by the Hamiltonian

$$H = \begin{pmatrix} \kappa & v \\ v & -\kappa \end{pmatrix} \text{ for } \kappa \in \left[ -\tfrac{1}{2}, \tfrac{1}{2} \right], \tag{4.39}$$

which is determined by the mean level spacing $2\kappa$ and the effective coupling $v > 0$. The ensemble average is performed by an average over $\kappa$.

If we use the results derived in Sec. 4.1 for the product measure we have to average Eq. (4.8) with $\lambda = v/(2\kappa)$,

$$M(v, \kappa) = \frac{(v/\kappa)^2}{1 + (v/\kappa)^2} = \frac{1}{1 + (\kappa/v)^2}, \tag{4.40}$$

over $\kappa$, which yields

$$\langle M(v, \kappa) \rangle_\kappa = 2v \arctan \frac{1}{2v}. \tag{4.41}$$

For small couplings $\langle M(v, \kappa) \rangle_\kappa$ is linear in the effective coupling $v$ and for large $v$ it approaches one, which corresponds to the case without a barrier,

$$\langle M(v, \kappa) \rangle_\kappa \approx \begin{cases} 2v \cdot \frac{\pi}{2} = \pi v & \text{for} \quad v \ll 1 \\ 2v \cdot \left( \frac{1}{2v} - \frac{1}{3(2v)^3} \right) = 1 - \frac{1}{3(2v)^2} & \text{for} \quad v \gg 1. \end{cases} \tag{4.42}$$

In order to fix the effective coupling strength $v$, we compare the linear regime in $v$ to the perturbative expression of Ref. [23]

$$\frac{\Delta_k^j}{f_k} \simeq \sqrt{2\pi\Lambda} \overset{!}{=} \pi v, \tag{4.43}$$

which determines the relation of $v$ and $\Lambda$

$$v = \sqrt{\frac{2}{\pi}} \sqrt{\Lambda} \approx 0.8 \sqrt{\Lambda}. \tag{4.44}$$

The prediction of Eq. (4.41) using Eq. (4.44) is plotted in Fig. 4.4. It reasonably agrees with the average product measure of the random matrix model introduced by Bohigas, Tomsovic, and Ullmo over the full range of $\Lambda$. It seems plausible that the $2 \times 2$-model of Bittrich is valid to describe the results here. The only difference between his approach and the random matrix model is the character of the two coupled sub-spectra. Namely here we have two chaotic regions and in the case of flooding we have one chaotic and one regular sub-system. For each individual regular state the coupling elements with the chaotic states are Gaussian distributed and the

variance is fixed by its regular-to-chaotic tunneling rate. Therefore the coupling is the same in both models.

By use of this $2 \times 2$-model, we approximate the strong coupling behavior of the ATW for the BTU model. Using Eqs. (4.42) and (4.44), we derive for strong coupling $\Lambda$

$$\langle M(\Lambda, \kappa) \rangle_\kappa \approx 1 - \frac{1}{24 \cdot \Lambda/\pi} \approx 1 - \frac{1}{7.6 \cdot \Lambda}. \tag{4.45}$$

As an alternative to using full GOE matrices, one may also diagonalize a GOE matrix and use its eigenvalues on the diagonal for the upper and the lower block or even diagonalize a COE matrix and use its eigenphases for the diagonal. Both approaches yield the same results as the approach presented above and we restrict ourselves to this approach in the following.

As discussed for the designed map (see Sec. 3.3.3), the distribution of the product measure of all eigenstates is a relevant quantity. At this point we restrict ourselves to the discussion of the main features of the distribution $d(M)$ for the BTU random matrix model shown in Fig. 4.5 for various values of the scaling parameter $\Lambda = \Phi/(\pi^2 h_{\text{eff}})$, where the $\Lambda$-flux relation of Eq. (4.31) is used. For small values of the scaling parameter $\Lambda$ the distribution $d(M)$ is mainly peaked around $M = 0$, but there are already states with $M$ close to one. That is, already for small couplings some of the states are close to the state uniformly distributed in both regions. For increasing scaling parameter the peak of the distribution moves to the value $M = 1$ and almost all states are uniformly distributed for large coupling strength.
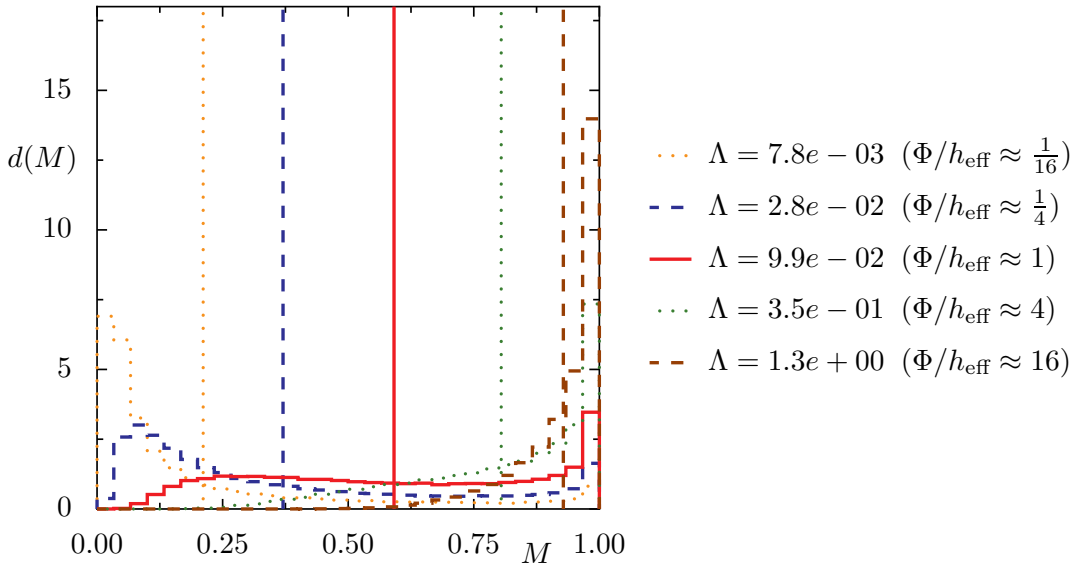


**Figure 4.5:** Distribution $d(M)$ of the product measure $M$ for the BTU model with $N_{\text{up}} = N_{\text{lo}} = 500$ using 1000 random matrices and various values of the scaling parameter. The vertical line indicates the location of the average value.

## 4.2.2 GOE blocks of different size

In this section we want to generalize the results of Sec. 4.2.1 to the case of sub-systems, which have different size. Therefore we consider the coupling of two blocks of size $N_{\text{up}} \neq N_{\text{lo}}$.

One approach is to start again with some large GOE matrix (of size $N_{\text{tot}} = N_{\text{up}} + N_{\text{lo}}$) and multiply the upper right and the lower left block – the coupling blocks – by a factor $\sigma_{\text{coupl}}$. In this case the mean level spacing of the uncorrelated superposition is given by (see Eq. (4.23))

$$\frac{1}{D} = \rho(E = 0) = \frac{2}{\pi} \left[ \sqrt{N_{\text{up}}} + \sqrt{N_{\text{lo}}} \right] \cdot \sqrt{A} \tag{4.46}$$

and the mean square coupling element is the same as in Eq. (4.32). Therefore the scaling parameter is given by

$$\Lambda = \frac{v^2}{D^2} = v^2 \rho^2(E = 0) \tag{4.47}$$

$$= \frac{\sigma_{\text{coupl}}^2}{4A} \frac{4A}{\pi^2} \left[ \sqrt{N_{\text{up}}} + \sqrt{N_{\text{lo}}} \right]^2 = \frac{\sigma_{\text{coupl}}^2}{\pi^2} \left[ \sqrt{N_{\text{up}}} + \sqrt{N_{\text{lo}}} \right]^2. \tag{4.48}$$

The product measure of Eq. (3.72)

$$M[\phi] = \frac{\mu_{\text{up}}[\phi]}{\mu_{\text{up}}[\Psi_{\text{uniform}}]} \frac{\mu_{\text{lo}}[\phi]}{\mu_{\text{lo}}[\Psi_{\text{uniform}}]}, \tag{4.49}$$
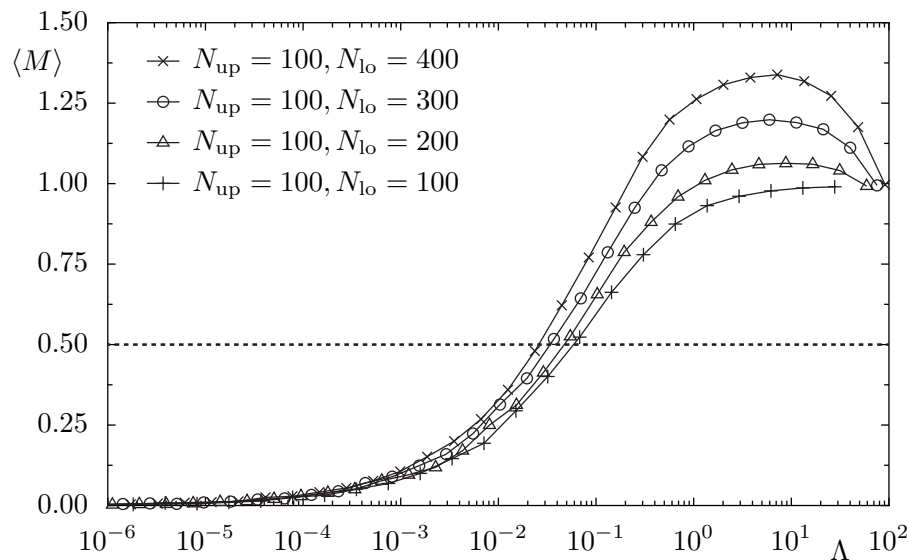


**Figure 4.6:** Average product measure $\langle M \rangle$ for the inappropriate implementation of the BTU model of different size as function of the scaling parameter $\Lambda$. All curves were averaged over 10% of the eigenstates of 100 random matrices with energy around $E = 0$. The results strongly depend on $N_{\text{lo}}$ and show non-universal behavior.

for the case of $N_{\mathrm{up}} \neq N_{\mathrm{lo}}$ obeys

$$M[\phi] = \frac{\mu_{\mathrm{up}}[\phi]}{N_{\mathrm{up}}/N_{\mathrm{tot}}} \frac{\mu_{\mathrm{lo}}[\phi]}{N_{\mathrm{lo}}/N_{\mathrm{tot}}}. \tag{4.50}$$

The resulting average product measure of this matrix model is shown in Fig. 4.7 and we find a dependence on the ratio $N_{\mathrm{lo}}/N_{\mathrm{up}}$. The results clearly deviate from the result of $N_{\mathrm{up}} = N_{\mathrm{lo}}$. For the limit of strong coupling (large $\Lambda$) the curves fall on top of each other, which is in agreement with the well defined limit of one large GOE matrix of the discussed ensemble. The deviations for different $N_{\mathrm{lo}}/N_{\mathrm{up}}$ arise due to the fact that the spectra of the uncoupled block extend over different energy ranges: $|E| \leq \sqrt{N_{\mathrm{up}}/A}$ for the upper levels and $|E| \leq \sqrt{N_{\mathrm{lo}}/A}$ for the lower levels according to Eq. (4.23).

We now correct the approach by choosing the same energy range for the upper and lower levels, which is reasonable according to Ref. [70]. In order to achieve that, different scales $A_{\mathrm{up}}$ and $A_{\mathrm{lo}}$ need to be introduced. Equal energy ranges correspond to

$$\frac{N_{\mathrm{up}}}{A_{\mathrm{up}}} = \frac{N_{\mathrm{lo}}}{A_{\mathrm{lo}}}. \tag{4.51}$$

That is, we introduce different repulsion strengths $A_{\mathrm{up}}$ and $A_{\mathrm{lo}}$ in the GOE blocks. In this case both sub-spectra contribute with their number of states to the density of states at zero energy

$$\rho(E = 0) = \frac{2}{\pi} \left[ \sqrt{N_{\mathrm{up}} \cdot A_{\mathrm{up}}} + \sqrt{N_{\mathrm{lo}} \cdot A_{\mathrm{lo}}} \right] = \frac{2}{\pi} \sqrt{\frac{A_{\mathrm{up}}}{N_{\mathrm{up}}}} \left[ N_{\mathrm{up}} + N_{\mathrm{lo}} \right] = \frac{2}{\pi} \sqrt{\frac{A_{\mathrm{up}}}{N_{\mathrm{up}}}} N_{\mathrm{tot}}. \tag{4.52}$$

This is in contrast to the density of states in Eq. (4.46), where both sub-spectra contribute with the square root of their number of states.

For the elements in the matrix model we therefore choose in the upper left block

$$\langle H_{ii}^2 \rangle = \frac{1}{2A_{\mathrm{up}}}, \tag{4.53}$$

$$\langle H_{ij}^2 \rangle = \frac{1}{4A_{\mathrm{up}}} \qquad \text{for } i \neq j \tag{4.54}$$

and in the lower right block

$$\langle H_{ii}^2 \rangle = \frac{1}{2A_{\mathrm{lo}}} = \frac{N_{\mathrm{up}}}{2N_{\mathrm{lo}}A_{\mathrm{up}}}, \tag{4.55}$$

$$\langle H_{ij}^2 \rangle = \frac{1}{4A_{\mathrm{lo}}} = \frac{N_{\mathrm{up}}}{4N_{\mathrm{lo}}A_{\mathrm{up}}} \qquad \text{for } i \neq j, \tag{4.56}$$

where $A_{\mathrm{lo}}$ is determined from $A_{\mathrm{up}}$ and the numbers of states $N_{\mathrm{up}}$ and $N_{\mathrm{lo}}$, respectively (see

Eq. (4.51)). The coupling elements are expressed relative to the upper left block, Eq. (4.54), as

$$v^2 = \sigma_{\text{coupl}}^2 \langle H_{ij}^2 \rangle = \frac{\sigma_{\text{coupl}}^2}{4A_{\text{up}}}. \tag{4.57}$$

The scaling parameter for this ensemble is

$$\Lambda = v^2 \rho^2(E = 0) \tag{4.58}$$

$$= \frac{\sigma_{\text{coupl}}^2}{4A_{\text{up}}} \frac{4}{\pi^2} \frac{A_{\text{up}}}{N_{\text{up}}} N_{\text{tot}}^2 = \frac{\sigma_{\text{coupl}}^2}{\pi^2 N_{\text{up}}} N_{\text{tot}}^2. \tag{4.59}$$

The scaling parameter is independent of the energy scale given by $A_{\text{up}}$. Note that the asymmetry of $\Lambda$ in the matrix sizes $N_{\text{up}}$ and $N_{\text{lo}}$ is due to the definition of the coupling strength $\sigma_{\text{coupl}}^2$ relative to the variance of the off-diagonal elements of the upper left block in Eq. (4.57).

   The resulting product measure of this matrix model is shown in Fig. 4.7 for several pairs $(N_{\text{up}}, N_{\text{lo}})$. We find that up to $\Lambda \approx 10$ the results for the BTU model with $N_{\text{up}} \neq N_{\text{lo}}$ (ensuring the same energy range) nicely agree with the previous results for sub-matrices of equal size. The disagreement for larger $\Lambda$ is not relevant. For increasing matrix size $N_{\text{tot}}$ this difference is moved further to the right, which indicates that for arbitrary large matrix size $N_{\text{tot}}$ the result for $N_{\text{up}} = N_{\text{lo}}$ is fully recovered. Similar effects are also mentioned in Ref. [39, Sec. 3.3.2].
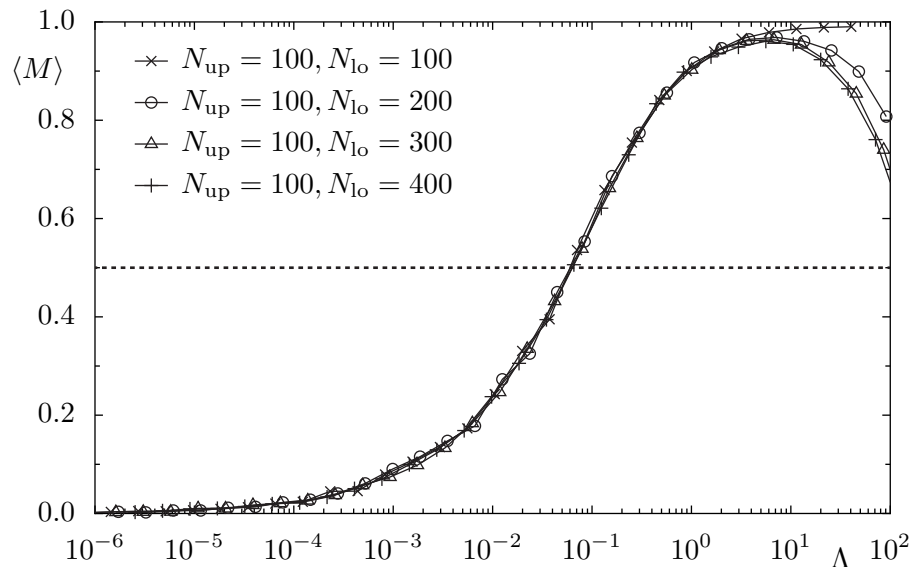


**Figure 4.7:** Average product measure $\langle M \rangle$ for the BTU model of different size $(N_{\text{up}} \neq N_{\text{lo}})$ as a function of the scaling parameter $\Lambda$. All curves were averaged over 100 realization of the random matrices. The results for different $N_{\text{lo}}$ nicely fall on top of each other. That is, universal behavior is found.

### 4.2.3  Equivalence of ATW and average product measure

Now we discuss the asymptotic transmitted weight, which is given by (see Eq. (3.52))

$$\text{ATW} \equiv \tilde{\mu}_\infty[\psi(t=0)] = \lim_{T\to\infty} \frac{1}{T} \sum_{t=0}^{T-1} \frac{\mu[\psi(t)]}{\mu[\Psi_\text{uniform}]} = \lim_{T\to\infty} \frac{1}{T} \sum_{t=0}^{T-1} \frac{\mu[\psi(t)]}{N_\mu/N_\text{tot}}. \tag{4.60}$$

The initial state $\psi(t=0)$ might be concentrated on any site $i_0$ in one of the regions, $\psi(t=0)_i = \delta_{i,i_0}$, and the measure $\mu$ is extended over the whole opposite region (either upper or lower). Therefore $N_\mu$ is either equal to $N_\text{up}$ or to $N_\text{lo}$. Following the derivation from Eq. (3.55) to Eq. (3.72) we obtain

$$\langle \tilde{\mu}_\infty[\psi(t=0)] \rangle_{\psi(t=0)} = \frac{1}{N_\text{tot}} \cdot \sum_{j=0}^{N_\text{tot}-1} \frac{\mu_\text{up}[\phi_j]}{N_\text{up}/N_\text{tot}} \frac{\mu_\text{lo}[\phi_j]}{N_\text{lo}/N_\text{tot}} = \frac{1}{N_\text{tot}} \cdot \sum_{j=0}^{N_\text{tot}-1} M[\phi_j], \tag{4.61}$$

which is an average over the product measure defined by Eq. (4.49). This is in contrast to the average product measure defined in Sec. 4.2.1, which includes only states close to $E = 0$. However, averaging over all states in the matrix model yields a meaningless quantity, because the scaling parameter strongly depends on the considered state if the mean level spacing is not fixed anymore. The average over all states would effectively include several $\Lambda$ leading to an additional average over $\Lambda$. Universal behavior can be found only as long as the averaged quantities are related to one value of the scaling parameter $\Lambda$. Hence the average in Eq. (4.61) needs to be restricted to states with fixed mean level spacing as in the previous sections (Sec. 4.2.1 and 4.2.2). This needs to be taken into account for the time evolution, too. In order to observe universal behavior the initial wave packet has to excite only states with fixed mean level spacing. We restrict ourselves in the following to averaging over the product measure, Eq. (4.61), to derive a transition curve for the ATW, which is compared to the map data.

### 4.2.4  Comparison to map data

In this section we compare the result of the BTU matrix model to the map data discussed in Sec. 3.3.3. As pointed out in Sec. 3.2.1 the mixing in phase space needs to be quick in order to compare the results with random matrix predictions. That is, the Ehrenfest time has to be small compared to the dwell time and the Heisenberg time in the quantum system. For the examples of map $F_\text{pb}$ and $F_\text{pb,rot}$ we determined the average finite time Lyapunov exponent, introduced in Sec. 2.3, and computed the Ehrenfest time according to Eq. (3.42) of Sec. 3.2.1. For the Lyapunov exponent we obtain values around two for all examples defined in Secs. 3.1.4 and 3.1.7. This yields an Ehrenfest time $t_{\text{E},i} \approx 1, ..., 2$ for $N = 1/h_\text{eff} = 100, ..., 50000$, which has to be compared with the dwell time $t_{\text{dwell},i} = 79, 346, 1284, 4100$ for example 1, 2, 3, and 4, respectively, and the Heisenberg time of the upper and lower region $t_{\text{H},i} = N_\text{up} = N_\text{lo} =$

$A_{\mathrm{ch,lo}}N \approx 0.4N$.

Figure 4.8 shows the average product measure of the map $F_{\mathrm{pb,rot}}$ of the Fig. 3.19 and additionally the resulting curve of the BTU matrix model. For large ratios $\Phi/h_{\mathrm{eff}}$ and therefore strong coupling, we find reasonable agreement between the matrix model and the map data. Both curves have a similar transition width. However, for small values of $\Phi/h_{\mathrm{eff}}$ there are clear deviations between the BTU matrix model and the map data. The BTU result overestimates the values of the quantum map.

The reason for this mismatch of the map data and the BTU matrix model could be the $\Lambda$-flux relation, Eq. (4.31). The assumption that the classical and the quantum rate are equal (see Sec. 3.2.2) is very well settled in the semiclassical regime of the partial barrier, $\Phi/h_{\mathrm{eff}} \gg 1$, but may fail in the quantum regime, where $h_{\mathrm{eff}}$ is of the same order or even larger than the classical flux $\Phi$. In Sec. 3.3.1 the transmitted weight as a function of time is discussed, but no relation of the quantum rate with the classical flux, which could replace the $\Lambda$-flux relation, is found. Therefore we will use this $\Lambda$-flux relation in the following.

Another possible reason for the mismatch of the map data and the BTU matrix model might be the overall Gaussian coupling assumed in the random matrix model. We will focus on this point in the following sections.
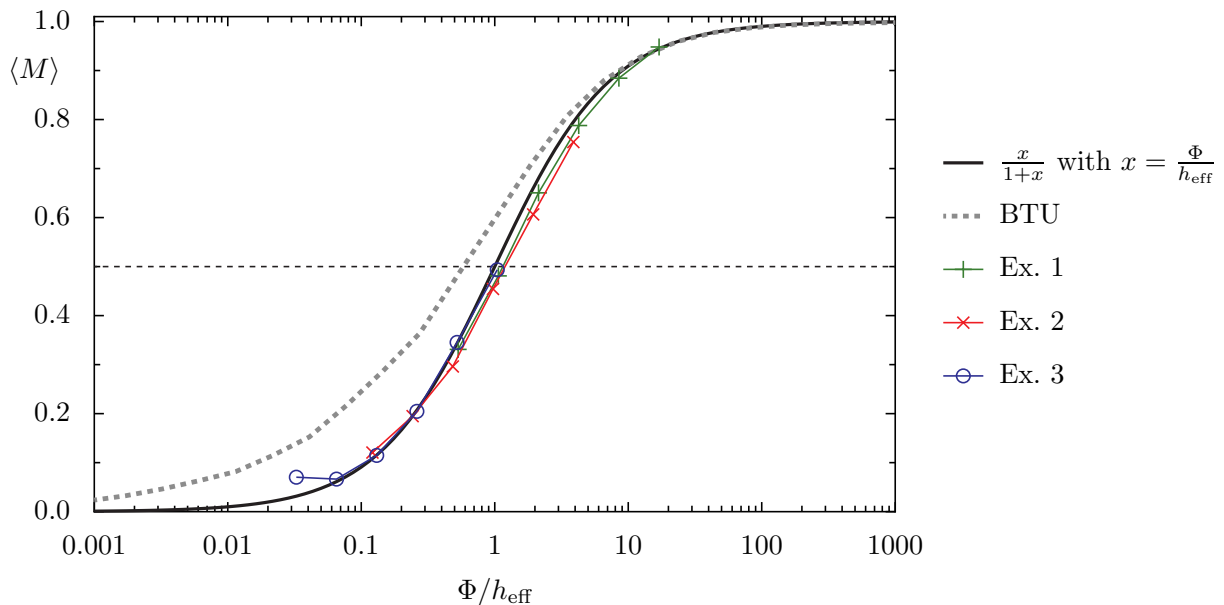


**Figure 4.8:** Average product measure $\langle M \rangle$ using the momentum measures for the examples 1, 2, and 3 of the map $F_{\mathrm{pb,rot}}$ (same as Fig. 3.19) in comparison to the result of the BTU matrix model with $\Phi/h_{\mathrm{eff}} = \pi^2 \Lambda$ (gray dashed line).

## 4.2.5  Two GOE coupled via one element

As pointed out in Sec. 4.2.4 the overall Gaussian coupling in the random matrix model proposed by Bohigas, Tomsovic, and Ullmo might be inappropriate to cover the features of a partial barrier. Hence we consider a reduction of the overall coupling to a coupling via one non-vanishing element in the coupling block only. We consider the matrix model introduced in Sec. 4.2.1 with $A = N_{\mathrm{tot}}$ and $N_{\mathrm{up}} = N_{\mathrm{lo}}$, which yields a mean level spacing of

$$D(E \approx 0) = \frac{\pi}{4\sqrt{N_{\mathrm{up}}A}} = \frac{\pi}{4\sqrt{2}N_{\mathrm{up}}} \tag{4.62}$$

around zero energy. However, this time there is only one non-vanishing coupling element in the coupling block (as well as its transposed partner to obtain a Hermitian matrix). It is chosen as a Gaussian random variable with zero mean and variance $\sigma_{\mathrm{coupl}}^2$. For the scaling parameter $\Lambda$ we find

$$\Lambda = \frac{\langle v^2 \rangle}{D^2} = \frac{\sigma_{\mathrm{coupl}}^2}{N_{\mathrm{up}}^2 D^2} = \frac{32\sigma_{\mathrm{coupl}}^2}{\pi^2}. \tag{4.63}$$

Note that the average coupling element $\langle v^2 \rangle$ is determined by averaging over all $N_{\mathrm{up}}^2$ elements of the coupling block.
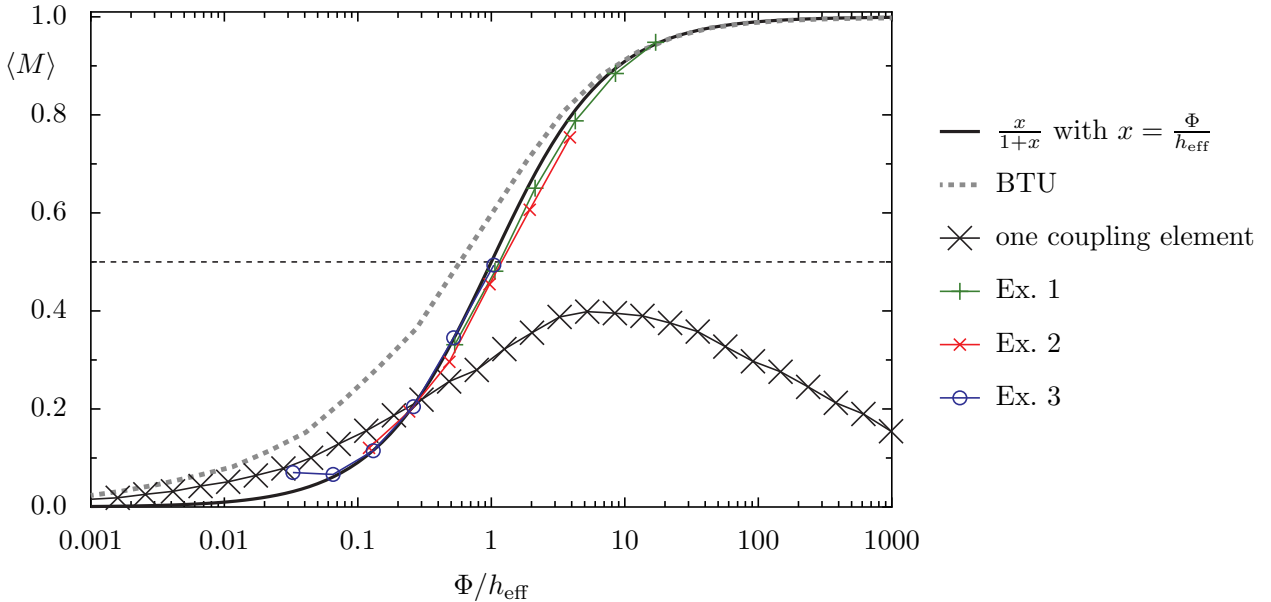


**Figure 4.9:** Average product measure $\langle M \rangle$ using the momentum measures for the examples 1, 2, and 3 of the map $F_{\mathrm{pb,rot}}$ (same as Fig. 3.19) in comparison to the result for the random matrix model, where two GOE matrices are coupled via only one matrix element with $\Phi/h_{\mathrm{eff}} = \pi^2 \Lambda$ (line with crosses). For the matrix model with one coupling element we used 10% of the eigenstates with energy around $E = 0$ of 1000 matrices with $N_{\mathrm{up}} = N_{\mathrm{lo}} = 500$. Moreover we compare to the BTU matrix model (gray dashed line) discussed in Sec. 4.2 and the result of the deterministic $2 \times 2$ model of Sec. 4.1 (black solid line).

The average product measure $\langle M \rangle$ of this matrix model is shown in Fig. 4.9. For large values of the scaling parameter $\Lambda$ the ATW decreases with increasing $\Lambda$. At this point a strong perturbation limit is reached and the modeling of the coupling of two separated regions fails. We find a clear reduction of the average product measure compared to the BTU matrix model. However, it is not appropriate to resolve the mismatch of the map data and the matrix modeling approaches discussed up to now.

## 4.3  Channel coupling

The random matrix model discussed in Sec. 4.2 uses a Gaussian coupling between all the upper and all the lower states of the uncoupled system to describe the impact of the partial barrier. From the classical point of view this seems quite unintuitive, because there is a deterministic transport from one site to the other if an orbit enters the turnstile. The coupling between the upper and the lower states happens at the bottle neck called turnstile. In analogy to this situation we consider two billiard systems, which are connected by a small channel, in which a finite number of modes $n$ can propagate. This idea is illustrated in Fig. 4.10. According to Stöckmann this situation is described by a random matrix model of the kind [77]

$$H = \begin{pmatrix} \boxed{\textbf{GOE}} & \sigma U V^T \\ \sigma V U^T & \boxed{\textbf{GOE}} \end{pmatrix}, \tag{4.64}$$

where the matrices $U$ and $V$ describe the coupling from the upper and the lower region to the channel (see Fig. 4.10) and are of size $N_{\text{up}} \times n$ and $N_{\text{lo}} \times n$, respectively. The model, Eq. (4.64),
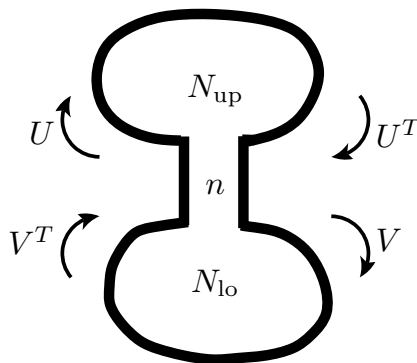


**Figure 4.10:** Illustration of the channel coupling for billiards. The matrices $V$ and $U$ express the coupling from the upper and lower billiard (with $N_{\text{up}}$ and $N_{\text{lo}}$ states) into the channel, in which $n$ modes can propagate.

is successfully applied in Ref. [75], in which the symmetry breaking in a system composed of two billiards is considered. Here the coupling between the two billiards occurs via one transverse electromagnetic mode. It is found that properties of the wave functions are different from the matrix model discussed in Sec. 4.2.

The coupling strength between the upper and the lower states is determined by the parameter $\sigma$ and we choose the matrix elements of $U$ and $V$ with zero mean $\langle U_{ij} \rangle = 0$ and unit variance $\langle U_{ij}^2 \rangle = 1$. In general $\sigma$ could be a diagonal matrix, which takes care of the individual coupling strengths ($\sigma_i \in \mathbb{R}$) for each mode

$$\sigma U V^T \to U \text{diag} \left( \sigma_1, \ldots, \sigma_n \right) V^T, \tag{4.65}$$

$$\sigma V U^T \to V \text{diag} \left( \sigma_1, \ldots, \sigma_n \right) U^T. \tag{4.66}$$

This implies knowledge about the distribution of the coupling strength to individual propagating modes. We will neglect this possibility here, but use it in Sec. 4.3.4.

The coupling blocks in Eq. (4.64), $\sigma U V^T$ and $\sigma V U^T$, are determined by $n \cdot N_{\text{up}} + n \cdot N_{\text{lo}}$ random numbers in contrast to $N_{\text{up}} \cdot N_{\text{lo}}$ random numbers in the matrix model of Sec. 4.2. During one time step all 'upper' elements of the wave function ($N_{\text{up}}$ complex numbers) are multiplied by $U^T$ and thereby give $n$ (complex) numbers. These $n$ numbers are a superposition of the former $N_{\text{up}}$ values and are redistributed onto $N_{\text{lo}}$ numbers using $V$.

To calculate the scaling parameter, we need the variance of the off-diagonal coupling

$$\sigma^2 \left\langle \left( U V^T \right)_{ij}^2 \right\rangle = \sigma^2 \left\langle \left( \sum_{l=1}^{n} u_{il} v_{jl} \right)^2 \right\rangle = \sigma^2 \left\langle \sum_{l=1}^{n} u_{il} v_{jl} \sum_{l'=1}^{n} u_{il'} v_{jl'} \right\rangle \tag{4.67}$$

$$= \sigma^2 \left\langle \sum_{l=1}^{n} u_{il}^2 v_{jl}^2 + \sum_{l \neq l'}^{n} u_{il} v_{jl} u_{il'} v_{jl'} \right\rangle. \tag{4.68}$$

The matrix elements $v_{jl}$ and $u_{il}$ are independent Gaussian random variables. Therefore they are uncorrelated and the expectation value of the product is the product of the expectation values. The same is true for the pair $(v_{jl}, v_{jl'})$ and the pair $(u_{il}, u_{il'})$ for $l \neq l'$. Because the mean values of all these random variables vanish, $\langle v_{ij} \rangle = \langle u_{ij} \rangle = 0$, the whole non-diagonal contribution vanishes. Hence, the off-diagonal coupling is

$$\sigma^2 \left\langle \left( U V^T \right)_{ij}^2 \right\rangle = \sigma^2 \sum_{l=1}^{n} \left\langle u_{il}^2 \right\rangle \cdot \left\langle v_{jl}^2 \right\rangle = n \sigma^2, \tag{4.69}$$

where in the last step it was used that $v_{jl}$ and $u_{il}$ have unit variance. Finally the scaling parameter is

$$\Lambda = \frac{n \cdot \sigma^2}{D^2} \tag{4.70}$$

with the mean level spacing $D$ of the uncorrelated superposition of the levels of the two GOE blocks. According to Eq. (4.52) the mean level spacing for $N_{\text{up}} \neq N_{\text{lo}}$ for small energies is

$$D(E \approx 0) = \frac{\pi}{2N_{\text{tot}}} \sqrt{\frac{N_{\text{up}}}{A_{\text{up}}}} = \frac{\pi}{2N_{\text{tot}}}, \tag{4.71}$$

where in the last step $A_{\text{up}} := N_{\text{up}}$ was chosen to fix the variance in the upper left block and therefore the variance in the lower left block ($A_{\text{lo}}$ follows from Eq. (4.51)).

We now discuss the results for different $\sigma$ in order to look for universal scaling behavior in this channel coupling model. Again we consider the product measure as defined by Eq. (3.72)

$$M[\phi] = \frac{\mu_{\text{up}}[\phi]}{\mu_{\text{up}}[\Psi_{\text{uniform}}]} \frac{\mu_{\text{lo}}[\phi]}{\mu_{\text{lo}}[\Psi_{\text{uniform}}]}. \tag{4.72}$$

Figure 4.11 shows the average product measure $\langle M \rangle$ for different ratios $\sigma/D$ as a function of the scaling parameter $\Lambda$. For small ratios $\sigma/D$ the results are in good agreement with the BTU model discussed in Sec. 4.2, whereas for larger ratios $\sigma/D$ the data does not scale with the parameter $\Lambda$.

According to Ref. [75] the variance $\sigma^2$ needs to be determined by system specific properties.
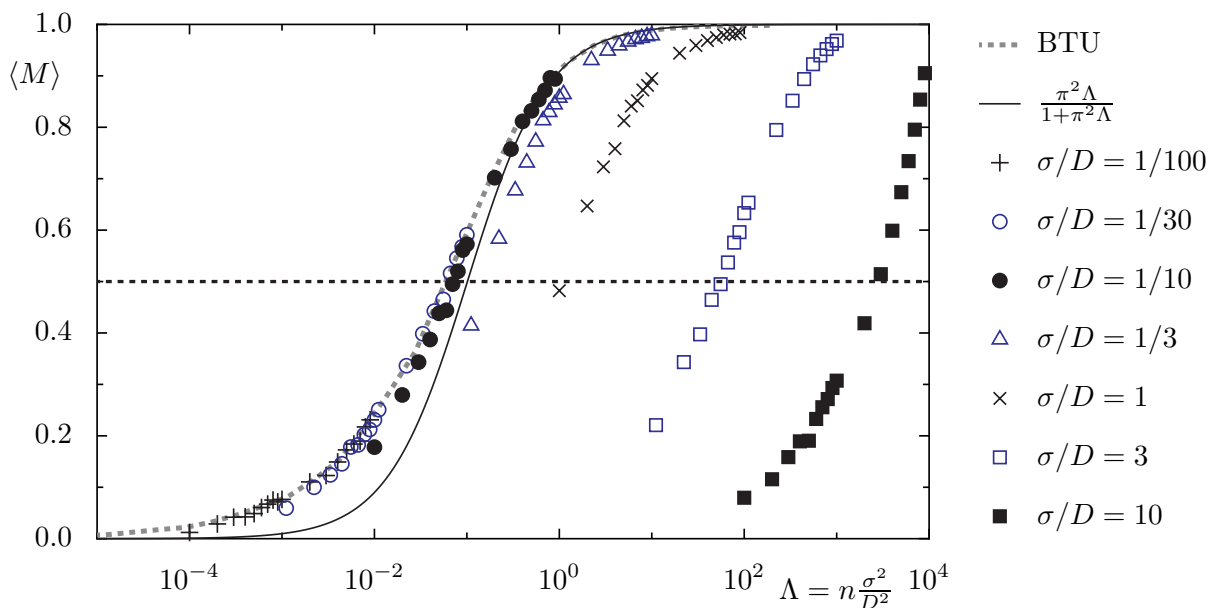


**Figure 4.11:** Average product measure $\langle M \rangle$ for the channel coupling model for several values of the ratio $\sigma/D$ (different markers). The data points are averaged over 10% of the states with energy around $E = 0$ and we used 100 matrices of size $N_{\text{up}} = N_{\text{lo}} = 100$. The results are compared to the BTU model discussed in Sec. 4.2 (dashed gray line) and the $2 \times 2$ result of Sec. 4.2.1 using $4\lambda^2 = \Phi/h_{\text{eff}} = \pi^2\Lambda$ (solid black line). We find agreement with the BTU model for small coupling variances $\sigma^2$. For larger $\sigma/D$ the the data points clearly deviate from the BTU matrix model.

That is, for a given number of transporting channels one has to deduce the scaling parameter $\Lambda$ to compute $\sigma$ for a given $D$. In order to fix the value of $\sigma$ and compare the results with the findings in the map system, we have to use the $\Lambda$-flux relation of Eq. (3.50),

$$\Lambda = \frac{1}{4\pi^2 f_{\mathrm{up}} f_{\mathrm{lo}}} \frac{\Phi}{h_{\mathrm{eff}}}, \tag{4.73}$$

and assume a relation between the number of propagating modes $n$ and the ratio $\Phi/h_{\mathrm{eff}}$. It is natural to associate $\Phi/h_{\mathrm{eff}}$ states to a phase-space area of size $\Phi$, because $1/h_{\mathrm{eff}}$ is the total number of states in the phase space of area one. Therefore we assume

$$n = \frac{\Phi}{h_{\mathrm{eff}}} \tag{4.74}$$

in the following. This is consistent with the discussion in Sec. 3.2.1, where $\Phi/h_{\mathrm{eff}}$ is associated with the number of open channels in an open system. Equations (4.70), (4.73), and (4.74) determine the coupling strength $\sigma$,

$$\sigma = \frac{D}{2\pi \sqrt{f_{\mathrm{up}} f_{\mathrm{lo}}}} = \frac{1}{4 N_{\mathrm{tot}} \sqrt{f_{\mathrm{up}} f_{\mathrm{lo}}}} = \frac{1}{4 \sqrt{N_{\mathrm{up}} N_{\mathrm{lo}}}}, \tag{4.75}$$

where in the last but one step Eq. (4.71) is used.

Fixing the value of $\sigma$ using $f_{\mathrm{up}} = f_{\mathrm{lo}} = \frac{1}{2}$,

$$\sigma = \frac{1}{2 N_{\mathrm{tot}}}, \tag{4.76}$$

and independently varying the size of the block matrices $N_{\mathrm{up}}$ and $N_{\mathrm{lo}}$ gives the data shown in Fig. 4.12. We find scaling with the parameter $\Lambda$ independent of the size of the upper and lower block $N_{\mathrm{up}}$ and $N_{\mathrm{lo}}$, respectively. Universal behavior arises for different block sizes and fixed $\sigma$. Fixing the value of $\sigma$ corresponds to associating a fixed coupling strength with each of the propagating modes, which give rise to the coupling between the two chaotic sub-systems.

The channel coupling model is limited to positive integer values of $n$ and therefore only the upper half of the transition curve can be predicted. The average product measure of the channel coupling is clearly smaller than the result of the BTU matrix model, but follows the same transitional behavior as the data of the map $F_{\mathrm{pb,rot}}$ and the deterministic $2 \times 2$ model discussed in Sec. 4.1 if we use the fitted prefactor 7 instead of $\pi^2$ (see Fig. 4.12).

Figure 4.13 shows the distribution of the product measure $d(M)$ of the individual eigenstates. As for the designed map and the BTU matrix model, the distributions perform a transition from broadly spread for $n = 1$ to a peak around $M = 1$ for large values of $n = \pi^2 \Lambda$.

We consider once again the channel coupling model with $N_{\mathrm{up}} \neq N_{\mathrm{lo}}$. In contrast to above, Eq. (4.76), we determine the coupling strength $\sigma$ according to Eq. (4.75) and thereby get
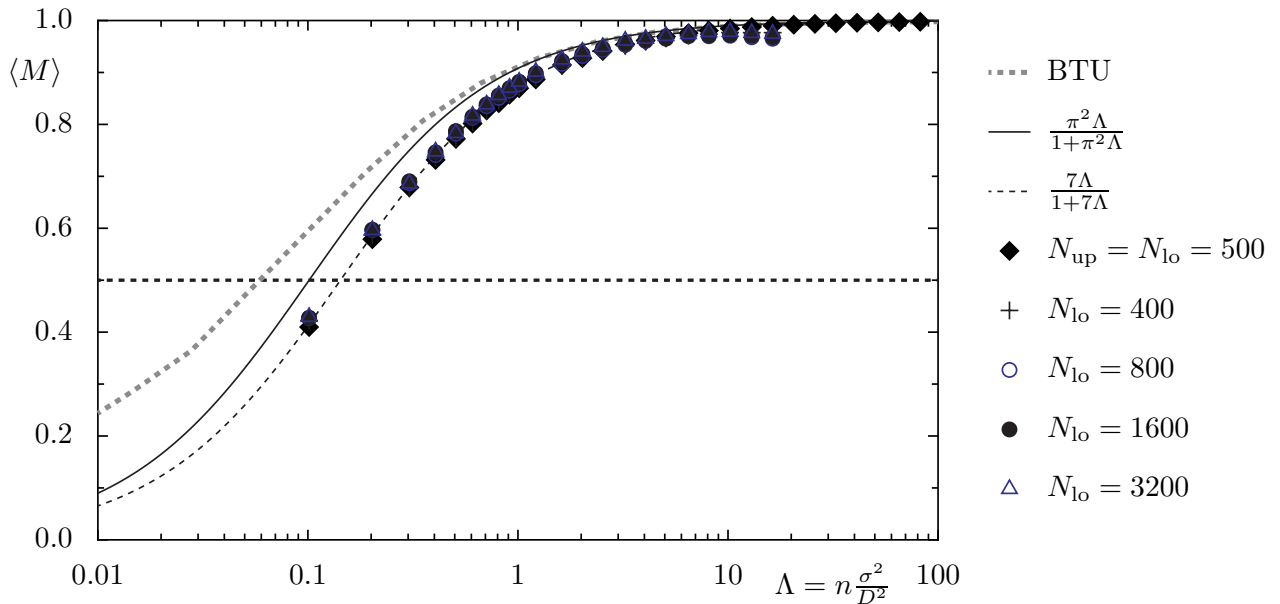
**Figure 4.12:** Average product measure $\langle M \rangle$ for the channel coupling model with $\sigma = 1/(2N_{\text{tot}})$ (Eq. (4.75) for $f_{\text{up}} = f_{\text{lo}} = 1/2$) for fixed $N_{\text{up}} = 200$ and various $N_{\text{lo}}$. The data points are averaged over 10% of the states with energy around $E = 0$ and we used 1000 random matrices. The data is compared to the BTU model shown as a thick dashed gray line. Furthermore we compare to the result of the deterministic $2 \times 2$-model discussed in Sec. 4.1 (solid black line and dashed black line with prefactor $\pi^2$ and 7).
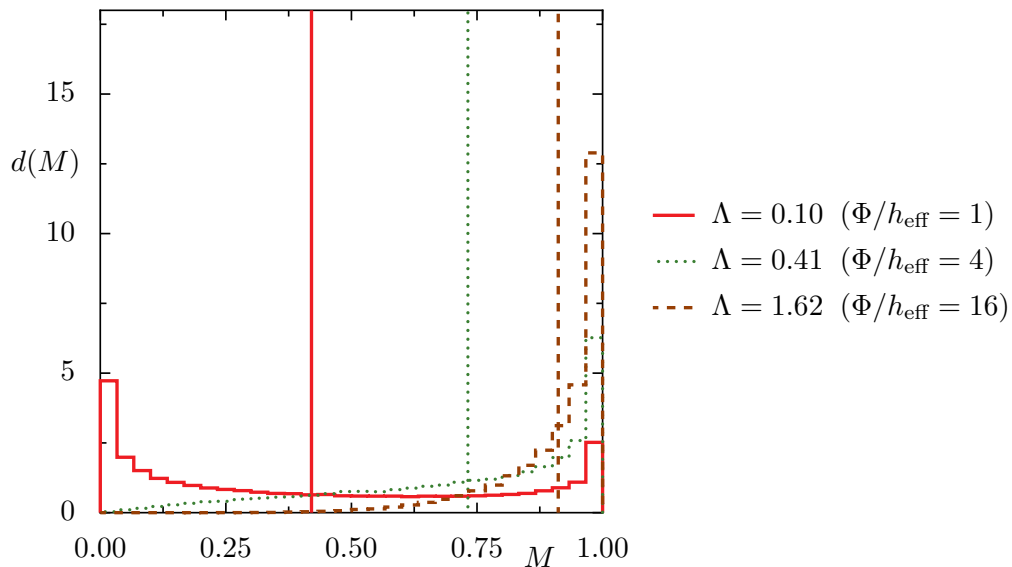


**Figure 4.13:** Distribution $d(M)$ of the product measure $M$ for the channel coupling model $N_{\text{up}} = N_{\text{lo}} = 500$ using 1000 random matrices and various values of the scaling parameter $\Lambda = \Phi/(\pi^2 h_{\text{eff}}) = n/\pi^2$. The vertical line indicates the location of the average value.
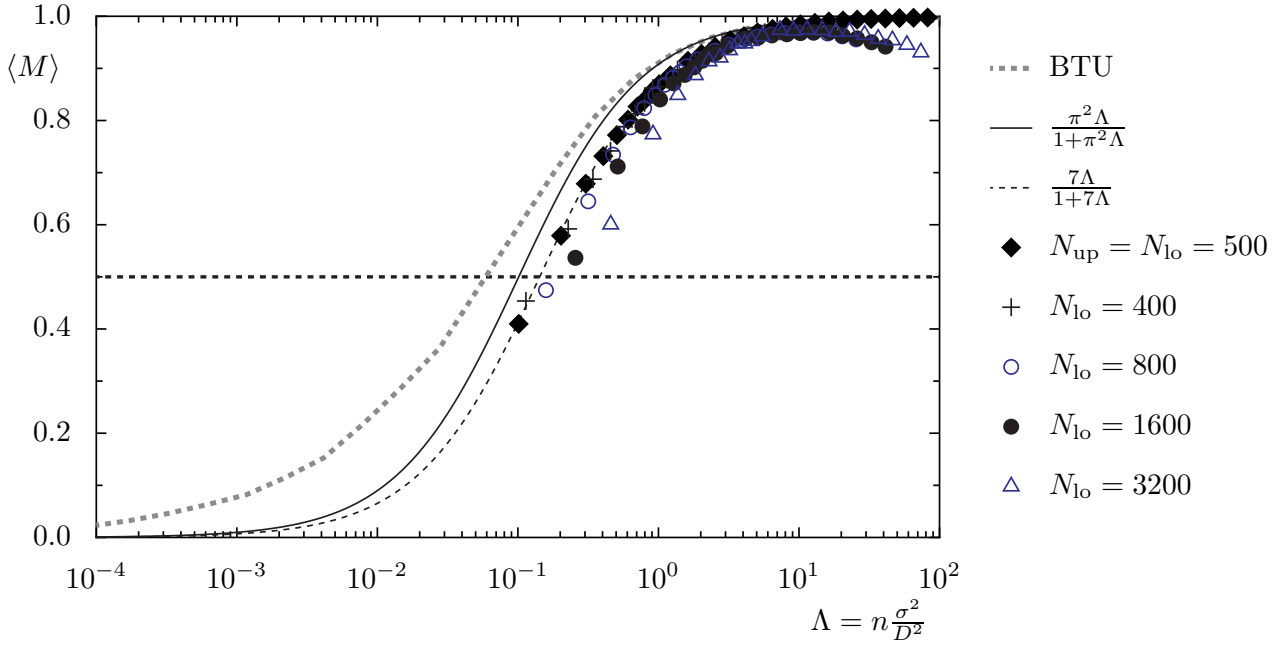
**Figure 4.14:** Average product measure for the channel coupling model for various pairs $(N_{\mathrm{up}}, N_{\mathrm{lo}})$ in comparison to the case with $N_{\mathrm{up}} = N_{\mathrm{lo}}$ (black diamonds) and the BTU matrix model (thick gray dashed line) as well as the $2 \times 2$-model discussed in Sec. 4.1 with prefactor 7 and $\pi^2$. The coupling strength $\sigma$ is given by Eq. (4.75).

different $\sigma$ for different ratios $N_{\mathrm{lo}}/N_{\mathrm{up}}$. The results are shown in Fig. 4.14. Here the resulting average product measure $\langle M \rangle$ does not scale with the parameter $\Lambda$. This is in contrast to Fig. 4.12, where we fixed $\sigma$ by Eq. (4.76) and varied $N_{\mathrm{up}}$ and $N_{\mathrm{lo}}$ independently. This missing scaling is the same as discussed for Fig. 4.11, where we used $N_{\mathrm{up}} = N_{\mathrm{lo}}$ and varied the coupling strength $\sigma$ over a wide range. Note that for large $\Lambda$ the data in Fig. 4.14 shows deviations similar to those discussed in Sec. 4.2.2 (see also Fig. 4.7), which disappear for large matrices. A final statement about the appropriate channel coupling model with $f_{\mathrm{up}} \neq f_{\mathrm{lo}}$ is not made here and we restrict ourselves to the comparison of the channel coupling model with $f_{\mathrm{up}} = f_{\mathrm{lo}}$ to our map data in Sec. 4.3.1.

## 4.3.1 Comparison to map data

We now compare the result of the channel coupling model to the data of map $F_{\mathrm{pb,rot}}$ discussed in Sec. 3.3.3. This data of Fig. 3.19 is shown again in Fig. 4.15, where the results for the BTU model and of the channel coupling model are included. For large ratios $\Phi/h_{\mathrm{eff}}$ the channel coupling result and the BTU result are in good agreement. For $\Phi/h_{\mathrm{eff}}$ around one, where the difference between BTU and channel coupling is most prominent, the channel coupling result is close to the map data and follows the same transition behavior. Therefore we conjecture that the reduced coupling in the channel coupling model compared to the overall coupling of the BTU model describes the situation of the quantum map more accurately.
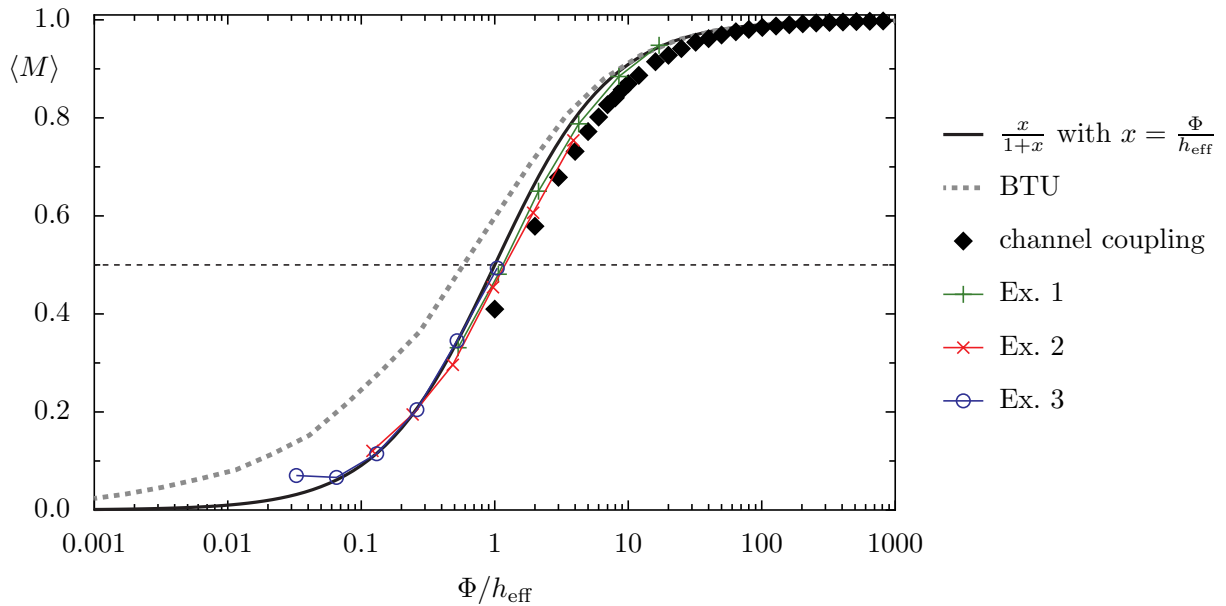
**Figure 4.15:** Average product measure $\langle M \rangle$ using the momentum measures for the examples 1, 2, and 3 of the map $F_{\text{pb,rot}}$ (same as Fig. 3.19) in comparison to the result of the BTU matrix model (gray dashed line) and of the channel coupling model (black diamonds) with $\Phi/h_{\text{eff}} = \pi^2 \Lambda$.

The drawbacks of the presented channel coupling model is that the number of open channels $n$ has to be an integer number such that $\langle M \rangle$ can be obtained at discrete values of $\Phi/h_{\text{eff}}$ only. Such a step function for the ATW or the average product measure is not observed in the data of the maps $F_{\text{pb}}$ and $F_{\text{pb,rot}}$. To overcome this discreteness, one could introduce a function for the onset of the next propagating mode and therewith allow for non-integer values for the number of propagating modes. The question is, how to perform this onset and which classical parameters complete the description given in terms of the ratio flux over Planck's constant. Some candidates are the mixing time or the Ehrenfest time, which is related to the Lyapunov exponent (see Sec. 3.2.1). An extension of the channel coupling model based on this idea is discussed in Sec. 4.3.4.

## 4.3.2  Diagonal coupling

The channel coupling model is equivalent to a matrix model, where the inter-block coupling is diagonal with $n$ non-vanishing elements as depicted in

$$H = \begin{pmatrix} \textbf{GOE} & \\ & \textbf{GOE} \end{pmatrix}, \tag{4.77}$$

where the nonzero elements $v_i$ in the coupling blocks have the fixed value $\sigma$. The mean coupling element squared is given by

$$\langle v^2 \rangle = \frac{n \cdot \sigma^2}{N_{\mathrm{up}} \cdot N_{\mathrm{lo}}} \tag{4.78}$$

and therefore the universal scaling parameter is (using Eq. (4.52) and choosing $A_{\mathrm{up}} = N_{\mathrm{up}}$)

$$\Lambda = \frac{\langle v^2 \rangle}{D^2} = \frac{n \cdot \sigma^2}{N_{\mathrm{up}} \cdot N_{\mathrm{lo}}} \frac{4 N_{\mathrm{tot}}^2}{\pi^2} = \frac{4 \cdot \sigma^2 \cdot n}{\pi^2 f_{\mathrm{up}} f_{\mathrm{lo}}}. \tag{4.79}$$

Relating this scaling parameter to the flux in the map system (see Eq. (4.73)) and assuming $n = \Phi/h_{\mathrm{eff}}$ the value of $\sigma$ is fixed and given by

$$\sigma = \frac{1}{4}. \tag{4.80}$$

This model yields the same average product measure as the channel coupling model, which is shown in Fig. 4.16. This is plausible, because for the original channel model the coupling strength $\sigma$ associated with a propagating mode is independent of the mode. Therefore all modes contribute equally. The additional Gaussian random coupling in the matrices $U$ and $V$, which couple the sub-systems to the channel, seems to have no relevant impact on the resulting
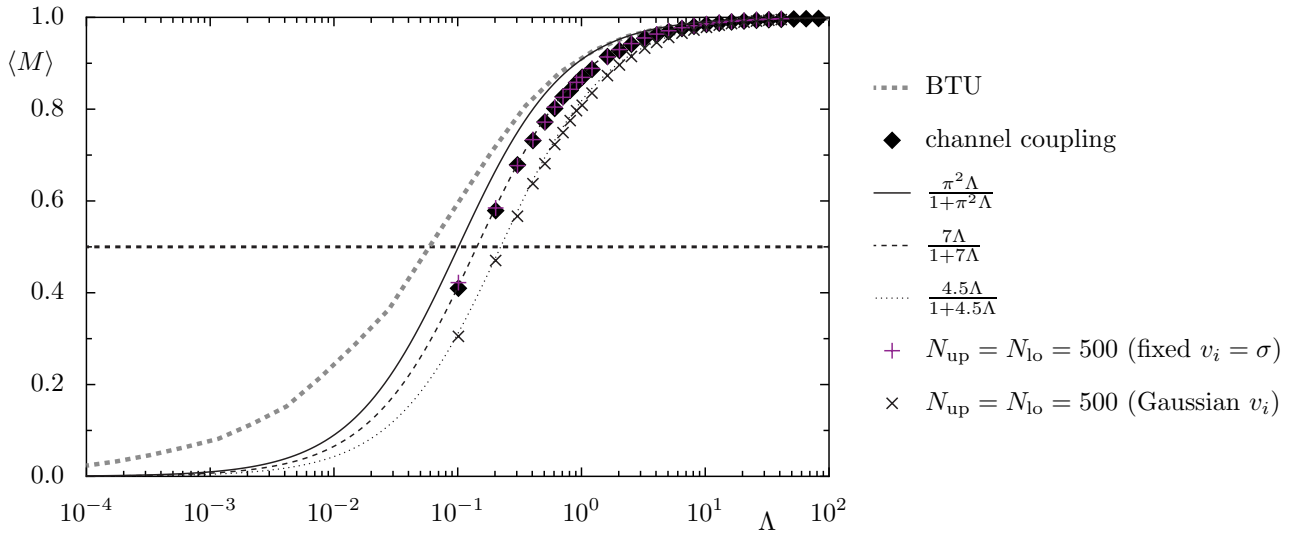


**Figure 4.16:** Average product measure for the matrix model, where two GOE matrices are coupled as in Eq. (4.77) with $n$ non-vanishing elements on the diagonal of the coupling blocks. The result for fixed coupling strength $v_i = \sigma$ (violet pluses) follows the channel coupling result (black diamonds) and the result of the Gaussian distributed coupling elements $v_i$ with zero mean and variance $\sigma^2$ (black crosses) yields smaller values. The results are compared to the BTU matrix model (thick gray dashed line) and the $2 \times 2$-model discussed in Sec. 4.1 with different prefactors.

average product measure $\langle M \rangle$. This additional randomness is already captured in the GOE nature of the upper and the lower block. However, if we choose the values on the diagonal $v_i$ as Gaussian random numbers with zero mean and variance $\sigma^2$ we find a different behavior. Namely, the resulting average product measure for a Gaussian distributed coupling strength is smaller than for fixed elements $v_i = \sigma$ as shown in Fig. 4.16. Therefore it matters whether the individual coupling strength is fixed as $v_i = \sigma$ or only its variance is fixed, $\langle v_i^2 \rangle = \sigma^2$.

## 4.3.3  One channel rising

As discussed in the first part of Sec. 4.3 the drawback of the channel coupling model is the discreteness of the number of propagating modes $n$. It is not possible to model less than one propagating mode. In this section we consider the onset of the first coupling element. That is, we fix $n = 1$ and vary the coupling strength $\sigma$ over a wide range.

Figure 4.17 shows the resulting average product measure. The result is similar to the one shown in Fig. 4.9 in Sec. 4.2.5, where the two GOE matrices are coupled via one Gaussian distributed element (variance $\sigma^2$) whereas here the value of the coupling element is fixed to $\sigma$ for all realizations. Therefore the difference between the results of Fig. 4.17 and Fig. 4.9 in Sec. 4.2.5 has the same origin as the difference between the channel coupling model with fixed couplings and with Gaussian distributed coupling elements discussed in Sec. 4.3.2. The result
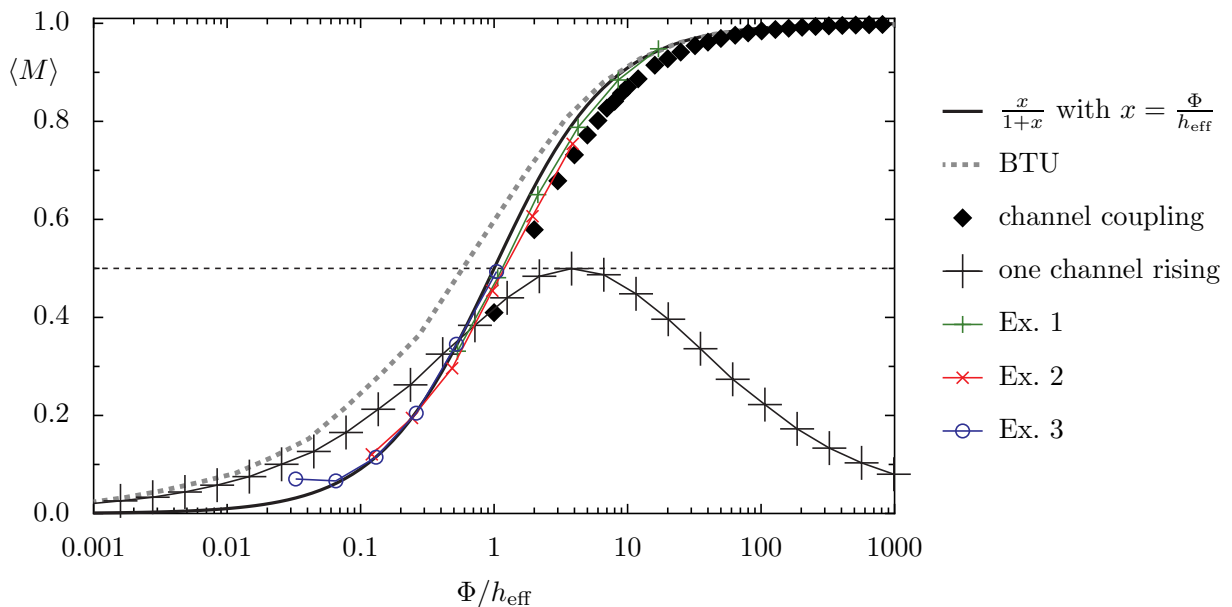


**Figure 4.17:** Average product measure $\langle M \rangle$ using the momentum measures for the examples 1, 2, and 3 of the map $F_{\mathrm{pb,rot}}$ (same as Fig. 3.19) in comparison to the result for the random matrix model, where two GOE matrices are coupled via one propagating mode (pluses; varying coupling strength $\sigma$, $N_{\mathrm{up}} = N_{\mathrm{lo}} = 500$ and using 1000 random matrices). Moreover we compare to the BTU matrix model (gray dashed line) discussed in Sec. 4.2.1 and the $2 \times 2$-model discussed in Sec. 4.1 (black solid line) using $4\lambda^2 = \Phi/h_{\mathrm{eff}} = \pi^2\Lambda$.

for the channel coupling model with fixed coupling elements is reached during the onset of the first coupling element discussed here and the curve of Sec. 4.2.5 approaches the result for the channel coupling model with Gaussian distributed coupling strength. For large values of the scaling parameter and thereby strong couplings the average product measure decreases.

As long as the universal scaling is described by $\Lambda = \langle v^2 \rangle / D^2$, the presented method is the only way of performing an onset of the first propagating mode. Any function relating the value of $\sigma$ to the ratio $\Phi/h_{\text{eff}}$ or to other map parameters like the mixing time or the Lyapunov exponent, finally gives the same curve because only the value of $\sigma$ enters.

### 4.3.4 Extension of the channel coupling model

At this point we want to overcome the discreteness of the number of propagating modes. Therefore we introduce the following modifications to the model, Eq. (4.77). Instead of a finite number of non-vanishing elements on the anti-diagonal, we use all elements on the anti-diagonal and their values follow a Fermi function. More precisely the squares of the matrix elements follow the Fermi function as

$$v_k^2 = \frac{\sigma^2}{1 + \exp\{-\beta(\Phi/h_{\text{eff}} - k - 1/2)\}} \quad \text{for} \quad k = 0, 1, 2, \ldots, N_{\text{up}} - 1 \tag{4.81}$$

with one free parameter $\beta$, which is the inverse temperature in thermodynamics. Figure 4.18 shows the square matrix elements for different values of $\beta$. For $\beta = \infty$ ('low temperature' limit) the step function of the original model is recovered and $\Phi/h_{\text{eff}}$ determines the number of
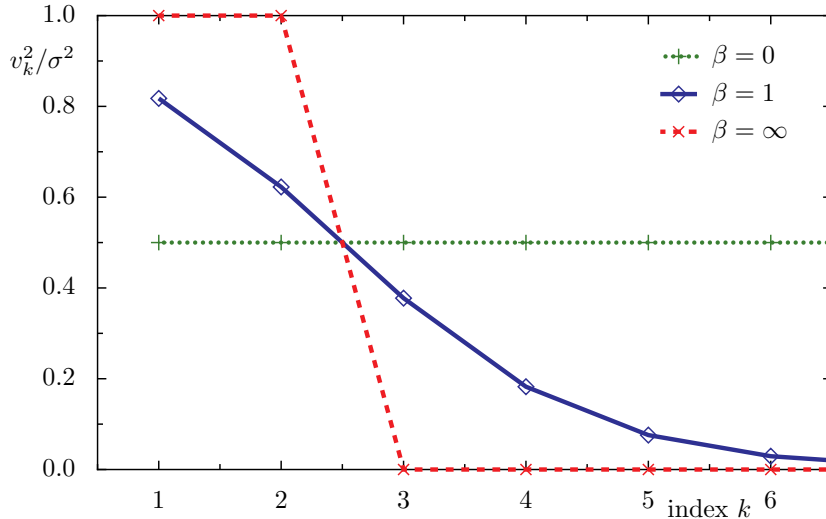


**Figure 4.18:** Square of the non-vanishing coupling elements according to Eq. (4.81) for $\Phi/h_{\text{eff}} = 2$ and different $\beta$. For $\beta = \infty$ the previously discussed step function is recovered and for $\Phi/h_{\text{eff}} = 2$ we find 2 non-vanishing elements. For finite $\beta$ this sharp transition is smoothed and for $\beta = 0$ all sites contribute equally.

propagating modes. For finite $\beta$ the coupling as a function of the mode index $k$ is smoothened and all modes contribute equally for vanishing $\beta$. The ratio $\Phi/h_{\text{eff}}$ determines the location of the symmetry point of the Fermi function and for decreasing ratio $\Phi/h_{\text{eff}}$ the distribution is smoothly shifted to the left. The scaling parameter $\Lambda$ in this situation reads

$$\Lambda = \frac{\sum_k v_k^2}{D^2 N_{\text{up}} N_{\text{lo}}}. \tag{4.82}$$

Here there is in general no simple relation of $\Lambda$ to the ratio $\Phi/h_{\text{eff}}$, as found for the previously discussed matrix models.

Such transmission probabilities described by a Fermi function arise often in the field of transition state theory (see for instance Ref. [78]). As an example we use the transmission over a harmonic saddle, which can be used to model the transition across a partial barrier [79]. It is described by the following Hamiltonian,

$$H(x, y, p_x, p_y) = \frac{p_x^2 + p_y^2}{2m} + \frac{m\omega_y^2}{2}y^2 - \frac{m\omega_x^2}{2}x^2. \tag{4.83}$$

As propagation direction we choose the $x$-direction and particles have to overcome the inverted harmonic oscillator in order to pass the saddle. In the perpendicular direction the particles are confined by a harmonic potential. The problem for the $y$-direction is solved by the quantization of the harmonic oscillator and the propagating modes have the energies

$$E_k^{(y)} = \hbar_{\text{eff}}\omega_y \left( k + \frac{1}{2} \right) \quad \text{for} \quad k = 0, 1, 2, \ldots . \tag{4.84}$$

The classical flux over the saddle at energy $E$ per time is given by an integration of the velocity $v_x = p_x/m$ over all possible positions $y$, all possible momenta $p_y$, and all forward propagating momenta $p_x > 0$

$$\Phi = \frac{\mathrm{d}}{\mathrm{d}E} \int\limits_{y_{\text{min}}}^{y_{\text{max}}} \mathrm{d}y \int\limits_{p_x^2+p_y^2\leq 2m[E-V(0,y)],p_x>0} \mathrm{d}p_x\mathrm{d}p_y \cdot \frac{p_x}{m} \tag{4.85}$$

$$= \frac{\mathrm{d}}{\mathrm{d}E} \int\limits_{y_{\text{min}}}^{y_{\text{max}}} \mathrm{d}y \int\limits_{-\pi/2}^{\pi/2} \mathrm{d}\varphi \int\limits_{0}^{\sqrt{2m[E-V(0,y)]}} \mathrm{d}p \cdot p \cdot \frac{p\cos\varphi}{m} \tag{4.86}$$

$$= \frac{\mathrm{d}}{\mathrm{d}E} \int\limits_{y_{\text{min}}}^{y_{\text{max}}} \mathrm{d}y \frac{2}{3m} \left[ 2m[E - V(0, y)] \right]^{3/2} . \tag{4.87}$$

The limits of the $y$-integration are the classical turning points for particles with energy $E$ at

$x = 0$

$$y_{\text{max}} = -y_{\text{min}} = \sqrt{\frac{2E}{m\omega_y^2}}. \tag{4.88}$$

Substituting $u := y/y_{\text{max}} = y\sqrt{m\omega_y^2}/\sqrt{2E}$ and performing the $u$-integration yields

$$\Phi = \frac{\mathrm{d}}{\mathrm{d}E} \int\limits_{-1}^{+1} \mathrm{d}u \left[1 - u^2\right]^{3/2} \frac{8E^2}{3\sqrt{\omega_y^2}} = \frac{2\pi E}{\omega_y}. \tag{4.89}$$

That is, the classical flux $\Phi$ in multiples of Planck's constant is determined by the number of propagating modes found below energy $E$,

$$\frac{\Phi}{h_{\text{eff}}} = \frac{E}{\hbar_{\text{eff}}\omega_y}. \tag{4.90}$$

The transmission coefficient of this setup can be calculated and we use the results of Ref. [80] for vanishing magnetic field $B = 0$. The characteristic energies are

$$E_1 = \frac{\hbar_{\text{eff}}}{2}\sqrt{\frac{2U_x}{m}} = \frac{\hbar_{\text{eff}}}{2}\omega_x, \tag{4.91}$$

$$E_2 = \hbar_{\text{eff}}\sqrt{\frac{2U_y}{m}} = \hbar_{\text{eff}}\omega_y \tag{4.92}$$

and the transmission probability is

$$T_k = \frac{1}{1 + \exp\{-\pi\epsilon_k\}} \quad \text{with} \quad \epsilon_k = \frac{2\omega_y}{\omega_x}\left[\frac{\Phi}{h_{\text{eff}}} - \left(k + \frac{1}{2}\right)\right] \quad \text{for} \quad k = 0, 1, 2, \ldots \tag{4.93}$$

The width of the inverted harmonic oscillator $\omega_x$ determines how fast particles pass this bottleneck. It is given by the Lyapunov exponent of the unstable fixed point at the top of the saddle, because the motion in $x$-direction of particles nearby the saddle is governed by $\ddot{x} = \omega_x^2 x$ and follows $x(t) = x_0 \exp\{\pm\omega_x t\}$. That is, $\omega_x$ takes the role of the Lyapunov exponent $L$ of the fixed point at the saddle. We use this to relate $\omega_x$ to properties of our designed maps. For the maps $F_{\text{pb}}$ and $F_{\text{pb,rot}}$ the Lyapunov exponent of the hyperbolic fixed point at $(\frac{1}{2}, p_{\text{fix}})$ can be calculated using the larger eigenvalue of the Jacobian matrix, Eq. (3.16), and we get

$$L = \log\left(1 + \frac{bK'}{2} + \sqrt{\left(1 + \frac{bK'}{2}\right)^2 - 1}\right) = \begin{cases} 1.566 & \text{for example 1} \\ 1.159 & \text{for example 2} \\ 0.963 & \text{for example 3.} \end{cases} \tag{4.94}$$

See Tab. 3.1 for the values of the parameters $b$ and $K'$.

Up to now we could not find a relation for the second frequency $\omega_y$ to parameters of the map. It might be related to the period of the hyperbolic fixed point similar to the description of scarring by Heller [60], where the product of the Lyapunov exponent and the period of the hyperbolic periodic orbit gives a criterion for an orbit to support scarred eigenstates. However, here we use $\omega_y$ as a fitting parameter. The factor $\beta = \frac{2\pi\omega_y}{L}$ governs the transmission probabilities and therewith the square of the non-vanishing matrix elements of Eq. (4.81). Using Eq. (4.93) we can relate the $\frac{1}{2}$ in the exponent of Eq. (4.81) to the ground state energy of the harmonic oscillator in Eq. (4.84).

The transmission probabilities of Eq. (4.93) determine the modulation of the squared matrix element $v_k$ with respect to $\sigma^2$: $v_k^2 = T_k \cdot \sigma^2$. This is plausible, because according to Fermi's golden rule the transition rates are compared with the square of the coupling matrix elements.
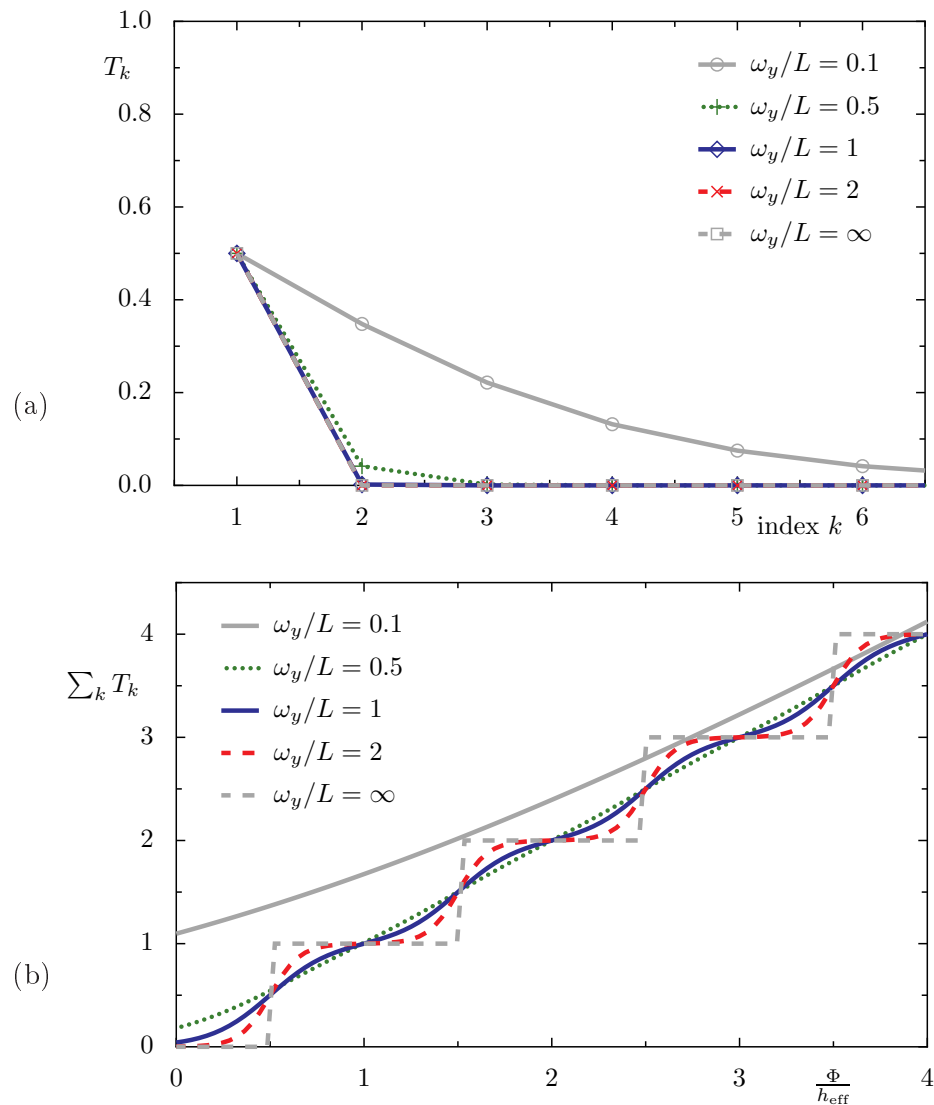


**Figure 4.19:** Transmission for the matrix model using Eq. (4.81). (a) Individual transmission probability of each site $k$ for $\Phi/h_{\text{eff}} = 1/2$. (b) Total transmission summed over all sites $k = 1, \dots$ as a function of $\Phi/h_{\text{eff}}$. For $\omega_y \to \infty$ we find steps in the total transmission whereas in the opposite limit, $\omega_y \to 0$, all sites have transmission $1/2$ and the total transmission diverges.

Figure 4.19(a) shows the transmission probability of each site $k$ for various values of the ratio $\omega_y/L$ and fixed ratio $\Phi/h_{\mathrm{eff}} = \frac{1}{2}$. Figure 4.19(b) shows the total transmission summed over all coupling sites. This total transmission has clear steps for $\omega_y/L \to \infty$ and they are smoothened for decreasing ratio $\omega_y/L$. For $\omega_y/L = 0$ all sites contribute equally and the total transmission diverges, independent of $\Phi/h_{\mathrm{eff}}$, with the total number of coupling elements.

Note that if we renormalize the couplings of Eq. (4.81) in order to have the same sum of squared elements as in the channel coupling model of Sec. 4.3.2,

$$\sum_{k=0}^{N_{\mathrm{up}}-1} v_k^2 = \frac{\Phi}{h_{\mathrm{eff}}}\sigma^2, \tag{4.95}$$

we recover the BTU result for small values of $\beta$ ($\beta \lesssim \frac{1}{2}$). For increasing $\beta$ the average product measure approaches the result of the channel coupling model. The range $n \in (0,1)$, which is excluded in the original channel coupling model, is in accordance with the results discussed in Sec. 4.3.3 about the onset of one propagating mode. In this way, the above model allows for a continuous transition between the BTU and the channel coupling result. However, this model with renormalization is not appropriate to describe our map data. Hence in the following we will use Eq. (4.81) without any renormalization.

Figure 4.20 shows the map data discussed in Sec. 3.3.3 in comparison to the result of the matrix model, where the coupling elements follow the Fermi function. The value $\beta = 2\pi\omega_y/L = 8$ is chosen such that the overall behavior of the map data is well described by the matrix model.
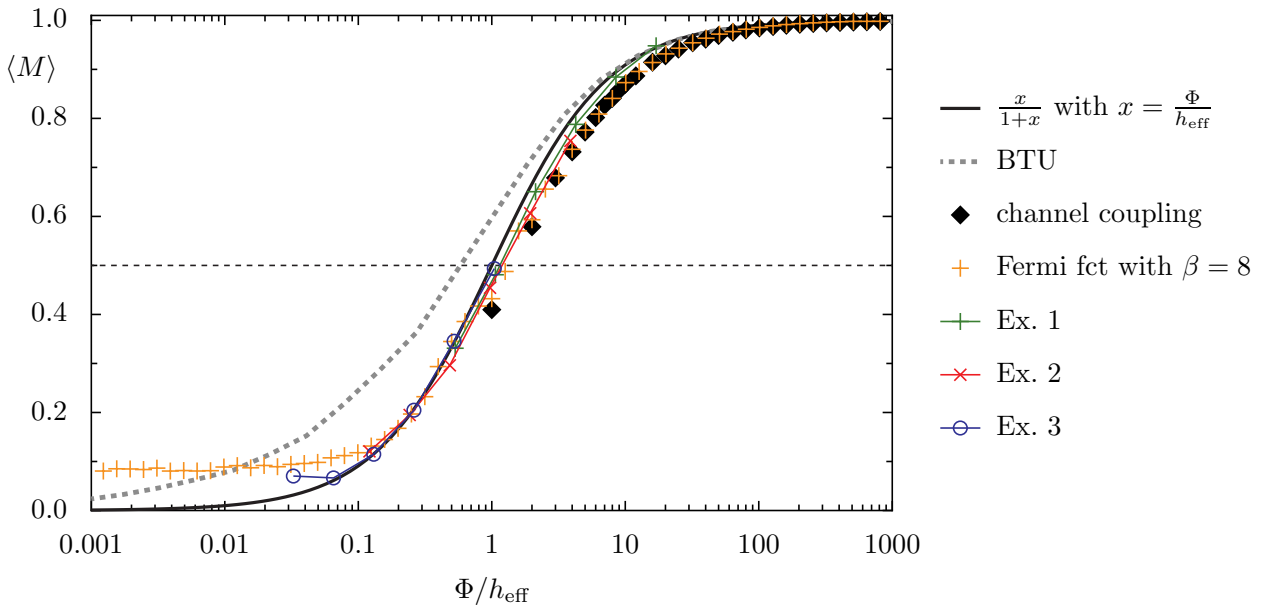


**Figure 4.20:** Average product measure $\langle M \rangle$ using the momentum measures for the examples 1, 2, and 3 of the map $F_{\mathrm{pb,rot}}$ (same as Fig. 3.19) in comparison to the result of the BTU matrix model (gray dashed line), the channel coupling with fixed elements (black diamonds) and the matrix model with elements following the Fermi function (orange pluses).

## 4.4 Unitary random matrix models

In contrast to the previous sections, where Hamiltonian matrices are modeled, we now consider unitary matrices in order to describe the impact of the partial barrier on the corresponding quantum system. The unitary equivalent of the Gaussian orthogonal ensemble is the circular orthogonal ensemble (COE) [67, Sec. 10.1]. Such COE matrices can be diagonalized by orthogonal transformations and their spectral statistics describe chaotic systems with time reversal invariance. One can build a random matrix according to the COE by generating a matrix of the circular unitary ensemble following Ref. [81], $U_{\mathrm{CUE}}$, and using $U_{\mathrm{COE}} = U_{\mathrm{CUE}}^{T}\, U_{\mathrm{CUE}}$ [67, Sec. 10.1], where the superscript $T$ denotes the transposition of the matrix.

The unitary matrix model of the time evolution operator for two uncoupled chaotic subsystems with time reversal invariance is

$$U_0 = \begin{pmatrix} \boxed{\text{COE}} & 0 \\ 0 & \boxed{\text{COE}} \end{pmatrix}, \tag{4.96}$$

which is block diagonal and contains one COE matrix for each sub-system. One approach to introduce a coupling between the sub-systems while preserving unitarity is the following. We compose the time evolution operator in Eq. (4.96) with a unitary matrix

$$U_{\mathrm{c}} = \begin{pmatrix} \diagdown & \vdots & 0 \\ \cdots & \blacksquare & \cdots \\ 0 & \vdots & \diagdown \end{pmatrix}, \tag{4.97}$$

which introduces couplings (blue square) between the former independent blocks (dashed lines). It consists of unity matrices (solid lines) and a coupling block $U_{\mathrm{m}}$ of size $2m \times 2m$ indicated in the center. One choice for $U_{\mathrm{m}}$ is a matrix $U_{\mathrm{m},1}$ with ones on the anti-diagonal. The resulting random matrix model is determined by the unitary matrix $U_1$ composed of $U_0$ and $U_{\mathrm{c},1}$,

$$U_1 = U_0 U_{\mathrm{c},1} = \begin{pmatrix} \boxed{\text{COE}} & 0 \\ 0 & \boxed{\text{COE}} \end{pmatrix} \begin{pmatrix} \diagdown & \vdots & 0 \\ & \diagup & \\ 0 & \vdots & \diagdown \end{pmatrix} = \begin{pmatrix} \blacksquare & \vdots & 0 \\ \cdots & & \cdots \\ 0 & \vdots & \blacksquare \end{pmatrix}, \tag{4.98}$$

in which the black lines indicate the ones on the diagonal and the anti-diagonal of $U_{\mathrm{m},1}$. Under time evolution with this matrix, a state initially located in the upper region is transmitted to the lower region via the lower left block of $U_1$. A state initially located in the lower region is

transmitted to the upper region via the upper right block. Except for the size of the block matrices this model has only one parameter; namely $m$, which determines the size of the matrix $U_{\mathrm{m},1}$. There are $m$ sites, which transfer weight from above to below and vice versa like the turnstile in the classical picture. This model is the first to account for directed transport between the two sub-systems. Such a directed transport is not possible in terms of a Hamiltonian matrix, as for those discussed in the previous sections, because this contradicts Hermiticity of the matrix.

For completeness we mention another possible choice for the matrix $U_{\mathrm{m}}$. Namely we choose a COE matrix for the coupling block $U_{\mathrm{m}}$ and consider the matrix model

$$U_2 = U_0 U_{\mathrm{c},2} = \begin{pmatrix} \text{COE} & 0 \\ 0 & \text{COE} \end{pmatrix} \begin{pmatrix} \diagdown & 0 \\ 0 & \diagdown \end{pmatrix} = \begin{pmatrix} \blacksquare & 0 \\ 0 & \blacksquare \end{pmatrix}. \qquad (4.99)$$

In this model the weight entering the $m$ transmitting sites of the upper region is distributed over all sites of the total system in contrast to the matrix model of Eq. (4.98), in which the weight is distributed over the lower sites only. Therefore the transmission to the lower region is reduced by a factor of two in comparison to the matrix model Eq. (4.98).

The aim of these models, Eqs. (4.98) and (4.99), is to relate the impact of the classical transport rate across the partial barrier to the corresponding quantum system in terms of a unitary matrix model. The classical escape rate from the upper chaotic region is given by the ratio of the classical flux $\Phi$ and the accessible area, Eq. (3.37) of Sec. 3.2.1,

$$\frac{\Phi}{A_{\mathrm{ch,up}}} = \frac{\Phi}{N_{\mathrm{up}} h_{\mathrm{eff}}}, \qquad (4.100)$$

where we introduced the number of states $N_{\mathrm{up}}$ associated with the upper region. This rate has to be compared with the transition rate of the two random matrix models corresponding to the part of a given vector, which is transported to the lower region. It is $m/N_{\mathrm{up}}$ for Eq. (4.98) and $m/(2N_{\mathrm{up}})$ for Eq. (4.99), where for the latter only half of the weight entering the $m$ sites is transported to the opposite region. We introduce the number of transporting sites $n$ as the number of sites times their transition probability. With this definition we get $n/N_{\mathrm{up}}$ as transition rate for both matrix models. Therewith the rates of Eq. (4.100) and of the matrix models are the same if we assume that the ratio $\Phi/h_{\mathrm{eff}}$ is the number of transporting sites $n$ in the COE model, which is reasonable according to Sec. 3.2.1, where this ratio is associated with the number of open channels in an open system.
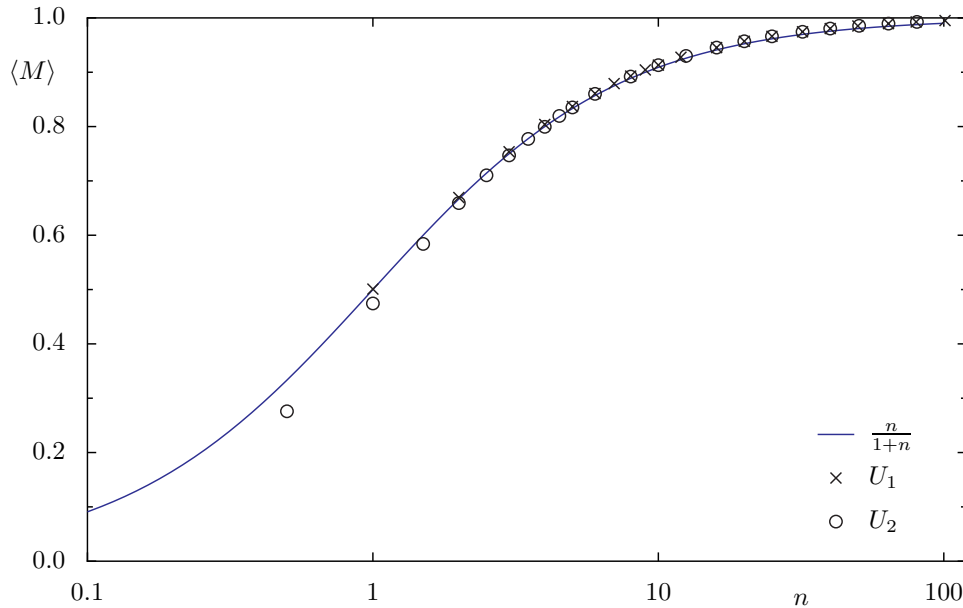
**Figure 4.21:** Average product measure $\langle M \rangle$ for the COE matrix models, $U_1$ of Eq. (4.98) and $U_2$ of Eq. (4.99), using $N_{\rm up} = N_{\rm lo} = 200$ and 1000 random matrices. The results for the two different matrix models follow the transitional behavior described by $n/(1+n)$.

The product measure is defined analogously to Eq. (3.72)

$$M[\phi] = \frac{\mu_{\rm up}[\phi]}{\mu_{\rm up}[\Psi_{\rm uniform}]} \frac{\mu_{\rm lo}[\phi]}{\mu_{\rm lo}[\Psi_{\rm uniform}]} \tag{4.101}$$

with the measures $\mu_{\rm up}[\Psi_{\rm uniform}] = f_{\rm up} = N_{\rm up}/(N_{\rm up} + N_{\rm lo})$ and $\mu_{\rm lo}[\Psi_{\rm uniform}] = f_{\rm lo} = N_{\rm lo}/(N_{\rm up} + N_{\rm lo})$ of the state $\Psi_{\rm uniform}$, which is uniformly distributed in both regions. For the two models introduced above the product measure averaged over the eigenstates is independent of $N_{\rm tot} = N_{\rm up} + N_{\rm lo}$ and shown in Fig. 4.21 for $N_{\rm lo} = N_{\rm up} = 200$. The results for both matrix models are in agreement with the curve

$$M(n) = \frac{n}{1+n}, \tag{4.102}$$

which describes the same transition behavior as the deterministic $2 \times 2$-model of Sec. 4.1, where

$$M(\lambda) = \frac{4\lambda^2}{1+4\lambda^2} \tag{4.103}$$

is found. For $n = 4\lambda^2$ the two Eqs. (4.102) and (4.103) are identical. Note that for the random matrix model of Eq. (4.98) the number of transporting sites $n$ can take only positive integer values whereas $n$ takes half-integer values for the model of Eq. (4.99). Hence only the upper half of the transition curve can be investigated. By an appropriate choice of $U_m$, one may extend the data to continuous values of $n$ and even values smaller than one half.
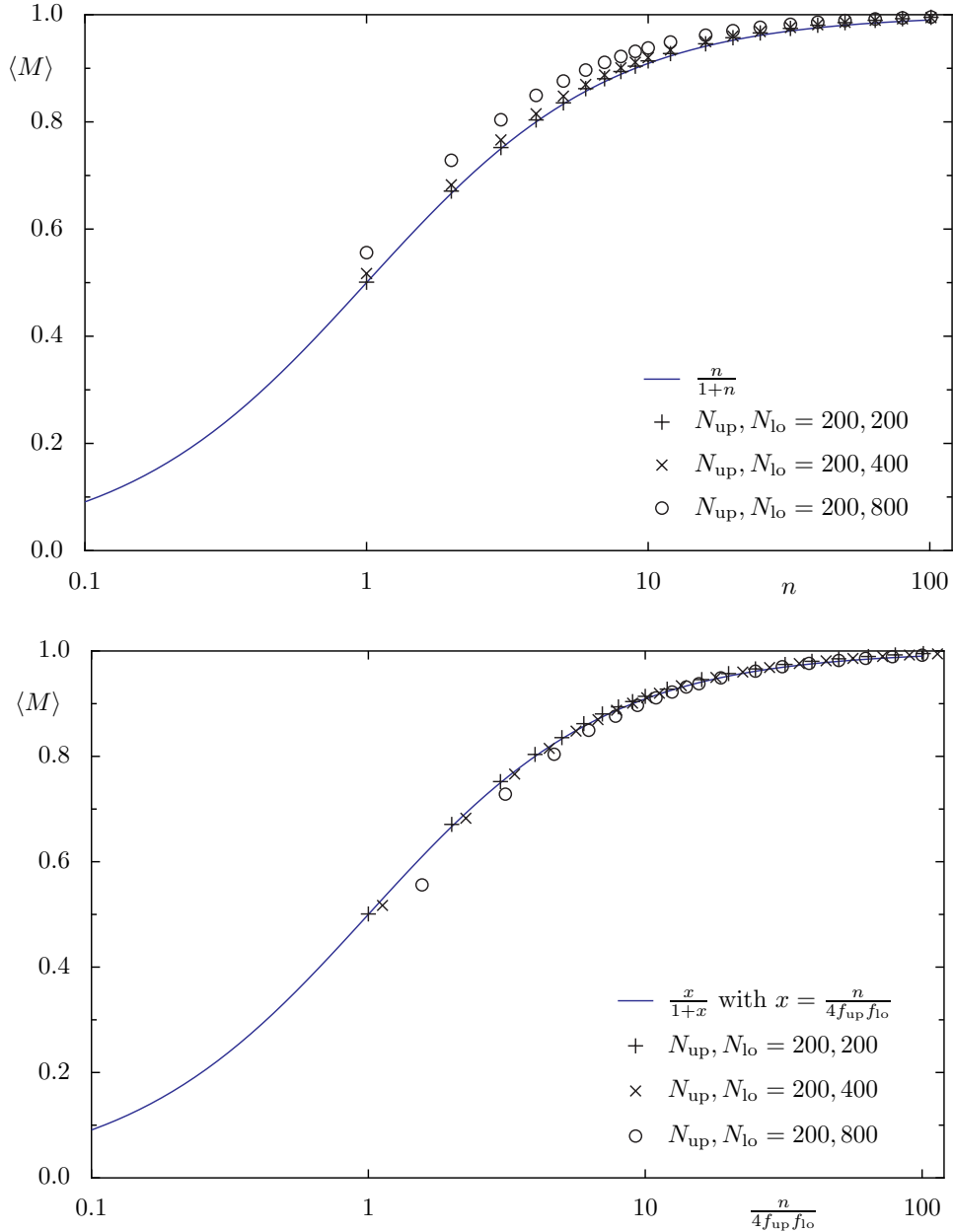
**Figure 4.22:** Average product measure $\langle M \rangle$ for the COE model of Eq. (4.98) as a function of $n$ and $n/(4f_{\text{lo}}f_{\text{up}})$. Here we considered $N_{\text{up}} \neq N_{\text{lo}}$ and 100 random matrices for each pair $(N_{\text{up}}, N_{\text{lo}})$.

Variation of the relative block sizes yields the data shown in Fig. 4.22 and we find scaling with $n/(4f_{\text{lo}}f_{\text{up}})$ rather than $n$ only. This is the same kind of scaling found in the $\Lambda$-flux relation of Sec. 3.2.2.

In Fig. 4.23 the average product measure of the unitary matrix model given by Eq. (4.98) is compared to $\langle M \rangle$ for the map $F_{\text{pb,rot}}$ discussed in Sec. 3.3.3. In the figure we compare the map data as a function of $\Phi/h_{\text{eff}}$ to the data of the matrix model as a function of $n$. The two data sets are in very good agreement and exhibit a common transition behavior.
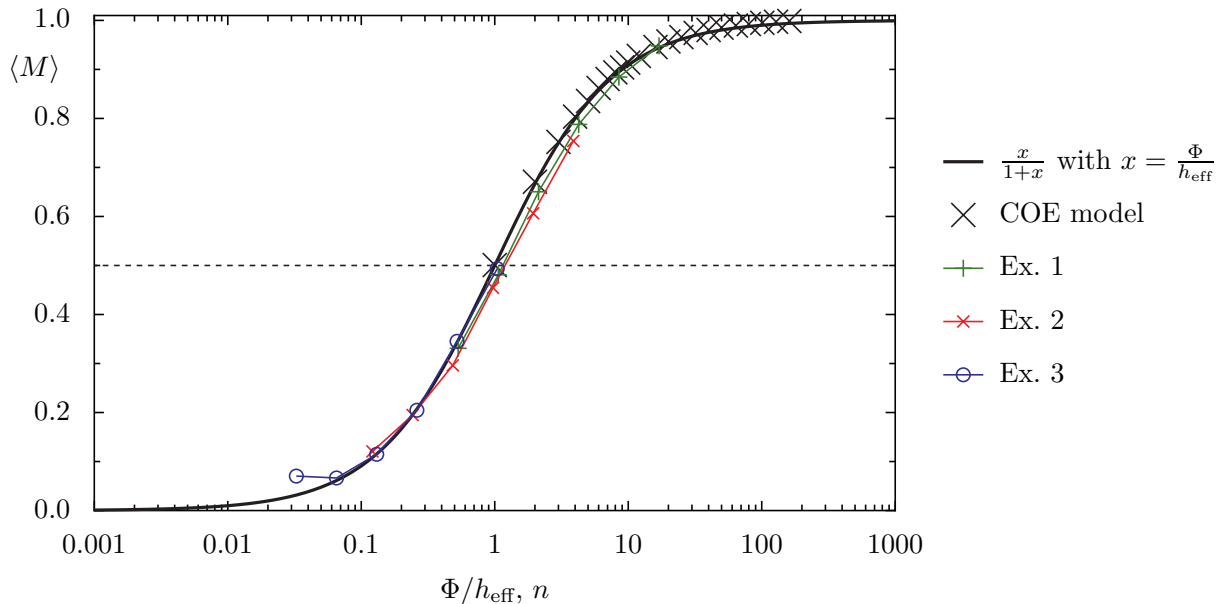
**Figure 4.23:** Average product measure $\langle M \rangle$ using the momentum measures for the examples 1, 2, and 3 of the map $F_{\mathrm{pb,rot}}$ as a function of $\Phi/h_{\mathrm{eff}}$ (same as Fig. 3.19) in comparison to the result of the COE matrix model Eq. (4.98) (crosses), where we use $n$ for the abscissa.

## 4.5 Summary of the modeling approaches

In the previous sections we discuss several matrix models to describe the quantum transition of a partial barrier from quantum suppression to classical transport, where the two limiting cases correspond to uncoupled chaotic sub-systems and strongly coupled chaotic sub-systems, respectively. We introduce a deterministic $2 \times 2$-model, one site for each chaotic region of the system with one partial barrier, which describes the same transition behavior found numerically for the designed map. The random matrix model proposed by Bohigas, Tomsovic, and Ullmo shows a transition behavior, which is different from the map data. We attribute this difference to the overall Gaussian coupling between all upper and all lower states. Therefore we introduce the channel coupling model with a more sophisticated coupling. It allows for a finite number of propagating modes between the two sub-systems. This number of propagating modes $n$ gives rise to $n$ non-vanishing coupling elements of fixed size $\sigma$ and equals the ratio $\Phi/h_{\mathrm{eff}}$. The results for the channel coupling model are in good agreement with the map data. We extend this matrix model with discrete coupling sites to a smooth version using Fermi-function like transition probabilities for each coupling site. Therewith we smoothen the transition curve of the channel coupling model and extend it to $\Phi/h_{\mathrm{eff}}$ smaller than one. In the last section we discuss unitary matrix models, which – in contrast to the Hermitian matrix models – allow for a directed transport between the upper and the lower region as it is the case for the classical partial barrier. These models follow the same transition behavior as the map data if we identify $\Phi/h_{\mathrm{eff}}$ with the number of transporting sites.

# 5 Spectral signatures of partial barriers in phase space

This chapter is dedicated to the spectral properties of the system with one isolated partial barrier $F_{\mathrm{pb,rot}}$. There are numerous possibilities to quantify system properties by means of spectral statistics. In order to observe universal behavior and to compare features of different systems, one has to unfold the spectrum of energy levels [82]. That is, one has to remove the smooth part of the density of states and thereby variations in the mean level spacing, which take place on larger scales. The universal behavior is found in the remaining oscillatory part of the density of states. From the huge number of available quantities of spectral statistics we restrict ourselves to the spectral form factor $K(\tau)$, which is discussed in Sec. 5.1, and the distribution of level spacings $P(s)$, which is presented in Sec. 5.2. We compare our findings to the random matrix model proposed by Bohigas, Tomsovic, and Ullmo and to the channel coupling model, whose ATW is in good agreement with the map data.

## 5.1 Spectral from factor $K(\tau)$

The spectral form factor is the Fourier transform of the two-point correlations function $R_2(E_1 - E_2)$ [83, Sec. 3.2.5] and has been studied extensively [65,84,85]. Its short time behavior translates into long-term correlations in the energy domain. It is appropriate to quantify spectral properties of a system with one partial barrier, because it incorporates the involved time scales, namely the Heisenberg time and the dwell time [65].

### 5.1.1 Definition of the spectral form factor

Consider a quantum system described by a unitary time evolution operator $U$ with the following eigenvalue equation,

$$U|k\rangle = e^{\mathrm{i}\varphi_k}|k\rangle \quad \text{for} \quad k = 1, \dots, N. \tag{5.1}$$

The spectral form factor as a function of time $m$ ($m \in \mathbb{Z}$) is given by [59, Sec. 4.14]

$$K(m) = \frac{1}{N} \sum_{j=1}^{N} \sum_{k=1}^{N} \exp\{i(\varphi_j - \varphi_k) \cdot m\} \tag{5.2}$$

$$= \frac{1}{N} \left| \sum_{k=1}^{N} \exp\{i\varphi_k \cdot m\} \right|^2 = \frac{1}{N} |\text{Tr } U^m|^2 . \tag{5.3}$$

It measures correlations between the levels, which are the eigenphases $\{\varphi_k\}$ in the case of a quantum map.

To compare the spectral form factor of different systems, we have to unfold the spectrum in order to obtain the same mean level spacing for all levels. Furthermore we have to introduce a typical time for a temporal rescaling. As discussed in Sec. 3.2.1 the time associated with the mean level spacing is the Heisenberg time

$$t_{\text{H}} = \frac{2\pi}{\langle \Delta\varphi \rangle} = N. \tag{5.4}$$

That is, for quantum maps the Heisenberg time is given by the number of states $N$ of the system considered. Analogously the Heisenberg time corresponding to a sub-system is the number of states associated with this sub-system as mentioned in Sec. 3.2.1. The rescaled time $\tau$ is the time in multiples of the Heisenberg time,

$$\tau = \frac{t}{t_{\text{H}}} = \frac{m}{N}. \tag{5.5}$$

As pointed out in Sec. 4.2 the spectral properties of chaotic systems can be modeled by random matrices. For a chaotic system obeying time reversal invariance the universality class is the Gaussian orthogonal ensemble (GOE). The GOE prediction for the so called two-level form factor $b(\tau)$, which is related to the spectral form factor by

$$b(\tau) = 1 - K(\tau), \tag{5.6}$$

is given by (see Eq. C.9 of Ref. [86] on page 191)

$$b_{\text{GOE}}(\tau) = \begin{cases} 1 - 2\tau + \tau \log(2\tau + 1) & \text{for} \quad \tau < 1 \\ -1 + \tau \log \frac{2\tau+1}{2\tau-1} & \text{otherwise.} \end{cases} \tag{5.7}$$

This yields for the spectral form factor of one GOE spectrum

$$K_{\text{GOE}}(\tau) = \begin{cases} 2\tau - \tau \log(2\tau + 1) & \text{for} \quad \tau < 1 \\ 2 - \tau \log \frac{2\tau+1}{2\tau-1} & \text{otherwise} \end{cases} \tag{5.8}$$

and its Taylor expansion reads

$$K_{\text{GOE}}(\tau) = 2\tau - 2\tau^2 + 2\tau^3 \mp \dots \quad \text{for} \quad \tau \ll 1. \tag{5.9}$$

If we consider a spectrum composed of two independent spectra, with $f_i$ being the fraction of levels belonging to the $i$-th component, the two-level form factor resulting from the superposition is the weighted sum of the individual form factors $b_{(i)}$, [86, Eq. D.3],

$$b_{\text{total}}(\tau) = \sum_i f_i \, b_{(i)}(\tau/f_i). \tag{5.10}$$

Each form factor gets as argument the time measured in multiples of the corresponding Heisenberg time of region $i$

$$\frac{\tau}{f_i} = \frac{t}{f_i t_H} = \frac{t}{t_{\text{H},i}}. \tag{5.11}$$

For the case of two independent spectra of equal size, i.e. $f_1 = f_2 = \frac{1}{2}$, we have

$$b_{\text{total}}(\tau) = \frac{1}{2}b_{(1)}(2\tau) + \frac{1}{2}b_{(2)}(2\tau) = b_{\text{partial}}(2\tau) \,, \tag{5.12}$$

where in the last step it was assumed that both spectra belong to the same universality class. For the spectral form factor this means

$$K_{\text{total}}(\tau) = 1 - b_{\text{total}}(\tau) = 1 - b_{\text{partial}}(2\tau) = K_{\text{partial}}(2\tau) \tag{5.13}$$

For the uncorrelated superposition of two GOE spectra we have

$$K_{\text{2GOE}}(\tau) = K_{\text{GOE}}(2\tau) = \begin{cases} 4\tau - 2\tau \log(4\tau + 1) & \text{for} \quad 2\tau < 1 \\ 2 - 2\tau \log \frac{4\tau+1}{4\tau-1} & \text{otherwise,} \end{cases} \tag{5.14}$$

and for small $\tau$

$$K_{\text{2GOE}}(\tau) = 4\tau - 8\tau^2 + 16\tau^3 \mp \dots \quad \text{for} \quad \tau \ll 1. \tag{5.15}$$

## 5.1.2  Time scales

In Sec. 3.2.1 the time scales occurring in the designed system $F_{\text{pb,rot}}$ are discussed. Besides the Heisenberg time of the total system $t_\text{H} = N$ and the Heisenberg time $t_{\text{H},i} = N_{\text{ch},i} = A_{\text{access},i}N = A_{\text{access},i}t_\text{H}$ associated with some phase-space region $A_{\text{access},i}$, the dwell time in region $i$, Eq. (3.37),

$$t_{\text{dwell},i} = \frac{A_{\text{access},i}}{\Phi} \quad i = 1, 2, \tag{5.16}$$

is important to describe the impact of the partial barrier connecting the two chaotic sub-systems. According to Eq. (3.40) the ratio of the flux and Planck's constant can be related to the ratio of the Heisenberg time and the dwell time of the sub-system $i$

$$\frac{\Phi}{h_{\text{eff}}} = \frac{t_{\text{H},i}}{t_{\text{dwell},i}} \quad i = 1, 2. \tag{5.17}$$

For open systems this ratio corresponds to the number of channels in the opening and we will use $n$ as abbreviation of the ratio in Eq. (5.17) for reasons of readability.

### 5.1.3  Results for the designed map $F_{\text{pb,rot}}$

We consider the map $F_{\text{pb,rot}}$ introduced in Sec. 3.1.6, whose classical phase space is composed of two chaotic regions and a turnstile of size $\Phi$ connecting them. To investigate the transition from two uncoupled chaotic spectra to one chaotic spectrum for increasing ratio $n = \Phi/h_{\text{eff}}$, we remove the regular levels from the resulting spectrum. Identifying regular states is possible since they are localized in momentum space around $p = 0$ or $1$ by means of periodic boundary conditions. Therefore we calculate the variance around $p = 0$ for each eigenstate $\psi$ using its momentum representation $\psi(p_i) = \langle p_i | \psi \rangle$ as

$$\sum_{i=0}^{N/2-1} |\psi(p_i)|^2 (p_i - 0)^2 + \sum_{i=N/2}^{N} |\psi(p_i)|^2 (p_i - 1)^2. \tag{5.18}$$

Regular states have small variance compared to the chaotic states and therefore can be extracted. We remove $N_{\text{reg}} = \lceil A_{\text{reg}} N \rceil$ states. The remaining chaotic levels are used to determine $K(\tau)$ according to Eq. (5.3) taking $N_{\text{ch}} = N - N_{\text{reg}}$ as total number of states. We averaged the data over the Bloch phase $\theta_q$ as system average in order to smoothen the resulting $K(\tau)$, because $K(\tau)$ is not self-averaging [87]. In the following we restrict ourselves to the case of upper and lower chaotic region being equal in size, which yields the same dwell time for both, $t_{\text{dwell},1} = t_{\text{dwell},2}$.

The determined spectral form factor $K(\tau)$ for the map $F_{\text{pb,rot}}$ is shown in Fig. 5.1 for different ratios $n = \Phi/h_{\text{eff}}$. Our findings have to be compared with the two limiting cases of one large GOE, Eq. (5.8), and the uncorrelated superposition of two GOE spectra, Eq. (5.14). For increasing ratio $n = \Phi/h_{\text{eff}}$ we find a transition from the uncorrelated superposition of two GOE matrices to one GOE matrix. Furthermore, each curve follows the result of two uncorrelated GOE spectra at times smaller than the dwell time $t_{\text{dwell},i}$, which is indicated by an arrow, and the result of one GOE spectrum at times larger than $t_{\text{dwell},i}$. As discussed in Sec. 3.2.1 at times smaller than the dwell time a typical classical orbit will not have visited the second region and therefore semiclassically the spectral properties of the quantum system are described by the uncorrelated superposition of two GOE spectra. At times large compared to the dwell time,
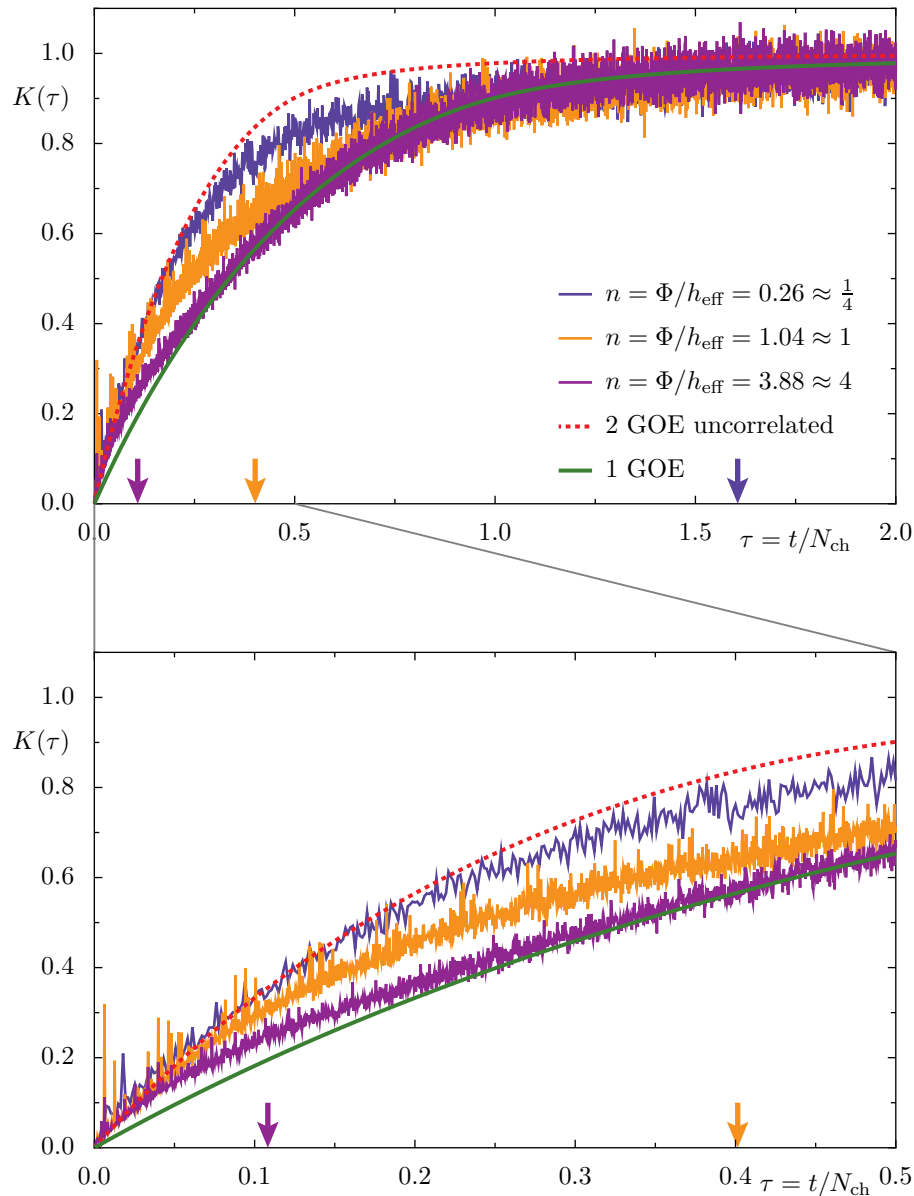
**Figure 5.1:** $K(\tau)$ for the map $F_{\mathrm{pb,rot}}$ for different ratios $n = \Phi/h_{\mathrm{eff}} = t_{\mathrm{H},i}/t_{\mathrm{dwell},i}$. The shown data are of example 3 ($\Phi \approx 1/3000$) using $1/h_{\mathrm{eff}} = 800$ and $3200$ as well as example 2 ($\Phi \approx 1/800$) using $1/h_{\mathrm{eff}} = 3200$. These data sets illustrate the typical behavior and we find scaling with $\Phi/h_{\mathrm{eff}}$ (not shown). The data is averaged over 1000 values of the Bloch phase $\theta_q$. The lower picture is a magnification of the upper for small $\tau$. The arrows indicate the dwell time in one of the chaotic regions $t_{\mathrm{dwell},i}$ in multiples of the Heisenberg time $t_{\mathrm{H,ch}} = N_{\mathrm{ch}}$ of the chaotic sea. The results for the map $F_{\mathrm{pb,rot}}$ lie in between the curves of the uncorrelated superposition of two GOE spectra (dashed red line; Eq. (5.14)) and one GOE spectrum (solid green line; Eq. (5.8)).

classical orbits will explore the second region and semiclassically the spectral properties are described by one GOE spectrum. At the dwell time the resulting $K(\tau)$ curves are half way between the two limiting cases.

## 5.1.4 Description of the results

The aim of this section is to discuss descriptions of the results presented in the previous section. The first paper on the issue of transport limitation due to partial barriers in the context of the spectral form factor is Ref. [65] of Smilansky, Tomsovic, and Bohigas from 1992. They discuss the implication of the finite probability to go from one region to another on the form factor. By expressing the form factor in terms of periodic orbits and performing Berry's diagonal approximation [88] they rewrite the spectral form factor for time reversal invariant systems as

$$K(\tau) = 1 - b(\tau) \approx 2\tau I(\tau), \tag{5.19}$$

where $I(\tau)$ is an averaged sum over periodic orbits. They point out that $I(\tau)$ has a simple classical interpretation. It is the probability that a given orbit returns to its initial point after time $\tau$ in multiples of the probability of being found anywhere in the phase space. This interpretation is valid as long as the mixing time is smaller than all other time scales involved, Heisenberg time and dwell time. Using the Master-equation approach discussed in Sec. 3.3.1 they are able to determine $I(\tau)$ and to give an estimate for $K(\tau)$, [65, Eq. (2.19)]),

$$K_{\mathrm{STB}}(\tau) = 2\tau \left[1 + \exp\{-\Gamma\tau\}\right], \tag{5.20}$$

with the decay rate of a state nonuniformly distributed with respect to the two regions of volumes $V_1$ and $V_2$

$$\Gamma = \Phi_{\mathrm{H}} \left[V_1^{-1} + V_2^{-1}\right], \tag{5.21}$$

where $\Phi_{\mathrm{H}}$ is the flux between these regions per Heisenberg time. Both terms in Eq. (5.21) can be rewritten using the flux per unit time $\Phi$ and the Heisenberg time $t_{\mathrm{H,ch}}$ as

$$\frac{\Phi_{\mathrm{H}}}{V_i} = \frac{\Phi \cdot t_{\mathrm{H,ch}}}{V_i} = \frac{t_{\mathrm{H,ch}}}{t_{\mathrm{dwell},i}} = \frac{t_{\mathrm{H},i}}{f_i t_{\mathrm{dwell},i}} \tag{5.22}$$

with the fraction of region $i$ relative to the chaotic sea $f_i$. The ratio of $t_{\mathrm{H},i}$ and $t_{\mathrm{dwell},i}$ for region $i$ can be replaced by $\Phi/h_{\mathrm{eff}}$ for the quantum map, according to Eq. (5.17),

$$\Gamma = \frac{\Phi}{h_{\mathrm{eff}}} \left[f_1^{-1} + f_2^{-1}\right]. \tag{5.23}$$

For the case of two chaotic regions of equal size $f_1 = f_2 = \frac{1}{2}$ we obtain for Eq. (5.20)

$$K_{\mathrm{STB}}(\tau) = 2\tau \left[1 + \exp\left\{-4\frac{\Phi}{h_{\mathrm{eff}}}\tau\right\}\right] = \begin{cases} 4\tau & \text{for} \quad \frac{\Phi}{h_{\mathrm{eff}}} \to 0 \\ 2\tau & \text{for} \quad \frac{\Phi}{h_{\mathrm{eff}}} \to \infty. \end{cases} \tag{5.24}$$

As a function of $n = \Phi/h_{\text{eff}}$ the spectral form factor performs a smooth and monotonous transition between the linear behavior $4\tau$ of two uncorrelated GOE spectra, Eq. (5.15), and $2\tau$ of one GOE spectrum, Eq. (5.9), which can be seen in Fig. 5.2. The Taylor expansion of Eq. (5.24) reads

$$K_{\text{STB}}(\tau) = 4\tau - 8\frac{\Phi}{h_{\text{eff}}}\tau^2 + 16\left(\frac{\Phi}{h_{\text{eff}}}\right)^2\tau^3 \mp \ldots \quad \text{for} \quad \tau \ll 1 \tag{5.25}$$

For a finite ratio $\Phi/h_{\text{eff}}$ the linear behavior is $4\tau$ and thus at small times always the result of two GOE spectra is recovered. This is in agreement with our previous findings that at small times compared to the dwell time the second region is not resolved and the spectral properties are described by two independent spectra.

The data of map $F_{\text{pb,rot}}$ strongly fluctuates. At small $\tau$ it is even larger than the 2-GOE prediction. Therefore the diagonal approximation might not yield good agreement. In order to achieve better agreement with our results, Kuipers calculated the spectral form factor for two chaotic systems connected with each other by summing over periodic orbits [89]. The only parameter is the number of channels $n$. It determines the strength of the coupling and is given by the ratio of the Heisenberg and the dwell time in one region,

$$n = \frac{t_{\text{H},i}}{t_{\text{dwell},i}} = \frac{\Phi}{h_{\text{eff}}}, \tag{5.26}$$

as discussed earlier. The resulting spectral form factor is [89]

$$\begin{aligned} K_{\text{JK}}(\tau) = {}& 2\tau[1 + \exp\{-4n\tau\}] && \ldots \text{diagonal contribution} \\ & - 2\tau^2[1 + \exp\{-4n\tau\}] - 4\tau^2[1 - n\tau]\exp\{-4n\tau\} && \ldots \text{Sieber-Richter,} \end{aligned} \tag{5.27}$$

where we explicitly indicated the diagonal contribution and the contribution by Sieber-Richter pairs of periodic orbits. The diagonal contribution is exactly the same as the result of Ref. [65] derived using a Master equation rewritten in Eq. (5.24) using Eq. (5.26). This is consistent, as both are diagonal approximations of the spectral form factor.

Figure 5.3 shows a magnification of the map data shown in Fig. 5.1 including the prediction of Smilansky et al., Eq. (5.24), and the prediction of Kuipers, Eq. (5.27). The data for map $F_{\text{pb,rot}}$ strongly fluctuates for small $\tau$ and significantly exceeds the 2-GOE result. Therefore fitting the linear regime is not useful and we find agreement for the diagonal approximation only for the largest ratio $n = \Phi/h_{\text{eff}} = 4$ (lowest curve). Adding the second order term in $K(\tau)$ seems to underestimate the determined $K(\tau)$. Adding more terms might yield better agreement, but has not been done up to now.

Next we compare the resulting $K(\tau)$ for $F_{\text{pb,rot}}$ to those of the matrix model proposed by Bohigas, Tomsovic, and Ullmo (see Sec. 4.2) and the channel coupling model (see Sec. 4.3).
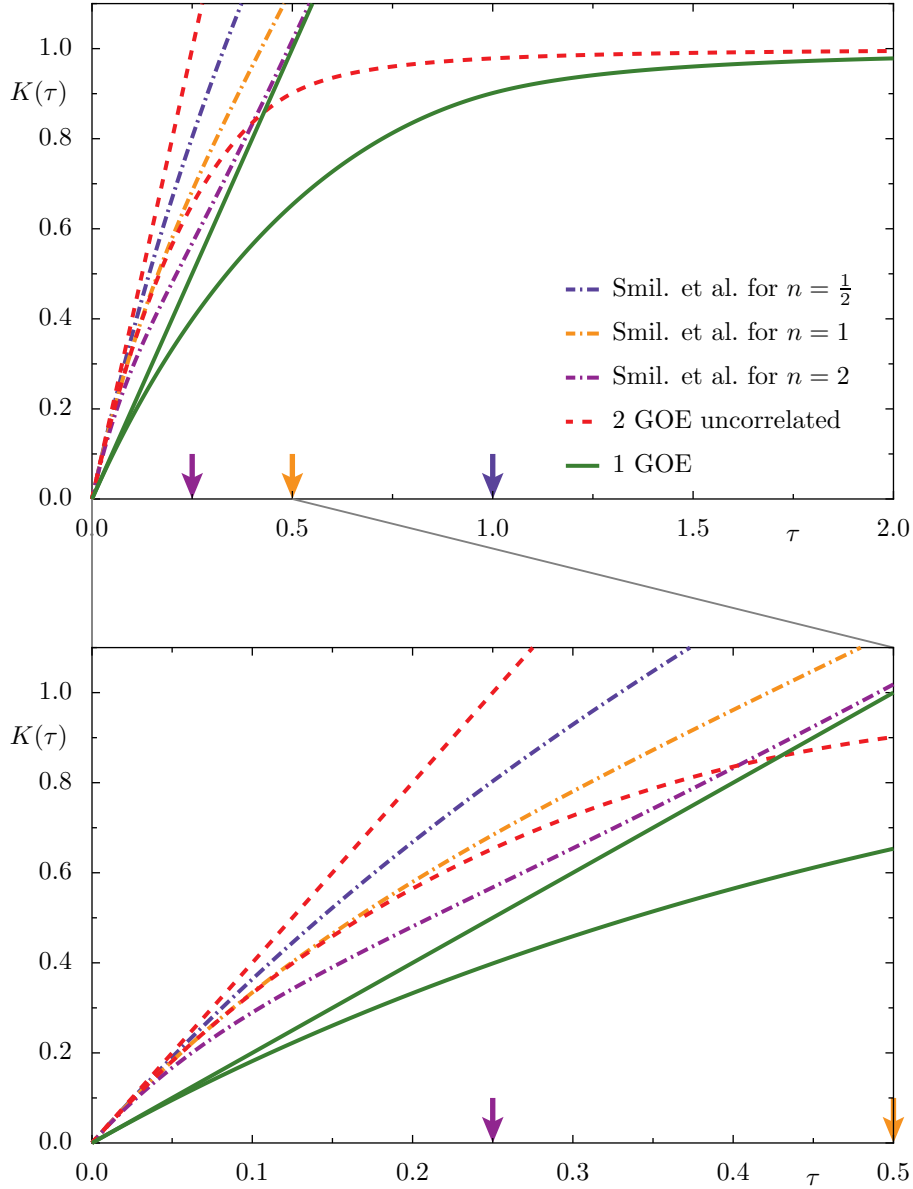
**Figure 5.2:** The estimation of Smilansky et al. of $K(\tau)$ in Eq. (5.24) for different $n = \Phi/h_{\mathrm{eff}}$ (dash-dotted lines) in comparison to the result of an uncorrelated superposition of two GOE spectra (dashed red line; Eq. (5.14) and linear approximation $2\tau$) and one GOE spectrum (solid green line; Eq. (5.8) and linear approximation $4\tau$). The arrows indicate the dwell time in one of the chaotic regions $t_{\mathrm{dwell},i}$ in multiples of the Heisenberg time. The lower picture is a magnification of the upper for small $\tau$.

This is done in Fig. 5.4(a) and (b), respectively. For the BTU model we use $\Lambda = n/\pi^2$ (see $\Lambda$-flux relation in Sec. 3.2.2) in order to relate the data with the ratio $n = \Phi/h_{\mathrm{eff}}$. Using this, one may also define a dwell time of one region in multiples of the total Heisenberg time for the BTU model using

$$\frac{t_{\mathrm{dwell},i}}{t_{\mathrm{H}}} = \frac{t_{\mathrm{dwell},i}}{2t_{\mathrm{H},i}} = \frac{1}{2n} = \frac{1}{2\pi^2\Lambda}. \tag{5.28}$$
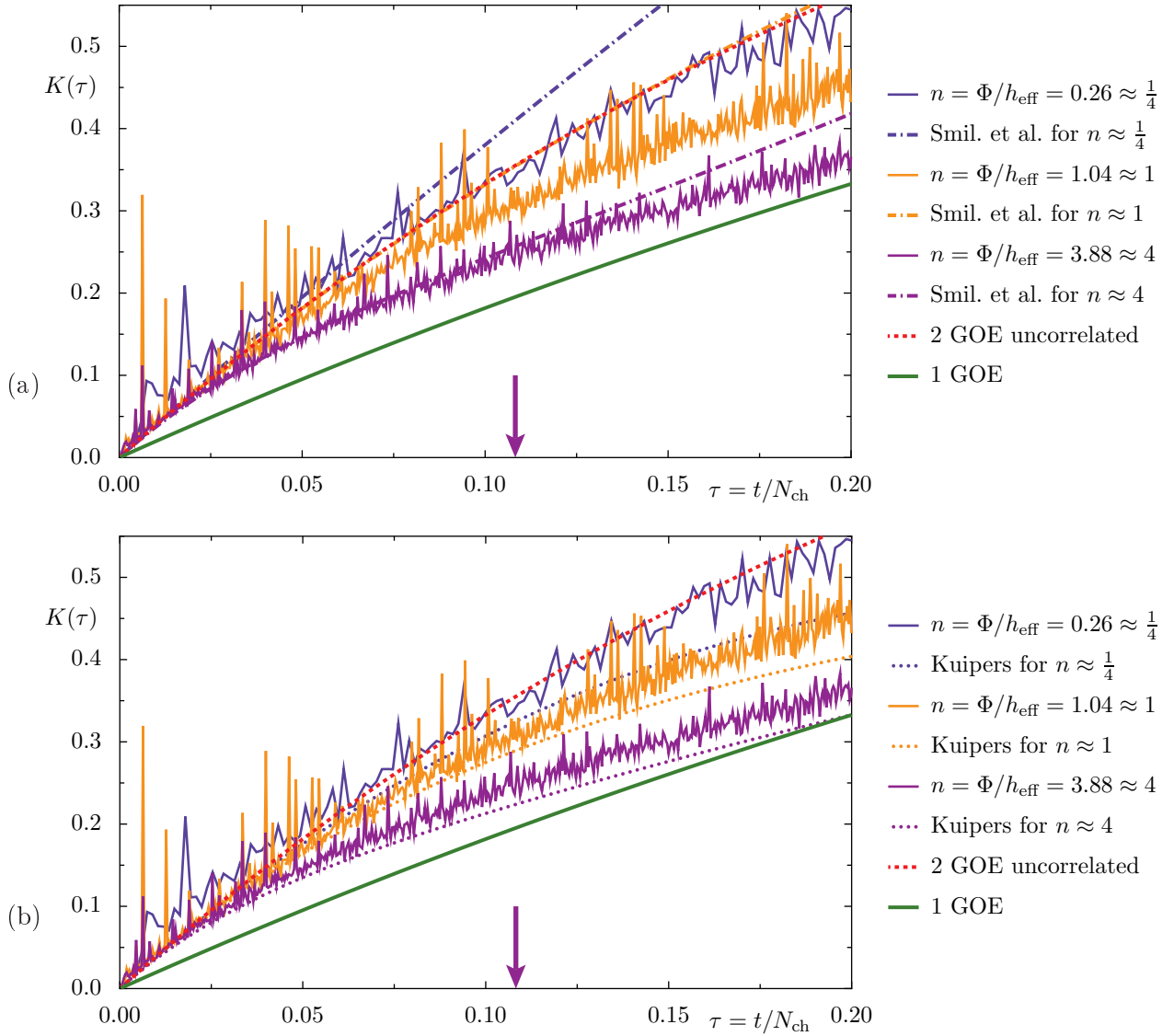
**Figure 5.3:** Magnification of Fig. 5.1 for small $\tau$. For comparison the diagonal approximation Eq. (5.24) of Smilansky et al. (dash-dotted) in (a) and the result including Sieber-Richter pairs Eq. (5.27) of Kuipers (dotted) in (b) are shown. Again the arrows indicate the position of the dwell time.

The results for the BTU model for $n \leq 1$ lie below the form factor $K(\tau)$ for the map $F_{\text{pb,rot}}$, Fig. 5.4(a). This means for the same scaling parameter the BTU model is ahead of the map $F_{\text{pb,rot}}$ on the transition towards one GOE, which is consistent with the findings for the ATW and the average product measure in Chap. 3. For large $n = \Phi/h_{\text{eff}}$ the BTU and the map data are quite close to each other. For the channel coupling we find reasonable agreement with the spectral form factor of the map $F_{\text{pb,rot}}$, Fig. 5.4(b), similar to the observations for the ATW. Therefore again we conclude that for $n$ being small there arise differences between the BTU and the channel coupling model, where the latter seems to describe the data of the map $F_{\text{pb,rot}}$ better.
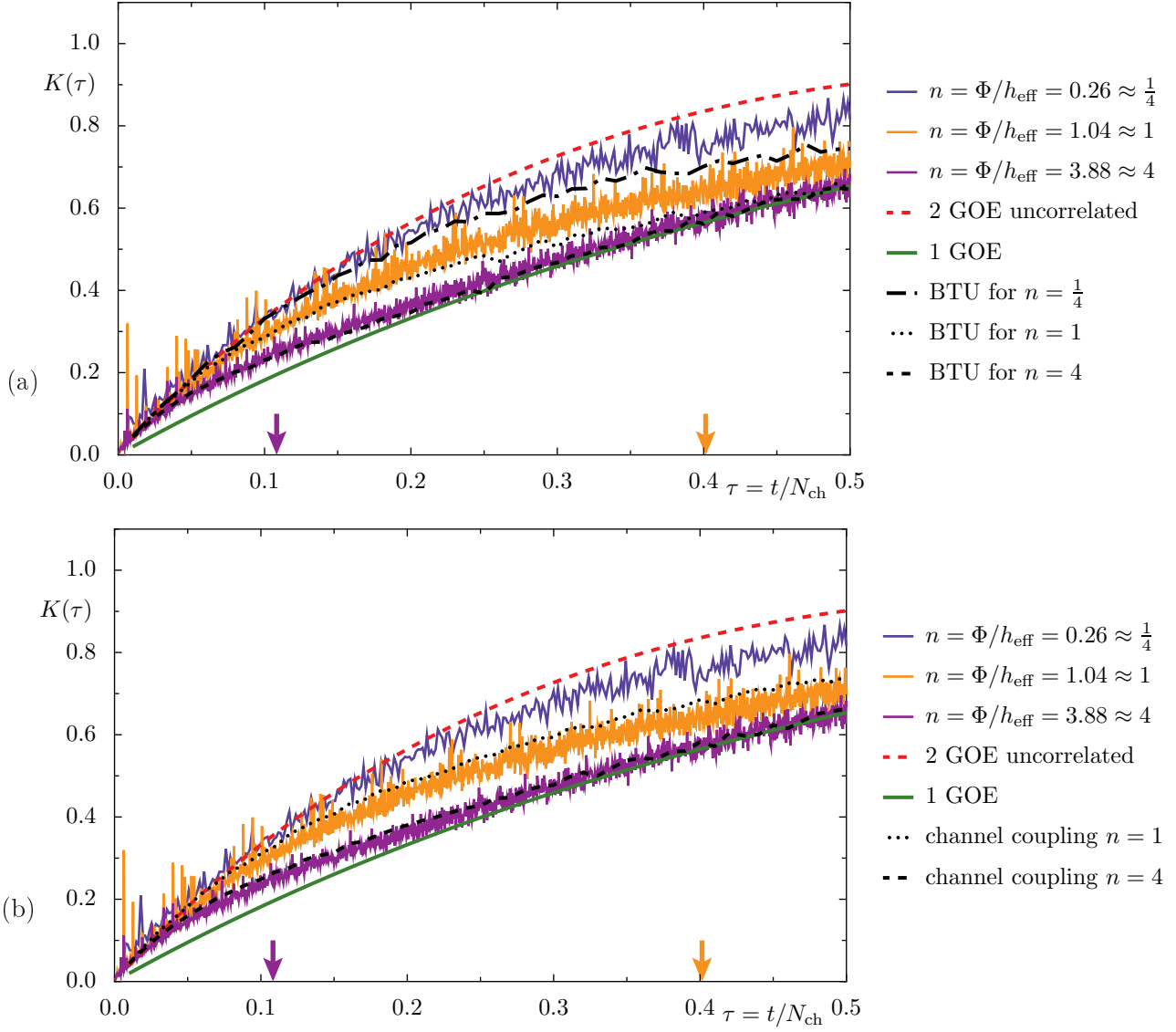
**Figure 5.4:** Data of Fig. 5.1 in comparison to the resulting $K(\tau)$ for (a) the BTU matrix discussed in Sec. 4.2 model and (b) the channel coupling model discussed in Sec. 4.3.

Note that the overall shape of the BTU model is quite well described, by an interpolation between $K_{\mathrm{GOE}}(\tau)$ and $K_{\mathrm{2GOE}}(\tau)$ based on the diagonal part proposed by Kuipers [89],

$$K_{\mathrm{interpolation}}(\tau) = [1 - \exp\{-4n\tau\}] \cdot K_{\mathrm{GOE}}(\tau) + \exp\{-4n\tau\} \cdot K_{\mathrm{GOE}}(2\tau). \tag{5.29}$$

## 5.2  Nearest-neighbor level-spacing distribution $P(s)$

The nearest-neighbor level-spacing distribution is one of the most important tools to determine properties of level spectra [68, 82, 90, 91]. It is suitable to measure features of the involved coupling strengths, which govern the distribution at small energy spacings [92, 93].

## 5.2.1  Definition of the nearest-neighbor level-spacing distribution

As we study spacing statistics of quantum maps we unfold the spectrum of eigenphases

$$\varphi_k \mapsto \frac{N_{\mathrm{ch}}\varphi_k}{2\pi} \quad \text{for} \quad k = 1, ..., N_{\mathrm{ch}}. \tag{5.30}$$

Note that the number of considered levels occurs here, which equals the number of chaotic states $N_{\mathrm{ch}}$ in the map system. For monotonically increasing eigenphases $\varphi_k$, we define the nearest-neighbor level-spacing as [82]

$$s_k := \frac{N_{\mathrm{ch}}}{2\pi}(\varphi_{k+1} - \varphi_k) \tag{5.31}$$

and consider its distribution $P(s)$. By construction it is normalized and has unit mean level spacing, i.e.

$$\int_0^\infty \mathrm{d}s\, P(s) = 1, \tag{5.32}$$

$$\int_0^\infty \mathrm{d}s\, s\, P(s) = 1. \tag{5.33}$$

For time reversal invariant systems, which have the same spectral properties as GOE random matrices, the level-spacing distribution $P(s)$ is reasonably well described by the Wigner surmise,

$$P_{\mathrm{ch}}(s) = \frac{\pi f_{\mathrm{ch}}^2 s}{2} \exp\left\{-\frac{\pi f_{\mathrm{ch}}^2 s^2}{4}\right\}. \tag{5.34}$$

It only depends on the fraction of chaotic states $f_{\mathrm{ch}}$, which is the density of levels in the unfolded spectrum (mean level spacing $1/f_{\mathrm{ch}}$). $P(s)$ increases linearly for small $s$. That is, neighboring levels tend to repel each other. This behavior is typical for chaotic systems and is referred to as level repulsion [68].

In order to derive the level-spacing distribution $P(s)$ for the uncorrelated superposition of subspectra, one has to introduce the gap probability $Z(s)$ [91]. We define the following quantities

$$F(s) = \int_s^\infty \mathrm{d}s' P(s'), \tag{5.35}$$

$$Z(s) = \int_s^\infty \mathrm{d}s' F(s'). \tag{5.36}$$

Here, $F(s)$ is the probability that there is a spacing greater or equal to $s$ and $f \cdot Z(s)$ characterizes the probability that an interval of length $s$ is a gap in the considered spectrum. These quantities

can also be defined for each sub-spectrum individually. For a time reversal invariant sub-system of size $f_{\rm ch}$ these quantities are integrated versions of the Wigner surmise in Eq. (5.34)

$$F_{\rm ch}(s) = \exp\left\{-\frac{\pi f_{\rm ch}^2 s^2}{4}\right\}, \tag{5.37}$$

$$Z_{\rm ch}(s) = \frac{2}{f_{\rm ch}\sqrt{\pi}} \int\limits_{\sqrt{\pi}f_{\rm ch}s/2}^{\infty} {\rm d}x \exp\left\{-x^2\right\}. \tag{5.38}$$

For the uncorrelated superposition of sub-spectra with densities $f_{\rm ch,1}$ and $f_{\rm ch,2}$ the gap probability of the total spectrum is given by the product of the individual contributions [91]

$$Z(s) = f_{\rm ch,1}Z_{\rm ch,1}(s)f_{\rm ch,2}Z_{\rm ch,2}(s). \tag{5.39}$$

The latter property is plausible, because of the meaning of $Z(s)$. That is, we will find a gap of size $s$ in the total spectrum if both spectra have a gap of size $s$. The corresponding level-spacing distribution $P(s)$ can be derived by differentiating the gap probability $Z(s)$ twice. This gives

$$P(s) = f_{\rm ch,1}P_{\rm ch,1}(s)f_{\rm ch,2}Z_{\rm ch,2}(s) + f_{\rm ch,1}Z_{\rm ch,1}(s)f_{\rm ch,2}P_{\rm ch,2}(s) + 2f_{\rm ch,1}F_{\rm ch,1}(s)f_{\rm ch,2}F_{\rm ch,2}(s). \tag{5.40}$$

The first term of the sum corresponds to spacings from the first sub-spectrum embedded inside a gap of the second sub-spectrum and the second term originates from spacings from the second sub-spectrum embedded inside a gap of the first. The last term in Eq. (5.40) counts spacings between a level of the first sub-spectrum and a level of the second sub-spectrum. For small $s$ the first two terms exhibit level repulsion due to $P_{\rm ch,i}(s)$. However, the last term gives a constant offset $2f_{\rm ch,1}f_{\rm ch,2}$ for small spacings, because $F_{\rm ch,i}(s \approx 0) = 1$. Thus, the level repulsion of the individual sub-spectra is destroyed due to clustering of levels from distinct sub-spectra.

For the uncorrelated superposition of two GOE spectra of equal size ($f_{\rm ch,1} = f_{\rm ch,2} = \frac{1}{2}$) the spacing distribution is

$$P(s) = \frac{1}{2}P_{\rm ch}\left(s, f_{\rm ch} = \frac{1}{2}\right) Z_{\rm ch}\left(s, f_{\rm ch} = \frac{1}{2}\right) + \frac{1}{2}F_{\rm ch}^2\left(s, f_{\rm ch} = \frac{1}{2}\right) \tag{5.41}$$

with $P_{\rm ch}, F_{\rm ch}$, and $Z_{\rm ch}$ given in Eqs. (5.34), (5.37), and (5.38), respectively. For $s = 0$ we find $P(s = 0) = \frac{1}{2}$, which determines the probability $P(s \approx 0){\rm d}s$ to have two levels of different sub-spectra at distance smaller than ${\rm d}s$. Levels of different spectra do not repel each other and therefore yield nonzero $P(s = 0)$.

## 5.2.2 Results for the designed map $F_{\rm pb,rot}$

In order to determine the spacing distribution for the chaotic levels of the designed map $F_{\rm pb,rot}$, we remove the regular levels from the spectrum as discussed in Sec. 5.1.3. The resulting spacing

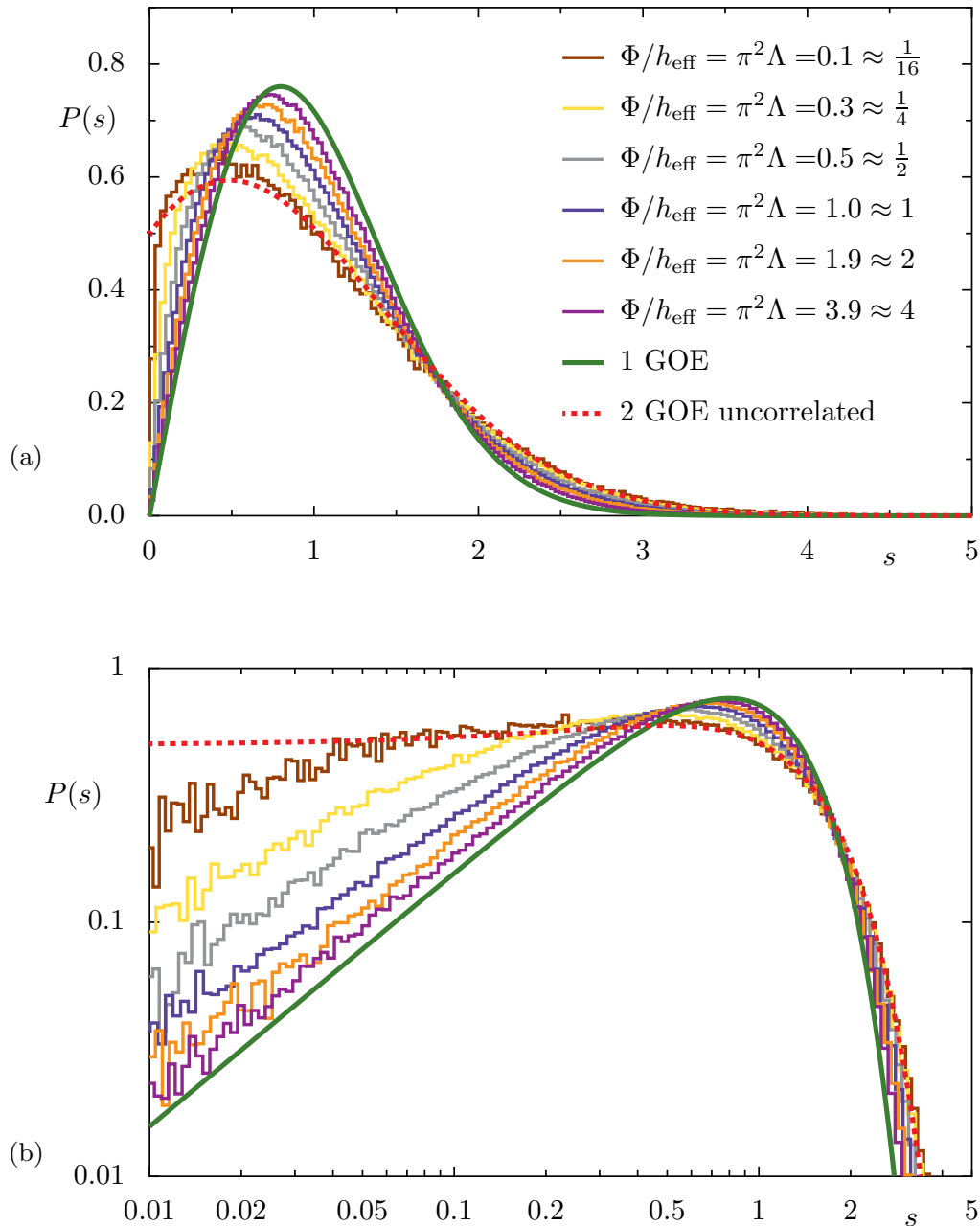**Figure 5.5:** Level-spacing distribution $P(s)$ of the map $F_{\mathrm{pb,rot}}$ for different ratios $\Phi/h_{\mathrm{eff}} = \pi^2\Lambda$. The parameters for the numerical data of the map $F_{\mathrm{pb,rot}}$ are given in Tab. 5.1. Their displayed histograms lie in between the curve for the uncorrelated superposition of two GOE spectra (dashed red line; Eq. (5.41)) and the Wigner surmise for one GOE spectrum (solid green line; Eq. (5.34)). The lower picture shows the same distributions on a double-logarithmic scale, which reveals a power-law increase $s^\beta$ for small $s$ with exponent $\beta$ between 0 (uncorrelated superposition of two GOE) and 1 (one GOE).

distributions for several ratios $\Phi/h_{\mathrm{eff}} = \pi^2\Lambda$ are shown in Fig. 5.5. The shown data sets illustrate the typical behavior and we find scaling with the ratio $\Phi/h_{\mathrm{eff}}$ as in Chap. 3. Moreover we vary the width of the regular region as described in Sec. 3.3.5 and find no dependence of $P(s)$ on this width. That is, the behavior of $P(s)$ is determined by the properties of the partial barrier only.

For increasing coupling parameter $\Phi/h_{\mathrm{eff}}$ the results perform a transition from two uncoupled GOE spectra, Eq. (5.41), to one GOE spectrum, Eq. (5.34). The lower picture of Fig. 5.5 shows the distribution on a double-logarithmic scale to emphasize the behavior of small spacings $s$. The increase is algebraically $s^\beta$ with an exponent $\beta$ increasing from zero to one for increasing $\Phi/h_{\mathrm{eff}}$.

Now we consider the BTU matrix model, discussed in Sec. 4.2. This model incorporates a typical coupling strength, Eq. (4.32), $v = D \cdot \sqrt{\Lambda}$ with the mean level spacing of the uncorrelated superposition $D$ (considering levels around $E = 0$ like in Sec. 4.2) and the scaling parameter $\Lambda$. The corresponding nearest-neighbor spacing-distribution is studied in Ref. [40, 70, 71, 76] and an analytic expression is derived in Ref. [92]. The main idea of the analytic expression is to replace the second term of Eq. (5.41), namely the contribution of levels from distinct sub-spectra by a first order perturbation expansion. The level spacings of the uncorrelated superposition $s_0$ are replaced by $s = \sqrt{s_0^2 + \bar{v}^2}$, where the unfolded coupling strength $\bar{v}$ enters, which is given by $\bar{v} = v/D = \sqrt{\Lambda}$. In Fig. 5.6 the distributions are plotted for various $\Lambda$. Because they agree excellently with numerical determined histograms, we only show the analytic prediction. Again for increasing coupling strength we find a transition from two uncoupled GOE spectra to one GOE spectrum, but the transition behavior is quite different from Fig. 5.5. This is most prominent seen in the lower picture, which shows the distribution on a double-logarithmic scale. For one typical coupling strength $P(s)$ increases linearly for $s$ below this coupling strength. No fractional power-law behavior as shown in Fig. 5.5 for map $F_{\mathrm{pb,rot}}$ is found.

Figure 5.7 shows the level-spacing distribution for the channel coupling model introduced in Sec. 4.3. The $P(s)$ distributions for $n = 1$, 2, and 4 are in good agreement with the $P(s)$ for the map $F_{\mathrm{pb,rot}}$ in Fig. 5.5 for $\Phi/h_{\mathrm{eff}} = 1$, 2, and 4. This is consistent with our findings that the ATW of the map is well described by the channel coupling model (see Sec. 4.3). The shown $P(s)$ distributions in Fig. 5.7 also indicate the power-law behavior found for the map data in Fig. 5.5. For the original channel coupling model the number of propagating modes $n$ cannot be smaller than one. Therefore further investigations are needed to search for a power-law behavior in the channel coupling model, e.g. by use of the extension discussed in Sec. 4.3.4.

| Example | flux $\Phi$ | $N = 1/h_{\mathrm{eff}}$ | $\Phi/h_{\mathrm{eff}}$ |
|---|---|---|---|
| 3 | $\approx 1/3000$ | 200 | $\approx 1/16$ |
| 3 | $\approx 1/3000$ | 800 | $\approx 1/4$ |
| 3 | $\approx 1/3000$ | 1600 | $\approx 1/2$ |
| 3 | $\approx 1/3000$ | 3200 | $\approx 1$ |
| 2 | $\approx 1/800$ | 1600 | $\approx 2$ |
| 2 | $\approx 1/800$ | 3200 | $\approx 4$ |

**Table 5.1:** Considered examples and used total number of states $N = 1/h_{\mathrm{eff}}$ of the data shown in Fig. 5.5. The parameters for the examples are given in Tab. 3.1 and Tab. 3.2. Each data set is collected over 1000 values of the Bloch phase $\theta_q$.
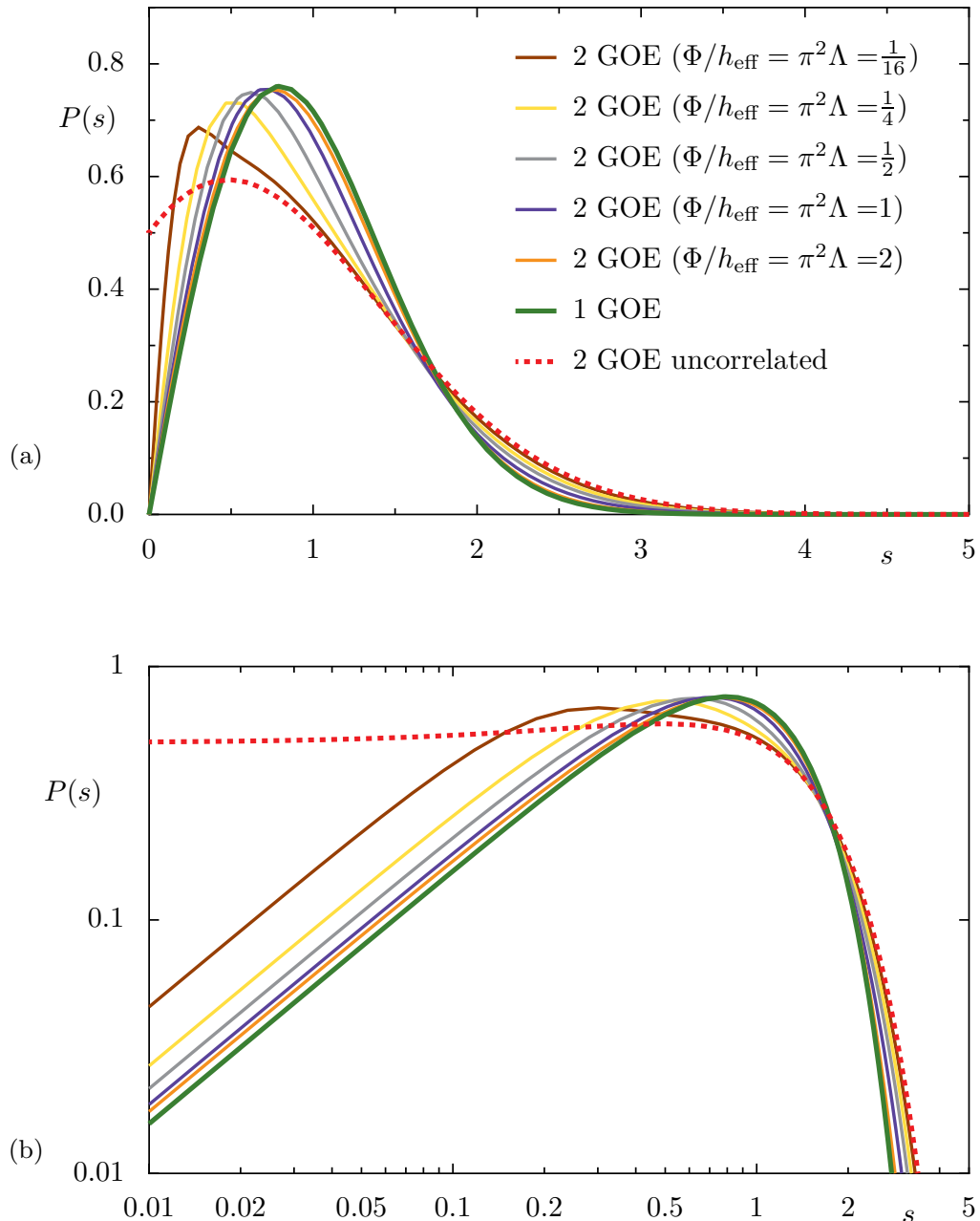
**Figure 5.6:** Analytic level-spacing distribution $P(s)$ for two chaotic regions, which are coupled via one typical coupling strength $v$ determined by $v/D = \sqrt{\Lambda}$. These distributions are in excellent agreement with numerically determined $P(s)$ distributions for the BTU matrix model [92]. For increasing coupling strength $\Lambda$ the distributions perform a transition from two uncoupled GOE spectra to one GOE spectrum. For spacings smaller than the coupling strength $\sqrt{\Lambda}$ the distributions increase linearly similar to the GOE spectrum.

According to Ref. [93] a fractional power-law behavior in $P(s)$ indicates that the coupling between the two sub-systems cannot be described by a single number, rather several different coupling strengths need to be considered. That is, the couplings are distributed according to a power-law or a sum of Gaussian distributions with different variance. In Ref. [93] the coupling
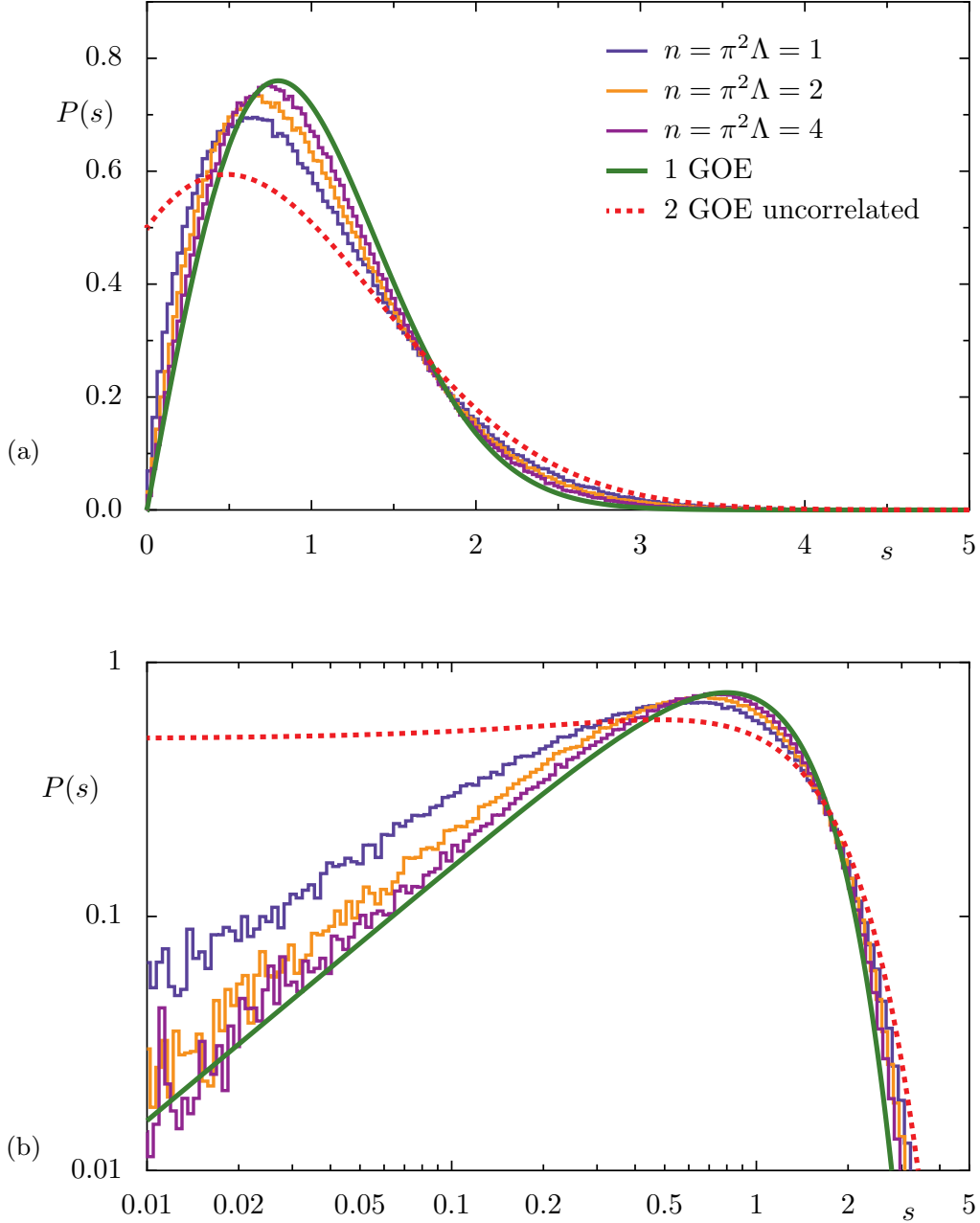
**Figure 5.7:** Level-spacing distribution $P(s)$ for the channel coupling model ($N_{\mathrm{up}} = N_{\mathrm{lo}} = 500$ and according to Eq. (4.76) $\sigma = 1/(4N_{\mathrm{up}})$) and number of propagating modes $n = 1, 2, 4$. The shown distributions include levels of $10^4$ random matrices, where $10\%$ of levels around $E = 0$ are considered.

of regular and chaotic states is investigated. However, on the level of the used $2 \times 2$-model description this is just the same as two chaotic regions being coupled. Therefore we attribute the difference of the nearest-neighbor distribution of map $F_{\mathrm{pb,rot}}$ and the BTU matrix model to different distributions of couplings between states of the upper and the lower chaotic region. For the BTU matrix model this distribution is Gaussian and we deduce a power-law distribution or at least a sum of Gaussian distributions with different variance from the found $P(s)$.

# 6 Summary and outlook

In this thesis we study the impact of partial barriers, which limit the transport between chaotic regions in phase space. Classically these partial barriers lead to a drastic change in the distribution of recurrence times. It changes from exponential, in the fully chaotic case, to algebraic for the chaotic component of a mixed phase space, in which partial barriers are arranged in a hierarchical manner. They limit the transport for intermediate times. At large times, however, one expects that almost all chaotic orbits spread uniformly into the whole chaotic region as if there was no barrier.

Quantum mechanically these partial barriers are even more restrictive and quantum suppression of transport is found, if the effective Planck's constant $h_{\text{eff}}$ is larger than the classical flux $\Phi$, $h_{\text{eff}} \gg \Phi$. That is, time evolved wave packets cannot pass the partial barrier and will therefore localize in the initial region. In the opposite regime where $h_{\text{eff}}$ is much smaller than the classical flux, $h_{\text{eff}} \ll \Phi$, the wave packets follow the classical transport across the partial barrier. At large times they extend uniformly over the whole chaotic region as if there was no barrier. In between the limiting cases one finds a transition.

The aim of this thesis is to quantify this quantum transition of a partial barrier between quantum suppression and classical transport. For this we introduce the asymptotic transmitted weight (ATW), which describes the weight transmitted across the partial barrier at large times. Moreover we relate the ATW to the average of an eigenstate measure, called product measure, which captures the deviation of eigenstates from the uniformly distributed state. If Planck's constant is large compared to the classical flux, $h_{\text{eff}} \gg \Phi$, the ATW and thereby the individual product measure of the eigenstates vanishes. In this limit eigenstates are localized on one side of the partial barrier and have no weight on the other side. In the limit of classical transport, $h_{\text{eff}} \ll \Phi$, all of the chaotic eigenstates are uniformly distributed over both regions and ignore the partial barrier.

For a generic system with a mixed phase space infinitely many partial barriers exist in the chaotic part of phase space and might yield relevant transport barriers. Studying their impact on the corresponding quantum system is a hard task. Therefore we introduce a designed system with a particularly simple phase space, which consists of two chaotic regions, that are separated by one isolated partial barrier. For this system, we numerically find that the ATW scales with the ratio $\Phi/h_{\text{eff}}$. The transition from quantum suppression to classical transport takes place at $\Phi = h_{\text{eff}}$. It has a width of almost two orders of magnitude in $\Phi/h_{\text{eff}}$. Moreover we extend our

considerations to the generic standard map and obtain results that are in good agreement with our findings for the designed map.

In order to quantitatively describe the quantum transition of a partial barrier we discuss several matrix models in Chap. 4. The transition behavior of our map data is well described by a deterministic $2 \times 2$-model, in which each site in the model is associated with one chaotic region. Moreover we evaluate the ATW for the random matrix model proposed by Bohigas, Tomsovic, and Ullmo [23]. We find that this matrix model does not describe the overall behavior of the ATW found for the designed map. Especially for $\Phi/h_{\text{eff}} \lesssim 1$ we find clear deviations. We attribute this difference to the overall Gaussian coupling between all upper and all lower states included in the BTU matrix model. Therefore we propose a channel coupling model to describe the impact of a partial barrier for the quantum system. In this model $n = \Phi/h_{\text{eff}}$ modes can propagate and couple the upper and lower states. We find very good agreement with the map data and conclude that this model is appropriate to describe the bottle-neck of quantum transport across a partial barrier. In addition we consider a smoothed version of the channel coupling model using Fermi-function like transition probabilities and also find good agreement. As an alternative approach we examine unitary matrix models, which allow for a directed transport between the two regions separated by the partial barrier. Also this model describes the transitional behavior of a partial barrier.

Complementary to the investigations of time evolution and eigenstate properties in Chap. 3, we examine the spectral signatures of partial barriers in Chap. 5. As relevant quantities we consider the spectral form factor $K(\tau)$ and the nearest-neighbor level-spacing distribution $P(s)$. For the interpretation of the results for the spectral form factor $K(\tau)$ it is useful to relate the ratio $\Phi/h_{\text{eff}}$ to the Heisenberg time $t_{\text{H},i}$ and the dwell time $t_{\text{dwell},i}$ of region $i$, $\Phi/h_{\text{eff}} = t_{\text{H},i}/t_{\text{dwell},i}$. If the Heisenberg time is small compared to the dwell time, $t_{\text{H},i} \ll t_{\text{dwell},i}$, a typical orbit of the length of the Heisenberg time will not have visited the other region in phase space. In this case semiclassically the quantum spectrum has the same properties as the uncorrelated superposition of two distinct spectra. In the opposite limit $t_{\text{H},i} \gg t_{\text{dwell},i}$ we have classical transport and quantum mechanics resolves the other region, which yields one chaotic spectrum. For fixed $\Phi/h_{\text{eff}} = t_{\text{H},i}/t_{\text{dwell},i}$ we find a transition of the spectral form factor from the result of the uncorrelated superposition of two distinct spectra at small times to the result of one GOE spectrum at large times $t \gg t_{\text{dwell},i}$. We find scaling with the ratio $\Phi/h_{\text{eff}}$ for the spectral form factor $K(\tau)$ and the level-spacing distribution $P(s)$ and observe transitions between the result of the uncorrelated superposition of two GOE spectra to one GOE spectrum for increasing ratio $\Phi/h_{\text{eff}}$. The level-spacing distribution $P(s)$ for small spacings reveals the nature of the coupling between the upper and lower states. We find a power-law behavior $s^{\beta}$ for small spacings $s$ with an exponent $\beta$ between zero, which is the limit of quantum suppression, and one, which corresponds to the level repulsion found in one chaotic system. We attribute this power-law behavior to a distribution of couplings, which clearly differs from the Gaussian distribution with

one typical coupling strength used by the BTU matrix model. However, the channel coupling model is in good agreement with the spectral form factor and the level spacing distribution for our example systems.

In the future one may gain further insight into the complex mechanism behind the quantum suppression of transport by modeling the full time-dependent transmitted weight rather than the ATW only. In order to answer the question whether the transition behavior is governed by the ratio $\Phi/h_{\text{eff}}$ only, further analysis is needed. Especially more examples are required, where the size of the upper and lower chaotic region are different, in order to test the scaling behavior of the transition.

In the regime $\Phi \ll h_{\text{eff}}$ the classical transport is suppressed. If the ratio $\Phi/h_{\text{eff}}$ is small enough, we expect that the main contribution to the transport across the partial barrier originates from tunneling across the barrier rather than turnstile transport. Therefore in this regime we expect a scaling with Planck's constant only. The theoretical description of this tunneling process is an open problem.

Also the introduced designed map allows for further investigations. It can be used to study the tunneling across a single regular torus and to construct a partial barrier due to a cantorus. However, up to now it is not clear how to find a good approximation of the cantorus. If the flux $\Phi$ across the cantorus is large enough to investigate quantum signatures, the approximating orbits are very unstable and therefore numerical approximations fail.

The fact that partial barriers are nontransparent for wave packets with $h_{\text{eff}} \gg \Phi$ might be used for applications, e.g. to build high-pass filters, which discard wave packets of low frequency. Up to now experimentally the quantum transition of a partial barrier is investigated only qualitatively. However, quantitative measurements are required to verify the transitional behavior found in this thesis. Promising candidates for these quantitative measurements are microcavities, in which the impact of partial barriers on the emission properties is of interest, e.g. to build microlasers.

# Bibliography

[1] E. N. Lorenz: *Deterministic Nonperiodic Flow*, J. Atmos. Sci. **20** (1963), 130–141.

[2] E. N. Lorenz: *Atmospheric Predictability as Revealed by Naturally Occurring Analogues*, J. Atmos. Sci. **26** (1969), 636–646.

[3] E. Ott: *Chaos in Dynamical Systems*, (Cambrige University Press, The Pitt Building, Trumpington Street, Cambrige, United Kingdom), 2nd edn., (2002).

[4] L. Markus and K. Meyer: *Generic Hamiltonian Dynamical Systems are neither Integrable nor Ergodic*, no. 114 in Mem. Amer. Math. Soc., (American Mathematical Society, Providence, Rhode Island), (1974).

[5] W. Bauer and G. F. Bertsch: *Decay of ordered and chaotic systems*, Phys. Rev. Lett. **65** (1990), 2213–2216.

[6] B. V. Chirikov and D. L. Shepelyansky: *Statistics of Poincaré Recurrences and the Structure of the Stochastic Layer of a Nonlinear Resonance*, Tech. Rep. PPPL–TRANS–133, Princeton Univ., (1983).

[7] N. Friedman, A. Kaplan, D. Carasso, and N. Davidson: *Observation of Chaotic and Regular Dynamics in Atom-Optics Billiards*, Phys. Rev. Lett. **86** (2001), 1518–1521.

[8] A. Kaplan, N. Friedman, M. Andersen, and N. Davidson: *Observation of Islands of Stability in Soft Wall Atom-Optics Billiards*, Phys. Rev. Lett. **87** (2001), 274101.

[9] G. Contopoulos: *Orbits in Highly Perturbed Dynamical Systems. III. Nonperiodic Orbits*, Astron. J. **76** (1971), 147–156.

[10] B. V. Chirikov: *A universal instability of many-dimensional oscillator systems*, Phys. Rep. **52** (1979), 263–379.

[11] J. M. Greene: *A method for determining a stochastic transition*, J. Math. Phys. **20** (1979), 1183–1201.

[12] C. F. F. Karney: *Long-time correlations in the stochastic regime*, Physica D **8** (1983), 360–380.

[13] B. V. Chirikov and D. L. Shepelyansky: *Correlation properties of dynamical chaos in Hamiltonian systems*, Physica D **13** (1984), 395–400.

[14] R. S. MacKay, J. D. Meiss, and I. C. Percival: *Stochasticity and Transport in Hamiltonian Systems*, Phys. Rev. Lett. **52** (1984), 697–700.

[15] R. S. MacKay, J. D. Meiss, and I. C. Percival: *Transport in Hamiltonian systems*, Physica D **13** (1984), 55–81.

[16] D. Bensimon and L. P. Kadanoff: *Extended chaos and disappearance of KAM trajectories*, Physica D **13** (1984), 82–89.

[17] J. D. Hanson, J. R. Cary, and J. D. Meiss: *Algebraic Decay in Self-Similar Markov Chains*, J. Stat. Phys. **39** (1985), 327–345.

[18] J. D. Meiss: *Class renormalization: Islands around islands*, Phys. Rev. A **34** (1986), 2375–2383.

[19] J. D. Meiss and E. Ott: *Markov-Tree Model of Intrinsic Transport in Hamiltonian Systems*, Phys. Rev. Lett. **55** (1985), 2741–2744.

[20] J. D. Meiss and E. Ott: *Markov Tree Model of Transport in Area- Preserving Maps*, Physica D **20** (1986), 387–402.

[21] R. S. MacKay and J. D. Meiss: *Relation between quantum and classical thresholds for multiphoton ionization of excited atoms*, Phys. Rev. A **37** (1988), 4702–4706.

[22] J. Meiss: *Symplectic maps, variational principles, and transport*, Rev. Mod. Phys. **64** (1992), 795–848.

[23] O. Bohigas, S. Tomsovic, and D. Ullmo: *Manifestations of classical phase space structures in quantum mechanics*, Phys. Rep. **223** (1993), 43–133.

[24] R. C. Brown and R. E. Wyatt: *Quantum mechanical manifestation of cantori: Wave-packet localization in stochastic regions*, Phys. Rev. Lett. **57** (1986), 1–4.

[25] T. Geisel, G. Radons, and J. Rubner: *Kolmogorov-Arnol'd-Moser Barriers in the Quantum Dynamics of Chaotic Systems*, Phys. Rev. Lett. **57** (1986), 2883–2886.

[26] T. Geisel and G. Radons: *Nonlinear phenomena associated with cantori in classical and quantum systems*, Phys. Scripta **40** (1989), 340–345.

[27] N. T. Maitra and E. J. Heller: *Quantum transport through cantori*, Phys. Rev. E **61** (2000), 3620–3631.

[28] C.-M. Goletz, F. Grossmann, and S. Tomsovic: *Investigating quantum transport with an initial value representation of the semiclassical propagator*, Phys. Rev. E **80** (2009), 031101.

[29] K. Vant, G. Ball, H. Ammann, and N. Christensen: *Experimental evidence for the role of cantori as barriers in a quantum system*, Phys. Rev. E **59** (1999), 2846–2852.

[30] R. Ketzmerick, L. Hufnagel, F. Steinbach, and M. Weiss: *A new class of eigenstates in generic Hamiltonian systems*, Phys. Rev. Lett. **85** (2000), 1214–1217.

[31] J.-B. Shim, S.-B. Lee, S. W. Kim, S.-Y. Lee, J. Yang, S. Moon, J.-H. Lee, and K. An: *Uncertainty-Limited Turnstile Transport in Deformed Microcavities*, Phys. Rev. Lett. **100** (2008), 174102.

[32] S. Shinohara, T. Harayama, T. Fukushima, M. Hentschel, T. Sasaki, and E. E. Narimanov: *Chaos-Assisted Directional Light Emission from Microcavity Lasers*, Phys. Rev. Lett. **104** (2010), 163902.

[33] J. Wiersig and M. Hentschel: *Combining Directional Light Output and Ultralow Loss in Deformed Microdisks*, Phys. Rev. Lett. **100** (2008), 033901.

[34] S. Shinohara, M. Hentschel, J. Wiersig, T. Sasaki, and T. Harayama: *Ray-wave correspondence in limaçon-shaped semiconductor microcavities*, Phys. Rev. A **80** (2009), 031801.

[35] J. Yang, S.-B. Lee, J.-B. Shim, S. Moon, S.-Y. Lee, S. W. Kim, J.-H. Lee, and K. An: *Enhanced nonresonant optical pumping based on turnstile transport in a chaotic microcavity laser*, Appl. Phys. Lett. **93** (2008), 061101.

[36] A. Bäcker, R. Ketzmerick, S. Löck, J. Wiersig, and M. Hentschel: *Quality factors and dynamical tunneling in annular microcavities*, Phys. Rev. A **79** (2009), 063804.

[37] A. Bäcker, R. Ketzmerick, and A. G. Monastra: *Flooding of Chaotic Eigenstates into Regular Phase Space Islands*, Phys. Rev. Lett. **94** (2005), 054102 (4 pages).

[38] A. Bäcker, R. Ketzmerick, and A. G. Monastra: *Universality in the flooding of regular islands by chaotic states*, Phys. Rev. E **75** (2007), 066204.

[39] L. Bittrich: *Flooding of Regular Phase Space Islands by Chaotic States*, Ph.D. thesis, Technische Universität Dresden, Fachbereich Physik, (2010).

[40] N. Rosenzweig and C. E. Porter: *"Repulsion of Energy Levels" in Complex Atomic Spectra*, Phys. Rev. **120** (1960), 1698–1714.

[41] B. V. Chirikov: *A universal instability of many-dimensional oscillator systems*, Phys. Rep. **52** (1979), 263–379.

[42] R. S. MacKay: *A Renormalisation Approach to Invariant Circles in Area-Preserving Maps*, Physica D **7** (1983), 283–300.

[43] J. N. Mather: *A criterion for the non-existence of invariant circles*, Publications Mathématiques de l'IHÉS **63** (1986), 153–204.

[44] J. D. Meiss: *Average exit time for volume-preserving maps*, Chaos **7** (1997), 139–147.

[45] G. M. Zaslavsky, M. Edelmann, and B. A. Niyazov: *Self-similarity, renormalization, and phase space nonuniformity of Hamiltonian chaotic dynamics*, Chaos **7** (1997), 159–181.

[46] G. M. Zaslavsky and M. Edelmann: *Hierarchical structures in the phase space and fractional kinetics: I. Classical systems*, Chaos **10** (2000), 135–146.

[47] M. Weiss, L. Hufnagel, and R. Ketzmerick: *Universal Power-Law Decay in Hamiltonian Systems?*, Phys. Rev. Lett. **89** (2002), 239401.

[48] M. Weiss, L. Hufnagel, and R. Ketzmerick: *Can simple renormalization theories describe the trapping of chaotic trajectories in mixed systems?*, Phys. Rev. E **67** (2003), 046209.

[49] J. P. Keating and F. Mezzadri: *Pseudo-symmetries of Anosov maps and spectral statistics*, Nonlinearity **13** (2000), 747–775.

[50] S.-J. Chang and K.-J. Shi: *Evolution and exact eigenstates of a resonant quantum system*, Phys. Rev. A **34** (1986), 7–22.

[51] R. Ketzmerick: *Chaos and quantum chaos*, University Lecture, Technische Universität Dresden, (2005).

[52] F. Grossmann: *Theoretical Femtosecond Physics: Atoms and Molecules in Strong Laser Fields*, Springer series on atomic, optical and plasma physics, (Springer, Berlin, Heidelberg), (2008).

[53] S. Löck: *Dynamical Tunneling in Systems with a Mixed Phase Space*, Ph.D. thesis, Technische Universität Dresden, Fachbereich Physik, (2010).

[54] A. Ishikawa, A. Tanaka, and A. Shudo: *Quantum suppression of chaotic tunnelling*, J. Phys. A - Math. Theor. **40** (2007), F397–F405.

[55] N. V. C. Efthymiopoulos, G. Contopoulos and R. Dvorak: *Stickiness and cantori*, J. Phys. A - Math. Gen. **30** (1997), 8167–8186.

[56] M. V. Berry and J. P. Keating: *A rule for quantizing chaos?*, J. Phys. A **23** (1990), 4839–4849.

[57] J. P. Keating: *Periodic orbit resummation and the quantization of chaos*, Proc. R. Soc. Lon. Ser. A **436** (1992), 99–108.

[58] M. V. Berry and J. P. Keating: *A new asymptotic representation for $\zeta(\frac{1}{2}+it)$ and quantum spectral determinants*, Proc. R. Soc. Lon. Ser. A **437** (1992), 151–173.

[59] F. Haake: *Quantum Signatures of Chaos*, (Springer-Verlag, Berlin), 3rd edn., (2010).

[60] E. J. Heller: *Bound-State Eigenfunctions of Classically Chaotic Hamiltonian Systems: Scars of Periodic Orbits*, Phys. Rev. Lett. **53** (1984), 1515–1518.

[61] C. H. Lewenkopf and R. O. Vallejos: *Open orbits and the semiclassical dwell time*, J. Phys. A - Math. Gen. **37** (2004), 131.

[62] C. H. Lewenkopf and R. O. Vallejos: *Classical-quantum correspondence for the scattering dwell time*, Phys. Rev. E **70** (2004), 036214.

[63] J. Kuipers and M. Sieber: *Semiclassical relation between open trajectories and periodic orbits for the Wigner time delay*, Phys. Rev. E **77** (2008), 046219.

[64] C. Cohen-Tannoudji: *Quantum Mechanics Vol. 2*, (Wiley, New York), (1995).

[65] U. Smilansky, S. Tomsovic, and O. Bohigas: *Spectral fluctuations and transport in phase space*, J. Phys. A - Math. Gen. **25** (1992), 3261.

[66] O. Bohigas, S. Tomsovic, and D. Ullmo: *Classical transport effects on chaotic levels*, Phys. Rev. Lett. **65** (1990), 5–8.

[67] M. L. Mehta: *Random Matrices*, (Elsevier Ltd.), 3rd edn., (2004).

[68] O. Bohigas, M.-J. Giannoni, and C. Schmit: *Characterization of chaotic quantum spectra and universality of level fluctuation laws*, Phys. Rev. Lett. **52** (1984), 1–4.

[69] J. B. French, V. K. B. Kota, A. Pandey, and S. Tomsovic: *Statistical properties of many-particle spectra V. Fluctuations and symmetries*, Ann. Phys. **181** (1988), 198 – 234.

[70] T. Guhr and H. A. Weidenmüller: *Isospin mixing and spectral fluctuation properties*, Ann. Phys. **199** (1990), 412 – 446.

[71] C. Ellegaard, T. Guhr, K. Lindemann, J. Nygård, and M. Oxborrow: *Symmetry Breaking and Spectral Statistics of Acoustic Resonances in Quartz Blocks*, Phys. Rev. Lett. **77** (1996), 4918–4921.

[72] H. Alt, C. I. Barbosa, H.-D. Gräf, T. Guhr, H. L. Harney, R. Hofferbert, H. Rehfeld, and A. Richter: *Coupled Microwave Billiards as a Model for Symmetry Breaking*, Phys. Rev. Lett. **81** (1998), 4847–4850.

[73] C. I. Barbosa and H. L. Harney: *Analyzing symmetry breaking within a chaotic quantum system via Bayesian inference*, Phys. Rev. E **62** (2000), 1897–1904.

[74] C. I. Barbosa, T. Guhr, and H. L. Harney: *Impact of isospin breaking on the distribution of transition probabilities*, Phys. Rev. E **62** (2000), 1936–1949.

[75] B. Dietz, T. Guhr, H. L. Harney, and A. Richter: *Strength Distributions and Symmetry Breaking in Coupled Microwave Billiards*, Phys. Rev. Lett. **96** (2006), 254101.

[76] J. X. de Carvalho, M. S. Hussein, M. P. Pato, and A. J. Sargeant: *Symmetry-breaking study with deformed ensembles*, Phys. Rev. E **76** (2007), 066212.

[77] H.-J. Stöckmann: private communication, (2008).

[78] H. Waalkens, R. Schubert, and S. Wiggins: *Wigner's dynamical transition state theory in phase space: classical and quantum*, Nonlinearity **21** (2008), R1–R118.

[79] S. Tomsovic: private communication, (2011).

[80] H. A. Fertig and B. I. Halperin: *Transmission coefficient of an electron through a saddle-point potential in a magnetic field*, Phys. Rev. B **36** (1987), 7969–7976.

[81] F. Mezzadri: *How to generate random matrices from the classical compact groups*, Not. Am. Math. Soc. **54** (2007), 592–604.

[82] F. Haake: *Quantum Signatures of Chaos*, (Springer-Verlag, Berlin), 2nd edn., (2001).

[83] H.-J. Stöckmann: *Quantum Chaos an introduction*, (Cambrige university press), (2000).

[84] F. J. Dyson and M. L. Mehta: *Random Matrices and the statistical theory of energy levels IV*, J. Math. Phys. **4** (1963), 701–712.

[85] M. Sieber and K. Richter: *Correlations between periodic orbits and their rôle in spectral statistics*, Phys. Scripta **T90** (2001), 128–133.

[86] O. Bohigas: *Random matrix theories and chaotic dynamics*, in: *Chaos and Quantum Physics* (Eds. M. J. Giannoni, A. Voros and J. Zinn-Justin), Les Houches 1989 Session L II, 87–199. North-Holland, Amsterdam, (1991).

[87] R. E. Prange: *The Spectral Form Factor Is Not Self-Averaging*, Phys. Rev. Lett. **78** (1997), 2280–2283.

[88] M. V. Berry: *Semiclassical theory of spectral rigidity*, Proc. R. Soc. Lon. Ser. A **400** (1985), 229–251.

[89] J. Kuipers: private communication, (2011).

[90] M. V. Berry and M. Tabor: *Level clustering in the regular spectrum*, Proc. R. Soc. Lon. Ser. A **356** (1977), 375–394.

[91] M. V. Berry and M. Robnik: *Semiclassical level spacings when regular and chaotic orbits coexist*, J. Phys. A **17** (1984), 2413–2421.

[92] D. M. Leitner: *Real symmetric random matrix ensembles of Hamiltonians with partial symmetry breaking*, Phys. Rev. E **48** (1993), 2536–2546.

[93] A. Bäcker, R. Ketzmerick, S. Löck, and N. Mertig: *Fractional-Power-Law Level Statistics Due to Dynamical Tunneling*, Phys. Rev. Lett. **106** (2011), 024101.

# Acknowledgments

---

The plots in this thesis were generated with the software PyXGraph which simplifies the usage of PyX (http://pyx.sourceforge.net/). The programs for numerical computations were written in Python (http://www.python.org) using NumPy and SciPy (http://www.scipy.org).

# Erklärung

Hiermit versichere ich, dass ich die vorliegende Arbeit ohne unzulässige Hilfe Dritter und ohne Benutzung anderer als der angegebenen Hilfsmittel angefertigt habe; die aus fremden Quellen direkt oder indirekt übernommenen Gedanken sind als solche kenntlich gemacht. Die Arbeit wurde bisher weder im Inland noch im Ausland in gleicher oder ähnlicher Form einer anderen Prüfungsbehörde vorgelegt.

Die Dissertation wurde in der Zeit März 2008 bis Juli 2011 unter der Betreuung von Herrn Prof. Dr. Roland Ketzmerick am Institut für Theoretische Physik der Technischen Universität Dresden angefertigt. Es haben keine früheren erfolglosen Promotionsverfahren stattgefunden. Ich erkenne die Promotionsordnung der Fakultät Mathematik und Naturwissenschaften an der Technischen Universität Dresden vom 23. Februar 2011 an.

Dresden, den 19.07.2011

Matthias Michler